DOCTORAL THESIS

Analysis of the Interaction of Halide Perovskite with Other Materials and its Effect on the Performance of Optoelectronic Devices

AUTHOR: NGO THI TUYEN
SUPERVISOR: IVÁN MORA SERÓ

UJI UNIVERSITAT JAUME I

UNIVERSITAT JAUME I

Universitat Jaume I, Doctoral School

Doctoral Programme in Science

Analysis of the Interaction of Halide Perovskite with Other Materials and its Effect on the Performance of Optoelectronic Devices

Report submitted in order to be eligible for a doctoral degree awarded by the Universitat Jaume I

Author

NGO THI TUYEN

Supervisor

IVAN MORA SERO

Castellón de la Plana, September 2019

<u>Funding</u>

Content

Annex I: Abbreviation and Acronym List

HP	Halide perovskite
PCE	Photoconversion efficiency
LED	Light emitting diode
MAPI	Methylammonium lead iodide
QDs	Colloidal quantum dots
C_{QDs}	Concentration of quantum dots
ETM	Electron transport material
ESC	Electron selective contact
HTM	Hole transport material
CB	Conduction band
VB	Valence band
PL	Photoluminescence
EL	Electroluminescence
IBSC	Intermediate band gap solar cell
MAI	Methylammonium iodide
MA	Methylammonium
FA	Formamidinium
FAI	Formamidinium iodide
CsPI	Cesium lead iodine
ABA	4-aminobenzoic acid
J-V curve	Current-Potential curve or current-voltage curve
E_g	Bandgap
3D, 2D, 1D, 0D	3, 2, 1 and 0 dimensions respectively
TEM	Transmission electron microscopy
PLQY	Photoluminescence quantum yield
SILAR	Successive ionic layer deposition
CBD	Chemical bath deposition
LiTFSI	Lithium bis(trifluoromethanesulfonyl)imide
HUMO	Highest occupied molecular orbital
LOMO	Lowest unoccupied molecular orbital
HATNA	Hexaazatrinaphthylene
APTES	3-aminopropyltriethoxysilane
SAM	Self-assembled monolayer
EDTA	Ethylene diamine tetraacetic acid
IPFB	Iodopentafluorobenzene
IDIC	Indacenodithiophene end-capped with 1.1-dicyanomethylene-3-indanone
DCL97	Bisthiadiazolefused tetraazapentacenequinone
PCBM	Phenyl-C61-butyric acid methyl ester
ALD	Atomic layer deposition

XPS	X-ray photoelectron spectroscopy
PEIE	Polyethylenimine ethoxylate
XRD	X-ray diffraction
DMF	N,N-dimethylformamide
DMSO	Dimethyl sulfoxide
SEM	Scanning electron microscopy
FWHM	Full width at half maximum
EDS	Energy dispersive x-ray spectrometer
WDS	Wavelength dispersive x-ray spectrometer
PV effect	Photovoltaic effect
E_{Fn}	Fermi level of electron
E_{Fh}	Fermi level of hole
V_F	Fermi voltage
R_s	Series resistance
J_{SC}	Short circuit photocurrent
V_{oc}	Open circuit voltage
P_m	Maximum power
J_m and V_m	Current and voltage values at maximum power
IPCE	Incident photon to current efficiency
q	Elementary charge
$\phi_{ph}(\lambda)$	Incident photon flux
λ	Wavelength
IS	Impedance spectroscopy
$\eta_{extraction}$	Extraction efficiency
eQE	External quantum efficiency
iQE	Internal quantum efficiency
n	Refractive index
NIR	Near infrared
HRTEM	High resolution transmission electron microscopy
STEM	Scanning tunneling electron microscope
DFT	Density functional theory
TA	Transient absorption
PSC	Perovskite solar cell
HMS	Hexamethyldisilathiane
ODE	1-octadecene
SRH recombination	Shockley-Read-Hall recombination
TPBI	2,2′,2″-(1,3,5-benzinetriyl)-tris(1-phenyl-1-H-benzimidazole)
DSSC	Dye-sensitized solar cell

Annex II: Published Papers

Publications included in this Thesis

1. Interaction Between Colloidal Quantum Dots and Halide Perovskites: Looking for Constructive Synergies. Thi Tuyen Ngo, Ivan Mora-Seró. Journal of Physical Chemistry Letters, 2019, *10,* 1099-1108

2. Single step deposition of an interacting layer of a perovskite matrix with embedded quantum dots. Thi Tuyen Ngo, Isaac Suarez, Rafael S. Sanchez, Juan P. Martinez-Pastor and Ivan Mora-Sero. Nanoscale, 2016, 8, 14379–14383

3. PbS Quantum Dots as Additives in Methylammonium Halide Perovskite Solar Cells: the Effect of Quantum Dot Capping. Thi Tuyen Ngo, Sofia Masi, P. F. Mendez, Miri Kazes, Dan Oron, and Iván Mora Seró. Nanoscale Adv., 2019,1, 4109-4118

4. Enhancement of the Performance of Perovskite Solar cells, LEDs and Optical Amplifiers by Anti-Solvent Additive Deposition. Thi Tuyen Ngo, Isaac Suarez, Gabriella Antonicelli, Diego Cortizo-Lacalle, Juan P. Martinez-Pastor, Aurelio Mateo-Alonso and Ivan Mora-Sero, Adv. Mater. 2017, 1604056

5. Spray-Pyrolyzed ZnO as Electron Selective Contact for Long-Term Stable Planar $CH_3NH_3PbI_3$ Perovskite Solar Cells. Thi Tuyen Ngo, Eva M. Barea, Ramon Tena-Zaera, and Iván Mora-Seró. ACS Appl. Energy Mater., 2018, 1 (8), pp 4057–4064

Publications not included in this Thesis

1. Perovskite-quantum dots interface: Deciphering its ultrafast charge carrier Dynamics. Pavel Galar, Piotr Piatkowski, Thi Tuyen Ngo, Mario Gutiérrez, Iván Mora-Ser, Abderrazzak Douhal. Nano Energy 49 (2018) 471–480

2. Impedance Spectroscopy Measurements in Perovskite Solar Cells: Device Stability and Noise Reduction. Pitarch-Tena, Didac; Ngo, Thi Tuyen; Valles-Pelarda, Marta; Pauporte, Thierry; Mora-Sero, Ivan. ACS Energy Letters, 2018, 3, 1044-1048

3. Homeopathic Perovskite Solar Cells: Effect of Humidity during Fabrication on the Performance and Stability of the Device. Contreras-Bernal, L.; Aranda, C.; Vallés-Pelarda, M.; Ngo, T.Tuyen; Ramos-Terrón, S.; Gallardo, J.Jesús; Navas, J.; Guerrero, A.; Mora-Seró, I.; Idígoras, J.; Anta, J.A. Journal of Physical Chemistry C, 2018, 122, 5341−5348.

4. Electron Transport Layer-Free Solar Cells Based on Perovskite–Fullerene Blend Films with Enhanced Performance and Stability. Jorge Pascual, Ivet Kosta, T. Tuyen Ngo, Andrey Chuvilin, German Cabanero, Hans J. Grande, Eva M. Barea, Ivan Mora-Sero, Juan Luis Delgado and Ramon Tena-Zaera. ChemSusChem 2016, 9, 1 – 8

Acknowledgement

First of all, I am heartily thankful my supervisor, associate professor Dr. Iván Mora-Seró who has guided and supported me from the initial to the final state of my doctoral study. His great expertise in film and device characterization such as photoluminescence, electroluminescence and impedance spectroscopy has allowed me getting a solid knowledge in the photovoltaic field. Our scientific discussion has always been very insightful and extraordinary creative which permits me to have a through grasp of project.

Next, I am very grateful to professor Dr. Juan Bisquert Mascarell who has brought me to the extremely interest project. He has always followed, encouraged and provided expert advices which significantly contributed to my progress during four years of doctoral study.

It is a pleasure for me to thank to professor Dr. Dan Oron who was the responsible of my international research stay at the Weizmann Institute of Science, Israel. He has transferred me his experience in the synthesis and characterization of colloidal quantum dots which is a crucially important part of my study. It is also a pleasure to thank Dr. Miri Kazes for giving me very useful advices to improve my study and for her help to adapt a new environment during my stay at Weizmann Institute of Science.

I would like to express my thankfulness to Dr. Antonio Abate for his supervision and his kind help during my research stay at the Helmholtz Zentrum Berlin, Germany.

It is an honour for me to thank the Ministerio de Economía y Competitividad of Spain for the financial support for my doctoral study at the Institute of Advanced Materials (INAM) of Jaume I university (UJI), Spain and for my international research stays at the Weizmann Institute of Science, Israel and at the Helmholtz Zentrum Berlin, Germany.

I would like to sincerely acknowledge to Dr. Isaac Zarazua for revising the parts of 'the current-voltage characteristic' and 'impedance spectroscopy' of this thesis.

And I am also appreciative to associate professor Dr. Francisco Fabregat-Santiago who involved me to the teaching activity at the Jaume I

university. This has been a great opportunity for me to perceive and improve a very important skill which is essential for my future career.

I owe my deeply gratitude to my family who has always supports me with joy and love. In particular my husband who always takes care of me and our little son with his boundless love. And I would like to thank my mother who all the time stands by my side and cheers on me.

Finally, I would like to acknowledge all my colleagues and my collaborators for helping and giving me useful suggestions during my doctoral study. A particularly warm to thank to my friends who spent memorable moments with. And lastly, I offer my regards and blessings to all of those who supported me in any aspect during the completion my doctoral study.

Abstract

Halide perovskite (HP) materials have recently attracted worldwide attention due to its fast progress in photovoltaic community. Photoconversion efficiencies (PCEs) of solar cells based on HP have increased quickly from 3.8% in 2009[1] to over 25%[2] in 2019, for single junction architecture exceeding the maximum efficiencies achieved with CdTe (22.1%) and CIGS (22.9%).[2] Moreover, HPs have been also applied not only for the preparation of high efficiency solar cells, but also photodetectors,[3] light emitting diodes (LEDs),[4-7] light amplifier[8-9] and lasers.[10-13] Such huge promising range of optoelectronic application is due to the outstanding versatility of HP materials. Structurally all components of HPs, with general chemical formula AMX_3, can be easily changed/modified for adapting the specific requirement of a concrete optoelectronic application. For an example different dimensionalities of HPs can be obtained by controlling the size of an organic cation A. In addition to this versatility the success of HPs is based on the low non-radiative recombination, even for polycrystalline samples, due to a benign defect physics.[14] Furthermore HPs can be prepared from solution methods at low temperatures and, consequently, using low cost fabrication techniques. Solution processes facilitate HPs to combine easily with other materials.

Combinations of materials with different nature has been a successful strategy in order to develop new materials with enhanced properties. As demonstrated in the past, adobe, stained glass and stainless steel are just some testimonies of great combined materials which have been supported for human life since centuries. This strategy is still useful nowadays when the development of chemistry, quantum mechanics and nanotechnology has created a revolution of material science. In the same strategy, the purpose of this thesis is to investigate the interaction of HP with other materials, in order to obtain properties and/or devices with enhanced functionalities and performance by the synergistic combination of different materials. Within the scope of this thesis, we have studied the interaction of methylammonium lead iodide (MAPI) HP with colloidal quantum dots (QDs), organic molecules and electron transport materials (ETMs).

QDs have been chosen for the combination with HP because QDs offer a huge versatility of optoelectronic properties such as tunable band gap, strong emission with highly pure color which are simply tuned by size or shape control due to the confinement effect. And QDs have been potentially applied in different optoelectronic devices such as LEDs[15-16] and solar cells.[17-18]

Among the different semiconductor colloidal QDs, in this thesis we selected PbS QDs to study their interaction with HP because those materials possess a similar crystal structure with a relatively low lattice mismatch.[19] The interaction of HP and QDs has been studied in the situation in which QDs were embedded in MAPI perovskite matrix. The presence of both PbS QDs and their capping ligands have a strong impact on the formation of HP. Small density of QDs intermixed in the precursor solution serves as nucleation centers promoting the growth of HP along a preferred direction. As a result, the morphological, optical and structural properties of HP were significantly improved. Consequently the performance of solar cells based on HP with embedded QDs was enhanced. Interestingly the properties and hybrid HP-QD films and those based devices were also dependent on the QD capping ligands. Moreover, the interaction between MAPI HP and QDs also resulted in a new property which is an emission of the exciplex state at energy lower than that of both HP and QDs.

Within the scope of this thesis we also studied the interaction of HP with organic molecules because organic molecules are very flexible materials. They present an unlimited number of structures that can be potentially synthesized and easily modified to meet the requirements of specific applications. In our study, organic molecules were introduced to HP films through the anti-deposition step. We have found that those organic molecules were preferentially located at the grain boundaries of HP. At the grain boundaries the structural disorders potentially can form defect states that can contribute to the degradation of the optoelectronic quality of the HP films. We show that the presence of organic molecules passivated efficiently those grain boundaries. Consequently, we obtained an improvement in performance of three different optoelectronic devices (solar cells, LEDs, and light amplifiers) based on HP with organic additives, comparing with references (without organic molecules).

Electron transport materials (ETMs) are very important in the performance of optoelectronic devices as they decide how efficient electrons can be extracted or injected. Additionally, in n-i-p configuration ETMs also have a crucial role on the formation of HP as it is directly deposited on ETM. It has been previously demonstrated that many factors of ETMs including nature,[20] roughness,[21] temperature,[22] crystallinity[23] and structure[24] affecting on the formation and thermal stability of HP films. In this thesis, we studied the interaction of HP with spray-pyrolyzed ZnO ETMs. And we found that different termination of ZnO surfaces, obtained by different gas component used during the spray pyrolysis, not only influences the formation of fresh MAPI HP films but also their evolution during storage and finally impacts in

the long-term stability of device performance. As a result, our HP solar cells based on ZnO ETMs showed not only a good stability but also an improvement in performance even after more than one month of preparation, under the storage condition of 35% humidity.

Through the study of the interaction of HP with three different materials and in three different situations where the interaction takes place including underneath, inside and up surface of HP layers, we demonstrate that combining HP with other materials of different nature is a promising strategy in order to create new material composites with enhanced properties which strongly influence, in turn, the optoelectronic development.

Resumen

Los materiales de perovskita de haluro (HP) han atraído recientemente la atención mundial debido a su rápido progreso en la comunidad fotovoltaica. Las eficiencias de fotoconversión (PCE) de las células solares basadas en HP han aumentado rápidamente de 3.8% en 2009[1] a más de 25%[2] en 2019, para una arquitectura de unión única que excede las eficiencias máximas logradas con CdTe (22.1%) y CIGS (22.9%).[2] Además, los HP también se han aplicado no solo para la preparación de células solares de alta eficiencia, sino también para fotodetectores,[3] diodos emisores de luz (LEDs),[4-7] amplificadores de luz[8-9] y láser.[10-13] Este prometedor rango de aplicaciones optoelectrónicas se debe a la excelente versatilidad de los materiales HP. Estructuralmente, todos los componentes de HP, con la fórmula química general AMX_3, pueden cambiarse/modificarse fácilmente para adaptar los requisitos específicos de una aplicación optoelectrónica en concreto. Por ejemplo, se pueden obtener diferentes dimensionalidades de los HP controlando el tamaño del catión orgánico A. Además de esta versatilidad, el éxito de los HP se basa en la baja recombinación no radiativa, incluso para muestras policristalinas, debido a un defecto físico benigno.[14] Adicionalmente, los HP pueden prepararse a partir de métodos de solución a bajas temperaturas, utilizando en consecuencia técnicas de fabricación de bajo costo. Los procesos de solución facilitan que los HP se combinen fácilmente con otros materiales.

Las combinaciones de materiales de diferente naturaleza han sido una estrategia exitosa para desarrollar nuevos materiales con propiedades mejoradas. Como se demostró en el pasado, el adobe, las vidrieras y el acero inoxidable son solo algunos testimonios de excelentes materiales combinados que han sido respaldados por la vida humana desde hace siglos. Esta estrategia sigue siendo útil hoy en día cuando el desarrollo de la química, la mecánica cuántica y la nanotecnología ha creado una revolución en la ciencia de los materiales. En esta línea, el objetivo de esta tesis es investigar la interacción de HP con otros materiales a fin de obtener propiedades y/o dispositivos con funcionalidades y rendimiento mejorados mediante la combinación sinérgica de diferentes materiales. Durante el curso de esta tesis, hemos estudiado la interacción del yoduro de plomo de metilamonio (MAPI) HP con puntos cuánticos coloidales (QD), moléculas orgánicas y materiales de transporte de electrones (ETM).

Los QD se han elegido para la combinación con HP porque los QD ofrecen una gran versatilidad de propiedades optoelectrónicas, como un intervalo de banda sintonizable, una fuerte emisión con colores muy puros que simplemente se ajustan por control de tamaño o forma debido al efecto de confinamiento. Los QD se han aplicado potencialmente en diferentes dispositivos optoelectrónicos como los LEDs[15-16] y las células solares.[17-18] Entre los diferentes QD coloidales de semiconductores, en esta tesis seleccionamos PbS QD para estudiar su interacción con HP porque esos materiales poseen una estructura cristalina similar con un desajuste de red relativamente bajo.[19] La interacción de HP y QD se ha estudiado en la situación en la que los QD se integraron en la matriz de perovskita MAPI. La presencia de ambos PbS QD y sus ligandos de protección tienen un fuerte impacto en la formación de HP. La pequeña densidad de QD entremezclados en la solución precursora sirve como centros de nucleación que promueven el crecimiento de HP en una dirección preferida. Como resultado, las propiedades morfológicas, ópticas y estructurales de HP mejoraron significativamente. En consecuencia, se mejoró el rendimiento de las células solares basadas en HP con QD integrados. Curiosamente, las propiedades y las películas híbridas de HP-QD y los dispositivos basados también dependían de los ligandos de protección QD. Además, la interacción entre MAPI HP y QD también dio como resultado una nueva propiedad que es una emisión del estado exciplex a una energía inferior a la de HP y QD.

Dentro del alcance de esta tesis, también estudiamos la interacción de HP con moléculas orgánicas porque las moléculas orgánicas son materiales muy flexibles. Presentan un número ilimitado de estructuras que pueden sintetizarse y modificarse fácilmente para cumplir con los requisitos de aplicaciones específicas. En nuestro estudio, las moléculas orgánicas se introdujeron en las películas de HP a través del paso de anti-deposición. Hemos encontrado que esas moléculas orgánicas se ubicaban preferentemente en los límites de grano de HP. En los límites del grano, los trastornos estructurales pueden potencialmente formar estados de defectos que pueden contribuir a la degradación de la calidad optoelectrónica de las películas de HP. Mostramos que la presencia de moléculas orgánicas pasivaba eficientemente esos límites de grano. En consecuencia, obtuvimos una mejora en el rendimiento de tres dispositivos optoelectrónicos diferentes (células solares, LED y amplificadores de luz) basados en HP con aditivos orgánicos, en comparación con las referencias (sin moléculas orgánicas).

Los materiales de transporte de electrones (ETM) son muy importantes en el rendimiento de los dispositivos optoelectrónicos, ya que deciden cómo se pueden extraer o inyectar electrones eficientemente. Además, en la

configuración n-i-p, los ETM también tienen un papel crucial en la formación de HP, ya que se deposita directamente en ETM. Se ha demostrado previamente que muchos factores de ETM incluyen la naturaleza,[20] la rugosidad,[21] la temperatura,[22] la cristalinidad[23] y la estructura[24] que afectan la formación y la estabilidad térmica de las películas de HP. En esta tesis, estudiamos la interacción de HP con ZnO ETM pirolizados por pulverización. Y descubrimos que la terminación diferente de las superficies de ZnO, obtenida por diferentes componentes de gas utilizados durante la pirólisis por pulverización, no solo influye en la formación de películas frescas de MAPI HP, sino también en su evolución durante el almacenamiento y finalmente impacta en la estabilidad a largo plazo del rendimiento del dispositivo. Como resultado, nuestras células solares HP basadas en ZnO ETM mostraron no solo una buena estabilidad sino también una mejora en el rendimiento incluso después de más de un mes de preparación, en condiciones de almacenamiento de 35% de humedad.

A través del estudio de la interacción de HP con tres materiales diferentes y en tres situaciones diferentes donde la interacción se lleva a cabo, incluida la superficie interior y superior de las capas de HP, demostramos que combinar HP con otros materiales de diferente naturaleza es una estrategia prometedora para para crear nuevos materiales compuestos con propiedades mejoradas que influyan fuertemente, a su vez, en el desarrollo optoelectrónico.

References

1. Kojima, A.; Teshima, K.; Shirai, Y.; Miyasaka, T. Organometal Halide Perovskites as Visible-Light Sensitizers for Photovoltaic Cells. *Journal of the American Chemical Society* **2009,** *131* (17), 6050-6051.
2. NREL photovoltaic efficiency chart: https://www.nrel.gov/pv/cell-efficiency.html
3. Dou, L.; Yang, Y.; You, J.; Hong, Z.; Chang, W.-H.; Li, G. Solution-processed hybrid perovskite photodetectors with high detectivity. *Nat Commun* **2014,** *5*.
4. Jaramillo-Quintero, O. A.; Sanchez, R. S.; Rincon, M.; Mora-Sero, I. Bright Visible-Infrared Light Emitting Diodes Based on Hybrid Halide Perovskite with Spiro-OMeTAD as a Hole-Injecting Layer. *The journal of physical chemistry letters* **2015,** *6* (10), 1883-1890.
5. Tan, Z.-K.; Moghaddam, R. S.; Lai, M. L.; Docampo, P.; Higler, R.; Deschler, F.; Price, M.; Sadhanala, A.; Pazos, L. M.; Credgington, D.; Hanusch, F.; Bein, T.; Snaith, H. J.; Friend, R. H. Bright light-emitting diodes based on organometal halide perovskite. *Nat Nano* **2014,** *9* (9), 687-692.
6. Alivisatos, A. P. Semiconductor Clusters, Nanocrystals, and Quantum Dots. *Science* **1996,** *271*, 933-937.
7. Lin, K.; Xing, J.; Quan, L. N.; de Arquer, F. P. G.; Gong, X.; Lu, J.; Xie, L.; Zhao, W.; Zhang, D.; Yan, C.; Li, W.; Liu, X.; Lu, Y.; Kirman, J.; Sargent, E. H.; Xiong, Q.; Wei, Z. Perovskite light-emitting diodes with external quantum efficiency exceeding 20 per cent. *Nature* **2018,** *562* (7726), 245-248.
8. Suárez, I.; Juárez-Pérez, E. J.; Bisquert, J.; Mora-Seró, I.; Martínez-Pastor, J. P. Polymer/Perovskite Amplifying Waveguides for Active Hybrid Silicon Photonics. *Advanced materials* **2015,** *27* (40), 6157-6162.
9. Suárez, I.; Hassanabadi, E.; Maulu, A.; Carlino, N.; Maestri, C. A.; Latifi, M.; Bettotti, P.; Mora-Seró, I.; Martínez-Pastor, J. P. Integrated Optical Amplifier–Photodetector on a Wearable Nanocellulose Substrate. *Advanced Optical Materials* **2018,** *6* (12), 1800201.
10. Deschler, F.; Price, M.; Pathak, S.; Klintberg, L. E.; Jarausch, D.-D.; Higler, R.; Hüttner, S.; Leijtens, T.; Stranks, S. D.; Snaith, H. J.; Atatüre, M.; Phillips, R. T.; Friend, R. H. High Photoluminescence Efficiency and Optically Pumped Lasing in Solution-Processed Mixed Halide Perovskite Semiconductors. *The journal of physical chemistry letters* **2014,** *5* (8), 1421-1426.
11. Zhu, H.; Fu, Y.; Meng, F.; Wu, X.; Gong, Z.; Ding, Q.; Gustafsson, M. V.; Trinh, M. T.; Jin, S.; Zhu, X. Y. Lead halide perovskite nanowire lasers with low lasing thresholds and high quality factors. *Nature materials* **2015,** *14* (6), 636-642.
12. Xing, G.; Mathews, N.; Lim, S. S.; Yantara, N.; Liu, X.; Sabba, D.; Grätzel, M.; Mhaisalkar, S.; Sum, T. C. Low-temperature solution-processed wavelength-tunable perovskites for lasing. *Nature materials* **2014,** *13* (5), 476-480.

13. Stranks, S. D.; Hoye, R. L. Z.; Di, D.; Friend, R. H.; Deschler, F. The Physics of Light Emission in Halide Perovskite Devices. *Advanced materials* **2018,** *0* (0), 1803336.
14. Wang, F.; Bai, S.; Tress, W.; Hagfeldt, A.; Gao, F. Defects engineering for high-performance perovskite solar cells. *npj Flexible Electronics* **2018,** *2* (1), 22.
15. Shirasaki, Y.; Supran, G. J.; Bawendi, M. G.; Bulovic, V. Emergence of colloidal quantum-dot light-emitting technologies. *Nat Photon* **2013,** *7* (1), 13-23.
16. Pal, B. N.; Ghosh, Y.; Brovelli, S.; Laocharoensuk, R.; Klimov, V. I.; Hollingsworth, J. A.; Htoon, H. 'Giant' CdSe/CdS core/shell nanocrystal quantum dots as efficient electroluminescent materials: strong influence of shell thickness on light-emitting diode performance. *Nano letters* **2012,** *12* (1), 331-6.
17. Nozik, A. J. Quantum Dot Solar Cells. *Physica E* **2002,** *14*, 115-200.
18. Lan, X.; Voznyy, O.; García de Arquer, F. P.; Liu, M.; Xu, J.; Proppe, A. H.; Walters, G.; Fan, F.; Tan, H.; Liu, M.; Yang, Z.; Hoogland, S.; Sargent, E. H. 10.6% Certified Colloidal Quantum Dot Solar Cells via Solvent-Polarity-Engineered Halide Passivation. *Nano letters* **2016,** *16* (7), 4630-4634.
19. Ning, Z.; Gong, X.; Comin, R.; Walters, G.; Fan, F.; Voznyy, O.; Yassitepe, E.; Buin, A.; Hoogland, S.; Sargent, E. H. Quantum-dot-in-perovskite solids. *Nature* **2015,** *523* (7560), 324-328.
20. Olthof, S.; Meerholz, K. Substrate-dependent electronic structure and film formation of MAPbI3 perovskites. *Scientific reports* **2017,** *7*, 40267.
21. Climent-Pascual, E.; Hames, B. C.; Moreno-Ramírez, J. S.; Álvarez, A. L.; Juarez-Perez, E. J.; Mas-Marza, E.; Mora-Seró, I.; de Andrés, A.; Coya, C. Influence of the substrate on the bulk properties of hybrid lead halide perovskite films. *Journal of Materials Chemistry A* **2016,** *4* (46), 18153-18163.
22. Zhang, H.; Zhao, C.; Li, D.; Guo, H.; Liao, F.; Cao, W.; Niu, X.; Zhao, Y. Effects of substrate temperature on the crystallization process and properties of mixed-ion perovskite layers. *Journal of Materials Chemistry A* **2019,** *7* (6), 2804-2811.
23. Yang, D.; Yang, R.; Zhang, J.; Yang, Z.; Liu, S.; Li, C. High efficiency flexible perovskite solar cells using superior low temperature TiO2. *Energy & Environmental Science* **2015,** *8* (11), 3208-3214.
24. Grancini, G.; Marras, S.; Prato, M.; Giannini, C.; Quarti, C.; De Angelis, F.; De Bastiani, M.; Eperon, G. E.; Snaith, H. J.; Manna, L.; Petrozza, A. The Impact of the Crystallization Processes on the Structural and Optical Properties of Hybrid Perovskite Films for Photovoltaics. *The journal of physical chemistry letters* **2014,** *5* (21), 3836-3842.

<u>Statement</u>

This thesis has been prepared in the journal article compilation style format. The thesis is composed by five published articles and each one corresponds to one chapter. All the publications included in the thesis have been accepted by all co-authors.

Critical overview

An extensive use of renewable energies is mandatory to reduce the strong dependence on fossil fuels of today's society. Taking into account that solar energy on the earth's surface is an abundant and clean source, the conversion of this energy directly into electrical energy ready to be used -by means of the photovoltaic effect- appears as one of the most attractive strategies in order to achieve an energy-sustainable society. However, the challenge for the photovoltaic industry is determining how to efficiently and economically convert that incident solar energy into usable electricity. A tremendous amount of work has been done along the way to test and upgrade developments to produce a cost-effective photovoltaic solar energy product. Recently halide perovskite (HP) materials have been emerged looking extremely attractive for photovoltaic application due to their promising properties such as high absorption coefficient,[1] low non-radiative recombination with long carrier diffusion length[2] and good charge transport even in polycrystalline films.[3] The efficiencies of HP solar cells have been progressed quickly, reaching more than 25%[4] after the first report in 2009 with the efficiency of 3.8%.[5] Moreover, perovskite has been also applied in other optoelectronic devices such as light emitting diodes (LEDs),[6-9] light amplifier,[10-11] photodetectors[12] and lasers.[13-16] In addition, HPs can be prepared by solution processes at low temperature, consequently allowing to reduce the fabrication cost, and permits the easy combination of HPs with other materials.

Combing materials with different nature has been an important strategy in the development of material science. As demonstrated in the past, new materials with enhanced properties could be successfully created by integrating different materials. Indeed adobe, stained glass and stainless steel are just some examples of great interest materials obtained by the combination of other ones which have been supported for human life since centuries. In the regard of the advantage of combining materials and the interest of HPs materials, the purpose of this thesis is to investigate the interaction of HPs with other materials, being colloidal quantum dots (QDs), organic molecules and electron transport materials, and its effect for the photovoltaic application. The interaction was studied in three different situations where the interaction was carried out within the bulk HP film (interaction with QDs) and at the surfaces (at the top and bottom of HP films, interaction with organic molecules and ETMs respectively). The interaction has been studied not only in term of thin films but also in the full devices (solar cells and LEDs).

Interaction of halide perovskite (HP) with colloidal quantum dots (QDs). HPs have been broadly combined with different materials showing important advantages. QDs are one of these materials, which are especially interesting because their band gap energy can be tunable by controlling the QD sizes, they can be synthesized by relative simple synthetic routes allowing an easy integration with HP. Different QDs have been investigated in the combination with HPs.[17] However PbS QDs have been likely the most employed ones due to their deeply tunable band gap energy in the infrared range (IR) and also due to the relatively low lattice mismatch.[18] Due to these considerations, we employed PbS QDs to study their interaction with HPs, concretely methylammonium lead iodine (MAPI) perovskite.

In chapter III we presented a small critical review on the interaction of HPs and colloidal QDs, providing our own insight regarding the state-of-the-art. The combination of HP and PbS QDs have been focused on different objectives as (i) the use of the selective and transport properties of one of the compounds. Hybrid HP-QDs were applied in QD LED devices where QDs are the light emitter while HP acts as the carrier-transporting matrix.[19] On the other hand, when the HP-QD interface forms type I band alignment, and consequently the transported carriers in HP matrix can be injected into embedded PbS QDs where they recombine radiatively, resulting in an increase in LED external quantum efficiency. (ii) HP-QD composite has been used as co-sensitizers as well. As HPs absorb well the solar light in the visible region but not in the IR. The addition of PbS QDs allows to attain broader the absorption up to IR, resulting an increase in photocurrent.[20] (iii) Passivating QD surface by a HP shell, enhancing the QD solar cell device performance is also one objective of combining HPs and QDs. [21] (iv) Eventually, the combination of HP and QDs have been investigated for the implementation of advanced solar cell or LED configurations. PbS QDs have been used as additives in order to obtain a better HP crystallization. When proper amounts of PbS QDs were embedded into HP matrix, they act as effective seed-like sites to promote the formation of HP grains, resulting in substantial morphological improvements in terms of grain size, surface coverage and uniformity. Moreover the structural and optical properties of HP also became better, with an enhancement of crystallinity, radiative recombination[22] and absorbance.[23]

We developed a method for a single step deposition of HP with embedded PbS/CdS QDs, analyzing the implications in the structural and optical properties of the layers, chapter IV. Interestingly, the combination of these materials rise new properties which do not exist for single materials. By

using a relative large bandgap of PbS/CdS QDs, we formed the type II alignment at HP/QD interface. Thereby the electrons in HP conduction band (CB) can possibly combine with holes in QD valence band (VB), forming a so call exciplex state. We have verified this point detecting the photoluminescence (PL) and electroluminescence (EL) from exciplex states at energy lower than the bandgap of both HP and QDs. The exciplex emission was previously detected in previous work from our group in which MAPbI$_{3-x}$Cl$_x$ perovskite and PbS/CdS QDs forming a bi-layer (HP/QDs and QDs/HP).[24] However, in our study, PbS/CdS QDs were embedded in MAPI matrix. Consequently in our situation the interaction of HP and QDs can take place deeply in the bulk film while their interaction, in the case of bi-layers HP/QDs and QDs/HP, can occur only at the HP surface. Furthermore, according to the reciprocal principle, if an electron and hole from an exciplex state can recombine creating a photon, the reciprocal process in which a photon can generate an eletron-hole pair at the exciplex state is also possible. Embedding PbS QDs in HP matrix also opens the door for the preparation of intermediate band gap solar cells (IBSCs).

After the characterization of thin films, the effect of the synergy between HP and PbS Colloidal QDs in the performance of full devices, concretely of solar cells, was analyzed. It has been observed that the performance of solar cells based on HP-QD hybrid is enhanced.[22-23] In the agreement with the literature, we also obtained a higher quality of MAPI HP films, including both morphological, structural and optical properties, by embedding PbS QD additives in HP matrix, resulting an improvement in solar cell performance, chapter V. In addition, the improvement in the structural property of HP was further interpreted. We observed that HP precursors (PbI$_2$ and methylammonium iodine (MAI)) converted more efficiently to HP when PbS QDs were introduced, confirming by the reduction of PbI$_2$ intensity in x-ray diffraction (XRD) spectra. And the preferential orientation of HP crystallites along (110) plane direction which was also improved. Moreover the incorporation of PbS QDs also results an enhancement in crystallinity of both (110) and (220) HP crystalline planes. Importantly, by the first time our study showed that the capping ligands of PbS QD additives have a strong influence on the formation of HP and the subsequent performance of the fabricated devices. We embedded PbS QDs with three different capping ligands, being MAPI, cesium lead iodine (CsPI) and 4-aminobenzoic acid (ABA), into MAPI HP matrix. For all three QD capping ligands, the incorporation of QDs improved the properties of HP films including morphological, optical and structural properties. However at the same QD concentration, the extent of improvement is dependent on the capping ligand. ABA ligand showed a highest influence on the morphology, resulting a largest grain size of HP,

while CsPI ligand impacted strongly on the optical property, highest photoluminescence (PL) intensity, i.e. lowest non-radiative recombination, was observed when CsPI ligand is used. As a consequence of the dependence of HP with embedded QDs film quality on the QD capping ligands, the performance of planar devices was also ligand-dependent. Dominant improvement in device performance was achieved for the use of ABA capping ligand. With this study we provide an approach towards the design high quality of HPs via the use of PbS QDs and their ligands, which paves the way to obtain efficient photovoltaic devices, pointing to future further implementation of advanced technologies as IBSCs.

Interaction of halide perovskite (HP) with organic molecules. As mentioned above, HP has been broadly combined with different materials and organic molecules are one of the families of materials with those that HPs have been combined with, pursuing different objectives. First, organic molecules have been prevalently applied as the charge carrier selective contacts for both holes[25-27] and electrons[28-29] in HP optoelectronics due to their advantage of the easy tuning of molecular properties, for example the energy band alignment among other properties, and the deposition processes required low temperature. Second, they have been used as an interlayer which is inserted between electron transport layers (ETMs) and HP with different roles: (i) The coating of organic molecules on ETMs has been exercised to modify the ETM's surface energy, and consequently to adjust the morphological, structural and optical properties of HP film.[30-31] (ii) The organic molecules have been also employed to passivate ETM surface defects, resulting the improvement in the electron extraction,[32-34] reduction of the hysteresis of the Current-Potential (J-V) curve,[33,35] and non-radiative recombination.[35] Third, the organic molecules have been utilized to passivate HP surface through under-coordinated atoms (iodine or lead), reducing the non-radiative recombination caused by the electrons (or holes) trapped at these under-coordinated atoms.[36-37] Fourth, they have been also used not only to interact with HP surface but also within HP film to passivate HP defects in the bulk film.[38] Fifth, those molecules have been broadly used to enhance the long term stability of HPs films and devices, protecting them from the degradation sources such as moisture, in this case taking advantage of the hydrophobic character of the molecules used.[39-41]

In HP polycrystalline films grains and grain boundaries play an important role, despite the general benign character of defect in these materials. Structural disorder at grain boundaries potentially can create defect states which possibly can degrade the optoelectronic quality of HP films, reducing the performance of HP devices. In fact, the studies of Yun et al. using

the Kelvin probe force microscopy and conductive atomic force microscopy have shown that the grain boundaries and grain interiors have different electrical potentials and grain boundaries show faster ion migrations.[42] On the other hand, de Quilettes et al. pointed out that grain boundaries exhibit shorter charge carrier lifetime and lower PL intensity in a comparison with grain interiors.[43] Those reports suggest grain boundaries are likely to be preferred sites for ion accumulation and migration, causing the PL quenching and non-radiative recombination. Hence passivation of HP grain boundaries could be an efficient strategy to enhance the performance of HP optoelectronic devices. In this sense, within this thesis we have employed organic molecules, named a twisted hexaazatrinaphthylene (HATNA) and a bisthiadiazolefused tetraazapentacenequinone (DCL97), to passivate MAPI HP through their grain boundaries. As a result, we obtained the improvement in performance of three different optoelectronic devices including solar cells, LEDs and light amplifiers, comparing with reference cells without organic additives, chapter VI. In addition, we also provided a new approach to introduce organic additives into HP. In our approach, organic additives are dissolved in the anti-solvent and deposited during the anti-solve preparation step. Thereby this procedure facilities the film preparation as no any additional step needed and opens the possibility to introduce other additives, not only organic molecules but also other materials following a similar protocol.

Interaction of halide perovskite (HP) with electron transport materials (ETM). In optoelectronic devices, generally active layer is sandwiched between electron and hole transport layers. In the case of HP devices with n-i-p configuration, HP is directly deposited on ETM. Therefore ETMs also have a great influence on the formation and properties of HP films as well as their stability. Consequently the device performance and device stability are not only dependent on the electron extraction efficiency of ETMs but also on the induced properties of HP films. Many characters of ETMs have been previously reported, affecting on the growth of HPs. The nature of ETMs chemically decides the bondings created on the ETM's surface which strongly influences the active layer.[44] Besides, the structures of ETMs including planar and mesoporous architecture with different porosities also have a significant impact on the grain sizes of HP. In the mesoporous scaffold, the growth of HP is limited by the pore sizes while in the planar structure, there is no limitation. Therefore in general HP formed in scaffolds shows smaller grain sizes comparing with those prepared on planar structures.[45-46] Another factor affecting on the formation of HP is the temperature of ETM during the spin-coating of HP films. Higher ETM temperature causes the faster evaporation of solvents, precursors and/or byproducts of precursors which strongly impacts on the nuclei creation and growth of HP.[47-49] On the hand, ETMs

affect on the stability of coated HP films as well. Yang et al. showed that the condition of ETM's preparation, concretely the annealing temperatures of ZnO nanoparticle films, determines the thermal stability of MAPI perovskite. High ZnO's annealing temperatures accelerate the evaporation of hydroxyl group and residual acetate ligand from the ZnO nanoparticle synthesis which supposedly cause thermal degradation of MAPI. Thereby, HP films present higher thermal stability with ZnO ETM prepared at higher temperatures.[50]

Within this thesis, we additionally show that the ETM's preparation conditions influence on the evolution of coated HP films during the storage, chapter VII. We also analyzed the impact of ETMs on the performance of fresh and aged devices. Concretely changing gas components during the spray pyrolysis process, by using N_2 or O_2 flow, we modified the formation of ZnO ETMs. And we observed this modification slightly affects the morphology and structural properties of fresh MAPI HP films coated on ZnO spray-pyrolyzed with these two gas. However, the important feature was detected regarding to the aging films. After 15 days stored under dark, at room temperature and at humidity of 35%, the morphology and structural properties of HP layers deposited on those ZnO substrates changed oppositely, improvement for ZnO_N_2/HP and degradation for ZnO_O_2/HP samples. We also checked the performance and stability (under the same storage conditions listed above) of solar cells based on those ZnO ETMs. In agreement with observed features of fresh and aged HP films, the performance of fresh devices was similar however the ZnO_N_2 ETM based cells not only showed a good stability but also an enhancement in PCEs even after more than one month of preparation. While, for the solar cells based on ZnO_O_2/HP the PCEs started to reduce after 13 days of fabrication. Interestingly for ZnO_O_2 based solar cells PCEs could be further improved, still increasing after 30 prepared days, by adjusting the spray pyrolysis conditions as precursor concentrations and substrate temperatures.

In summary, within this thesis, we have studied the interaction HPs with three different materials (including QDs, organic molecules and ETM) and in three different situations where the interaction carries out (inside the HP bulk film and at the bottom and top HPs surfaces). In all cases, we realize that due to the intrinsic flexible structure of HP materials, HP is easily to form, to distort and to decompose. The formation and properties of HP as well as its stability are strongly influenced by other materials that HP is in contact with. For the interaction with ETMs which were used as substrates for HP growth, the surface characters of ETMs affected on not only the formation of HP but also on the evolution of HP films. With suitable properties of ETM surface, the stability of HP films and later on of HP device performance and long-term

stability could be significantly improved. The interaction with colloidal QDs (PbS and PbS/CdS) in which QDs were dissolved in the solutions containing HP precursors, in order to prepare HP layers with embedded QDs, seems to be more effective. The crystallization of HP films takes place faster as QDs act as seed-like sites for the nuclei creation. Therefore the concentration of intermixed QDs and as well as the QD's ligands have a strong effect on the morphology and properties of HP films. The combination of HP with organic molecules does not result the change in MAPI structure, but a clear interfacial effect. The function of these organic molecules is to passivate the defects at grain boundaries, improving the quality of HP optoelectronic devices. As a general conclusion, a well-designed interaction of HP with other materials can be a very efficient strategy to enhance the outstanding properties of HPs for the preparation of optoelectronic devices, increasing the quality and stability of HP films and devices. On the other hand, the interaction between HP and other materials, being QDs for our case, could produce new properties which potentially can contribution to the development of advanced devices.

References.

1. De Wolf, S.; Holovsky, J.; Moon, S.-J.; Löper, P.; Niesen, B.; Ledinsky, M.; Haug, F.-J.; Yum, J.-H.; Ballif, C. Organometallic Halide Perovskites: Sharp Optical Absorption Edge and Its Relation to Photovoltaic Performance. *The journal of physical chemistry letters* **2014,** *5* (6), 1035-1039.
2. Stranks, S. D.; Eperon, G. E.; Grancini, G.; Menelaou, C.; Alcocer, M. J. P.; Leijtens, T.; Herz, L. M.; Petrozza, A.; Snaith, H. J. Electron-Hole Diffusion Lengths Exceeding 1 Micrometer in an Organometal Trihalide Perovskite Absorber. *Science* **2013,** *342* (6156), 341-344.
3. Brenner, T. M.; Egger, D. A.; Kronik, L.; Hodes, G.; Cahen, D. Hybrid organic—inorganic perovskites: low-cost semiconductors with intriguing charge-transport properties. *Nature Reviews Materials* **2016,** *1*, 15007.
4. NREL photovoltaic efficiency chart: https://www.nrel.gov/pv/cell-efficiency.html
5. Kojima, A.; Teshima, K.; Shirai, Y.; Miyasaka, T. Organometal Halide Perovskites as Visible-Light Sensitizers for Photovoltaic Cells. *Journal of the American Chemical Society* **2009,** *131* (17), 6050-6051.
6. Jaramillo-Quintero, O. A.; Sanchez, R. S.; Rincon, M.; Mora-Sero, I. Bright Visible-Infrared Light Emitting Diodes Based on Hybrid Halide Perovskite with Spiro-OMeTAD as a Hole-Injecting Layer. *The journal of physical chemistry letters* **2015,** *6* (10), 1883-1890.
7. Tan, Z.-K.; Moghaddam, R. S.; Lai, M. L.; Docampo, P.; Higler, R.; Deschler, F.; Price, M.; Sadhanala, A.; Pazos, L. M.; Credgington, D.; Hanusch, F.; Bein, T.; Snaith, H. J.; Friend, R. H. Bright light-emitting diodes based on organometal halide perovskite. *Nat Nano* **2014,** *9* (9), 687-692.
8. Alivisatos, A. P. Semiconductor Clusters, Nanocrystals, and Quantum Dots. *Science* **1996,** *271*, 933-937.
9. Lin, K.; Xing, J.; Quan, L. N.; de Arquer, F. P. G.; Gong, X.; Lu, J.; Xie, L.; Zhao, W.; Zhang, D.; Yan, C.; Li, W.; Liu, X.; Lu, Y.; Kirman, J.; Sargent, E. H.; Xiong, Q.; Wei, Z. Perovskite light-emitting diodes with external quantum efficiency exceeding 20 per cent. *Nature* **2018,** *562* (7726), 245-248.
10. Suárez, I.; Juárez-Pérez, E. J.; Bisquert, J.; Mora-Seró, I.; Martínez-Pastor, J. P. Polymer/Perovskite Amplifying Waveguides for Active Hybrid Silicon Photonics. *Advanced materials* **2015,** *27* (40), 6157-6162.
11. Suárez, I.; Hassanabadi, E.; Maulu, A.; Carlino, N.; Maestri, C. A.; Latifi, M.; Bettotti, P.; Mora-Seró, I.; Martínez-Pastor, J. P. Integrated Optical Amplifier–Photodetector on a Wearable Nanocellulose Substrate. *Advanced Optical Materials* **2018,** *6* (12), 1800201.
12. Dou, L.; Yang, Y.; You, J.; Hong, Z.; Chang, W.-H.; Li, G. Solution-processed hybrid perovskite photodetectors with high detectivity. *Nat Commun* **2014,** *5*.
13. Deschler, F.; Price, M.; Pathak, S.; Klintberg, L. E.; Jarausch, D.-D.; Higler, R.; Hüttner, S.; Leijtens, T.; Stranks, S. D.; Snaith, H. J.; Atatüre, M.; Phillips, R. T.; Friend, R. H. High Photoluminescence Efficiency and Optically Pumped Lasing in Solution-Processed Mixed Halide Perovskite Semiconductors. *The journal of physical chemistry letters* **2014,** *5* (8), 1421-1426.

14. Zhu, H.; Fu, Y.; Meng, F.; Wu, X.; Gong, Z.; Ding, Q.; Gustafsson, M. V.; Trinh, M. T.; Jin, S.; Zhu, X. Y. Lead halide perovskite nanowire lasers with low lasing thresholds and high quality factors. *Nature materials* **2015,** *14* (6), 636-642.

15. Xing, G.; Mathews, N.; Lim, S. S.; Yantara, N.; Liu, X.; Sabba, D.; Grätzel, M.; Mhaisalkar, S.; Sum, T. C. Low-temperature solution-processed wavelength-tunable perovskites for lasing. *Nature materials* **2014,** *13* (5), 476-480.

16. Stranks, S. D.; Hoye, R. L. Z.; Di, D.; Friend, R. H.; Deschler, F. The Physics of Light Emission in Halide Perovskite Devices. *Advanced materials* **2018,** *0* (0), 1803336.

17. Dirin, D. N.; Dreyfuss, S.; Bodnarchuk, M. I.; Nedelcu, G.; Papagiorgis, P.; Itskos, G.; Kovalenko, M. V. Lead Halide Perovskites and Other Metal Halide Complexes As Inorganic Capping Ligands for Colloidal Nanocrystals. *Journal of the American Chemical Society* **2014,** *136* (18), 6550-6553.

18. Ning, Z.; Gong, X.; Comin, R.; Walters, G.; Fan, F.; Voznyy, O.; Yassitepe, E.; Buin, A.; Hoogland, S.; Sargent, E. H. Quantum-dot-in-perovskite solids. *Nature* **2015,** *523* (7560), 324-328.

19. Gong, X.; Yang, Z.; Walters, G.; Comin, R.; Ning, Z.; Beauregard, E.; Adinolfi, V.; Voznyy, O.; Sargent, E. H. Highly efficient quantum dot near-infrared light-emitting diodes. *Nat Photon* **2016,** *10* (4), 253-257.

20. Etgar, L.; Gao, P.; Qin, P.; Graetzel, M.; Nazeeruddin, M. K. A hybrid lead iodide perovskite and lead sulfide QD heterojunction solar cell to obtain a panchromatic response. *Journal of Materials Chemistry A* **2014,** *2* (30), 11586-11590.

21. Yang, Z.; Janmohamed, A.; Lan, X.; García de Arquer, F. P.; Voznyy, O.; Yassitepe, E.; Kim, G.-H.; Ning, Z.; Gong, X.; Comin, R.; Sargent, E. H. Colloidal Quantum Dot Photovoltaics Enhanced by Perovskite Shelling. *Nano letters* **2015,** *15* (11), 7539-7543.

22. Li, S.-S.; Chang, C.-H.; Wang, Y.-C.; Lin, C.-W.; Wang, D.-Y.; Lin, J.-C.; Chen, C.-C.; Sheu, H.-S.; Chia, H.-C.; Wu, W.-R.; Jeng, U. S.; Liang, C.-T.; Sankar, R.; Chou, F.-C.; Chen, C.-W. Intermixing-seeded growth for high-performance planar heterojunction perovskite solar cells assisted by precursor-capped nanoparticles. *Energy & Environmental Science* **2016,** *9* (4), 1282-1289.

23. Han, J.; Luo, S.; Yin, X.; Zhou, Y.; Nan, H.; Li, J.; Li, X.; Oron, D.; Shen, H.; Lin, H. Hybrid PbS Quantum-Dot-in-Perovskite for High-Efficiency Perovskite Solar Cell. *Small* **2018,** *14* (31), 1801016.

24. Sanchez, R. S.; de la Fuente, M. S.; Suarez, I.; Muñoz-Matutano, G.; Martinez-Pastor, J. P.; Mora-Sero, I. Tunable light emission by exciplex state formation between hybrid halide perovskite and core/shell quantum dots: Implications in advanced LEDs and photovoltaics. *Science advances* **2016,** *2* (1), e1501104.

25. Lee, M. M.; Teuscher, J.; Miyasaka, T.; Murakami, T. N.; Snaith, H. J. Efficient Hybrid Solar Cells Based on Meso-Superstructured Organometal Halide Perovskites. *Science* **2012,** *338* (6107), 643-647.

26. Burschka, J.; Pellet, N.; Moon, S.-J.; Humphry-Baker, R.; Gao, P.; Nazeeruddin, M. K.; Gratzel, M. Sequential deposition as a route to high-performance perovskite-sensitized solar cells. *Nature* **2013,** *499* (7458), 316-319.

27. Saliba, M.; Correa-Baena, J.-P.; Wolff, C. M.; Stolterfoht, M.; Phung, N.; Albrecht, S.; Neher, D.; Abate, A. How to make over 20% efficient perovskite

solar cells in regular (n–i–p) and inverted (p–i–n) architectures. *Chemistry of Materials* **2018,** *30* (13), 4193-4201.

28. Zhao, D.; Zhu, Z.; Kuo, M.-Y.; Chueh, C.-C.; Jen, A. K.-Y. Hexaazatrinaphthylene Derivatives: Efficient Electron-Transporting Materials with Tunable Energy Levels for Inverted Perovskite Solar Cells. *Angewandte Chemie International Edition* **2016,** *55* (31), 8999-9003.

29. Zhu, Z.; Zhao, D.; Chueh, C.-C.; Shi, X.; Li, Z.; Jen, A. K. Y. Highly Efficient and Stable Perovskite Solar Cells Enabled by All-Crosslinked Charge-Transporting Layers. *Joule* **2018,** *2* (1), 168-183.

30. Yang, G.; Wang, C.; Lei, H.; Zheng, X.; Qin, P.; Xiong, L.; Zhao, X.; Yan, Y.; Fang, G. Interface engineering in planar perovskite solar cells: energy level alignment, perovskite morphology control and high performance achievement. *Journal of Materials Chemistry A* **2017,** *5* (4), 1658-1666.

31. Zuo, L.; Gu, Z.; Ye, T.; Fu, W.; Wu, G.; Li, H.; Chen, H. Enhanced Photovoltaic Performance of CH3NH3PbI3 Perovskite Solar Cells through Interfacial Engineering Using Self-Assembling Monolayer. *Journal of the American Chemical Society* **2015,** *137* (7), 2674-2679.

32. Abrusci, A.; Stranks, S. D.; Docampo, P.; Yip, H.-L.; Jen, A. K. Y.; Snaith, H. J. High-Performance Perovskite-Polymer Hybrid Solar Cells via Electronic Coupling with Fullerene Monolayers. *Nano letters* **2013,** *13* (7), 3124-3128.

33. Valles-Pelarda, M.; Hames, B. C.; García-Benito, I.; Almora, O.; Molina-Ontoria, A.; Sánchez, R. S.; Garcia-Belmonte, G.; Martín, N.; Mora-Sero, I. Analysis of the Hysteresis Behavior of Perovskite Solar Cells with Interfacial Fullerene Self-Assembled Monolayers. *The journal of physical chemistry letters* **2016,** *7* (22), 4622-4628.

34. Xu, Y.; Wang, Y.; Yu, J.; Feng, B.; Zhou, H.; Zhang, J.; Duan, J.; Fan, X.; Aken, P. A. v.; Lund, P. D.; Wang, H. Performance Improvement of Perovskite Solar Cells Based on PCBM-Modified ZnO-Nanorod Arrays. *IEEE Journal of Photovoltaics* **2016,** *6* (6), 1530-1536.

35. Wojciechowski, K.; Stranks, S. D.; Abate, A.; Sadoughi, G.; Sadhanala, A.; Kopidakis, N.; Rumbles, G.; Li, C.-Z.; Friend, R. H.; Jen, A. K. Y.; Snaith, H. J. Heterojunction Modification for Highly Efficient Organic–Inorganic Perovskite Solar Cells. *ACS nano* **2014,** *8* (12), 12701-12709.

36. Abate, A.; Saliba, M.; Hollman, D. J.; Stranks, S. D.; Wojciechowski, K.; Avolio, R.; Grancini, G.; Petrozza, A.; Snaith, H. J. Supramolecular Halogen Bond Passivation of Organic–Inorganic Halide Perovskite Solar Cells. *Nano letters* **2014,** *14* (6), 3247-3254.

37. Noel, N. K.; Abate, A.; Stranks, S. D.; Parrott, E. S.; Burlakov, V. M.; Goriely, A.; Snaith, H. J. Enhanced Photoluminescence and Solar Cell Performance via Lewis Base Passivation of Organic–Inorganic Lead Halide Perovskites. *ACS nano* **2014,** *8* (10), 9815-9821.

38. Xu, J.; Buin, A.; Ip, A. H.; Li, W.; Voznyy, O.; Comin, R.; Yuan, M.; Jeon, S.; Ning, Z.; McDowell, J. J.; Kanjanaboos, P.; Sun, J.-P.; Lan, X.; Quan, L. N.; Kim, D. H.; Hill, I. G.; Maksymovych, P.; Sargent, E. H. Perovskite–fullerene hybrid materials suppress hysteresis in planar diodes. *Nature communications* **2015,** *6,* 7081.

39. Yan, W.; Li, Y.; Li, Y.; Ye, S.; Liu, Z.; Wang, S.; Bian, Z.; Huang, C. Stable high-performance hybrid perovskite solar cells with ultrathin polythiophene as hole-transporting layer. *Nano Research* **2015,** *8* (8), 2474-2480.

40. Bai, Y.; Dong, Q.; Shao, Y.; Deng, Y.; Wang, Q.; Shen, L.; Wang, D.; Wei, W.; Huang, J. Enhancing stability and efficiency of perovskite solar cells with crosslinkable silane-functionalized and doped fullerene. *Nat. Commun.* **2016,** *7*, 12806.

41. Yang, S.; Wang, Y.; Liu, P.; Cheng, Y.-B.; Zhao, H. J.; Yang, H. G. Functionalization of perovskite thin films with moisture-tolerant molecules. *Nature Energy* **2016,** *1*, 15016.

42. Yun, J. S.; Seidel, J.; Kim, J.; Soufiani, A. M.; Huang, S.; Lau, J.; Jeon, N. J.; Seok, S. I.; Green, M. A.; Ho-Baillie, A. Critical Role of Grain Boundaries for Ion Migration in Formamidinium and Methylammonium Lead Halide Perovskite Solar Cells. *Advanced Energy Materials* **2016,** *6* (13), 1600330.

43. de Quilettes, D. W.; Vorpahl, S. M.; Stranks, S. D.; Nagaoka, H.; Eperon, G. E.; Ziffer, M. E.; Snaith, H. J.; Ginger, D. S. Impact of microstructure on local carrier lifetime in perovskite solar cells. *Science* **2015,** *348* (6235), 683-686.

44. Olthof, S.; Meerholz, K. Substrate-dependent electronic structure and film formation of MAPbI3 perovskites. *Scientific reports* **2017,** *7*, 40267.

45. Pascoe, A. R.; Yang, M.; Kopidakis, N.; Zhu, K.; Reese, M. O.; Rumbles, G.; Fekete, M.; Duffy, N. W.; Cheng, Y.-B. Planar versus mesoscopic perovskite microstructures: The influence of CH3NH3PbI3 morphology on charge transport and recombination dynamics. *Nano Energy* **2016,** *22*, 439-452.

46. Bastiani, M. D.; D'Innocenzo, V.; Stranks, S. D.; Snaith, H. J.; Petrozza, A. Role of the crystallization substrate on the photoluminescence properties of organo-lead mixed halides perovskites. *APL Materials* **2014,** *2* (8), 081509.

47. Zhang, H.; Zhao, C.; Li, D.; Guo, H.; Liao, F.; Cao, W.; Niu, X.; Zhao, Y. Effects of substrate temperature on the crystallization process and properties of mixed-ion perovskite layers. *Journal of Materials Chemistry A* **2019,** *7* (6), 2804-2811.

48. Wang, Y.; Liu, S.; Zeng, Q.; Wang, R.; Qin, W.; Cao, H.; Yang, L.; Li, L.; Ji, W.; Yin, S. Controllable Crystal Film Growth via Appropriate Substrate-Preheating Treatment for Perovskite Solar Cells Using Mixed Lead Sources. *IEEE Journal of Photovoltaics* **2018,** *8* (1), 162-170.

49. Tidhar, Y.; Edri, E.; Weissman, H.; Zohar, D.; Hodes, G.; Cahen, D.; Rybtchinski, B.; Kirmayer, S. Crystallization of Methyl Ammonium Lead Halide Perovskites: Implications for Photovoltaic Applications. *Journal of the American Chemical Society* **2014,** *136* (38), 13249-13256.

50. Yang, J.; Siempelkamp, B. D.; Mosconi, E.; De Angelis, F.; Kelly, T. L. Origin of the Thermal Instability in CH3NH3PbI3 Thin Films Deposited on ZnO. *Chemistry of Materials* **2015,** *27* (12), 4229-4236.

Chapter I. Introduction

I.1. Interest of perovskite materials

Conversion of solar energy directly into electrical energy, by means of the photovoltaic effect, appears as one of the most attractive strategies in order to achieve an energy-sustainable society. On one hand, reducing the dependence on the fossil fuels which become increasingly exhausted by the exploitation, on the other hand offering a clean alternative to palliate the climatic change. The historical challenge of the photovoltaic industry has been the production of energy at an economic cost similar to fossil fuel sources. A tremendous amount of work has been done along the way to test and upgrade developments to produce a cost-effective photovoltaic solar energy product. Recently, halide perovskite (HP) materials have been emerged as extremely attractive newcomers for photovoltaic applications. The interest of HP has been mainly originated by the impressive progress in the photoconversion efficiencies (PCEs). Since the first report in 2009 with the efficiency of 3.8%,[1] the number of publications on perovskite materials has been quickly increased (Fig I.1) as well as an increase in certified PCEs (Fig I.2). Within 10 years, the certified record PCE of HP solar cells according to NREL has been reached over 25%[2] in a single junction architecture and more than 28% in silicon based tandem solar cells (Fig I.2). Moreover, HPs have been successfully employed in other optoelectronic devices such as light emitting diodes (LEDs),[3-6] light amplifier[7-8] or lasers.[9-12]
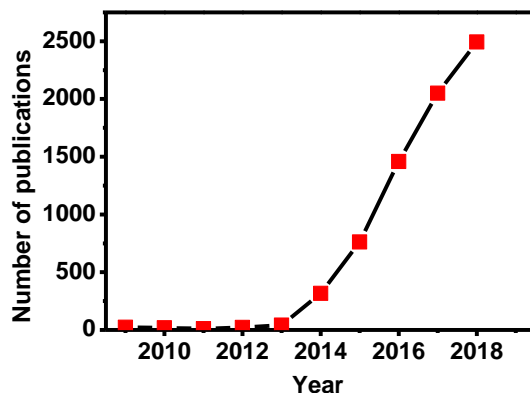

Fig I.1. Number of publications resulting from the search of "perovskite" on Web of Science, retrieved on 16/05/2019. The line is a guide for the eyes.
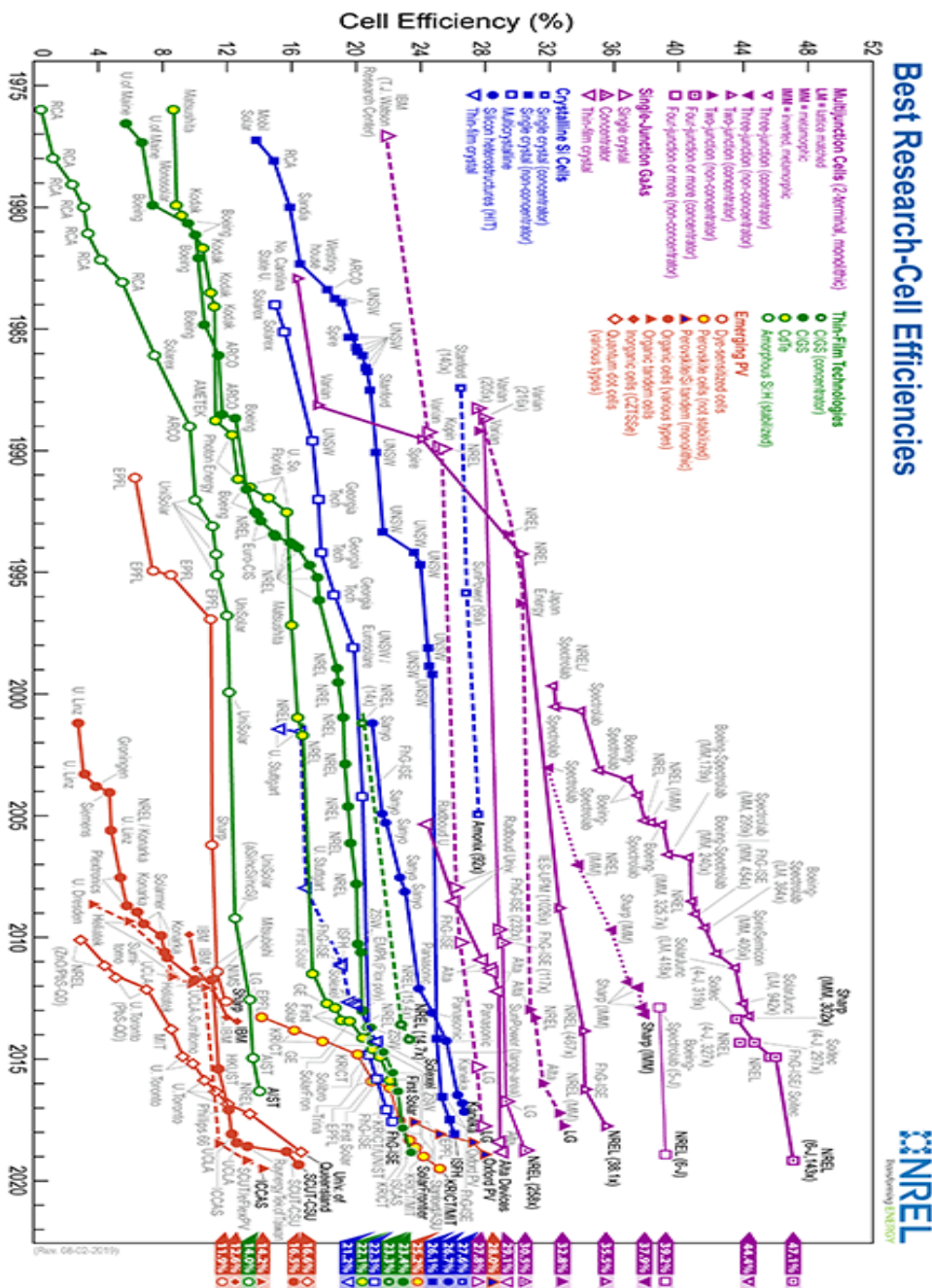
Fig I.2. NREL photovoltaic efficiency chart until 16/04/2019. Reproduced from ref.[2]

Halide perovskite has a crystal structure that could be described as AMX_3, where A is a monovalent organic or inorganic cation such as

2

methylammonium (MA^+), formamidinium (FA^+) or Cs^+; M is a metal divalent cation as Pb^{2+} or Sn^{2+}; and X is a halide anion as iodide (I^-), bromide (Br^-) and chloride (Cl^-) respectively. Structurally all three components can be easily changed/modified leading the variation in the electronic properties of HPs. In fact the outstanding versatility of HPs is one of the most appealing properties of this family of materials. The crystalline structure of HP is present in the Fig I.3. This structure can be described as a 3D lattice in which M^{2+} coordinates with X^- forming a regular octahedron MX_6 where M-site is located at the center; the A^+ cation is situated within the corner-sharing metal halide octahedra (simplified as octahedral cavity) forming an AX_{12} polyhedron.[13-15] The stability of such 3D perovskite structure can be predicted by the tolerance (t) and octahedral (µ) factors following the formulas below[13, 16]

$$t = \frac{r_A + r_X}{\sqrt{2}\,(r_M + r_X)} \qquad (eq\ I.1)$$

$$\mu = \frac{r_M}{r_X} \qquad (eq\ I.2)$$

where r_A, r_M and r_X are the radius of A, M and X components, respectively. In order to form the 3D perovskite structure, the tolerance and octahedral factors need to be preferently in the range of $0.8 \le t \le 1.0$ and $0.44 \le \mu \le 0.9$.[13]
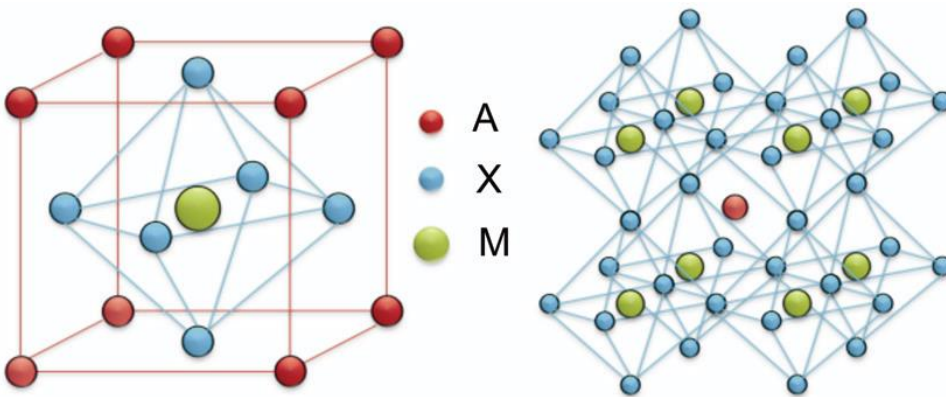

Fig I.3. Crystalline structure of perovskite. Reproduced with the permission of John Wiley and Sons from ref.[15]

The A^+ cation serves principally to balance the charge of the frame work.[13, 15] The component of A is very flexible, which can range in type from a single atom, Cs^+ for example, to a variety of organic molecules such as MA^+ and FA^+. As the A-site is located within the octahedral cavity (Fig I.3), its

3

nature and size have a significant influence on the orientation and dimensionality of the octahedron.[13] The A-component with a small size can be easily fit in the octahedral cavity. However, if its size is too small, the octahedral structure may be distorted. In contrast with too large A-site, the octahedral cavity can be destroyed.[14-15] Variation of the size of A^+ cation can expand or shrink the crystal structure of HPs, resulting a profound effect on the structure and properties. As an example, the substitution MA^+ by FA^+ increases the A radius, the lattice is expanded, consequently the bandgap (E_g) is reduced, the absorption is attained to longer wavelengths.[17-19] The partial replacing MA^+ by different ratio of FA^+ also results a gradual reduction of E_g (Fig I.4a).[19-20] Inversely, a replacement MA^+ by a smaller Cs^+ cation produces an increase of E_g, therefore the absorption is narrower (Fig I.4b-c).[21] Moreover the stability of HP can be also altered by the size of A^+ cation. It has been documented that by substituting MA^+ by a larger and heavier FA^+ cation, the thermal stability of devices can be enhanced. The thermal stability testing of $FAPbI_3$ and MAPI films heated at 150^oC under air showed that the $FAPbI_3$ film was still stable after 60 minutes of annealing while the MAPI was completely degraded, its color tuned from brown to yellow.[17] Besides the incorporation of Cs^+ into $FAPbI_3$ could gain the humidity stability. A stable film of $FA_{0.85}Cs_{0.15}PbI_3$ mixed cation perovskite was observed after 4 hours exposed to 90% of humidity while a pure $FAPbI_3$ film degraded after 2 hours.[22] In addition, a triple mixed cation Cs/MA/FA can be also practicably prepared. The incorporation of a small quantity of Cs^+ ions into mixed MA/FA perovskite one hand does not cause a significant increase in the E_g, thereby the absorption of Cs/MA/FA perovskite can be maintained similar as the absorption spectrum of MA/FA based perovskite. On the other hand, the triple mixed cation based perovskite can improve the stabilities. As an example Saliba et al. prepared a triple mixed Cs/MA/FA based perovskite by introducing a little amount of Cs^+ cation (below 15%) into MA/FA perovskite and achieved an efficient solar cells with the PCE as high as 21%, and with good stabilities including thermal stability (3 hours at 130^oC under a dry air) and illumination stability (250 hours of illumination in an inert atmosphere).[23] However the multiple A-site components may produce a segregated phase[21] which may give a drawback to the long term stability.
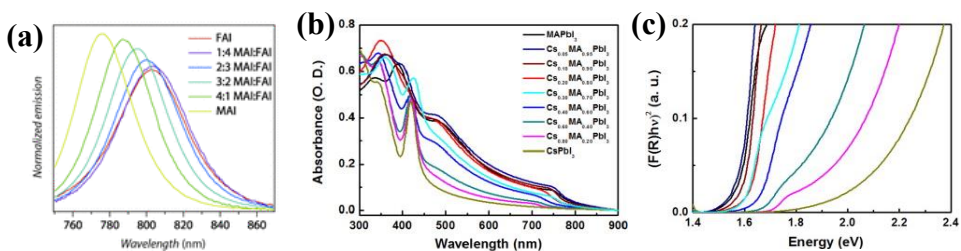
Fig I.4. (a) Emission of $MA_xFA_{1-x}PbI_3$ perovskite with different MA:FA mixed cation ratio. Reproduced with the permission of John Wiley and Sons from ref.[20] (b) UV–vis absorption and (c) transformed Kubelka–Munk spectra of $Cs_xMA_{1-x}PbI_3$ perovskite films with different Cs ratio. Reproduced with the permission of Elsevier from ref.[21]
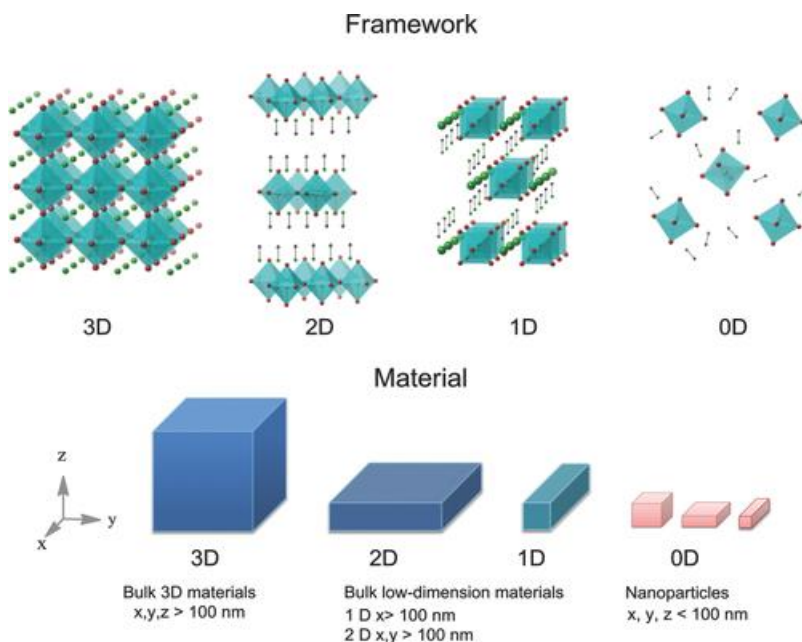

Fig I.5. Schematic representation of perovskite frameworks with different dimensionalities (3D, 2D, 1D, and 0D). Reproduced with the permission of John Wiley and Sons from ref.[24]

Nevertheless, bulky organic cation can also be incorporated into A-site. In this case, the octahedral structure can be destroyed, thereby the 3D perovskite structure cannot be maintained. However by using the size-controlled bulky organic molecules as the A-site, low dimensional perovskites, including 2D, 1D and 0D, can be formed, as illustrated in the Fig I.5. In 2D structure, the MX_6 octahedra are connected in layered sheets at the corners while in the 1D the MX_6 octahedra are connected in a chain (corners, edges or faces) and 0D perovskite the MX_6 octahedra are isolated. In all of them, the inorganic framework is surrounded by the organic cation.[24] A

5

particularly interesting, the hybrid 2D/3D dimensional perovskite can be formed by using an appropriate mixed organic cations (mixed A-site) in which the effective radius of one cation satisfies the 3D formability criteria with corresponding the MX_6 unit, while the second cation is too large to fit in the octahedral cavity, consequently 3D sheet with small cation are connected through the large cations forming quantum well 2D structure.[13] For a dimensionality lower than 3, it is necessary to use the bulky organic cation that if possesses a hydrophobic character, can improve the stability of perovskite because the bulky organic molecules can act as an encapsulator protecting perovskite from moisture or oxygen in atmosphere.[14] However the poor conductivity in a certain crystallographic direction of those dielectric bulky organic cations limits the performance of low dimensional perovskite based devices.[25]
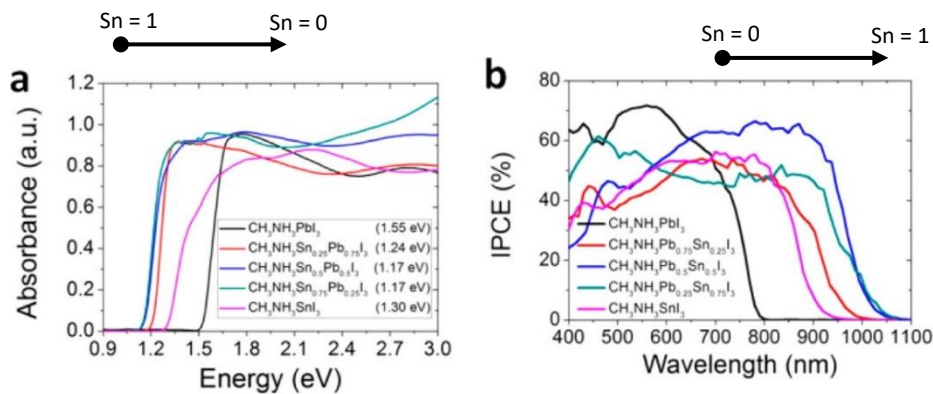

Fig I.6. Absorbance (a) and IPCE spectra (b) of the $CH_3NH_3Sn_{1-x}Pb_xI_3$ perovskite films and devices respectively. Reproduced with the permission of American Chemical Society from ref.[26]

The M-site of HPs is generally the divalent metal cations such as Pb^{2+}, Sn^{2+} and Ge^{2+}. It has been previously shown that the metal cation also provides the variation of perovskite properties. A partial substitution of M-component has a significant impact on the electronic properties.[27] However, M cation has a lower effect on the lattice parameters that are strongly influenced by the halide anion.[13] Using a mixed-metal cation, the conversion of light into electricity of $MA(Pb_{1-x}Sn_x)I_3$ can be attained to near infrared, up to ~ 1050 nm, due to the reduction of the E_g (Fig I.6).[26, 28] In fact, this property has brought a great attention to Pb/Sn mixed perovskite, as low bandgap absorbers for tandem solar cells. In addition, Sn is known to present lower toxicity than Pb. Consequently, the replacement of Pb by Sn has been broadly studied.

6

Nevertheless, Sn^{2+} is easily oxidized to Sn^{4+}, resulting a low stability of Sn^{2+} cation based perovskite devices. Although a promising performance and stability of lead-free CsSnX halide perovskite (X is I, Cl or Br) quantum rods based solar cells has been reported, achieving the PCE close to 13% with better stability than MAPI based devices.[29]
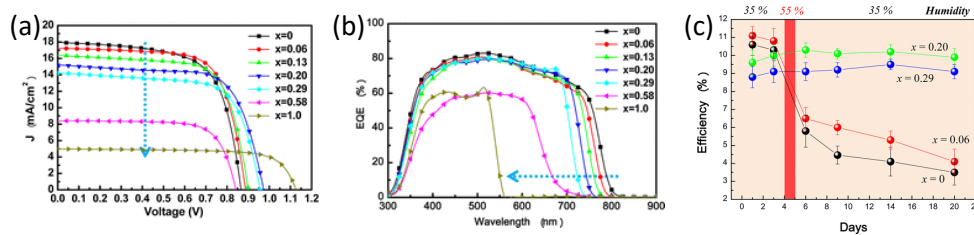

Fig I.7. Photocurrent-voltage characteristic (a), IPCE spectra (b) and long term stability versus humidity during the sample's preparation (c) of the MAPb($I_{1-x}Br_x)_3$ perovskite devices. Reproduced with the permission of American Chemical Society from ref.[30]

Similar to A and M components, the halide anion (X-site) also provides the variation in perovskite. The size of halide ion influences strongly on the lattice constant and consequently the material bandgap. Larger size of halide ion increases the lattice constant, resulting a reduction in the attraction towards to the metal atom (M-site), the electronegativity is reduced, reducing the bandgap of perovskite.[15, 31] Therefore, moving from chloride to bromide to iodide ions, the ionic radius is increasing, the decreasing in the bandgap and broadening the light absorption to longer wavelengths.[32] The bandgap of perovskite can be continuously controlled by mixing iodide and bromide, and chloride and bromide anions. As an example, Noh and co-workers varied the bandgap from 1.55eV to 2.28eV by changing the content of bromide from 0 to 1 in MAPbI$_{3-x}$Br$_x$ mixed halide perovskite.[33] And with a small incorporation of Br$^-$ (20%), the device obtained a slightly improvement in PCEs because of the higher Voc and better FF against the decrease of Jsc due to the increase in the band gap (Fig I.7a-b). However more importantly, the incorporation of Br$^-$ improved the humidity stability of devices (Fig I.7c). Differently to the case of I/Br mixed anion, the incorporation of chloride precursor for the formation of MAPI perovskite does not cause the change in the bandgap. This is supposedly due to the large ionic radius discrepancy of iodide and chloride, independently to the component ratio in the precursor solution, the concentration of incorporated chloride into iodide based perovskite is relatively low (below 3 - 4%).[13, 34] In some other studies, the low detected content of chloride in MAPbI$_{3-x}$Cl$_x$ is believably correlated with the decomposition of MACl due to thermal conversion.[35-36] Although, the

incorporation of chloride into MAPI perovskite influences the crystallization process with a great improvement in the morphology[37] and the optophysical properties. The diffusion length for both electrons and holes is increased around one order of magnitude and the lifetime of charge carriers is also significantly enhanced (Fig I.8).[38] In addition, by adjusting the ratio of mixed halide in nanocrystals $CsPb(I_{1-x}Br_x)_3$ and $CsPb(Cl_{1-x}Br_x)_3$ accompanying with controlled particle sizes, the optical absorption and emission spectra can be tuned across nearly the entire visible spectrum (Fig I.9).[39] However the halide segregation in mixed halide perovskite under continuous illumination limits seriously this theoretical large tunability and still remains a problem for long term stability.[40] Nonetheless, some strategies have been developed to diminish or avoid phase segregation in mixed halide perovskites.[41-42]

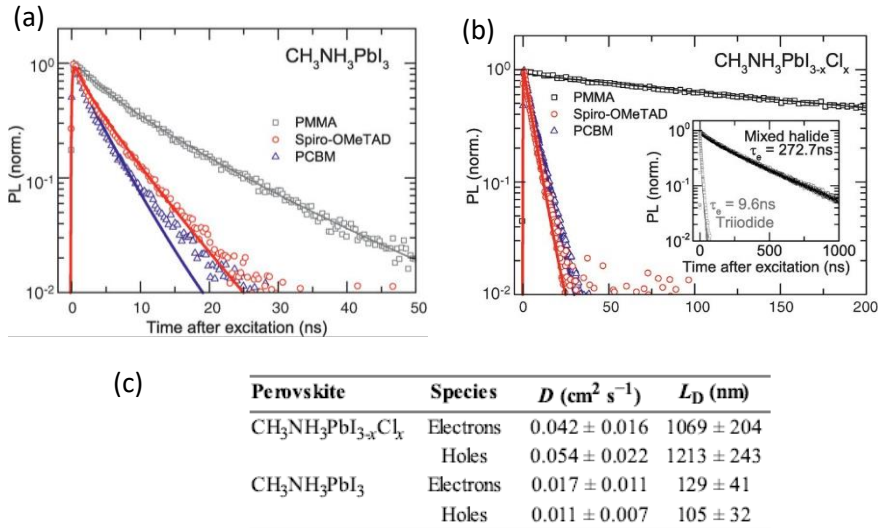| Perovskite	Species	D (cm^2 s^{-1})	L_D (nm)
$CH_3NH_3PbI_{3-x}Cl_x$	Electrons	0.042 ± 0.016	1069 ± 204
	Holes	0.054 ± 0.022	1213 ± 243
$CH_3NH_3PbI_3$	Electrons	0.017 ± 0.011	129 ± 41
	Holes	0.011 ± 0.007	105 ± 32

Fig I.8. Time-resolved photoluminescence (PL) measurements (a-b) taken at the peak emission wavelength of Glass/perovskite without (PMMA) and with HTM (Spiro-OMeTAD or PCBM) in which perovskite is MAPI (a) and $MAPbI_{3-x}Cl_x$ (b). And (c) is values for diffusion constants (D) and diffusion lengths (L_D) from fitting of PL decay in Fig b, c. Reproduced with permission of The American Association for the Advancement of Science from ref.[38]
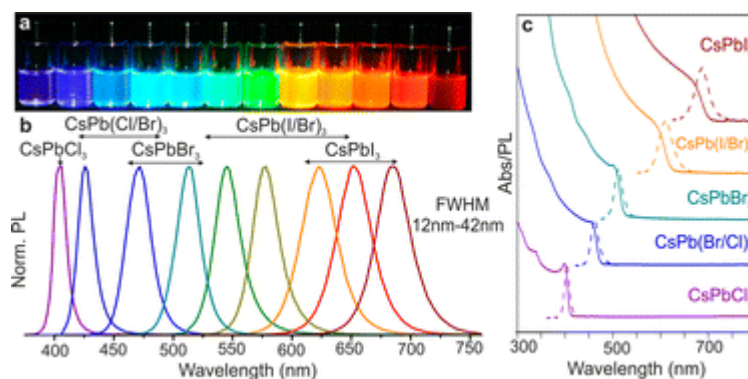
Fig I.9. Characterization of colloidal perovskite CsPbX (X: Cl, I or Br) nanoparticles prepared with different halide ratio. (a) Image of perovskite nanoparticle solutions under UV lamp (λ = 365 nm). (b-c) Photoluminescence (PL) and absorption respectively. Reproduced with permission of American Chemical Society from ref.[39]

In overall the halide perovskites are extremely interesting materials themselves whose components can be flexibly changed/modified adapting the specific requirement. Moreover, it can be used for tandem solar cells to increase the PCEs. Theoretical simulation proposed that the optimized perovskite/Si tandem solar cells could achieve over 30% of PCEs[43-44] while for perovskite/Ge[45] tandem cells the PCEs of ~ 25% is predicted. Actually the certified PCE higher than 28% for perovskite/Si tandem solar cells has been recorded (Fig I.2). Beyond the flexibility in the structure, HPs can be prepared by many different methods including simple solution processes, that allow an easily combination of perovskite with other materials. This interaction could have important implications and it is at the center of this thesis. In the following sections, the combination of perovskite with some different materials will be briefly discussed.

I.2. Brief introduction on the interaction of perovskite with other materials

HP has been illustrated as a promising material for photovoltaic applications, however, it is still showing some issues in which devices prepared with these materials can be improved, regarding, for example, the low stability under various conditions including moisture, temperature, oxygen and illumination, or the environmental problem. Studying the interaction of HP and other materials opens one hand the possibility to enhance the properties of HP system. On the other hand, the combination of materials also allows the integration of the good properties of the single materials into a composite, ameliorating the quality of hybrid materials and finally of the optoelectronic devices. In addition, the interaction of HP and other materials can rise new properties or phenomena which do not exist in single materials. The finding of new properties can contribute importantly to the development of photovoltaics. In following sections, we provide a general view about the interaction of HP with colloidal quantum dots (QDs), organic molecules and electron transporter materials (ETMs).

I.2.1. Interaction of perovskite with colloidal quantum dots

I.2.1.a. Colloidal quantum dots

Quantum dots are nanometric crystalline particles whose optical and electronic properties[46] are different from the bulk. In fact, bulk semiconductors are characterized by a composition-dependent bandgap energy which is defined by the minimum energy required to excite one electron to jump from the ground state in the valence band (VB) to the vacant in conduction band (CB). By absorbing a photon with the energy equal or higher than the energy gap, an electron in the VB is excited and moves to the CB, creating a hole in the VB which conventionally can be seen as a positive charge particle. The lowest electrostatic energy bounding a pair of negatively charged electron with a positively charged hole is known as exciton. The

relaxation of an excited electron in the CB to the VB cancels an exciton and may be accompanied by an emission of a photon whose energy is equal to the band gap of the semiconductor. This process is known as radiative recombination. When the size of a crystalline particle is smaller than the Bohr exciton radius, the motion of charge carriers are spatially confined in all the three dimensions, raising their energy.[47] The crystalline particles exhibiting quantum confinement effects in the three dimensions are called quantum dots (QDs). The degree of quantum confinement is size-dependent, higher confinement for smaller size, hence higher bandgap is found. Fig I.10 shows TEM images of QDs with different sizes and the dependence of absorbance and photoluminescence on the QD sizes.
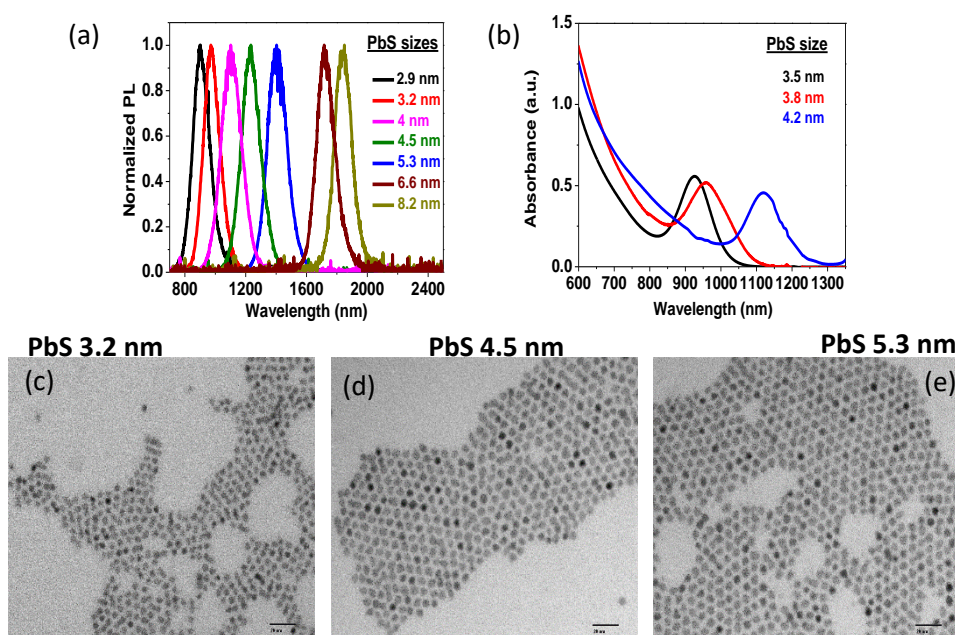

Fig I.10. Solution photoluminescence (a) and absorbance (b) spectra of PbS QDs synthesized with different sizes. TEM images of PbS QDs of 3.2 nm (c), 4.5 nm (d) and 5.3 nm (e). Scale bar is 20 nm.

QDs generally exhibit much higher photoluminescence (PL) quantum yield (PLQY) than bulk materials. Because in the bulk, charge carrier could be free to move in three dimensions, the exciton is not spatially confined and can be easily dissociated, increasing the probability of non-radiative recombination associated with crystalline defects. While in QDs, the wave functions of electron and hole strongly overlap due to the spatial confinement, enhancing the probability of radiative recombination.[47]

QDs can be prepared by different methods such as successive ionic layer deposition (SILAR)[48] and chemical bath deposition (CBD)[49] in which QDs are grown on a solid substrate. However solution processes,[50] resulting in the formation of colloidal QDs, are typically used due to the better size, monodispersity and shape control. In the solution methods, colloidal QDs are generally covered by a monolayer of surfactant ligand[47] that can passivate surface defect, which significantly influences on the optoelectronic properties of QDs,[51] and on the interaction of QDs with other materials. QDs presents a large surface area/volume ratio. The atoms on the surface are not completely bonded in the crystal lattice, hence the crystalline periodicity is disrupted, resulting dangling bonds which possibly create trap energy states within a bandgap energy.[47] These energy states can trap charge carriers, increasing the non-radiative recombination, and consequently reducing the PLQY. As a result, passivation of QD surface is an important factor deciding the quality of QDs and the device performance. In the following section, the effect of QD passivation in the interaction of QDs and halide perovskite (HP) will be involved in the discussion (chapter III). And the influence of PbS capping ligands on the interaction will be discussed in the chapter V.

Within this thesis, among different semiconductors QDs, PbS was selected to synthesize and to study their interaction with HP because PbS semiconductor possess a direct narrow gap transition with a bulk bandgap of 0.41 eV. PbS has a relatively large Bohr exciton radius, 18 nm, which permits to deeply turn the absorption or/and emission by changing the QD sizes.[52] PbS colloidal QDs were synthesized using a hot injection solution method. Our PbS QDs present a spherical shape (Fig I.10c-e) which contains lowest number of atoms on the surface comparing with other geometries. This in fact could reduce the number of dangling bonds, hence reducing the number of trap states and improving the quality of QDs. Different PbS QD sizes were achieved by controlling the reaction temperatures, reaction time and the concentration of precursors. These PbS QDs were used for the interaction with HP.

I.2.1.b. Interaction of perovskite and colloidal quantum dots

The interaction of halide perovskite (HP) and colloidal quantum dots (QDs) is described in the chapter III, IV and V. A small review on the previous interaction is presented in the chapter III and our contribution to the combination of HP and QDs is showed in the chapter IV and V.

I.2.2. Brief introduction on the interaction of perovskite with organic molecules

Organic molecules have been investigated broadly in HP optoelectronic devices since unlimited number of structures can be potentially synthesized and they can be prepared and/or modified to meet the requirements of a specific applications. In this section, we briefly summarize the different objectives of combining HP with organic molecules. Fig I.11 presents the possible situation of incorporated organic molecules in HP and their corresponding functions. First organic molecules have been used as the charge carrier selecting contacts in HP solar cells. Second, they have been integrated as an interlayer which is sandwiched between HP and ETM or HTM, with different roles. (i) The coating of organic molecule on ETM was used to modify the surface energy, consequently to control the morphology of HP coated on. (ii) Moreover, the organic coating functions as a passivation agent to passivate ETM surface defects, improving the electron extraction. (iii) Furthermore, the use of organic layer on ETM could reduce the hysteresis of HP solar cells. In addition, organic molecules have been intermixed in ETM films, obtaining similar effects as a thin organic coating on ETM layer. (iv) On the other hand, these molecules were deposited on HP as passivation agents to minimize the recombination traps at HP surface under-coordinated atoms (iodine or lead atoms) and/or at grain boundary. (v) Eventually, the organic layer on HP can act as an encapsulation agent to protect HP from degradation sources such as moisture, enhancing the long-term stability of HP optoelectronic devices. Third, the organic molecules have been also embedded into HP matrix, by dissolving them in the solution of HP precursors, to passivate HP film deeply in the bulk film.

Organic molecules have been prevalently used as hole transport materials (HTMs) in HP devices, and spiro-OMeTAD is the most common used.[53-55] However, as spiro-OMeTAD has low hole-mobility and low-conductivity, it needs to be doped in order to improve its transport properties.[56] It has been well documented that doping spiro-OMeTAD with oxygen can effectively increase its conductivity and enable higher device performance.[57] However, lithium bis(trifluoromethanesulfonyl)imide (LiTFSI) must be used in this process to facilitate the oxidative reaction between spiro-OMeTAD and O_2.[58] This doping process requires an open system to allow the ingress of oxygen and it is difficult to control the amount of oxidized spiro-OMeTAD formed as the oxidation is dependent on a number of factors including concentrations of Li^+ and oxygen present in the film.[58-59] The complication of

this doping process makes it hard to be reproduced. To alleviate this problem, McGehee et al. have described a dicationic spiro(TFSI)$_2$ to simplify the doping process. By forming pre-oxidized spiro-OMeTAD, spiro(TFSI)$_2$ could replace LiTFSI to provide an easier way for controllably increasing the conductivity of HTM without exposure to O$_2$.[60] On the other hand, proper molecular design of organic HTMs also has a critical influence on the charge extraction efficiency. As an example, Jeon et al. elucidated the importance of HTM molecular structures on the device performance by systematically changing the side-chain (-OMe) position in spiro-type arylamine HTM. The –OMe groups linked at different positions (para, meta and ortho) enabled to shift the LUMO and HOMO levels of spiro-OMeTAD derivatives, showing the highest LUMO level for HTM with the –OMe linked at ortho position. As the result, HP solar cells with –OMe group linked at ortho position gave highest photoconversion efficiency (PCE) due to the best efficiency in electron blocking.[61] In addition to spiro-OMeTAD, some polymers have been used as HTM in HP solar cells such as P3HT[62] and PTAA.[63]
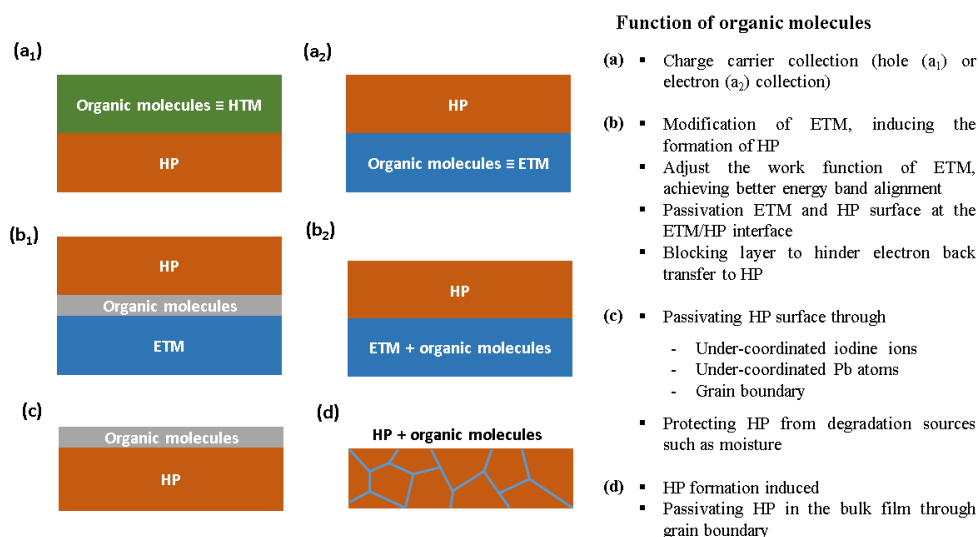

Fig I.11. Possible incorporated position of organic molecules to perovskite films and their corresponding function.

Beyond the use as HTM, organic molecules have been employed as electron transport materials (ETMs) as well. As an example, the group of Jen[64-65] has synthesized different hexaazatrinaphthylene (HATNA) derivatives with different energy levels in order to match with those of MAPI HP, and carried out the doping to increase the conductivity of HATNA. These HATNA derivatives act as ETMs in the inverted p-i-n HP solar cells. The potential of using organic molecules as ETMs were confirmed by achieving

high PCEs, 17 – 18%, with negligible hysteresis.[64-65] Moreover organic layer generally can be prepared at low temperatures, which opens a possibility for the preparation of flexible optoelectronic devices.[65] Furthermore some organic molecules naturally possess a hydrophobic character, hence in the p-i-n configuration, the organic ETM also works as a HP protection layer from degradation sources as moisture and oxygen, increasing consequently the stability of HP cells. In the studies of Jen's group, they also showed a good stability of HATNA ETMs based HP solar cells under a test of multi-degradation sources. Concretely these devices maintained 90% of initial PCE after 100 hours continuously heated at 70°C and under 1 sun illumination at ambient condition with the humidity level around 50%.[65]

In parallel, organic molecules have been previously used as an interlayer between HP and ETM. A coating of organic molecules on ETM can modify the surface of ETM, then influence on the formation of HP deposited on. Yang et al. showed that the deposition of 3-aminopropyltriethoxysilane (APTES) self-assembled monolayer (SAM) reduced the surface roughness of SnO_2 ETM.[66] In addition, the surface energy of ETM can be also adjusted. After APTES SAM modification, the SnO_2 surface became more hydrophilic, the contact angle was significantly reduced. Consequently this provided better interfacial contact with HP layer. As a result, the HP film coated on APTES modified SnO_2 possessed bigger grain sizes, comparing with HP depositing on bare SnO_2 without modification. Interestingly, the grain size of HP layer varied dependently on the amount of APTES (Fig I.12). Moreover, the crystallinity of HP films also exhibited an improvement. Better morphology and crystallinity also induces an enhancement in the absorption of HP.[66] Similar influence on the morphology, crystallinity and optical properties of HP layer has been observed for ZnO ETM modified by 3-aminopropanioc acid (C3) SAM.[67] This fact points out that the properties of HP film can be easily controlled by the introduction of a thin organic layer sandwiched between ETM and HP. Furthermore, the work function of ETM can be modified by the introduction of organic molecules. As an example, the work function of SnO_2 and ZnO was decreased after the modification with APTES SAM and C3 SAM respectively, leading a better energy band alignment of ETM/HP junction, consequently improving the performance of HP devices by a better charge extraction.[66-67] Importantly, the improvement of HP properties by introducing APTES SAM interlayer has an effect on the long term stability. The efficiency of HP solar cells based on APTES modified SnO_2 remained more than 90% after 1000 hours storing at 30% of humidity.[66]
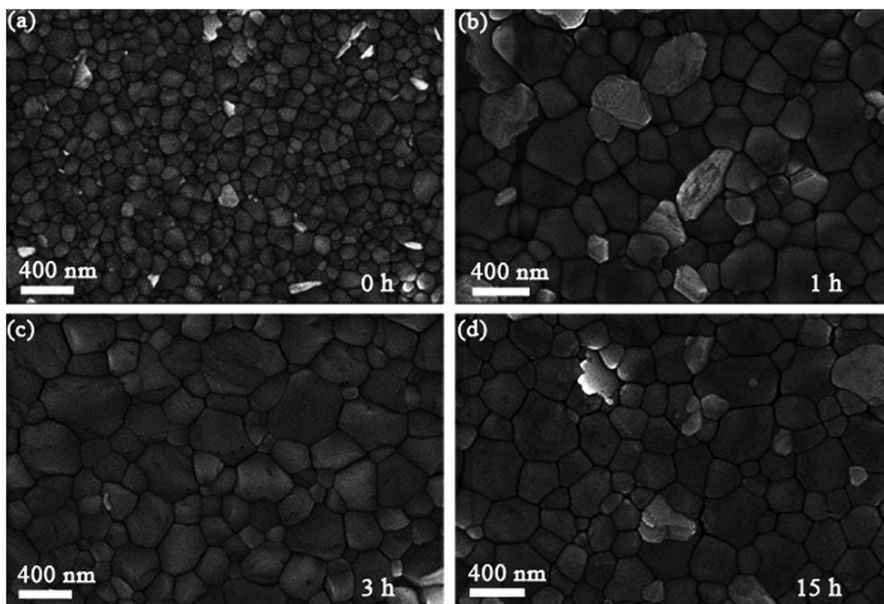
Fig I.12. Typical top view SEM images of perovskite films deposited on SnO$_2$ ETMs with different APTES SAM treatment times: (a) 0 hour; (b) 1 hour; (c) 3 hours; (d) 15 hours. Reproduced with permission of the Royal Society of Chemistry from ref.[66]

On the other hand, ETM layer, typically TiO$_2$ crystalline, contains inherent localized trap states due to under-coordinated surface Ti(IV) ions. These trap states significantly influences on the device performance. The coating of the organic molecules, commonly fullerene self-assembled monolayer, C60-SAM, produces good acceptor of electron on HP,[68-70] passivating efficiently the TiO$_2$ by binding to TiO$_2$ surface hydroxyl groups through the carboxylic acid anchoring group.[71] Better electron extraction by incorporation C60-SAM efficiently improved the performance of HP solar cells.[71-73] In addition, C60-SAM also passivated trap states in HP (at the interface), consequently reducing the non-radiative recombination, and finally increasing the EL efficiency.[72] Besides, the fullerene and its derivatives, as PCBM,[74] benzoic acid derivatives[75] have been also used to improve the electron extraction efficiency.

At the same time, the improvement in the electron transport by the incorporation of C60-SAM helped to reduce the hysteresis phenomenon in the photocurrent density-voltage characteristic.[72-73] The accumulation of charge at ETM/HP interface has been considered as one of the origins of the hysteresis effect in PCSs.[76] Bending HP bands with fullerene leaded better electron extraction, meanwhile reducing the electron accumulated at the interface, consequently reducing the hysteresis in the operation of HP solar

cells.[73] The reduction of hysteresis gives an important contribution to the accurate determination of HP device performance. In addition, a thin insulating organic interlayer between ETM and HP can hinder electron back transfer and reduce the recombination process at the interface effectively.[66]

In addition, organic molecules have been also employed to vary within the ETM films. The introduction of ethylene diamine tetraacetic acid (EDTA) in SnO_2 resulted the enhancement of electron mobility by the factor of three, equivalent with the hole mobility of spiro OMeTAD. More importantly EDTA modified SnO_2 induced the improvement of HP properties, concretely the grain size was enlarged three times, the crystallinity was also enhanced and the trap density was significantly reduced. As a consequent, the performance of devices was much better, the photoconversion efficiency (PCE) was increased to 21.6% with the negligible hysteresis while the reference cell possessed only 18.9% of PCE with the presence of hysteresis. Moreover, the stability of devices was significantly improved, only 8% of PCE was lost after 2880 hours stored in ambient condition with 35% of humidity, and 86% of PCE was remained after 120 hours illumination at 1 sun. Furthermore, EDTA modified SnO_2 leaded the improvement in HP devices not only for rigid substrates but also for flexible substrates, reaching to PCE of over 18% with a good bending stability.[77]
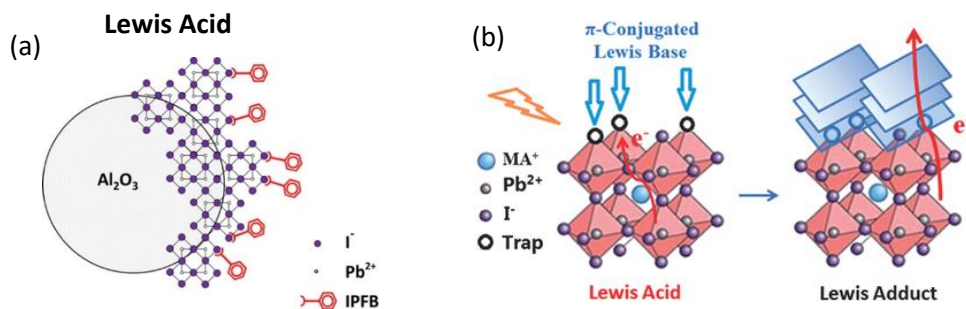

Fig I.13. Schematic representation of passivation of perovskite crystal by (a) supramolecular halogen bonding donor−acceptor complexation to passivated the perovskite crystal with iodopentafluorobenzene (IPFB) and (b) n-type π-conjugated molecules, indacenodithiophene end-capped with 1.1-dicyanomethylene-3-indanone (IDIC). Reproduced with permission of (a) American Chemical Society from ref[78] and of (b) John Wiley and Sons from ref.[79]

Organic molecules have been also used to passivate HP surface. Abate and coworkers[78] indicated that for HP materials, at the crystal surface the coordination number for ions is always lower than in the bulk material. The consequent nonstoichiometric material is comprised of a local excess of positive or negative ions. Such polar surfaces are unstable, and their apparent

natural occurrence has been associated with the adsorption of foreign atoms, which passivate the crystal surface by balancing the local excess charge. For HP material, the presence of under-coordinated iodines at the crystal surface gives rise to local excess of negative electrostatic charge, which acts as hole-trapping sites to create the charge accumulation and cause undesired charge recombination. By employing supramolecular halogen bonding donor−acceptor complexation to coat the perovskite crystal with iodopentafluorobenzene (IPFB), the electrostatic charge of under-coordinated iodines could be shielded, thereby leading an improvement of PCE from 13% to 15.7% (Fig I.13a).[78] Similarly, under-coordinated Pb atoms also act as electron-trapping sites, causing the non-radiative recombination. Lewis bases such as thiophene and pyridine could further be introduced to passivate these under-coordinate Pb atoms in HP surface. After being passivated with Lewis bases, non-radiative recombination was reduced significantly, resulting a very long HP photoluminescence lifetime of up to 2µs. In addition, the performance of HP solar cells was enhanced to 16.5% of PCE.[80] The Lewis base passivation of HP through under-coordinated Pb atoms has been also investigated in the inverted solar cell configuration. By selecting n-type л-conjugated molecules, indacenodithiophene end-capped with 1.1-dicyanomethylene-3-indanone (IDIC), the carbonyl and cyano groups concentrated negative charges, thereby the under-coordinated Pb atoms in HP could be passivated (Fig I.13b). On the other hand, IDIC possess the chemical properties to promote electron extraction and electron transport, and the LUMO and HOMO levels suitable with HP. Consequent, IDIC molecules were applied to act as both ETM and HP passivation agent. As a result, HP solar cells containing IDIC molecules presented the photoconversion efficiency (PCE) as high as 19.5%.[79]

In addition to the non-radiative recombination at under-coordinated iodine and Pb atoms, HPs also possess abundance of grain boundaries where dangling bonds form deep defect states significantly affecting on the charge recombination and transport in the photovoltaic devices. Indeed, the grain boundaries of perovskite films show optoelectronic properties that are different from the grain interiors and exhibit shorter charge carrier lifetime and weaker photoluminescence (PL) intensity.[37] Studies using Kelvin probe force microscopy and conductive atomic force microscopy have shown that the grain boundaries and the grain interiors have different electrical potentials and that grain boundaries have faster ion migration.[81] Hence passivation of HP grain boundary has been also a strategy to improve the electronic device performance.

Following this strategy, within the scope of this thesis, we employed organic molecules, named a twisted hexaazatrinaphthylene (HATNA) and a

bisthiadiazolefused tetraazapentacenequinone (DCL97), to passivate the HP grain boundaries. As a result, after the passivation, the quality of MAPI HP was significantly improved. Consequently we observed an improvement in the performance of three different optoelectronic devices such as solar cells, LEDs and light amplifiers in a comparison with reference cell, without organic additive. The effect of the organic additives (HATNA and DCL97) on the device performance was discussed more detail in the chapter VI and VIII. Additionally, in the term of sample preparation, additives were introduced taking the advantage of the anti-solvent deposition method. Thus, we also provided a novel approach to introduce additives to HP films. In the anti-solvent deposition method, during the spin-coating process of HP precursor solution, a non-polar solvent, in which HP precursors are not soluble, is poured onto the sample. This exposure produces the saturation of the solution and the fast precipitation of the precursors creating numerous perovskite nucleation centers and the corresponding formation of a flat, uniform, and pinhole-free perovskite layer. In our approach, additives, being organic molecules in our case, are dissolved in a non-polar solvent and introduced in HP films through the anti-solvent deposition step. Consequently, our method facilitates the combination of HP with other materials, not only organic molecules, without introducing any additional step.

Differently to our approach, organic molecules were also incorporated to the solution of HP precursors, showing their important role in the growth of HP film and having a great impact on the film's morphology and electronic properties.[82] Xu et al. dissolved phenyl-C61-butyric acid methyl ester (PCBM) in HP precursor solution, then formed HP-PCBM hybrid film by spin-coating. They pointed out that PCBM was homogeneously distributed throughout the hybrid film at HP grain boundaries. In this context, PCBM passivated the PbI_3^- antisite defects, in which iodine occupies the Pb site and forms a trimer with neighbouring iodine atoms, during the HP self-assembly. At the same time, by tying up iodide-rich surface sites, or simply unincorporated iodide anions, PCBM can reduce anion migration through defects at grain boundaries. As a result, hybrid HP-PCBM solar cell showed an enhancement in photovoltage and a high reduction in hysteresis.[82] Beside of using organic molecules, long-chain polymers have been also investigated to passivate HP within the bulk film as polymers can form more stable and reliable interactions with the HP grains and could conceivably cross-link grains to improve film stability.[83-85] On the other hand, polymer has been previously used as a matrix to deposit HP nanoparticles, improving the humidity stability of LEDs.[86]

Organic molecules have been also used to protect HP, reducing the degradation especially from moisture. The hydrophobic HTM[87-88] or ETM[89] in p-i-n heterojunction structure were employed. The devices showed a clear improvement in a long-term stability. This approach shows a good advantage, the organic layer can have a bi-function as HTM (or ETM) and HP protector, reducing the device preparation process. However this may require the design of materials which can have some limit in the practical application. A similar effect can be achieved in an easier way, introducing a hydrophobic interlayer. The hydrophobic layers are generally made from small molecules with alkyl groups and have been deposited on the HP layer.[90-91] Such layers can protect the HP film under high relative humidity (90%) over 30 days.[91]

In this section, we have briefly provide an overview of how researchers have combined organic molecules with HP in different ways, obtaining an advantage of their combination. We also brought our own study contributing to the development of integrating these materials.

I.2.3. Brief introduction on the interaction of perovskite with electron transport materials

Electron transport materials (ETMs) play an important role in the performance of HP optoelectronic devices as they decide how efficiently electrons are extracted. To have a good device performance, ETM layer has to satisfy some basic requirements. ETM has to ensure the light is transmitted into HP absorber. Consequently, ETMs need to have a good optical transmittance. ETM is required to have matched energy levels with those of HP and a good electron mobility to improve the electron extraction efficiency. Moreover, in the n-i-p heterojunction, HP is deposited directly on ETM. Consequently ETMs also have a great influence on the formation and crystallization of HP which determine the properties of HP films, as well as the performance of HP devices and their stabilities. In this section, we briefly introduce the impact of ETMs, simplified considering substrates, on the growth of HP and bring our contribution to further clarify the influence.

It has been previously demonstrated that the nature of substrate has a significant impact on the formation and properties of HP. As an example, Climent-Pascual and co-authors selected different substrates including glass, FTO, TiO_2 and PEDOT:PSS to investigate their influence on the formation and properties of MAPI HP.[92] Interestingly they observed that these substrates with different natures and roughness strongly influence the structure of HP coated on. Although, the tetragonal crystalline phase of HP was obtained for all the analyzed substrates with a preferential orientation along (110) direction, the crystallite size for (110) grain and the preferred orientation partially depended on the substrate's type. For the use of FTO, TiO_2 and PEDOT:PSS, with the surface roughness reported as 15.3, 6.8 and 0.8 respectively, the crystallite size for (110) grain increased as increasing the substrate roughness while the preferred orientation and HP surface roughness had an opposite trend, reducing with an increase of substrate roughness. On the other hand, the nature of substrate also plays a role. As glass with surface roughness of 3.2, much lower than that of FTO and TiO_2, induced a formation of HP with the biggest crystallite size for (110) grain, much higher than that of HP coated on TiO_2 and FTO, and with the highest HP surface roughness. In addition, the thickness of HP layer deposited on all four substrates were also different although those layers were prepared in the same conditions.[92] Another example, the effect of substrate's nature on the formation of HP is clearly showed. It has been previously demonstrated that on some ZnO[93-94] and SiO_2 [93] substrates, HP could formed at room temperature after few minutes

of spin-coating, even for the case of HP precursors containing chloride while HP was not formed on TiO$_2$ prepared by atomic layer deposition (ALD-TiO$_2$) and FTO.[94]

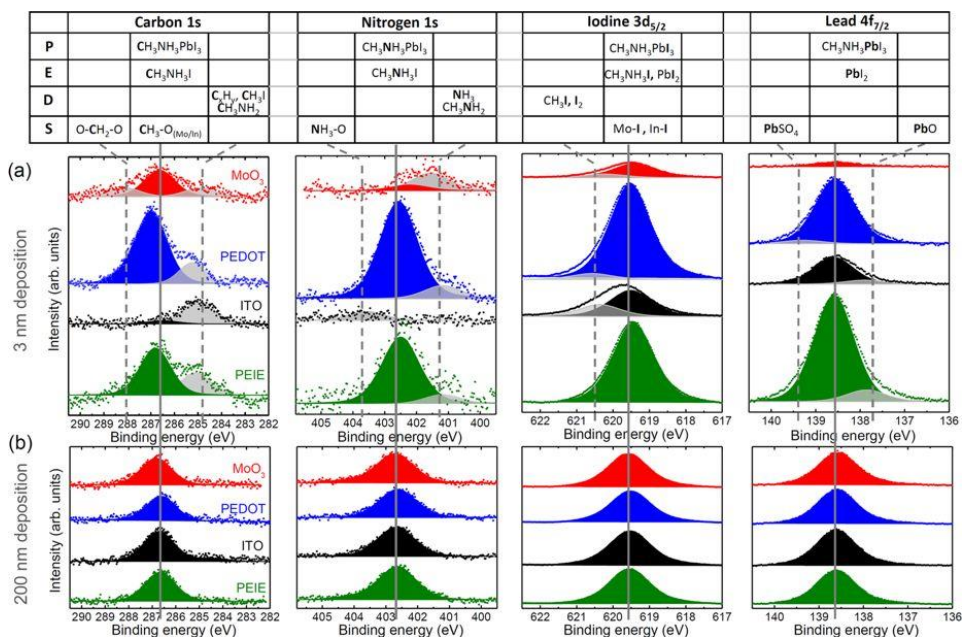|	Carbon 1s			Nitrogen 1s		Iodine 3d$_{5/2}$		Lead 4f$_{7/2}$	
P	CH$_3$NH$_3$PbI$_3$			CH$_3$NH$_3$PbI$_3$		CH$_3$NH$_3$PbI$_3$		CH$_3$NH$_3$PbI$_3$	
E	CH$_3$NH$_3$I			CH$_3$NH$_3$I		CH$_3$NH$_3$I, PbI$_2$		PbI$_2$	
D			C$_2$H$_4$, CH$_3$I CH$_3$NH$_2$		NH, CH$_3$NH$_2$	CH$_3$I, I$_2$			
S	O-CH$_2$-O	CH$_3$-O$_{(Mo/In)}$		NH$_3$-O		Mo-I, In-I		PbSO$_4$	PbO

Fig I.14. XPS spectra of different elements (carbon, nitrogen, iodine, and lead) involved in MAPI formation on the four different substrates (MoO$_3$, PEDOT:PSS, ITO and PEIE) during the evaporation. The solid vertical lines mark the expected binding energy in perovskite for each element, while the dashed lines show the positions of additional chemical environments observed at low coverage before the stoichiometrically correct perovskite is formed. Reproduced from ref.[95]

Olthof and co-workers shed light on how the nature of substrate affects the growth of HP by using x-ray photoelectron spectroscopy (XPS) technique.[95] Four different substrates such as ITO, MoO$_3$, PEDOT:PSS and polyethylenimine ethoxylate (PEIE) were selected for MAPI HP evaporation. By analysing the XPS spectra of four elements (C, N, I and Pb) involved in HP formation, they found that there was an induction period in the growth of HP during which the volatile compounds were formed and catalysed by the substrates (Fig I.14). On the catalytically inactive PEIE and PEDOT:PSS, HP specific C and N were formed readily. At the initial phase of layer formation (~ 3 nm of precursor co-deposition), 30% of the layer was made of HP, the remaining material consisted of physisorbed MAI, methylamine and hydrocarbons. Therefore HP was formed readily, mixed with the by-products. For thicker evaporated layers, pure HP was attained confirming by no additional bonding states. While on the oxide surfaces (ITO and MoO$_3$), MAI

was catalytically disintegrated, leading to negligible amounts of C and N at low evaporated thickness. On the ITO substrate, after the evaporation of 3 nm, the effective layer thickness was merely ~ 0.6 nm. No HP was formed due to the lack of N_2, mostly PbI_2 as well as iodine bound to surface oxygen with addition traces of methyl iodine and hydrocarbons. And in the case of MoO_3 substrate, the effective layer thickness was ~ 1 nm. No HP was formed yet either, here it was due to the lack of Pb probably caused by the formation of highly volatile tetramethyl-lead. Mostly iodine and carbon bound to the surface, as well as some MAI dissociation products. On the two metal oxide substrates the film formation was hindered due to the formation of volatile compounds. The pure HP film could only start forming once the surface has been passivated by C and I surface bonds and as well as MAI dissociation products. This passivation layer could be estimated to be approximately 10 nm and < 30 nm for MoO_3 and ITO respectively.[95] In this report, the nature of substrate accompanying with the formation of volatile compounds hindered the formation of HP. However, the formation of HP is affected by the nature of substrate probably differently in case that HP is prepared by another technique such as solution processes (one and sequent spin coater method).

As discussed above, substrates with different natures, providing different properties, significantly affect the formation of HP.[92, 95-96] Moreover with the same nature of substrate (same material), the structure of substrates including planar, mesoporous structure and even mesoporous structure with different porosity also shows an influence on HP's growth. It has been reported that an ordered arrangement of organic cation in MAPI crystallites grew on planar substrate while a fully random orientation of organic cation in MAPI crystallites grew in the mesoporous scaffold.[97] This was confirmed by the observation of the strong decrease in intensity of the organic torsional mode and the organic vibration mode in Raman spectra[97-98] for MAPI deposited on a planar substrate in a comparison with that coated on scaffold. The x-ray diffraction (XRD) measurement also pointed the same direction, the crystal grown on the planar substrate presented grains that were much more oriented respect to the mesoporous substrate.[97] In addition, the grain size of polycrystalline HP films were found to be much bigger for the planar substrate in a comparison with the mesoporous scaffold as in the mesoscopic architecture the grain size is limited by the pore size within the nanoparticle of scaffold.[99] Changing the porosity of the scaffold, by changing the nanoparticle size, also leads to the variation of HP's morphology.[100] Beside the effect in the structure and morphology, the architecture of substrate affects the optical properties of HP films as well. The absorption onset and PL peak were shifted[100-101] and the PL decay became shorter for the mesoporous scaffold[99] in a comparison with the planar structure. For the mesoscopic

architecture, the PL decay was faster for smaller porosities.[100] This correlation found between grain sizes and PL decay was relatively in agreement with the report of de Quilettes and co-workers, where shorter PL lifetime and lower PL intensity at grain boundaries respect to grain interiors was observed.[37] Different crystal sizes of HP forming on those different substrate structures also have an effect on the charge transport. In fact, faster charge mobility was found in the case of using planar TiO_2 substrate where larger grain sizes were achieved.[99] Again the adverse effect of grain boundaries was shown clearly. The advantage of HP planar architecture was seen here. Larger grain size, longer PL lifetime and higher charge mobility.

The crystallinity of substrates also has an effect on the formation of HP. As an example, the grain sizes of HP films coated on amorphous TiO_2 was smaller than those coated on crystalline TiO_2 ETM. However, the charge transfer from HP to amorphous TiO_2 was more efficient due to a better energy band alignment at amorphous TiO_2/HP interface.[102] Although this behaviour is strongly dependent on the preparation of amorphous and crystalline TiO_2 films. In the literature, for TiO_2 ETM based devices mostly high PCEs have been achieved for crystalline TiO_2.[55, 103] Another example, HP films formed on SnO_2 ETM with different crystallinities (obtaining by different heated temperatures) exhibited a difference in grain sizes. Bigger grain size was obtained for the case of low temperature-SnO_2 while the absorbance spectra of HP deposited on those SnO_2 were identical. The performance of HP devices was found much better for low temperature-SnO_2 however mainly due to better properties of SnO_2 ETM as better film coverage, higher electron mobility and wider bandgap. At high annealing temperature, SnO_2 particles became agglomerate, resulting uncovered films with poor device performance.[104] In literature, high PCEs have been also found for low temperature SnO_2 based ETMs.[55, 105] The change in morphology of HP due to different heated temperatures of substrates that is discussed here was the change in fresh HP films. It has been also reported that the modifying chemically substrate's surface due to heated temperatures affects the thermal stability of HP. Yang et al. showed that the thermal stability of MAPI HP films for an annealing at 100°C strongly depended on ZnO substrates which were prepared at different temperatures from 25°C to 400°C. HP films were more stable for ZnO ETM heated at higher temperatures. Concretely HP layer degraded after 7 minutes annealed at 100°C for ZnO prepared at 25°C while HP film was still stable after 40 minutes and degraded after 80 minutes of annealing for ZnO prepared at 400°C (Fig I.15b). The difference in HP stability was caused by different amount of hydroxyl group and residual acetate ligands, by-products of the ZnO nanoparticle synthesis, on ZnO's surfaces. At high heating temperature, hydroxyl group and residual acetate

ligands evaporated, reducing their amount on ZnO surface (Fig I.15a), consequently the thermal stability of coated HP films was enhanced.[93]
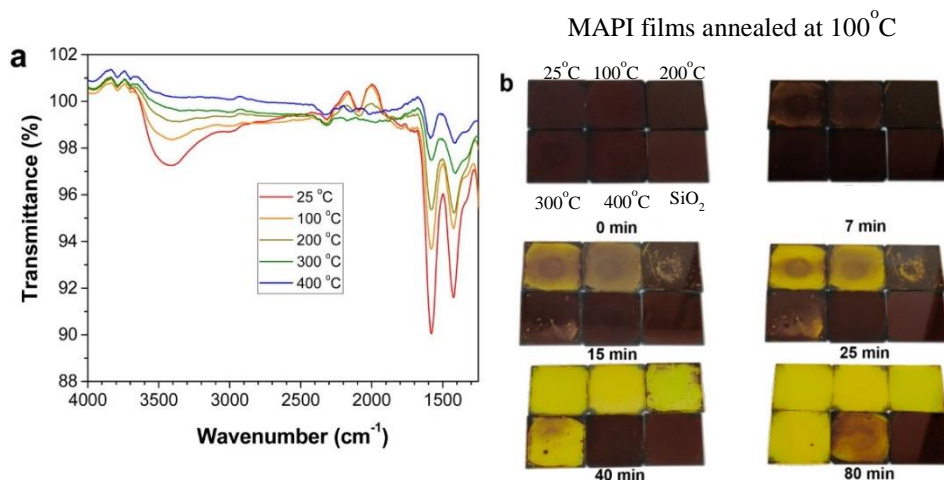

Fig I.15. (a) Fourier-transform infrared spectra of glass/ZnO films annealed at various temperatures. The stretching modes of surface hydroxyl groups at 3410 cm^{-1} and residual acetate ligands at 1580 cm^{-1} and 1420 cm^{-1}. (b) Photographs of MAPI films annealed at 100ºC, in which MAPI films were deposited on those ZnO (prepared at from 25ºC to 400ºC) and SiO$_2$ substrates. Reproduced with permission of American Chemical Society from ref.[93] Copyright © 2015, American Chemical Society.

Temperature of substrates where HP is deposited on is another factor affecting the formation of HP. Zhang and co-workers reported a study on the effect of TiO$_2$ pre-heated temperatures on the crystallization of mixed perovskite which was deposited from a solution containing MABr, PbBr$_2$, FAI and PbI$_2$ dissolved in a co-solvents (dimethylformamide (DMF) and dimethyl sulfoxide (DMSO)).[106] In their work, HP was spin-coated immediately when the temperatures of TiO$_2$ ETM reached a designed temperature. The effect of substrate's temperature was clearly seen by naked eyes, the color of as-deposited HP films changed from reddish brown to charcoal, the light transmittance dropped from translucent to opaque when temperatures of TiO$_2$ increased from 30ºC to 70ºC. The optical microscopy photos and scanning electron microscopy (SEM) measurement confirmed the gradual change in HP morphology from dendritic to island structure. The HP surface's roughness was also dependent on those temperature of TiO$_2$ substrates, higher roughness for higher temperature. The XRD measurement of annealed HP films pointed out that those substrate's temperatures influenced on the crystal orientation. The authors proposed that the dependence of HP crystallization process on the temperatures of TiO$_2$ ETM was mainly caused by the evaporation of DMSO at those temperatures (Fig I.16). During the spin-coating process, PbI$_2$

preferentially reacted with DMSO to FAI (and/or MABr) as its reaction was stronger. At low substrate temperature, DMSO evaporated slowly due low saturated pressure, the rest of DMSO coordinated with PbI_2 forming an intermediate phase with a dendritic morphology. However, DMSO evaporated faster when increasing the substrate temperature, probably resulted from the limitation of DMSO molecules for the reaction with PbI_2. Consequently PbI_2 reacted with FAI (and/or MABr) to form a non-perovskite phase, δ-phase. In addition, raising the substrate temperature induced an increase of surface tension of the solvate, thereby microscale fluid flows were generated due to the strong volatilization of the solvent. These flows carried around the nuclei of the intermediate phase and δ phase, which aggregated together in the solvate and eventually formed islands.[106] The dependence of HP formation and properties on the substrate temperatures has been also found in some other works. In which the evaporation of anion type's by-products was the highest impact on the growth of HP.[36, 107] Because MAI,[95] MACl[36] and MAAc,[107] common precursors for the preparation of HP, are known to be thermally unstable, their by-products are easily removed by annealing. Therefore during the spin-coating process, at elevated substrate temperatures, the evaporation of those by-products possibly causes an unbalance of ions in HP precursors, affecting the formation and properties of HP film. However, it certainly depends on the molar ratio of HP precursors in a solution, as well as the temperatures of substrates.
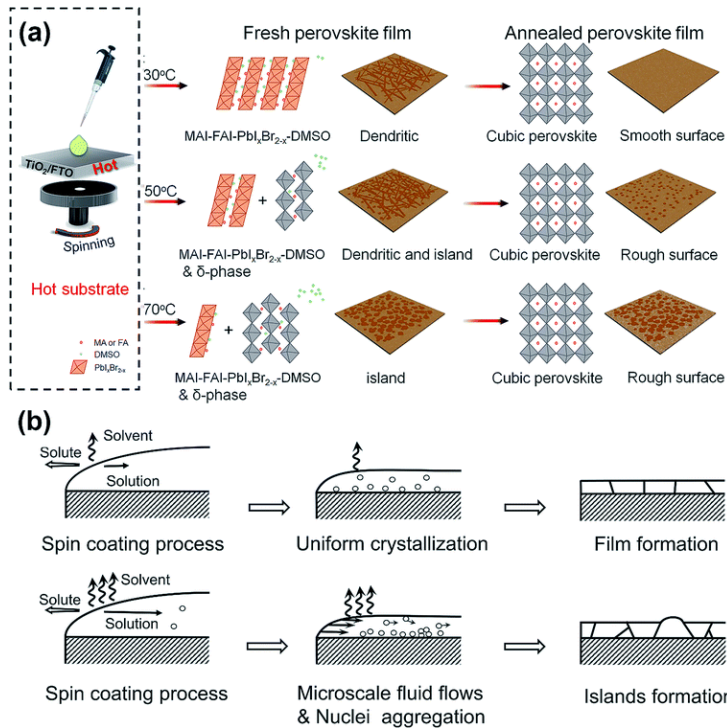
Fig I.16 (a) Schematic of the whole crystallization process and (b) schematic diagram of the morphology evolution of the perovskite films fabricated at different substrate temperatures. Reproduced with permission of Royal Society and Chemistry from ref.[106]

We have just seen many factors such as nature, roughness, structure, temperature of substrates in general and of ETMs in particular affecting the formation as well as the thermal stability of HP films. Within this thesis, we additionally showed that the terminations of ZnO ETM, resulted from the preparation method, have an influence on the formation and the evolution of HP films during the storage, with the consequent impact on the performance of fresh and aged devices. By using different gas components, N_2 and O_2 flows during a spray pyrolysis, at high FTO-substrate's temperature, we proposed ZnO ETMs were formed differently due to the difference of thermal decomposition and oxidation of precursors caused by difference amount of oxygen presented. As a result, different properties of HP films coated on those ZnO ETMs were found. Slightly bigger grain sizes and higher preferential orientation along (110) plane for ZnO_O_2/HP sample was observed. Interestingly after 15 days stored under dark, at room temperature and ~ 35% of humidity, HP films coated on ZnO_N_2 and ZnO_O_2 substrates changed in an opposite way. We observed an increase in HP grain sizes probably caused by the coalescence of smaller crystallites within HP film into larger ones, and higher preferential orientation for aged ZnO_N_2/HP sample in a comparison

27

with the fresh one. While aged ZnO_O_2/HP did not show an appreciable change in grain size. However, it showed the HP degradation detecting by the formation of a platelet-like grains, suggesting PbI_2 formation. In addition, the degree of preferential orientation was reduced comparing with the fresh one. The degradation of aged ZnO_O_2/HP sample should related to the O_2 rich condition of ZnO_O_2 surface as both ZnO_N_2/HP and ZnO_O_2/HP films were stored at the same condition and we did not observe the degradation for ZnO_N_2/HP film.

As the consequent of different evolution behaviours of HP films coated on ZnO_N_2 and ZnO_O_2 ETMs, the stability of HP solar cells based on those ZnO ETMs were very distinct. In fact, ZnO_N_2 based devices showed the enhancement of PCEs even after more than one month of preparation under the storage conditions listed above. While the PCEs of ZnO_O_2 based cells strongly increased after 7 days of preparation however slightly decreased after 13 days which was in agreement with the degradation of 15-days-old HP film. We found here an interesting feature which was the improvement device performance for both ZnO_O_2 and ZnO_N_2 after one week of preparation and with the same percentage (36%). Because the conditions for HP film preparation and device storage were the same, the improvement in both two type of devices should have the same origin which was the coalescence of smaller crystallites into larger one. Therefore we proposed in ZnO_O_2 based devices, there were two competitive processes including the coalescence of HP crystallites and the degradation due to defects caused by the O_2 rich condition during the spray pyrolysis. More detail discussion is described in the chapter VII and VIII.

As mentioned above the nature of substrate has a great impact on the formation of HP. Therefore the modification of substrate's nature, leading the change in the substrate characters also has an influence on the growth and crystallization of HP. In the previous section (section I.2.2), we commented that the modification of ETMs by organic molecules produce a change in HP morphology (Fig I.12) and crystallinity, consequently affecting the performance of devices as well as their stability.[66-67, 77] In p-i-n heterojunction, the modification of HTMs surface by organic molecules also showed an influence on the HP properties.[108] Beside of using organic molecules to modify ETM surfaces,[109-110] doping has been verified as a method to change the properties of ETMs. The 0.5% incorporation of yttrium changed the lattice parameters of TiO_2 nanoparticles, increasing a lattice while reducing c parameter. As a result, the dimension of HP nanoparticles supported Y-TiO_2 were obtained smaller, leading a higher loading of HP on the mesoporous Y-TiO_2. Consequently with the same thickness of the mesoporous layer, the

enhancement in the whole wavelength range of HP's absorbance and of Y-TiO$_2$/HP based device performance respectively were obtained.[111]

In summary, we have shown that in the n-i-p heterojunction, ETMs beyond their own properties also affect greatly the formation and crystallization of HPs. The influence of ETM's characters including nature, roughness, structures (planar and mesoporous architectures), crystallinity, temperature and surface termination on the morphology and properties of HP films have been discussed. The induced effects of these factors on the device performance and stability have been also listed.

I.3. Outline and scope

I.3.1. Objective

Conversion of solar light into electricity, by means of the photovoltaic effect, is a crucial key to reduce the strong dependence on the on fossil fuels of today's society. The challenge for the photovoltaic industry is determining how to efficiently and economically convert that incident solar energy into usable electricity. The lifespan of the photovoltaic devices is also an extremely important factor deciding the possibility of those devices to become commercialization. Recently halide perovskite (HP) appears to be a very promising material for photovoltaic application. HP solar cells become the fastest-advancing solar technology to date with the impressively the progress in photoconversion efficiencies (PCEs) from 3.8% to over 25% in a very short time, within 10 years (Fig I.2). The progress in PCEs of HP solar cells is much faster than that of silicon solar technology which has been investigated in a very early state, since ~ 1975 with the PCEs of ~ 14% and up to date, after ~ 45 years of investigation, its PCE has been recorded of ~ 27%. Hence the laboratory achieved PCE of HP solar cells is close to those of silicon. The PCEs for commercial silicon solar cells nowadays is in the range of 15 – 22% for monocrystalline and 12 – 18% for polycrystalline silicon based devices. The comparison between those PCEs of commercial silicon solar cells and the recorded PCE of HP cells highly demonstrates the potential commercialization of HP solar cells. Moreover HP material and electronic devices can be prepared by low cost techniques. The remained question is why HP solar cells have not become commercialization yet. The answer is mainly due to the low stability. The silicon solar panel has a lifespan over 25 years while the lifetime of HP devices can be counted by days. The major contribution to the low stability of HP devices is the intrinsic properties of HP material which can be easily degraded under number of factors such as moisture, temperature, ultraviolet light or oxygen. Therefore improving the quality/properties of HP is very important for the development of HP technology.

Studying the interaction of HP with other materials is a promising strategy to not only overcome the issues of HP, as stability and hysteresis, but also can improve its quality and finally ameliorate the device performance. On the other hand, the combination of materials can also open the possibility to

integrate all good properties of single materials into a composite, producing a constructive synergy. As demonstrated in the past, adobe, stained glass and stainless steel are just some examples of great combined materials which have been supported for human life since centuries. In addition, the interaction of HP and other materials can rise new properties or phenomena which do not exist in single materials. The finding of new properties could importantly contribute to the development of optoelectronic. In this regard, the purpose of this doctoral study is to investigate the interaction of HP with other materials, looking for the potential application in photovoltaics. To reach this goal several objectives have been targeted:

➢ Preparation of high and controllable quality of HP thin films and HP devices which are used as references to evaluate/compare the film properties and device performance with modified systems.

➢ Combining HP with colloidal QDs. This study will require the synthesis and characterization of QDs, the control of the QD capping and its exchange to another capping.

➢ Analyze the interaction of HP with different materials affecting different parts of a complete device. Within this doctoral thesis, we have studied the interaction of HP with three different materials and the interaction was regarded in three different situations:

- The interaction between HP and electron transporter materials (ETMs) in which HP was grown directly on ETM substrates.

- The interaction between HP and QDs was studied in the situation where QDs were embedded into HP matrix.

- The interaction between HP and organic molecules which were introduced to HP up surface.

I.3.2. Structure of the Thesis

The interaction between halide perovskite (HP) and other materials is presented throughout the body of this doctoral thesis. In the chapter I, we explain the reason of choosing HP as a central material for the investigation, as well as the importance of studying its interaction with other materials. We

also provide a general view on its interaction, in particular with materials that we experimentally investigated. The chapter II describes the characterization methods used to evaluate the interaction between HP and other materials. The interaction between HP and QDs is reported in the chapter III, IV and V while the chapter VI and VII show the interaction of HP with organic molecules and with electron transporter materials (ETMs), respectively. The chapter VIII provides a general discussions of all obtained results within this doctoral thesis. In the last chapter, chapter IX, we present a general conclusion and give suggested future investigation. This doctoral thesis is composed by five articles which have published in the international journals, targeting the objectives mentioned in the previous section. We summarize here the main results achieved in each publications:

Chapter III: Interaction Between Colloidal Quantum Dots and Halide Perovskites: Looking for Constructive Synergies. In this publication, we provide a small review on how colloidal QDs interact with HP, and how scientist have combined these materials. We also briefly show our own contribution. Through the review, we found that the combination of QDs and HP can produce a constructive synergy. Each material gets the benefit from the combination. HP can efficiently passivate QD surface and protect QDs from oxidation and corrosion, leading high performance of QD devices as solar cells. While QDs present a nucleation center role to promote a proper crystallization of HP lattice structure, resulting in better morphological, optical and structural properties, and consequently reporting better device performance. Moreover, HP matrix can act as an excellent charge carrier transporter into QDs in view of type I junction, contributing to the development of LEDs and photodetectors. Furthermore the band alignment between HP and QDs can be tailored favouring the charge carrier injection from one into the other. On the other hand, the combination of two these materials can also attain the absorption spectrum to near infrared. In addition, the interaction between QDs and HP can raise a new property/phenomenon which is described more details in the chapter IV.

Chapter IV: Single step deposition of an interacting layer of a perovskite matrix with embedded quantum dots. By using a relative large band gap of PbS/CdS QDs, we formed the type II junction at the interface of QDs/HP. Due to the band alignment, electrons in the CB of HP can recombine with holes in VB of QDs, forming an emission at the exciplex state whose energy is lower than that of both HP and QDs. The exciplex emission was detected by both optical pumping and electrical injection. The observation of the exciplex emission is important for the development of LEDs, in particular in IR region. On the other hand, the detection of exciplex emission also creates

a new device configuration. Considering that an electron and hole can recombine emitting a photon at the exciplex state, these photon can be also absorbed at the exciplex state generating an electron-hole pair. This opens a possibility to prepare an intermediate band solar cells (IBSCs) in which QDs are embedded in HP matrix, the exciplex state will form an intermediate band within the band gap of HP. The intermediate band will act as step-stone to move electron from HP's VB to its CB through the absorption of multi-photons at energy lower than HP's band gap.

Chapter V: PbS Quantum Dots as Additives in Methylammonium Halide Perovskite Solar Cells: the Effect of Quantum Dot Capping. In this study, we confirmed the nucleation center role of QDs in the crystallization of HP, resulting in the improvement in morphological, optical and structural properties of HP. We further clarified the improvement in the structure properties. With a small quantity of intermixed PbS QDs in the solution, HP precursors converted more efficiently to HP, illustrated by lower percentage of PbI_2 intensity for HP-PbS hybrid films in a comparison with the reference film, without QDs. Moreover the preferential orientation along (110) HP crystalline plane and the crystallinity of both (110) and (220) planes were enhanced when PbS QDs were introduced into the films. As a result of the improvement in the film quality, the performance of planar solar cells was increased respect to the reference cells. Importantly by the first time, we observed the dependence of HP film properties on the PbS capping. In this study, we tested three different PbS capping ligands being methylammonium lead iodide (MAPI), cesium lead iodide (CsPI) and 4-aminobenzoic acid (ABA). The ABA capping had a higher impact on the morphology while CsPI had a greater influence on the optical property. This observation pointed to an improved interaction of perovskite with the organic ligand affecting the morphology, while the CsPI likely produces a better passivation of the perovskite-QD interface. Consequently, the dependence of HP solar cell performance on the PbS capping was also observed in our study, obtaining the better results with ABA capping. Our results emphasize the interest of PbS QD additives for the development of HP optoelectronic devices, providing an approach to improve the performance by the control of the surface properties of QDs using different capping ligands.

Chapter VI: Enhancement of the Performance of Perovskite Solar cells, LEDs and Optical Amplifiers by Anti-Solvent Additive Deposition. In this publication, we studied the interaction between halide perovskite (HP) and organic molecules, being twisted hexaazatrinaphthylene (HATNA) and a bisthiadiazolefused tetraazapentacenequinone (DCL97). These molecules were introduced to HP through the anti-solvent deposition step. Systematic

characterization pointed out that the introduction of organic molecules did not significantly modify the structure of HP however a clearly interfacial effect was observed. The PL mapping and the impedance measurements were commentary showing that those molecules were localized at the grain boundaries of HP and efficiently passivated them, thereby reducing the recombination. As a result, the performance of three devices including solar cells, LEDs and light amplifiers was strongly improved.

Chapter VII: Spray-Pyrolyzed ZnO as Electron Selective Contact for Long-Term Stable Planar CH$_3$NH$_3$PbI$_3$ Perovskite Solar Cells. The electron transporter materials (ETMs) is usually needed to extract generated electrons to the external circuit or to inject electrons into HP layer in HP solar cells or LEDs respectively. Additionally in the regular n-i-p configuration in which HP is directly deposited on ETM surfaces. Therefore ETM surface may have some effect on the formation of HP films which is the study of this publication. Using different gas components (being N$_2$ or O$_2$ flow) in the spray pyrolysis process, we found that the ZnO formed (ZnO_N$_2$ and ZnO_O$_2$) had different properties, such as grain size, conductivity and optical band off set. HP films deposited on those ZnO ETMs were different in the term of grain size and degree of preferential orientation along (110) crystalline plane. The interesting feature was observed for aging films. After 15-storage-days the evolution of HP films deposited on those different ZnO ETMs were opposite, improving in morphological and structural properties for ZnO_N$_2$ substrate and degrading for ZnO_O$_2$ substrate although those sample were stored in the same conditions. Consequently the performance of HP solar cells was enhanced even after one month of preparation for ZnO_N$_2$ ETM based samples while other devices based on ZnO_O$_2$ showed a decrease in performance after 13 days. In addition, the performance of ZnO_O$_2$ based devices could be improved, increasing after one month of preparation by modifying the condition in the spray pyrolysis such as FTO temperature and precursor concentration. This study emphasizes that beside the role in the electron extraction or injection, ETMs show a significant effect on the formation and evolution of HP films, impacts on the performance and long term stability of HP devices which can be improved with a proper surface properties of ETMs used.

References

1. Kojima, A.; Teshima, K.; Shirai, Y.; Miyasaka, T. Organometal Halide Perovskites as Visible-Light Sensitizers for Photovoltaic Cells. *Journal of the American Chemical Society* **2009,** *131* (17), 6050-6051.
2. NREL photovoltaic efficiency chart: https://www.nrel.gov/pv/cell-efficiency.html
3. Jaramillo-Quintero, O. A.; Sanchez, R. S.; Rincon, M.; Mora-Sero, I. Bright Visible-Infrared Light Emitting Diodes Based on Hybrid Halide Perovskite with Spiro-OMeTAD as a Hole-Injecting Layer. *The journal of physical chemistry letters* **2015,** *6* (10), 1883-1890.
4. Tan, Z.-K.; Moghaddam, R. S.; Lai, M. L.; Docampo, P.; Higler, R.; Deschler, F.; Price, M.; Sadhanala, A.; Pazos, L. M.; Credgington, D.; Hanusch, F.; Bein, T.; Snaith, H. J.; Friend, R. H. Bright light-emitting diodes based on organometal halide perovskite. *Nat Nano* **2014,** *9* (9), 687-692.
5. Alivisatos, A. P. Semiconductor Clusters, Nanocrystals, and Quantum Dots. *Science* **1996,** *271*, 933-937.
6. Lin, K.; Xing, J.; Quan, L. N.; de Arquer, F. P. G.; Gong, X.; Lu, J.; Xie, L.; Zhao, W.; Zhang, D.; Yan, C.; Li, W.; Liu, X.; Lu, Y.; Kirman, J.; Sargent, E. H.; Xiong, Q.; Wei, Z. Perovskite light-emitting diodes with external quantum efficiency exceeding 20 per cent. *Nature* **2018,** *562* (7726), 245-248.
7. Suárez, I.; Juárez-Pérez, E. J.; Bisquert, J.; Mora-Seró, I.; Martínez-Pastor, J. P. Polymer/Perovskite Amplifying Waveguides for Active Hybrid Silicon Photonics. *Advanced materials* **2015,** *27* (40), 6157-6162.
8. Suárez, I.; Hassanabadi, E.; Maulu, A.; Carlino, N.; Maestri, C. A.; Latifi, M.; Bettotti, P.; Mora-Seró, I.; Martínez-Pastor, J. P. Integrated Optical Amplifier–Photodetector on a Wearable Nanocellulose Substrate. *Advanced Optical Materials* **2018,** *6* (12), 1800201.
9. Deschler, F.; Price, M.; Pathak, S.; Klintberg, L. E.; Jarausch, D.-D.; Higler, R.; Hüttner, S.; Leijtens, T.; Stranks, S. D.; Snaith, H. J.; Atatüre, M.; Phillips, R. T.; Friend, R. H. High Photoluminescence Efficiency and Optically Pumped Lasing in Solution-Processed Mixed Halide Perovskite Semiconductors. *The journal of physical chemistry letters* **2014,** *5* (8), 1421-1426.
10. Zhu, H.; Fu, Y.; Meng, F.; Wu, X.; Gong, Z.; Ding, Q.; Gustafsson, M. V.; Trinh, M. T.; Jin, S.; Zhu, X. Y. Lead halide perovskite nanowire lasers with low lasing thresholds and high quality factors. *Nature materials* **2015,** *14* (6), 636-642.
11. Xing, G.; Mathews, N.; Lim, S. S.; Yantara, N.; Liu, X.; Sabba, D.; Grätzel, M.; Mhaisalkar, S.; Sum, T. C. Low-temperature solution-processed wavelength-tunable perovskites for lasing. *Nature materials* **2014,** *13* (5), 476-480.
12. Stranks, S. D.; Hoye, R. L. Z.; Di, D.; Friend, R. H.; Deschler, F. The Physics of Light Emission in Halide Perovskite Devices. *Advanced materials* **2018,** *0* (0), 1803336.
13. Manser, J. S.; Christians, J. A.; Kamat, P. V. Intriguing Optoelectronic Properties of Metal Halide Perovskites. *Chemical reviews* **2016,** *116* (21), 12956-13008.

14. Zhang, Y.; Zhang, H.; Zhang, X.; Wei, L.; Zhang, B.; Sun, Y.; Hai, G.; Li, Y. Major Impediment to Highly Efficient, Stable and Low-Cost Perovskite Solar Cells. *Metals* **2018,** *8* (11), 964.

15. Ma, Y.; Wang, S.; Zheng, L.; Lu, Z.; Zhang, D.; Bian, Z.; Huang, C.; Xiao, L. Recent Research Developments of Perovskite Solar Cells. *Chinese Journal of Chemistry* **2014,** *32* (10), 957-963.

16. Cheng, Z.; Lin, J. Layered organic–inorganic hybrid perovskites: structure, optical properties, film preparation, patterning and templating engineering. *CrystEngComm* **2010,** *12* (10), 2646-2662.

17. Eperon, G. E.; Stranks, S. D.; Menelaou, C.; Johnston, M. B.; Herz, L. M.; Snaith, H. J. Formamidinium lead trihalide: a broadly tunable perovskite for efficient planar heterojunction solar cells. *Energy & Environmental Science* **2014,** *7* (3), 982-988.

18. Chueh, C.-C.; Li, C.-Z.; Jen, A. K. Y. Recent progress and perspective in solution-processed Interfacial materials for efficient and stable polymer and organometal perovskite solar cells. *Energy & Environmental Science* **2015,** *8* (4), 1160-1189.

19. Lee, J.-W.; Seol, D.-J.; Cho, A.-N.; Park, N.-G. High-Efficiency Perovskite Solar Cells Based on the Black Polymorph of HC(NH2)2PbI3. *Advanced materials* **2014,** *26* (29), 4991-4998.

20. Pellet, N.; Gao, P.; Gregori, G.; Yang, T.-Y.; Nazeeruddin, M. K.; Maier, J.; Grätzel, M. Mixed-Organic-Cation Perovskite Photovoltaics for Enhanced Solar-Light Harvesting. *Angewandte Chemie International Edition* **2014,** *53* (12), 3151-3157.

21. Choi, H.; Jeong, J.; Kim, H.-B.; Kim, S.; Walker, B.; Kim, G.-H.; Kim, J. Y. Cesium-doped methylammonium lead iodide perovskite light absorber for hybrid solar cells. *Nano Energy* **2014,** *7*, 80-85.

22. Li, Z.; Yang, M.; Park, J.-S.; Wei, S.-H.; Berry, J. J.; Zhu, K. Stabilizing Perovskite Structures by Tuning Tolerance Factor: Formation of Formamidinium and Cesium Lead Iodide Solid-State Alloys. *Chemistry of Materials* **2016,** *28* (1), 284-292.

23. Saliba, M.; Matsui, T.; Seo, J.-Y.; Domanski, K.; Correa-Baena, J.-P.; Nazeeruddin, M. K.; Zakeeruddin, S. M.; Tress, W.; Abate, A.; Hagfeldt, A.; Grätzel, M. Cesium-containing triple cation perovskite solar cells: improved stability, reproducibility and high efficiency. *Energy & Environmental Science* **2016,** *9* (6), 1989-1997.

24. González-Carrero, S.; Galian, R. E.; Pérez-Prieto, J. Organometal Halide Perovskites: Bulk Low-Dimension Materials and Nanoparticles. *Particle & Particle Systems Characterization* **2015,** *32* (7), 709-720.

25. Boix, P. P.; Agarwala, S.; Koh, T. M.; Mathews, N.; Mhaisalkar, S. G. Perovskite Solar Cells: Beyond Methylammonium Lead Iodide. *The journal of physical chemistry letters* **2015,** *6* (5), 898-907.

26. Hao, F.; Stoumpos, C. C.; Chang, R. P. H.; Kanatzidis, M. G. Anomalous Band Gap Behavior in Mixed Sn and Pb Perovskites Enables Broadening of Absorption Spectrum in Solar Cells. *Journal of the American Chemical Society* **2014,** *136* (22), 8094-8099.

27. Clark, S. J.; Donaldson, J. D.; Harvey, J. A. Evidence for the direct population of solid-state bands by non-bonding electron pairs in compounds of the type CsMX3(M= Ge, Sn, Pb; X = Cl, Br, I). *Journal of Materials Chemistry* **1995,** *5* (11), 1813-1818.

28. Ogomi, Y.; Morita, A.; Tsukamoto, S.; Saitho, T.; Fujikawa, N.; Shen, Q.; Toyoda, T.; Yoshino, K.; Pandey, S. S.; Ma, T.; Hayase, S. CH3NH3SnxPb(1−x)I3 Perovskite Solar Cells Covering up to 1060 nm. *The journal of physical chemistry letters* **2014,** *5* (6), 1004-1011.

29. Chen, L.-J.; Lee, C.-R.; Chuang, Y.-J.; Wu, Z.-H.; Chen, C. Synthesis and Optical Properties of Lead-Free Cesium Tin Halide Perovskite Quantum Rods with High-Performance Solar Cell Application. *The journal of physical chemistry letters* **2016,** *7* (24), 5028-5035.

30. Noh, J. H.; Im, S. H.; Heo, J. H.; Mandal, T. N.; Seok, S. I. Chemical Management for Colorful, Efficient, and Stable Inorganic–Organic Hybrid Nanostructured Solar Cells. *Nano letters* **2013,** *13* (4), 1764-1769.

31. Tao, S. X.; Cao, X.; Bobbert, P. A. Accurate and efficient band gap predictions of metal halide perovskites using the DFT-1/2 method: GW accuracy with DFT expense. *Scientific reports* **2017,** *7* (1), 14386.

32. Mosconi, E.; Umari, P.; De Angelis, F. Electronic and optical properties of MAPbX3 perovskites (X = I, Br, Cl): a unified DFT and GW theoretical analysis. *Physical Chemistry Chemical Physics* **2016,** *18* (39), 27158-27164.

33. Noh, J. H.; Im, S. H.; Heo, J. H.; Mandal, T. N.; Seok, S. I. Chemical Management for Colorful, Efficient, and Stable Inorganic–Organic Hybrid Nanostructured Solar Cells. *Nano letters* **2013,** *13* (4), 1764-1769.

34. Colella, S.; Mosconi, E.; Fedeli, P.; Listorti, A.; Gazza, F.; Orlandi, F.; Ferro, P.; Besagni, T.; Rizzo, A.; Calestani, G.; Gigli, G.; De Angelis, F.; Mosca, R. MAPbI3-xClx Mixed Halide Perovskite for Hybrid Solar Cells: The Role of Chloride as Dopant on the Transport and Structural Properties. *Chemistry of Materials* **2013,** *25* (22), 4613-4618.

35. Yu, H.; Wang, F.; Xie, F.; Li, W.; Chen, J.; Zhao, N. The Role of Chlorine in the Formation Process of "CH3NH3PbI3-xClx" Perovskite. *Advanced functional materials* **2014,** *24* (45), 7102-7108.

36. Tidhar, Y.; Edri, E.; Weissman, H.; Zohar, D.; Hodes, G.; Cahen, D.; Rybtchinski, B.; Kirmayer, S. Crystallization of Methyl Ammonium Lead Halide Perovskites: Implications for Photovoltaic Applications. *Journal of the American Chemical Society* **2014,** *136* (38), 13249-13256.

37. de Quilettes, D. W.; Vorpahl, S. M.; Stranks, S. D.; Nagaoka, H.; Eperon, G. E.; Ziffer, M. E.; Snaith, H. J.; Ginger, D. S. Impact of microstructure on local carrier lifetime in perovskite solar cells. *Science* **2015,** *348* (6235), 683-686.

38. Stranks, S. D.; Eperon, G. E.; Grancini, G.; Menelaou, C.; Alcocer, M. J. P.; Leijtens, T.; Herz, L. M.; Petrozza, A.; Snaith, H. J. Electron-Hole Diffusion Lengths Exceeding 1 Micrometer in an Organometal Trihalide Perovskite Absorber. *Science* **2013,** *342* (6156), 341-344.

39. Protesescu, L.; Yakunin, S.; Bodnarchuk, M. I.; Krieg, F.; Caputo, R.; Hendon, C. H.; Yang, R. X.; Walsh, A.; Kovalenko, M. V. Nanocrystals of Cesium Lead Halide Perovskites (CsPbX3, X = Cl, Br, and I): Novel Optoelectronic Materials

Showing Bright Emission with Wide Color Gamut. *Nano letters* **2015,** *15* (6), 3692-3696.

40. Hoke, E. T.; Slotcavage, D. J.; Dohner, E. R.; Bowring, A. R.; Karunadasa, H. I.; McGehee, M. D. Reversible photo-induced trap formation in mixed-halide hybrid perovskites for photovoltaics. *Chemical science* **2015,** *6* (1), 613-617.

41. Gualdrón-Reyes, A. F.; Yoon, S. J.; Barea, E. M.; Agouram, S.; Muñoz-Sanjosé, V.; Meléndez, Á. M.; Niño-Gómez, M. E.; Mora-Seró, I. Controlling the Phase Segregation in Mixed Halide Perovskites through Nanocrystal Size. *ACS energy letters* **2019,** *4* (1), 54-62.

42. Gualdrón-Reyes, A. F.; Yoon, S. J.; Mora-Seró, I. Recent insights for achieving mixed halide perovskites without halide segregation. *Current Opinion in Electrochemistry* **2018,** *11*, 84-90.

43. Foster, S.; John, S. Light-trapping design for thin-film silicon-perovskite tandem solar cells. *Journal of Applied Physics* **2016,** *120* (10), 103103.

44. Filipič, M.; Löper, P.; Niesen, B.; De Wolf, S.; Krč, J.; Ballif, C.; Topič, M. CH3NH3PbI3 perovskite / silicon tandem solar cells: characterization based optical simulations. *Optics express* **2015,** *23* (7), A263-A278.

45. Zi, W.; Ren, X.; Ren, X.; Wei, Q.; Gao, F.; Liu, S. F. Perovskite/germanium tandem: A potential high efficiency thin film solar cell design. *Optics Communications* **2016,** *380*, 1-5.

46. Debellis, D.; Gigli, G.; Ten Brinck, S.; Infante, I.; Giansante, C. Quantum-confined and enhanced optical absorption of colloidal PbS quantum dots at wavelengths with expected bulk behavior. *Nano letters* **2017,** *17* (2), 1248-1254.

47. Smith, A. M.; Nie, S. Semiconductor nanocrystals: structure, properties, and band gap engineering. *Accounts of chemical research* **2009,** *43* (2), 190-200.

48. Heo, J. H.; Jang, M. H.; Lee, M. H.; Shin, D. H.; Kim, D. H.; Moon, S. H.; Kim, S. W.; Park, B. J.; Im, S. H. High-Performance Solid-State PbS Quantum Dot-Sensitized Solar Cells Prepared by Introduction of Hybrid Perovskite Interlayer. *ACS applied materials & interfaces* **2017,** *9* (47), 41104-41110.

49. Choudhury, N.; Kalita, P. K.; Sarma, B. K. Preparation and optical characterization of PbS quantum dots. *AIP Conference Proceedings* **2009,** *1147* (1), 160-165.

50. Sanchez, R. S.; Binetti, E.; Torre, J. A.; Garcia-Belmonte, G.; Striccoli, M.; Mora-Sero, I. All solution processed low turn-on voltage near infrared LEDs based on core-shell PbS-CdS quantum dots with inverted device structure. *Nanoscale* **2014,** *6* (15), 8551-8555.

51. Kroupa, D. M.; Vörös, M.; Brawand, N. P.; McNichols, B. W.; Miller, E. M.; Gu, J.; Nozik, A. J.; Sellinger, A.; Galli, G.; Beard, M. C. Tuning colloidal quantum dot band edge positions through solution-phase surface chemistry modification. *Nature communications* **2017,** *8*, 15257.

52. Pan, Y.; Li, Y. R.; Zhao, Y.; Akins, D. L. Synthesis and Characterization of Quantum Dots: A Case Study Using PbS. *Journal of Chemical Education* **2015,** *92* (11), 1860-1865.

53. Lee, M. M.; Teuscher, J.; Miyasaka, T.; Murakami, T. N.; Snaith, H. J. Efficient Hybrid Solar Cells Based on Meso-Superstructured Organometal Halide Perovskites. *Science* **2012,** *338* (6107), 643-647.

54. Burschka, J.; Pellet, N.; Moon, S.-J.; Humphry-Baker, R.; Gao, P.; Nazeeruddin, M. K.; Gratzel, M. Sequential deposition as a route to high-performance perovskite-sensitized solar cells. *Nature* **2013,** *499* (7458), 316-319.

55. Saliba, M.; Correa-Baena, J.-P.; Wolff, C. M.; Stolterfoht, M.; Phung, N.; Albrecht, S.; Neher, D.; Abate, A. How to make over 20% efficient perovskite solar cells in regular (n–i–p) and inverted (p–i–n) architectures. *Chemistry of Materials* **2018,** *30* (13), 4193-4201.

56. Leijtens, T.; Lim, J.; Teuscher, J.; Park, T.; Snaith, H. J. Charge Density Dependent Mobility of Organic Hole-Transporters and Mesoporous TiO2 Determined by Transient Mobility Spectroscopy: Implications to Dye-Sensitized and Organic Solar Cells. *Advanced materials* **2013,** *25* (23), 3227-3233.

57. Cappel, U. B.; Daeneke, T.; Bach, U. Oxygen-Induced Doping of Spiro-MeOTAD in Solid-State Dye-Sensitized Solar Cells and Its Impact on Device Performance. *Nano letters* **2012,** *12* (9), 4925-4931.

58. Abate, A.; Leijtens, T.; Pathak, S.; Teuscher, J.; Avolio, R.; Errico, M. E.; Kirkpatrik, J.; Ball, J. M.; Docampo, P.; McPherson, I.; Snaith, H. J. Lithium salts as "redox active" p-type dopants for organic semiconductors and their impact in solid-state dye-sensitized solar cells. *Physical Chemistry Chemical Physics* **2013,** *15* (7), 2572-2579.

59. Ono, L. K.; Schulz, P.; Endres, J. J.; Nikiforov, G. O.; Kato, Y.; Kahn, A.; Qi, Y. Air-Exposure-Induced Gas-Molecule Incorporation into Spiro-MeOTAD Films. *The journal of physical chemistry letters* **2014,** *5* (8), 1374-1379.

60. Nguyen, W. H.; Bailie, C. D.; Unger, E. L.; McGehee, M. D. Enhancing the Hole-Conductivity of Spiro-OMeTAD without Oxygen or Lithium Salts by Using Spiro(TFSI)2 in Perovskite and Dye-Sensitized Solar Cells. *Journal of the American Chemical Society* **2014,** *136* (31), 10996-11001.

61. Jeon, N. J.; Lee, H. G.; Kim, Y. C.; Seo, J.; Noh, J. H.; Lee, J.; Seok, S. I. o-Methoxy Substituents in Spiro-OMeTAD for Efficient Inorganic–Organic Hybrid Perovskite Solar Cells. *Journal of the American Chemical Society* **2014,** *136* (22), 7837-7840.

62. Ulfa, M.; Zhu, T.; Goubard, F.; Pauporté, T. Molecular versus polymeric hole transporting materials for perovskite solar cell application. *Journal of Materials Chemistry A* **2018,** *6* (27), 13350-13358.

63. Ko, Y.; Kim, Y.; Lee, C.; Kim, Y.; Jun, Y. Investigation of Hole-Transporting Poly(triarylamine) on Aggregation and Charge Transport for Hysteresisless Scalable Planar Perovskite Solar Cells. *ACS applied materials & interfaces* **2018,** *10* (14), 11633-11641.

64. Zhao, D.; Zhu, Z.; Kuo, M.-Y.; Chueh, C.-C.; Jen, A. K.-Y. Hexaazatrinaphthylene Derivatives: Efficient Electron-Transporting Materials with Tunable Energy Levels for Inverted Perovskite Solar Cells. *Angewandte Chemie International Edition* **2016,** *55* (31), 8999-9003.

65. Zhu, Z.; Zhao, D.; Chueh, C.-C.; Shi, X.; Li, Z.; Jen, A. K. Y. Highly Efficient and Stable Perovskite Solar Cells Enabled by All-Crosslinked Charge-Transporting Layers. *Joule* **2018,** *2* (1), 168-183.

66. Yang, G.; Wang, C.; Lei, H.; Zheng, X.; Qin, P.; Xiong, L.; Zhao, X.; Yan, Y.; Fang, G. Interface engineering in planar perovskite solar cells: energy level alignment, perovskite morphology control and high performance achievement. *Journal of Materials Chemistry A* **2017,** *5* (4), 1658-1666.

67. Zuo, L.; Gu, Z.; Ye, T.; Fu, W.; Wu, G.; Li, H.; Chen, H. Enhanced Photovoltaic Performance of CH3NH3PbI3 Perovskite Solar Cells through Interfacial Engineering Using Self-Assembling Monolayer. *Journal of the American Chemical Society* **2015,** *137* (7), 2674-2679.

68. Docampo, P.; Ball, J. M.; Darwich, M.; Eperon, G. E.; Snaith, H. J. Efficient organometal trihalide perovskite planar-heterojunction solar cells on flexible polymer substrates. *Nature communications* **2013,** *4*, 2761.

69. Wang, Q.; Shao, Y.; Dong, Q.; Xiao, Z.; Yuan, Y.; Huang, J. Large fill-factor bilayer iodine perovskite solar cells fabricated by a low-temperature solution-process. *Energy & Environmental Science* **2014,** *7* (7), 2359-2365.

70. Malinkiewicz, O.; Yella, A.; Lee, Y. H.; Espallargas, G. M.; Graetzel, M.; Nazeeruddin, M. K.; Bolink, H. J. Perovskite solar cells employing organic charge-transport layers. *Nature Photonics* **2013,** *8*, 128.

71. Abrusci, A.; Stranks, S. D.; Docampo, P.; Yip, H.-L.; Jen, A. K. Y.; Snaith, H. J. High-Performance Perovskite-Polymer Hybrid Solar Cells via Electronic Coupling with Fullerene Monolayers. *Nano letters* **2013,** *13* (7), 3124-3128.

72. Wojciechowski, K.; Stranks, S. D.; Abate, A.; Sadoughi, G.; Sadhanala, A.; Kopidakis, N.; Rumbles, G.; Li, C.-Z.; Friend, R. H.; Jen, A. K. Y.; Snaith, H. J. Heterojunction Modification for Highly Efficient Organic–Inorganic Perovskite Solar Cells. *ACS nano* **2014,** *8* (12), 12701-12709.

73. Valles-Pelarda, M.; Hames, B. C.; García-Benito, I.; Almora, O.; Molina-Ontoria, A.; Sánchez, R. S.; Garcia-Belmonte, G.; Martín, N.; Mora-Sero, I. Analysis of the Hysteresis Behavior of Perovskite Solar Cells with Interfacial Fullerene Self-Assembled Monolayers. *The journal of physical chemistry letters* **2016,** *7* (22), 4622-4628.

74. Xu, Y.; Wang, Y.; Yu, J.; Feng, B.; Zhou, H.; Zhang, J.; Duan, J.; Fan, X.; Aken, P. A. v.; Lund, P. D.; Wang, H. Performance Improvement of Perovskite Solar Cells Based on PCBM-Modified ZnO-Nanorod Arrays. *IEEE Journal of Photovoltaics* **2016,** *6* (6), 1530-1536.

75. Zhu, L. F.; Xu, Y. Z.; Shi, J. J.; Zhang, H. Y.; Xu, X.; Zhao, Y. H.; Luo, Y. H.; Meng, Q. B.; Li, D. M. Efficient perovskite solar cells via simple interfacial modification toward a mesoporous TiO2 electron transportation layer. *RSC advances* **2016,** *6* (85), 82282-82288.

76. Rong, Y.; Hu, Y.; Ravishankar, S.; Liu, H.; Hou, X.; Sheng, Y.; Mei, A.; Wang, Q.; Li, D.; Xu, M.; Bisquert, J.; Han, H. Tunable hysteresis effect for perovskite solar cells. *Energy & Environmental Science* **2017,** *10* (11), 2383-2391.

77. Yang, D.; Yang, R.; Wang, K.; Wu, C.; Zhu, X.; Feng, J.; Ren, X.; Fang, G.; Priya, S.; Liu, S. High efficiency planar-type perovskite solar cells with negligible hysteresis using EDTA-complexed SnO2. *Nature communications* **2018,** *9* (1), 3239.

78. Abate, A.; Saliba, M.; Hollman, D. J.; Stranks, S. D.; Wojciechowski, K.; Avolio, R.; Grancini, G.; Petrozza, A.; Snaith, H. J. Supramolecular Halogen

Bond Passivation of Organic–Inorganic Halide Perovskite Solar Cells. *Nano letters* **2014,** *14* (6), 3247-3254.

79. Lin, Y.; Shen, L.; Dai, J.; Deng, Y.; Wu, Y.; Bai, Y.; Zheng, X.; Wang, J.; Fang, Y.; Wei, H.; Ma, W.; Zeng, X. C.; Zhan, X.; Huang, J. π-Conjugated Lewis Base: Efficient Trap-Passivation and Charge-Extraction for Hybrid Perovskite Solar Cells. *Advanced materials* **2017,** *29* (7), 1604545.

80. Noel, N. K.; Abate, A.; Stranks, S. D.; Parrott, E. S.; Burlakov, V. M.; Goriely, A.; Snaith, H. J. Enhanced Photoluminescence and Solar Cell Performance via Lewis Base Passivation of Organic–Inorganic Lead Halide Perovskites. *ACS nano* **2014,** *8* (10), 9815-9821.

81. Yun, J. S.; Seidel, J.; Kim, J.; Soufiani, A. M.; Huang, S.; Lau, J.; Jeon, N. J.; Seok, S. I.; Green, M. A.; Ho-Baillie, A. Critical Role of Grain Boundaries for Ion Migration in Formamidinium and Methylammonium Lead Halide Perovskite Solar Cells. *Advanced Energy Materials* **2016,** *6* (13), 1600330.

82. Xu, J.; Buin, A.; Ip, A. H.; Li, W.; Voznyy, O.; Comin, R.; Yuan, M.; Jeon, S.; Ning, Z.; McDowell, J. J.; Kanjanaboos, P.; Sun, J.-P.; Lan, X.; Quan, L. N.; Kim, D. H.; Hill, I. G.; Maksymovych, P.; Sargent, E. H. Perovskite–fullerene hybrid materials suppress hysteresis in planar diodes. *Nature communications* **2015,** *6*, 7081.

83. Chaudhary, B.; Kulkarni, A.; Jena, A. K.; Ikegami, M.; Udagawa, Y.; Kunugita, H.; Ema, K.; Miyasaka, T. Poly(4-Vinylpyridine)-Based Interfacial Passivation to Enhance Voltage and Moisture Stability of Lead Halide Perovskite Solar Cells. *ChemSusChem* **2017,** *10* (11), 2473-2479.

84. Li, X.; Ibrahim Dar, M.; Yi, C.; Luo, J.; Tschumi, M.; Zakeeruddin, S. M.; Nazeeruddin, M. K.; Han, H.; Grätzel, M. Improved performance and stability of perovskite solar cells by crystal crosslinking with alkylphosphonic acid ω-ammonium chlorides. *Nature chemistry* **2015,** *7*, 703.

85. Zuo, L.; Guo, H.; deQuilettes, D. W.; Jariwala, S.; De Marco, N.; Dong, S.; DeBlock, R.; Ginger, D. S.; Dunn, B.; Wang, M.; Yang, Y. Polymer-modified halide perovskite films for efficient and stable planar heterojunction solar cells. *Science advances* **2017,** *3* (8), e1700106.

86. Xi, L.; Boothroyd, C. B.; Salim, T.; Borghardt, S.; Lam, Y. M.; Kardynał, B. E. Facile in situ synthesis of stable luminescent organic–inorganic lead halide perovskite nanoparticles in a polymer matrix. *Journal of Materials Chemistry C* **2017,** *5* (29), 7207-7214.

87. Yan, W.; Li, Y.; Li, Y.; Ye, S.; Liu, Z.; Wang, S.; Bian, Z.; Huang, C. Stable high-performance hybrid perovskite solar cells with ultrathin polythiophene as hole-transporting layer. *Nano Research* **2015,** *8* (8), 2474-2480.

88. Zheng, L.; Chung, Y.-H.; Ma, Y.; Zhang, L.; Xiao, L.; Chen, Z.; Wang, S.; Qu, B.; Gong, Q. A hydrophobic hole transporting oligothiophene for planar perovskite solar cells with improved stability. *Chemical communications* **2014,** *50* (76), 11196-11199.

89. Bai, Y.; Dong, Q.; Shao, Y.; Deng, Y.; Wang, Q.; Shen, L.; Wang, D.; Wei, W.; Huang, J. Enhancing stability and efficiency of perovskite solar cells with crosslinkable silane-functionalized and doped fullerene. *Nature communications* **2016,** *7*, 12806.

90. Zhang, J.; Hu, Z.; Huang, L.; Yue, G.; Liu, J.; Lu, X.; Hu, Z.; Shang, M.; Han, L.; Zhu, Y. Bifunctional alkyl chain barriers for efficient perovskite solar cells. *Chemical communications* **2015,** *51* (32), 7047-7050.

91. Yang, S.; Wang, Y.; Liu, P.; Cheng, Y.-B.; Zhao, H. J.; Yang, H. G. Functionalization of perovskite thin films with moisture-tolerant molecules. *Nature Energy* **2016,** *1*, 15016.

92. Climent-Pascual, E.; Hames, B. C.; Moreno-Ramírez, J. S.; Álvarez, A. L.; Juarez-Perez, E. J.; Mas-Marza, E.; Mora-Seró, I.; de Andrés, A.; Coya, C. Influence of the substrate on the bulk properties of hybrid lead halide perovskite films. *Journal of Materials Chemistry A* **2016,** *4* (46), 18153-18163.

93. Yang, J.; Siempelkamp, B. D.; Mosconi, E.; De Angelis, F.; Kelly, T. L. Origin of the Thermal Instability in CH3NH3PbI3 Thin Films Deposited on ZnO. *Chemistry of Materials* **2015,** *27* (12), 4229-4236.

94. Dong, X.; Hu, H.; Lin, B.; Ding, J.; Yuan, N. The effect of ALD-Zno layers on the formation of CH3NH3PbI3 with different perovskite precursors and sintering temperatures. *Chemical communications* **2014,** *50* (92), 14405-14408.

95. Olthof, S.; Meerholz, K. Substrate-dependent electronic structure and film formation of MAPbI3 perovskites. *Scientific reports* **2017,** *7*, 40267.

96. Bi, C.; Wang, Q.; Shao, Y.; Yuan, Y.; Xiao, Z.; Huang, J. Non-wetting surface-driven high-aspect-ratio crystalline grain growth for efficient hybrid perovskite solar cells. *Nature communications* **2015,** *6*, 7747.

97. Grancini, G.; Marras, S.; Prato, M.; Giannini, C.; Quarti, C.; De Angelis, F.; De Bastiani, M.; Eperon, G. E.; Snaith, H. J.; Manna, L.; Petrozza, A. The Impact of the Crystallization Processes on the Structural and Optical Properties of Hybrid Perovskite Films for Photovoltaics. *The journal of physical chemistry letters* **2014,** *5* (21), 3836-3842.

98. Quarti, C.; Grancini, G.; Mosconi, E.; Bruno, P.; Ball, J. M.; Lee, M. M.; Snaith, H. J.; Petrozza, A.; De Angelis, F. The Raman Spectrum of the CH3NH3PbI3 Hybrid Perovskite: Interplay of Theory and Experiment. *The journal of physical chemistry letters* **2014,** *5* (2), 279-284.

99. Pascoe, A. R.; Yang, M.; Kopidakis, N.; Zhu, K.; Reese, M. O.; Rumbles, G.; Fekete, M.; Duffy, N. W.; Cheng, Y.-B. Planar versus mesoscopic perovskite microstructures: The influence of CH3NH3PbI3 morphology on charge transport and recombination dynamics. *Nano Energy* **2016,** *22*, 439-452.

100. Bastiani, M. D.; D'Innocenzo, V.; Stranks, S. D.; Snaith, H. J.; Petrozza, A. Role of the crystallization substrate on the photoluminescence properties of organo-lead mixed halides perovskites. *APL Materials* **2014,** *2* (8), 081509.

101. Grancini, G.; Marras, S.; Prato, M.; Giannini, C.; Quarti, C.; De Angelis, F.; De Bastiani, M.; Eperon, G. E.; Snaith, H. J.; Manna, L.; Petrozza, A. The Impact of the Crystallization Processes on the Structural and Optical Properties of Hybrid Perovskite Films for Photovoltaics. *The journal of physical chemistry letters* **2014,** *5* (21), 3836-3842.

102. Yang, D.; Yang, R.; Zhang, J.; Yang, Z.; Liu, S.; Li, C. High efficiency flexible perovskite solar cells using superior low temperature TiO2. *Energy & Environmental Science* **2015,** *8* (11), 3208-3214.

103. Bi, D.; Tress, W.; Dar, M. I.; Gao, P.; Luo, J.; Renevier, C.; Schenk, K.; Abate, A.; Giordano, F.; Correa Baena, J.-P.; Decoppet, J.-D.; Zakeeruddin, S. M.; Nazeeruddin, M. K.; Grätzel, M.; Hagfeldt, A. Efficient luminescent solar cells based on tailored mixed-cation perovskites. *Science advances* **2016,** *2* (1), e1501170.

104. Ke, W.; Zhao, D.; Cimaroli, A. J.; Grice, C. R.; Qin, P.; Liu, Q.; Xiong, L.; Yan, Y.; Fang, G. Effects of annealing temperature of tin oxide electron selective layers on the performance of perovskite solar cells. *Journal of Materials Chemistry A* **2015,** *3* (47), 24163-24168.

105. Correa-Baena, J.-P.; Tress, W.; Domanski, K.; Anaraki, E. H.; Turren-Cruz, S.-H.; Roose, B.; Boix, P. P.; Grätzel, M.; Saliba, M.; Abate, A.; Hagfeldt, A. Identifying and suppressing interfacial recombination to achieve high open-circuit voltage in perovskite solar cells. *Energy & Environmental Science* **2017,** *10* (5), 1207-1212.

106. Zhang, H.; Zhao, C.; Li, D.; Guo, H.; Liao, F.; Cao, W.; Niu, X.; Zhao, Y. Effects of substrate temperature on the crystallization process and properties of mixed-ion perovskite layers. *Journal of Materials Chemistry A* **2019,** *7* (6), 2804-2811.

107. Wang, Y.; Liu, S.; Zeng, Q.; Wang, R.; Qin, W.; Cao, H.; Yang, L.; Li, L.; Ji, W.; Yin, S. Controllable Crystal Film Growth via Appropriate Substrate-Preheating Treatment for Perovskite Solar Cells Using Mixed Lead Sources. *IEEE Journal of Photovoltaics* **2018,** *8* (1), 162-170.

108. Kim, H.; Hong, J.; Kim, C.; Shin, E.-Y.; Lee, M.; Noh, Y.-Y.; Park, B.; Hwang, I. Impact of Hydroxyl Groups Boosting Heterogeneous Nucleation on Perovskite Grains and Photovoltaic Performances. *The Journal of Physical Chemistry C* **2018,** *122* (29), 16630-16638.

109. Cao, J.; Yin, J.; Yuan, S.; Zhao, Y.; Li, J.; Zheng, N. Thiols as interfacial modifiers to enhance the performance and stability of perovskite solar cells. *Nanoscale* **2015,** *7* (21), 9443-9447.

110. Shih, Y. C.; Wang, L. Y.; Hsieh, H. C.; Lin, K. F. Enhancing the photocurrent of perovskite solar cells via modification of the TiO2/CH3NH3PbI3 heterojunction interface with amino acid. *Journal of Materials Chemistry A* **2015,** *3* (17), 9133-9136.

111. Qin, P.; Domanski, A. L.; Chandiran, A. K.; Berger, R.; Butt, H.-J.; Dar, M. I.; Moehl, T.; Tetreault, N.; Gao, P.; Ahmad, S.; Nazeeruddin, M. K.; Grätzel, M. Yttrium-substituted nanocrystalline TiO2 photoanodes for perovskite based heterojunction solar cells. *Nanoscale* **2014,** *6* (3), 1508-1514.

Chapter II. Characterization methods

In this chapter we briefly describe the fundamentals of the characterization methods which have been most extensively used in the analysis of our samples including films and devices. For film characterization, we have used systematically x-ray diffraction, scanning electron microscopy, absorbance and photoluminescence to characterize the structural, morphological and optical properties respectively. Complete devices have been evaluated by photocurrent-voltage curves, incident photon to current efficiency, impedance spectroscopy and electroluminescence.

II.1. X-ray diffraction

X-ray diffraction (XRD) is a very useful tool to determine the composition and the structure of materials. The diffraction effect is observed when the electromagnetic wave of radiation striking on periodic structures with geometrical variations on the magnitude of the radiation wavelength. When the electromagnetic wave of incoming radiation impinges on the atoms of a crystalline structure, all electrons of atoms vibrate, emiting a radiation with the same wavelength of incoming radiation and the radiation is emitted in all direction (Fig II.1).[1-2] At the incident angles that satisfy the Bragg's condition, which is described below, the constructive interference occurs and the emitted radiation intensity is rapidly enhanced.

$$\text{Bragg's law:} \qquad n\lambda = dsin\theta \qquad \text{(eq II.1)}$$

where d is the spacing between planes in the atomic lattice, λ and θ are the wavelength and incident angle of incoming radiation, n is the integral number determined by the order given.

(a)

(b)
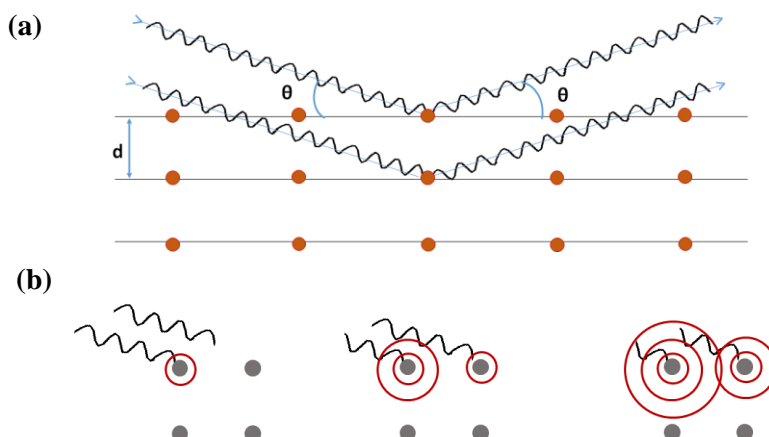
Fig II.1. (a) Geometry of x-ray radiation scattered on atoms of periodic crystalline structure following Bragg's law. (b) Constructive interference occurs of scattered waves from adjacent atoms.

The concept of Bragg diffraction is applied in crystallography to measure the diffraction of powder, single crystal or polycrystalline materials. A diffraction pattern is obtained by measuring the intensity of scattered radiation as a function of scattering angles. For a single crystal only one family of peaks corresponding with the orientation of the crystal is observed in the XRD spectrum, for example the detection of diffraction peaks corresponding only to (100), (200), (300)… planes. In polycrystalline films of many individual grains or crystallites, each one can be considered as a single crystal with its corresponding orientation, within which the atomic structure has a long range order. Therefore diffraction peaks from different family crystalline plains are observed in the XRD spectrum. In contrast, amorphous materials have no long-range order, there is no diffraction peak.

XRD spectra can be used to determine the crystal atomic structure, to analyse the strain and to calculate the crystallite sizes. The peak positions are determined by the size and shape of unit cell.[2] The strain will modify the diffraction peaks. The uniform strain causes the shift in the peak position while non-uniform strain broadens the diffraction peak.[3] The amplitude of scattered waves is proportional to the number of electrons in the atom and the atomic number, hence light elements as carbon or oxygen are therefore poor scatter for x-ray and heavy elements as lead are good scatter.[1] The detection limits of XRD is severely influenced by this effect caused by the nature of materials.

The crystallite size, D, can be also estimated by using Scherrer's equation:[3]

$$D = \frac{K\lambda}{dcos\theta} \qquad (eq\ II.2)$$

where K, d, λ, θ are crystallite shape factor, full width at half maximum (FWHM), wavelength and angle of incident radiation respectively. In order to have an accurate estimated crystallite size, the distribution of crystallites in materials needs to be sufficiently uniform, providing reliable diffraction peak profile. However if the diameter of crystallite becomes small, the measured diffraction profiles broaden out.[3]

II.2. Scanning electron microscopy

Scanning electron microscopy (SEM) is a powerful magnification tool to obtain the information of surface topography, film thickness and material composition which is obtained from the interaction between electron beam and sample.

When the electron beam from the electron gun strikes on sample surface, the energetic electrons penetrate into the sample for some distance until they encounter and collide with the atoms of the sample. Thereby the incident electrons produce an excitation region from which many signal is generated. Fig II.2 presents several signals produced by the incident electron-sample interaction and from which region the corresponding signals can be obtained. The size and shape of this region is strongly dependent on the electron beam energy and on the atomic number of the atoms of the sample. For the same electron beam energy, the shape of the interaction volume is water drop for low atomic number samples and becomes hemisphere for sample with high atomic number. The depth and volume of the interaction region is proportional with the energy of the incident electron beam and inversely proportional with the atomic number of the atoms of the sample.[4]

Secondary electron. Incident electrons impinge on a specimen and can inelastically interact with electrons of specimen atom, transferring their energy to atoms. The amount of energy loss depends on a number of electrons which are excited and the binding energy between electron and atom. As a result, the excitation of electrons during the ionization of atoms may lead to emit electrons which are referred as secondary electrons. As the secondary electrons have a low energy (3-5 eV), they can only escape from a region within a few nm of the sample surface. Therefore secondary electrons

accurately mark the position of the electron beam and give the topographic information.[4-5] Secondary electrons are used for the topographic contrast in SEM, visualizing the surface texture and roughness. The topographic image is strongly dependent on how many secondary electrons reaching the detector. The number of detected secondary electrons is significantly influenced by the angle of incident electrons, a position of detector and surface of specimen. The region where a sample surface is tilted towards to the detector possess much higher signal than those tilted away, giving a shadow.[5] And the emission of secondary electrons is greatly enhanced on the tip of surface peak.[4]
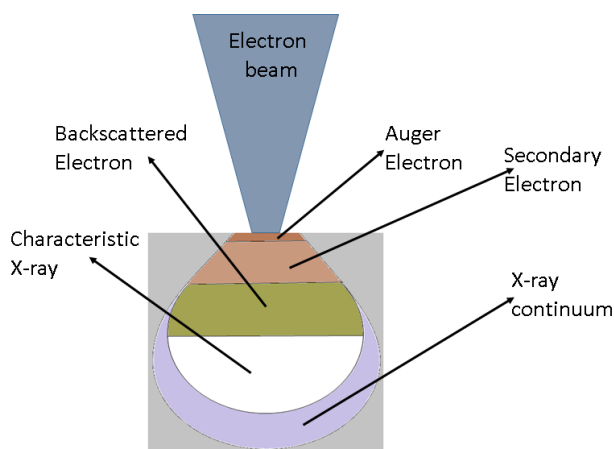
Fig II.2. Interaction of electron beam with sample in the Scanning electron microscopy measurement. Possible obtained information from the interaction is indicated. Reproduced with the permission of Springer Nature from ref.[4]

Backscattered electron. The elastic collision between electron beam and atomic nucleus of samples causes a bounce back of electrons with wide-angle directional change, these electrons are referred as backscattered electrons. The electron beam may undergoes some scattering events before elastically collides with atomic nucleus resulting a loss of energy in a comparison with initial energy of incident electron beam. Roughly 10-50% electrons are backscattered back to their source and 60-80% initial energy is remained, backscattered electrons have an energy higher than 50 eV. Because of possessing large energy, which prevents of being absorbed by specimen, the region where the backscattered electrons are generated is larger than that of secondary electrons. Therefore the resolution of backscattered electron image is worse than that of secondary electron image. However the backscattered electrons carry information of sample feature deeply beneath the surface.[4] The backscattered electron signal is also proportional with atomic

number of specimen, consequently can differentiate region with atoms with high atomic number from regions with atoms with low atomic number.

Emission of photons (characteristic x-rays and x-ray continuum). When the incident electron beam impinges on a specimen, it may excite an electron from inner-shell of an atom to unoccupied state. Consequent, an outer shell electron falls into the inner-shell to re-establish the proper charge balance, following the ionization of an atom. By emitting a characteristic x-ray, an ionized atom turns back to its ground state.[4-5] The characteristic x-rays are rich of chemical information. And in SEM, they can be analysed by using energy or wavelength dispersive x-ray spectrometers (EDS or WDS), depending on their energies (usually EDS is used for low characteristic x-ray energies), to get information of sample's chemical composition. In addition, the interaction of electron beam and sample also generates x-ray radiation with continuous energy distribution that its maximum energy is equivalent to an energy of incident electrons. The continuous energy is resulted by the deceleration of incident electrons when it passes through the coulomb field of atoms, losing energy and its released energy can be any value and emitted as electromagnetic radiation.[5] This continuous x-ray emission constitutes to the background noise and needs to be removed to have proper analysis of chemical composition.

Auger electrons. The incident electrons excite an inner shell electron to unoccupied state. The vacancy of an inner shell state may be substituted by an electron from an outer shell electron with higher energy. The released energy may transfer to another electron possessing of low binding energy. If the transferred energy is large enough, the electron can be excited, escaped from specimen surface. The electron is referred as Auger electron.[5] Typically the Auger electrons have low energies and can be emitted near the sample surface. The Auger electron signal can be useful to analyse the chemical composition.[4]

II.3. Absorbance and photoluminescence

Absorbance is the logarithm of the ratio of incident to transmitted light through a material. Hence the absorbance measurement is a useful characterization defining which wavelength region can be absorbed by a material. Its bandgap can be determined by analysing the absorbance data. The absorbance is also a prerequisite measurement showing the condition for the photoluminescence characterization, which is the excitation energy. In order

to obtain the photoluminescence spectrum, a material needs to be excited by photons whose energies are higher or equal to its bandgap.
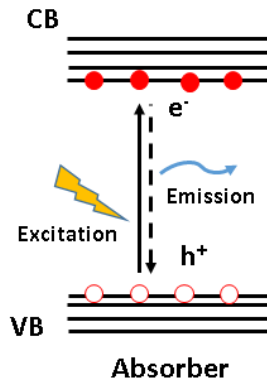

Fig II.3. Schematic diagram of the absorption and emission under illumination of a semiconductor absorber.

Photoluminescence. Under illumination the absorption of photons can generate electron-hole pairs in semiconductors. The generation of charge carriers (electrons and holes) is described more detail in the section below. Generated electrons and holes can recombine either radiatively or non-radiatively. If the energy released through recombination is in the form of a photon, the process is known as radiative recombination (Fig II.3), and the photoluminescence (PL) spectrum can be recorded by counting number of emitted photons as a function of wavelength. The most common cases, electrons move fully from the CB to the VB, hence the emitted photon energy is approximately equal to the optical bandgap energy of the semiconductor.[6] Therefore PL measurement can be also used as the technique to determine the bandgap energy of semiconductors or to detect some defects/modification at lower energies than the bandgap. On the other hand, the comparison of the intensity of PL spectra of different samples, which are measured under the same conditions, can refer to the extent conversion of excitation to emitted photons.

II.4. Current density – voltage characteristic

Photovoltaic (PV) effect. The PV effect is the basis of the conversion of light directly into electricity. The term "photo" means light and "voltaic," electricity. Described simply, the PV effect is as follows: light is composed of photons packets of solar energy. These photons contain different amounts of energy that correspond to the different wavelengths of the solar spectrum. When photons strike a PV cell, also known as 'solar cells' which is a semiconductor device, they may be reflected or absorbed, or transmitted through the device. Only the absorbed photons, which possess higher energy than the bandgap of the semiconductor light absorber, can generate electricity. The energy of an absorbed photon is transferred to an electron in the VB that is promoted to the CB, leaving a hole in the VB (Fig II.4). States in the CB are non-localized states and the electron is now free to travel along the crystal until it recombines with a hole or it is extracted from the semiconductor light absorber. An analogous process occurs for holes in the VB. In order to take advantage of the solar energy and convert it into electricity,[7-8] electrons and holes have to be extracted before they recombine (i.e. they lose their energy). For this reason selective electron and hole extracting contacts are mandatory for an efficient energy conversion. Finally, electron and holes are transported to the external load through the electron and hole transport materials (ETM and HTM) respectively, (Fig II.4).
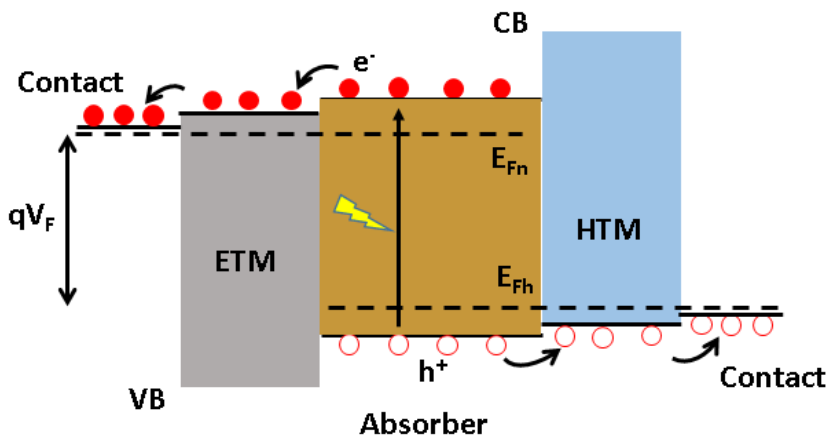
Fig II.4. Schematic of operation mechanism of a solar cells based on the photovoltaic effect.

Current density – voltage curve. Current density-voltage (JV) curve is a very important measurement in the characterization of solar cells, as it

permits easily to evaluate the photoconversion efficiency (PCE) from light into electricity. Under illumination, the absorption of light in semiconductor absorber generates charge carriers (electron-hole pairs). The excess of charge carriers produces a splitting of the Fermi levels of electron (E_{Fn}) and of holes (E_{Fh}), creating a Fermi voltage ($qV_F = E_{Fn} - E_{Fh}$, where q is the elementary charge), Fig II.4. In solar cells, the absorber layer is sandwiched between electron and hole transport materials which are favourable for electron and hole selective extraction, rejecting consequently holes and electrons respectively. Such arrangement allows the Fermi level in the contacts to equilibrate with the separate Fermi levels of electrons and holes, producing an external voltage, to extract carriers giving the photocurrent in the external circuit.[9]
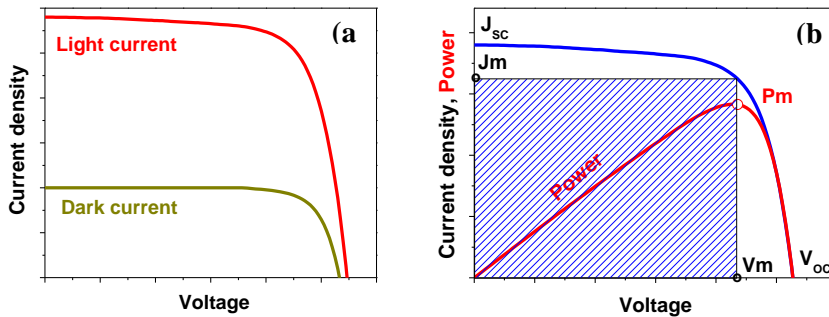
Fig II.5. (a) Typical current-voltage characteristics and (b) and corresponded power of a solar cell. Photovoltaic parameters including short circuit current density (Jsc), open circuit voltage (Voc), maximum power point (Pm) to determine a solar cell's performance are illustrated.

In a JV measurement, a current is measured at a slow scan of bias from a short circuit condition to open circuit condition, or in the opposite direction. The voltage at output, or applied voltage takes also into account the series resistance, R_s:

$$V_{app} = V_F + V_s = V_F + JR_s \qquad (eq\ II.3)$$

The photocurrent J of a solar cell under illumination is calculated following the equation below:[10]

$$J = J_{SC} - J_o\left(e^{\frac{qV_F}{mKT}} - 1\right) \qquad (eq\ II.4)$$

where q, K, T and m are elementary charge, Boltzmann's constant, temperature in Kelvin degrees and the ideality factor respectively. J_{SC} is the

short circuit photocurrent. J_o is the saturated current and it is constant, which differentiates one diode from another. The photocurrent J strongly correlates with the absorption and charge generation in the semiconductor absorber. Smaller bandgap of the semiconductor absorber leads to higher light absorption, consequently higher photocurrent. In the same line, higher incident light intensity results in a higher generated photocurrent as higher number of photons strikes to the cell, and reverse. Fig II.5a shows the typical current density-voltage curves of solar cells in dark and illumination conditions. When the contacts are isolated, the potential difference has its maximum value which is known as open circuit voltage Voc. In this condition the current is zero and taking into account eq. II.4 the Voc is determined as:[10]

$$Voc = \frac{mKT}{q} \ln\left(\frac{J_{SC}}{J_o} + 1\right) \qquad (eq\ II.5)$$

The Voc is dependent on the photogenerated current and on the recombination process, higher photocurrent and lower recombination result in a higher Voc.

In the operating regime, from 0 to Voc, solar cells deliver the power density: $P = JV$. At maximum current density (J_{SC}) and maximum voltage (Voc), the power of solar cells is zero. The cells have to work at the maximum power point, Pm, in order to maximize their photoconversion efficiencies. In this point the current and voltage values are defined as Jm and Vm, respectively. Comparing, J_{SC} and Voc with Jm and Vm another important parameter can be extracted. The fill factor (FF) determines the squareness of solar cells, Fig II.5b, and it is defined as:

$$FF = \frac{J_m V_m}{J_{SC} V_{oc}} \qquad (eq\ II.6)$$

Real devices appear also parasitic resistances including series and shunt (or parallel) resistance, which affect the FF and consequently the performance of solar cells. The series resistance arises from the resistance of the cell material to current flow and from resistive contacts. And the shunt resistance arises from the leakage of current through the cell, around the edges of device and between contacts. For efficient cells, the series resistance needs to be as small as possible and the shunt resistance needs to be as large as possible.[10]

The photoconversion efficiency (PCE) is defined as the ratio of the energy output from the solar cells to input energy from incident solar power density Ps:

$$PCE = \frac{J_m \, V_m}{P_s} = \frac{J_{SC} \, V_{oc} \, FF}{P_s} \qquad (eq \; II.7)$$

As it can be seen, the photoconversion efficiency is the product of all three parameters Jsc, Voc and FF. Consequently, any change in any of these values produces a change in the efficiency. In order to have high efficiency, high values of all three parameters are required. These parameters are depend on the measurement conditions, as light spectrum and intensity or temperature. Therefore the conditions under which the solar cell efficiency is measured need to be carefully controlled in order to compare samples measured in different laboratories. The defined standard test solar cell condition is air mass 1.5 (AM 1.5) spectrum, an incident power density of 100 mW/cm^2 and at temperature of 25°C.

II.5. Incident photon to current efficiency

Incident photon to current efficiency (IPCE) is a measure of the ratio of the photocurrent versus the rate of incident photon as a function of wavelength. The IPCE is defined with the following formula:[9]

$$IPCE(\lambda) = \frac{J_{sc}(\lambda)}{q\phi_{ph}(\lambda) \, \Delta(\lambda)} \qquad (eq.II.8)$$

where q is the elementary charge and $\phi_{ph}(\lambda)$ is the incident photon flux. Considering the IPCE definition, the Jsc under given light source can be determined as:

$$J_{sc} = \int_{\lambda_{min}}^{\lambda_{max}} IPCE(\lambda) q \phi_{ph}^{source}(\lambda) d\lambda \qquad (eq.II.9)$$

where λ_{min} and λ_{max} are the wavelength where the IPCE vanished, ϕ_{ph}^{source} is the photon flux of source used.

The IPCE measurement is also useful to verify the Jsc, comparing with the Jsc value obtaining from the photocurrent-voltage curve, as a wrong calibration can produce an inaccurate Jsc value from JV curve. On the other hand, the IPCE is also a proper method to determine the bandgap of materials because only absorbed photons can generate charge carriers.

II.6. Impedance spectroscopy

Impedance spectroscopy (IS) is a frequency domain technique where the ratio between applied voltage and current is obtained for a fixed DC bias with a small perturbation AC at different frequencies. In the IS measurement of a solar cell, the device is set at a certain steady state of illumination with generation and recombination rates $\bar{G}$ and $\bar{U}$ respectively; applied voltage $\bar{V}$ and the corresponding current $\bar{J}$ given in the eq. II. 4. IS is performed by perturbing the sample through applying an alternating voltage $\hat{V}(t)$:

$$\hat{V}(t) = V_o \sin(\omega t) = V_o e^{i\omega t} \quad (eq.\,II.\,10)$$

Therefore the voltage of a system is: $V(t) = \bar{V} + \hat{V}(t)$ (eq. II.11).[9] The current response of the system is $J(t) = \bar{J} + \hat{j}(t)$ (eq. II.12) in which $\hat{j}(t)$ is an additional current resulted from a perturbation of a steady voltage and is described as:

$$\hat{j}(t) = j_o \sin(\omega t + \varphi) = j_o e^{i(\omega t + \varphi)} \quad (eq.\,II.\,13)$$

where V_o and j_o are the amplitude of the voltage and current signal respectively, ω is the angular frequency related to the frequency f through the formula $\omega = 2\pi f$, and φ is the delay phase between voltage and current. The perturbed impedance of sample can be obtained by applying the Ohm's law:

$$Z = \frac{\hat{V}(t)}{\hat{j}(t)} = \frac{V_o}{j_o} e^{-i\varphi} = Z_o e^{-i\varphi} \quad (eq.\,II.\,14)$$

Impedance spectroscopy is a relatively simple measurement to perform. However to obtain an appropriate information about the relaxation process in samples, choosing appropriate measurement parameters are very important. The applied alternating voltage signal $\hat{V}(t)$: needs to be small in order to not cause a nonlinear change in the current response. In other words, with a small applied $\hat{V}(t)$, the amplitude of current response j_o varies linearly with the amplitude V_o of applied alternating voltage. Nevertheless, the $\hat{V}(t)$ also needs to be high enough to produce a noise-free signal.[11] Thereby the impedance spectrum is independent on the amplitude V_o. The frequency range of measurement is determined by the time scale of the relaxation process in samples that is probed. In general the impedance spectroscopy of photovoltaic devices is measured in the frequency range from megahertz (microsecond) to

sub-hertz (less than a second).[12] Measuring impedance at lower or higher frequencies is possible, but could present a technical challenge in order to obtain reliable data. At lower frequencies, the measurement is time-intensive and affecting significantly the stability of samples. And at higher frequencies, inductive effects from set-up, usually cables, can result to artifices in the impedance spectrum.

Analysing the perturbed impedance allows to reveal the physical processes happening in a solar cell devices, decoupling processes with different characteristic time such as charge recombination, charge transfer or charge accumulation. In order to analyse the impedance spectroscopy data, selecting an equivalent circuit model accounting the process taking place in sample is also very important. Fig II.6 presents a typical Nyquist plot of an impedance spectrum with two arcs and an equivalent circuit model of a solar cell. The impedance Z obtained in the IS measurement is composed by all elements where the resistance of a resistor is defined as $Z_R = R$ and the reactance of a capacitor is calculated as: $Z_C = (i\omega C)^{-1}$. The high frequency arc is defined by the R_1C_1 product, meanwhile the low frequency arc is defined by R_2C_2 product.
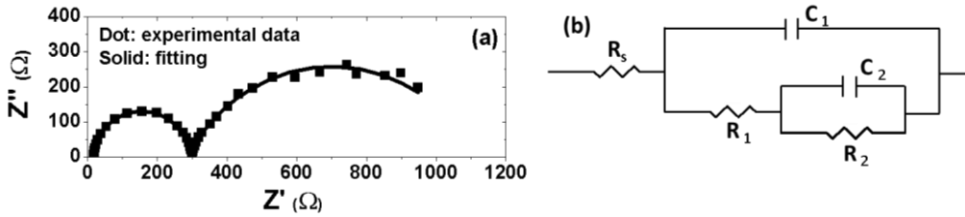
Fig II.6. (a) Nyquist plot of an impedance spectrum and (b) equivalent circuit of a solar cell. The dot and solid lines in Fig II.6a corresponds to the experimental data and the fitting using the circuit presented in the Fig II.6b.

The capacitance relates to the charge carrier accumulation and distribution in the cell, and is obtained from the derivative of the carrier density n:[9]

$$C = V_{eff}q^2\frac{\partial n}{\partial E_F} \qquad (eq.\,II.\,15)$$

where V_{eff} is the effective volume of the absorber film, E_F is the variation of Fermi level produced by applying an alternative voltage $\hat{V}(t)$. The carrier density n is defined as $n(t) = \bar{n} + \hat{n}(t)$ where $\bar{n}$ is the carrier density in the steady state, and is determined as:

$$\bar{n} = n_o e^{\frac{qV_F}{mKT}} \qquad (eq.\,II.16)$$

And $\hat{n}(t)$ is the carrier density associated with $\hat{j}(t)$. The variation of Fermi level is:[9]

$$E_F(t) = \overline{E_F} + q\hat{V}(t) \qquad (eq.\,II.17)$$

The resistance relates to the charge transfer or transport and charge recombination in the system. The recombination resistance which indicates the probability to recombine of an electron with a hole is proportional to the recombination current j_{rec} and the area A of the film:[9]

$$R_{rec} = \frac{1}{A}\left(\frac{\partial j_{rec}}{\partial E_F}\right)^{-1} = \frac{1}{q^2 V_{eff}}\left(\frac{\partial U}{\partial E_F}\right)^{-1} = \frac{1}{C}\left(\frac{\partial U}{\partial n}\right)^{-1} \qquad (eq.\,II.18)$$

where the recombination current is $j_{rec} = qLU$, with U is the recombination rate and L is thickness of absorber layer. The effective volume $V_{eff} = AL$. The carrier lifetime is defined as:

$$\tau = \left(\frac{\partial U}{\partial n}\right)^{-1} \text{ hence } \tau = R_{rec}C \qquad (eq.\,II.19)$$

The transport resistance which indicates how easy to move the charge in the cell is calculated:[9]

$$R_{tr} = \hat{j}\frac{\partial\hat{V}}{\partial x} \qquad (eq.\,II.20)$$

In the particular case of perovskite solar cells, it has been reported that the high frequency capacitance C_1 is the dielectric bulk capacitance. The low capacitance C_2 is related with interfacial processes, but its exact physical meaning is under discussion. It has been also found that the addition of high and low frequency resistances $R = R_1 + R_2$ plus one third of the transport resistance is related to the resistive.[13] The series resistance R_s is related to the contribution of wires, collecting electrodes and contacts.

II.7. Electroluminescence

Similarly to the PL, the electroluminescence (EL) is also the radiative recombination of excess carriers, however in this case the excess of carriers is caused by a current injection instead of an optical pumping. Basically the mechanism of light emitting diodes (LEDs) is opposite to solar cells. In solar cells, excess carriers (electrons and holes) are generated by illumination and are driven to the external load while in LEDs electrons and holes are injected to the devices through the external load, forcing them recombine radiatively and emitting photons.
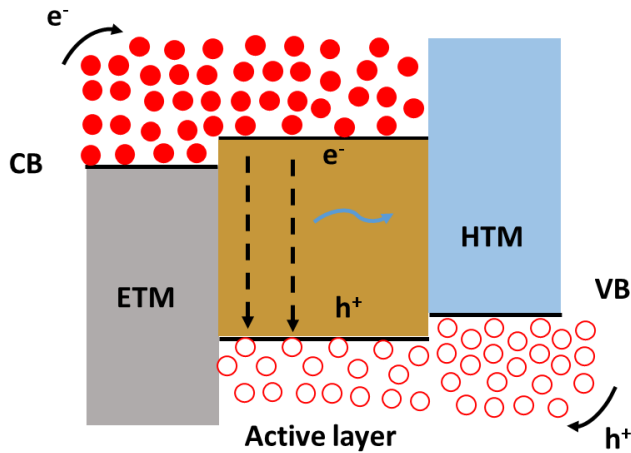
Fig II.7. Schematic of operation mechanism of a light emitting device (LED) under the injection of current.

Under the applied bias, electrons and holes are injected into the active area, radiatively recombine and emit photons (Fig II.7). The energy of emitted photons is equal to the bandgap of a semiconductor. In order to achieve the emitted photons or EL signal, the drive voltage V of a LED needs to be equal (or higher) than the bandgap energy E_g divided by the elementary charge q:[14]

$$V \geq \frac{h\upsilon}{q} \approx \frac{E_g}{q} \qquad (eq. II.21)$$

where h is the Planck's constant and υ is frequency of emitted photons. The internal quantum efficiency (iQE) of a LED is defined as:[14]

$$iQE = \frac{number\ of\ photons\ from\ active\ area\ persecond}{number\ of\ electrons\ injected\ into\ LED\ per\ second} \qquad (eq.II.22)$$

An ideal LED has a unit internal quantum efficiency, it means one injected electron results in the emission of one photon. The emitted photons in the active area should escape from the LED device. For an ideal LED, all the emitted photons can escape into free space, leading a unity extraction efficiency. However in real LEDs, not all photons can escape into free space, some photons may never leave the semiconductor. This is due to some possible reasons: (i) the emitted photons can be reabsorbed by active or/and substrate materials, (ii) due to the phenomenon of total internal reflection, the photons are trapped inside an active area. The extraction and external quantum efficiencies, termed as $\eta_{extraction}$ and eQE respectively, of an LED are defined following:[14]

$$\eta_{extraction} = \frac{number\ of\ photons\ emitted\ into\ free\ space\ persecond}{number\ of\ photons\ emitted\ from\ active\ area\ per\ second} \qquad (eq.II.23)$$

$$eQE = \frac{number\ of\ photons\ emitted\ into\ free\ space\ persecond}{number\ of\ electrons\ injected\ into\ LED\ per\ second} \qquad (eq.II.24)$$

Or

$$eQE = iQE * \eta_{extraction} \qquad (eq.II.25)$$

As mentioned above, some generated photons cannot escape into free space partially due to the total internal reflection phenomenon. Generated photons come to the semiconductor/air interface then are refracted (Fig II.8a), obeying the Snell's law:

$$n_s\ sin\alpha = n_{air}\ sin\theta \qquad (eq.II.26)$$

where n_s, n_{air} are the refractive index of the semiconductor and air respectively. $\boldsymbol{\alpha}$ and θ are an incident and refracted angles of a photon. The critical angle α_c for total internal reflection is obtained using the condition $\theta = 90^o$, as described in the Fig II.8b and using the Snell's law:

$$\alpha_c = arcsin\frac{n_{air}}{n_s} \approx \frac{n_{air}}{n_s} \qquad (eq.II.27)$$
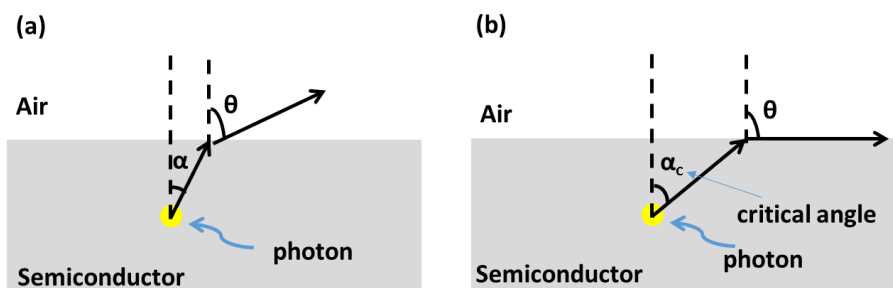
Fig II.8. Schematic of an emitted photon refracted at the semiconductor/air interface before escaping to the free space following the Snell's law for an arbitrary incident angle (a) and for a critical angle (b).

The generated photons come to the interface of semiconductor/air with the angle larger than the critical angle, they will be reflected back to the semiconductor, resulting a lower eQE. Generally semiconductors have high refractive index, leading small critical angles, consequently a large number of photons cannot escape to free space due to the total internal reflection. In LED devices generated photons have to pass several refraction times before can escape to free space as a LED device contains several layers.

References

1. Stanjek, H.; Häusler, W. Basics of X-ray Diffraction. *Hyperfine interactions* **2004,** *154* (1-4), 107-119.
2. Birkholz, M. *Thin film analysis by X-ray scattering*. John Wiley & Sons: 2006.
3. Waseda, Y.; Matsubara, E.; Shinoda, K. *X-ray diffraction crystallography: introduction, examples and solved problems*. Springer Science & Business Media: 2011.
4. Zhou, W.; Wang, Z. L. *Scanning microscopy for nanotechnology: techniques and applications*. Springer science & business media: 2007.
5. Dehm, G.; Howe, J. M.; Zweck, J. *In-situ electron microscopy: applications in physics, chemistry and materials science*. John Wiley & Sons: 2012.
6. Peddinti, V. K. Light Emitting Diodes (LEDs). *electrical engineering material spring* **2008**.
7. Cook, G. *Photovoltaic Fundamentals*. Solar Energy Research Institute: 1991.
8. NSPRI, O. M. Fundamentals of Photovoltaic Materials. *National Solar power institute, Inc* **1998,** *12*, 21-98.
9. Fabregat-Santiago, F.; Garcia-Belmonte, G.; Mora-Seró, I.; Bisquert, J. Characterization of nanostructured hybrid and organic solar cells by impedance spectroscopy. *Physical Chemistry Chemical Physics* **2011,** *13* (20), 9083-9118.
10. Nelson, J. *The physics of solar cells*. World Scientific Publishing Company: 2003.

11. Pitarch-Tena, D.; Ngo, T. T.; Vallés-Pelarda, M.; Pauporté, T.; Mora-Seró, I. Impedance Spectroscopy Measurements in Perovskite Solar Cells: Device Stability and Noise Reduction. *ACS energy letters* **2018,** *3* (4), 1044-1048.

12. von Hauff, E. Impedance Spectroscopy for Emerging Photovoltaics. *The Journal of Physical Chemistry C* **2019,** *123* (18), 11329-11346.

13. Yoo, S.-M.; Yoon, S. J.; Anta, J. A.; Lee, H. J.; Boix, P. P.; Mora-Seró, I. An Equivalent Circuit for Perovskite Solar Cell Bridging Sensitized to Thin Film Architectures. *Joule* **2019**.

14. Schubert, E. F. *Light-Emitting Diodes (2006)*. E. Fred Schubert: 2006.

Chapter III

Interaction Between Colloidal Quantum Dots and Halide Perovskites: Looking for Constructive Synergies

III.1. Candidate's contribution

The nature and extent of my contribution to the work in the chapter III is described following:

Nature of contribution	Extent of contribution
- Review the existing studies in the literature and evaluation on the possible combination of perovskite and quantum dots. - Bring our own contribution to the-state-of-art - Prepare the first manuscript draft - Edit the manuscript according to the comments of referees - Write the draft for replying the referees	**65 %**

III.2. Published manuscript

Interaction Between Colloidal Quantum Dots and Halide Perovskites: Looking for Constructive Synergies

Thi Tuyen Ngo,[1] and Iván Mora-Seró[1,*]

[1] Institute of Advanced Materials (INAM), Universitat Jaume I, 12006 Castelló, Spain.

*Corresponding Authors: sero@uji.es

Abstract

Colloidal Quantum Dots (QDs) have received an extensive attention during the last few decades due to their amazing properties emerging from the quantum confinement. In parallel, halide perovskites have attracted attention by the demonstration of very high performances especially in solar cell and LEDs, and other optoelectronic devices. Both families of materials can be prepared in a relatively simple way, facilitating their integration. There are several examples of their interaction enhancing the properties of the final nanocomposite. Perovskite can effectively passivate QDs, or act as efficient charge transporters. While QDs can be used to modify the selective contacts in perovskite devices or can be used as efficient light emitters or absorbers for enhanced LEDs and Photodetectors, respectively. Moreover, QD can seed the perovskite crystal growth, improving the morphology and ultimately the solar cell performance. In addition, new advanced devices can appear by the constructive synergy between both families of materials.

TOC

Quotes

- Combinations of materials with different nature has been a successful strategy in order to develop new materials with enhanced properties.

-   The combination of halide perovskites and colloidal quantum is a promising strategy looking for constructive synergies where the whole is more than the sum of the parts.
-   Combination of halide perovskites and colloidal quantum have improved the performance of solar cells, LEDs and photodetectors.
-   Advanced configurations as tunable LEDs and Intermediate Band Gap Solar cells could be potentially implemented if non-radiative recombination can be avoided.

Combinations of materials with different nature has been a successful strategy in order to develop new materials with enhanced properties. Adobe, concrete, stained glass, stainless steel are just some examples of how this strategy has provided some of the most employed materials that has been used for the humankind for centuries even for millennia. This strategy is still useful nowadays when the development of chemistry, quantum mechanics and nanotechnology has created a revolution of material science. Two paradigmatic relatively new materials with a clear applicability in optoelectronics are halide perovskites (HPs) and semiconductor quantum dots (QDs). Both families of materials are exciting by themselves and they are somewhat easy to combine, consequently there is a huge interest in building up constructive synergies in order to obtain properties and/or devices with enhanced functionalities and performance by their combined use.

Halide Perovskite (HP) is a family of materials with outstanding versatility not only for the preparation of high efficiency solar cells, with certified efficiencies higher than 23%,[1] but also photodetectors,[2] light emitting diodes (LEDs),[3-6] light amplifier[7-8] and lasers.[9-12] Although HPs has been studied in the past,[13] the interest for these materials has reached its maximum level in the last few years. This interest has been mainly originated by the impressive photovoltaic conversion efficiencies reported in perovskite solar cells (PSCs) and how this efficiency has increased quickly from 10% to 23% in less than six years.[1, 14-18] In PSCs it has been shown that HP not only acts as excellent light harvester[19] but also as Electron Transporting Material (ETM),[14] Hole Transporting (HTM),[20] or both in planar devices with no mesoporous scaffold.[21] Perovskite is able to accumulate charge by itself,[22] constituting a new class of photovoltaic device differentiated from its ancestor, the dye sensitized solar cells. Additionally HPs can be prepared from solution methods at low temperatures and, consequently, using low cost fabrication techniques. Solution processes also allows HPs to combine easily with other materials such as organic compounds[23] and QDs.[23-26]

On the other hand, colloidal QDs offer a high versatility with tunable bandgap just by size or shape control, due to quantum confinement effect, pure

color and bright emission, and generally better stability than organic chromophores.[5, 27-28] Consequently, QDs have attracted considerable attention due to their unique and suitable electro-optical properties for the application of QDs in LEDs,[27, 29-31] solar cells[32-38] and other optoelectronic devices.[27] Besides, solar cells prepared with QD thin films have demonstrated certified photovoltaic conversion efficiencies as high as 13.4 %,[39] while for sensitized configuration efficiencies close to 13% have been reached.[40]

Considering all these outstanding properties for HPs and colloidal QDs the combination of both systems is a promising strategy looking for constructive synergies where the whole is more than the sum of the parts. There are previous examples of constructive combination of different family materials as molecular dyes and colloidal QDs that can provide enhanced charge photoinjection into TiO_2,[41] and consequently increase the performance of the sensitized solar cells.[42] In this case, the obtained photocurrent is not just the consequence of the addition of materials absorbing at different light wavelengths but higher. The internal recombination inside the QDs of the photogenerated carriers before being injected is highly suppressed due to a fast hole extraction towards the attached dye.[42] This is a clear example of a constructive synergy.

As both HPs and QDs are promising for optoelectronic devices, their combination could benefit of the advantages of these two materials such as the strong luminescent efficiency of QDs and long range charge carrier transport of HPs. Here we summarize important studies on the interaction between HPs and QDs which has been applied for the development of optoelectronic devices such as solar cells[43-46], LEDs[25-26, 47-48] and photodetectors,[49-51] and discuss the perspectives of the synergistic interaction between them.

HPs and QDs can be fabricated using relatively simple synthetic routes allowing an easy integration of both materials and consequently favored the apparition of different works which explored the integration of both materials after the breakthrough of the first reports on all-solid PSCs. Different QDs have been investigated in order to combine with HPs. The PbS QDs have been likely the most employed ones due to their bandgap that can be tuned deeper in the IR than HPs and also due to the relatively low lattice mismatch.[24] In fact the lattice mismatch can be further reduced by the use of mixed halide I-Br perovskite,[48] or the use of inorganic perovskites.[52] Researchers have combined HPs with colloidal QDs following different objectives as the use of the selective and transport properties of one of the compounds, attain a broader light absorption range, the passivation of QD surface or the implementation of advanced solar cell or LED configurations.

QDs have been used as HTM in PSCs. Having a proper band energy alignment is a key parameter to achieve a good performance of optoelectronic devices in general and solar cells in particular. Hu et al. synthesized PbS QDs with tuned bandgap from 0.7 to 2.1 eV and used them as HTM in PSCs with a structure of ITO/PbS QDs/MAPI/PCBM/Al.[43] By tuning the size of PbS colloidal QDs, they engineered the energy alignment between PbS QD acting as HTM and HP active layer. The use of PbS QDs HTM allowed to harvest photons up to 1000 nm wavelength and increased significantly the performance respect cells with no HTM but far of the efficiency obtained with the most common HTMs.[43]

Co-sensitization of HPs and QDs is one of the possibilities that have awaken more interest regarding the combination of the two material families. In this combination the purpose is to use the broader absorption range of the PbS QDs in the IR with the good transport properties of HPs. The combination of HPs and QDs has been used as a co-sensitizer in a heterojunction solar cells. $CH_3NH_3PbI_3$ (MAPI) has an excellent absorption of the solar spectrum in the visible range but not in the near infrared range because of its bandgap (1.57 eV). The use of co-sensitizer HP and QDs can overcome this absorption limitation as suggested the first time by Etgar et al.[44] QDs act as an absorber in NIR region, see Figure III.1a, resulting a higher short circuit current density, J_{sc}, than for single MAPI devices,[44, 53-54] with contribution to the photocurrent of photons harvested by the two co-absorbers as it is observed from IPCE measurements, see Figure III.1b. On the other hand, the study of Vinh et al. pointed out a synergistic effect of the addition of PbS QDs as it induced hydrophobic modification of the perovskite surface, leading to an improvement of the device stability in air atmosphere. [54]
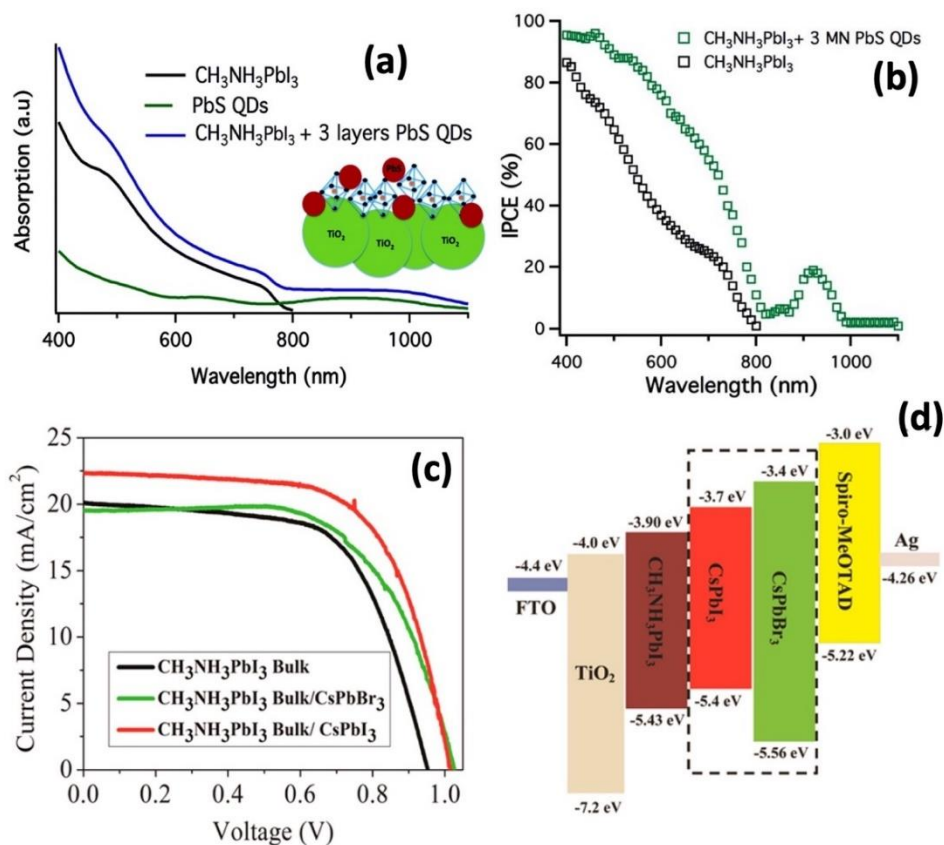
Figure III.1: (a) Absorption spectra on mesoporous TiO_2 substrate of the PbS QDs, lead iodide perovskite and lead iodide perovskite with 3 layers of PbS QDs. **(b)** Incident photon to current efficiency (IPCE) spectra of the PbS QDs, lead iodide perovskite and lead iodide perovskite with 3 layers of PbS QDs. Reproduced with permission of the Royal Society of Chemistry.[44] **(c)** J−V curves spectra of perovskite solar cells incorporating $CsPbX_3$ QDs between the $CH_3NH_3PbI_3$ (MAPI) active layer and the HTM **(d)** Energy band diagram of each material within the perovskite/$CsPbX_3$ structure, with energy levels given in eV. Reproduced with permission of the American Chemical Society.[55]

Interface Engineering in PSCs using perovskite QD layer sandwiched between the perovskite active layer and the HTM has produced a performance enhancement.[55-57] Cha et al. reported an increase of PSC photoconversion efficiency by the deposition of $MAPbBr_{0.9}I_{2.1}$ Quantum Dots between MAPI and spiro-OMeTAD HTM.[57] Moreover, inorganic perovskite QDs present higher stability as Sidhik et al. pointed out.[55] The thin layer of HP ($CsPbX_3$, X is Br or I) QDs deposited on top a MAPI layer acted as the electron blocking of the perovskite/HTM interface, reducing interfacial recombination and increasing consequently the open circuit potential, see Figure III.1c. With an appropriated band alignment, using $CsPbI_3$ (CsPI) QDs (see Figure III.1d), the hole injection is not hindered and the photocurrent can be also enhanced, see

66

Figure III.1c.[55] There are some other related studies regarding the interaction of perovskite QD with perovskite thin layers that have been recently summarized in a perspective article by Yang et al.[56]

On the other hand, one of the key issues on the efficiency improvement experienced in the last decade in colloidal QD solar cells, both on depleted heterojunction[58] and in sensitized configuration,[40] has been the passivation of surface trap states of colloidal QDs. HPs also exhibit good performance as passivation agents of QDs surface. Typically, colloidal QDs are synthesized with long-chain organic ligands which stabilize, control size and afford an excellent monodispersity. However, the bulky organic ligands create electronic barriers that compromise efficient charge transport of QD films in optoelectronic devices. To build a high-quality QD-based photovoltaic device, interdot electronic communication needs to be improved. On the other hand, organic ligands also act as surface passivators. QDs possess an inherent large surface-to-volume ratio, resulting in unsaturated dangling bonds, creating undesired electronic trap states within the bandgap of QDs. These trap states increase the chance of carrier recombination, curtailing the efficiency of charge extraction. The ligand exchange procedure opens the possibility to exchange to short ligand, improving the interdot electronic communication, and moreover passivate the trap states. Among various ligand exchange schemes, HPs, including HP precursors, shows a strong passivation and well-protection from oxygen, resulting an improvement in a device performance and stability.

There are several examples of exchange of bulky organic capping layer of colloidal QDs by HPs or HPs precursor shell. In 2014, Dirin et al. presented a broad study of the use of HPs and other metal halide complexes as inorganic capping ligands for colloidal nanocrystals (PbS, CdSe, CdS, CdSe/CdS, InP, Au and Pd),[59] showing that MAPI was the first example of hybrid capping of PbS able to retain highly efficient IR photoluminescence quantum yield (PLQY) of PbS QDs. In the same year, Ning et al. carried out the solution-phase ligand exchange from the oleic acid capping of PbS QDs to methylammonium iodide (MAI).[60] Short-ligand exchanged PbS QDs could be directly deposited in a single step, with no requirement of solid-state exchange, rendering it compatible with roll-to-roll processes such as screen printing, spray coating, and blade coating. Moreover MAI capped PbS QD films provided a good stability at 100°C annealing temperature. These QD films with MAI short-capping were applied to fabricate QD solar cells, reaching a photovoltaic conversion efficiency of 6.10%.[60]

Next year, taking advantage of the similar crystal structure and lattice match between PbS and MAPI Yang et al. used MAPI to exchange the ligand

of PbS QDs, see the Figure III.2a.[46] High resolution transmission electron microscopy (HRTEM) measurements and the analysis of lattice fringes from scanning tunneling electron microscope (STEM) pointed out the core-shell structure of PbS/MAPI QDs after ligand exchange. An annealing is necessary to transform HP precursors into thin crystalline matrix to archive good solar cell efficiency. By introducing the coherently lattice-matching thin shell of MAPI, QDs were passivated, limiting the aggregation and thus achieving a better balance of open circuit potential, V_{oc}, and J_{sc}, yielding improved device performance, reaching 8.95% of photoconversion efficiency, using the depleted heterojunction quantum dot solar cell configuration. [46] The main mechanism in the ligand exchange from organic QD capping to MAI or MAPI shell is based on the binding of iodine anions to lead atoms on the QD surface.[60] However, agglomeration could be produced. With a proper optimization of the ligand exchange process the inclusion of iodine on QD surface was done without the detrimental effect of fusion.[61] A co-solvent system was employed to tune the solvent polarity in order to achieve the solvation of MAI and the dispersion of hydrophobic PbS QDs simultaneously in a homogeneous phase enhancing the performance of QD solar cells to 10.6%.[61] This strategy has been further improved using lead halide passivators reaching a solar cell efficiency of 11.28%.[62] Moreover the passivation of lead halide also improved the stability of devices, 90% of initial efficiency was maintained after 1000 hours stored in ambient conditions.[62]

MAPI shell showed an excellent passivation of PbS QDs however QD solar cells strongly suffer from hysteresis in photocurrent-voltage curves.[46] An interesting alternative to hybrid halide perovskite is the use of inorganic halide perovskites as $CsPbI_3$ (CsPI), that exhibits higher stability.[63] Although, perovskite α-phase is not stable for bulk CsPI, it can be stabilized in CsPI QDs.[64] On the other hand, it also possesses similar crystal structure and low lattice mismatch (less than 5%) comparing with those of PbS.[52] Very recently, Zhang et al. used CsPI to passivate PbS QDs.[65] Similar to the case of MAPI, after ligand exchange from organic capping to CsPI, a PbS/CsPI core-shell QD structure also formed. CsPI shell passivates the PbS QD surface, diminishing the trap states, hence improving the charge collection and reducing the charge recombination rate, allowing to obtain performances as high as 10.5%. In addition, colloidal QD solar cells based on PbS/CsPI QDs present extremely low hysteresis, see Figure III.2b, not only in the different scanning directions but also in different scan sweep steps. Moreover these devices also show a good stability not only under long illumination, 46 hours at continuously one sun illumination, see Figure III.2c, but also under ambient conditions (42 days).[65]

Perovskite passivation of PbS QDs have been also used successfully in QD sensitized solar cell configuration.[45, 66] MAPI layer coated on PbS QDs in sensitized solar cells, passivates QD surface, reducing significantly the defects as the $PbSO_3$ oxidation, resulting finally in a better charge extraction with an improvement of the performance of the photovoltaic device.
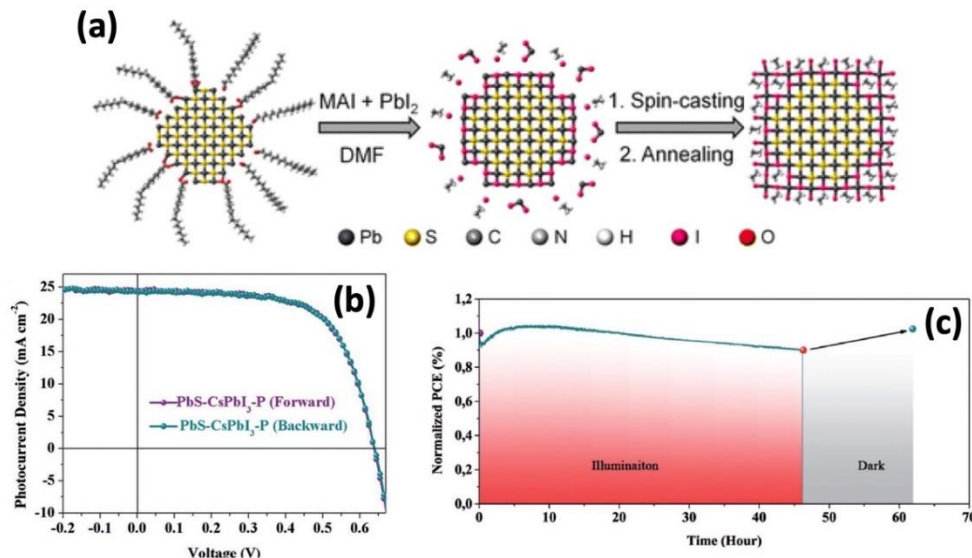

Figure III.2: (a) Schematic of solution ligand exchange with MAPI perovskite precursors and corresponding colloidal QD film preparation. Reproduced with permission of the American Chemical Society.[46] **(b)** Forward and backward *J–V* curves under 1 sun AM1.5G illumination of PbS/CsPbI₃ (PbS/CsPI) based colloidal QD solar cell. **(c)** Photostability test of the PbS/CsPI based QD solar cell under illumination and after stored during 16 h in ambient conditions under dark after the illumination test. The photostability test was performed in N_2 atmosphere under one sun equivalent illumination provided by a white LED lamp. Reproduced with permission of Wiley.[65]

Nevertheless, beyond of the use of halide perovskite as mere passivation agent of colloidal QDs, likely the most appealing results have been obtained when a more synergistic interaction was stablished between both materials. In 2015, Ning et al. reported by first time the preparation of thin films with perovskite matrix and embedded colloidal QDs.[24] PbS and MAPI possess a related crystal structure, each having a six-coordinated Pb atom, and with Pb–Pb distances (MAPI, 6.26A˚; PbS, 5.97A˚, ~ 5% lattice mismatch), see Figure III.3a-b. Their analysis of density functional theory (DFT) of an interface formation between PbS (100) and MAPI (110) plane showed an interfacial energy less than 10 meV·Å^{-2}, suggesting that growth of HP on PbS at room temperature is nearly as feasible as homoepitaxy of PbS on PbS or HP on HP. DFT further reveals that the epitaxial three-dimensional embedding of PbS CQDs inside a HP matrix is achieved without the formation of interfacial defects; that is, the bandgap is predicted to remain open, with no in-gap defects

predicted. They concluded structurally PbS QDs lattice has a relative good match with MAPI HP structure both three dimensionally and two dimensionally.[24] Perovskite matrix with embedded QDs increased significantly the PL emission from PbS QDs as photogenerated electrons and holes in HP were transferred to PbS QDs with a value exceeding 80% of efficiency. Since this first demonstration, HP films with embedded QDs were applied as an active layer in different optoelectronic devices such as solar cells[67-68], LEDs[26, 48] and photodetectors.[49-51] In these works, embedding QDs inside HPs matrix showed an improvement respect to the reference devices, without embedded QDs.
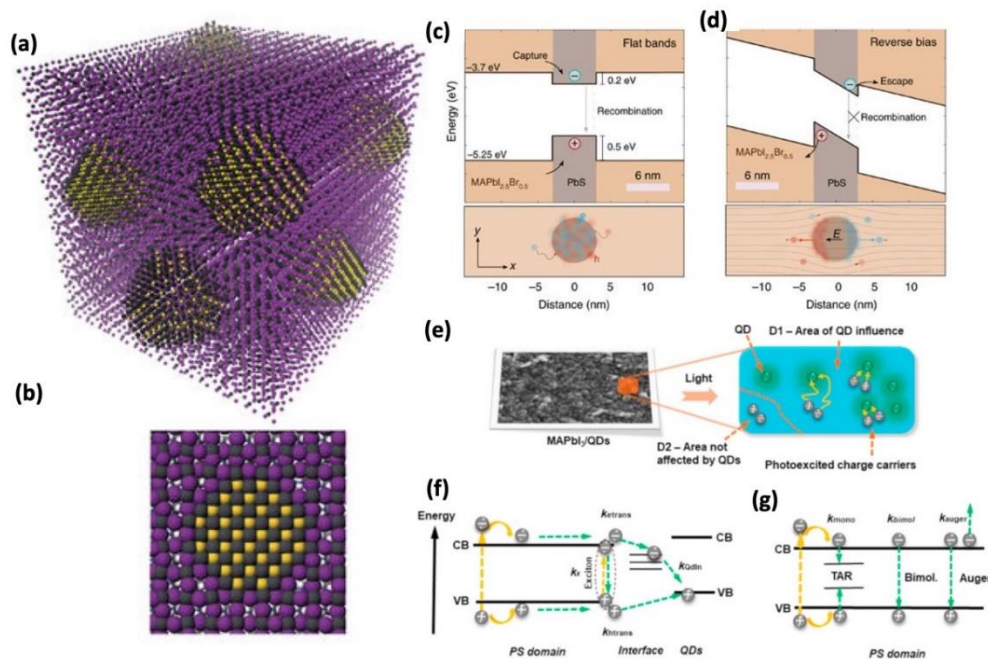
Figure III.3: **(a)** Three-dimensional atomistic model and **(b)** Cross-section (two-dimensional view) of PbS QDs embedded in a halide perovskite matrix. **(a-b)** Reproduced with permission of Nature.[24] **(c, d)** Band alignment of PbS QDs embedded in mixed halide perovskite matrix as calculated with a SCAPS model at **(c)** no bias and **(d)** reverse bias conditions. In the absence of an imposed electric field photogenerated charges are uniformly distributed across the dot (bottom panels). At sufficient reverse bias conditions they are spatially separated and can inject into the $MAPbI_{2.5}Br_{0.5}$ host, favoring carrier recirculation over capturing. **(c-d)** Reproduced with permission of Nature.[50] **(e)** SEM of MAPI layer with embedded PbS/CdS core/shell QDs and the cartoon showing the areas of QDs influence (D1) and without their influence (D2) upon excitation over the band gap of perovskite. **(f)** Energy diagram showing the dynamics of photoexcited charge carriers in MAPI-QDs film in D1 area and **(g)** D2 area upon excitation over the band gap. For clarity, **(f)** only shows the processes involving the influence of QDs, while those in **(g)** representing the classical events in pure perovskite. k_{etrans} and k_{htrans} characterize the effective transfer processes of charge carriers from perovskite to the interface or/and QDs. k_x is the exciton recombination rate constant. k_{QdIn} is the recombination rate constant between trapped electrons and holes in QDs. **(e-g)** Reproduced with permission from Elsevier.[69]

The introduction of PbS QDs into HP matrix has increased photoconversion performance of PSCs by the effect of QDs in the crystallization process of perovskite layer. Li et al. prepared solar cells with $MAPbI_{3-x}Cl_x$ matrix and embedded PbS QDs by dispersing a small quantity of core/shell PbS/MAI QDs in the solution containing the HP precursors. PbS acted as effective seed-like sites to promote the formation of HP grains, resulting in substantial morphological improvements in terms of grain size, surface coverage and uniformity. Similar effect in the grain size by QD addition have been also observed in other works.[26] The PSC performance observed by the appropriate incorporation of PbS, with concentration 1.0wt%, reached 17.4%, proximately a 25% of improvement respect the reference devices.[67] Recently, Han et al. attained a performance of 18.6% with the QD in perovskite strategy.[68]

In this sense, the maximum photoconversion efficiency with hybrid QD and HP films have been obtained with QDs acting with a passive role, as additives in order to obtain a better perovskite crystallization. This is not the case in hybrid QD-HP LEDs where the QDs are the active light emitters and HPs act as carrier transporting matrix. Gong et al. reduced the lattice mismatch between HP and PbS QDs (with exciton peak at 1391 nm) by incorporating a small quantity (17%) of bromide into MAPI matrix, forming a mixed halide $MAPbI_{3-x}Br_x$.[48] The introduction of bromide reduced on one hand the strain at the interface of HP and QDs, and on the other hand the amount of defect on PbS surface. The function of a mixed halide perovskite is to transport generated charger carriers into PbS QDs. The selected HP and PbS QDs presented a type I band alignment, see Figure III.3c, and the transported carriers in the perovskite matrix are finally injected into the PbS QDs where they recombine radiatively, resulting in an increase of the LED external quantum efficiency (EQE), reaching 4.9%, two folds higher than pure QDs devices.[48] This approach has been also used by the same group but with layered 2D perovskites, incorporating longer amine molecules, butylamine, pentylamine and hexylamine. The substitution of MA^+ cation by these amine molecules with longer carbon backbones breaks the symmetry of the 3D structure and introduces 2D structuring layered along c-axis. The QDs exchanged were easily deposited in a single step. By using 2D HP passivated PbS QDs as an active layer, the authors could increase the operating voltages of LEDs up to 7.5 V due to better stability of 2D HPs in a comparison with 3D HPs.[47]

Embedding QDs inside HPs matrix was applied in photodetectors as well. Liu et al. pointed out that the incorporation of PbS QDs induced traps-assisted charge injection.[49] PbS QDs produced traps residing on the surface of

MAPI thin films. Under illumination, excitons formed in HP layer rapidly would dissociate into electrons and holes. Then, electrons would be trapped at the HP-PbS QD surface which would shift downward the conduction band (CB) energy level of HP-QD nanocomposites, followed by the re-alignment of its fermi level with the work function of the Al cathode. The trapped electrons can be considered as a heavy-doping on the surface of HP-QDs layer, which dramatically narrow the depletion region formed at the interface. Thus injected holes from Al cathode can be easily tunneled through the hole blocking layers (PC61BM/BCP) at low external biases, resulting an EQE of ~4500%, a photoresponsivity of ~15,000 mA/W and a detectivity of over 6×10^{13} Jones (1 Jones=1 cm·Hz$^{1/2}$·W^{-1}) at a small bias of 2 V, and a photoresponse time of 11.5 µs.[49]

Moreover, following the strategy of lattice matching developed by Gong et al.[48] a further study on the interaction between HP and PbS QDs under applied reverse bias condition for the development of photodetectors has been performed by the same group.[50] The lattice of mixed HP was adjusted, by optimizing the ratio between iodide and bromide MAPbI$_{2.5}$Br$_{0.5}$ to suitable to that of PbS QDs (exciton peak at 1240 nm, ~ 1 eV). The photodiode has been prepared using a structure of FTO/compact TiO$_2$/PbS QDs embedded in HP matrix/spiro-OMeTAD/Au. Under no external electrical field, generated excitons are confined inside QDs due to the type I junction forming between HP and QDs, and lose their energy via the recombination, radiative or non-radiative, see Figure III.3c. However, under the presence of a suitably large electric field, Figure III.3d, the excitons photogenerated in the QDs will then separate, and the charges may be ejected from the dots, under the action of the field, into the host perovskite matrix. Escape charge carriers can be potentially re-captured into QDs, as determined by the competition between carrier thermalization and extraction time. This structure allowed the preparation of photodetectors with specific detectivities that exceed 10^{12} Jones.[50]

In order to further improve the performance of optoelectronic devices developed with HP-QD systems, the understating of the deep interaction of these materials is mandatory. Recently, we have furthermore elucidated the interaction mechanism between HP and QDs. We studied the charge carrier dynamics of HP-QDs hybrid films as function of QD concentrations (C$_{QDs}$) using ultrafast UV–VIS transient absorption (TA) and THz spectroscopies measurements.[69] By photogenerating charge carriers over the band gap of MAPI (~ 1.55 eV) in the HP-QDs hybrid material, we observed fast and efficient charge carrier deactivation due to their transfer to the QDs. The TA decay becomes shorter upon increasing C$_{QDs}$. For samples containing C$_{QDs}$ lower than 0.18 wt%, the TA decays were governed by the behavior of neat HP while for higher concentrations a progressive faster decay was observed.[69]

The observed dynamics were analyzed in terms of two different domains of the HP layer: a domain D1 where photocarriers are influenced by the presence of QDs and a domain D2 where they do not interact with QDs. The events happened in D1 were described in Figure III.3f: (i) charge carriers transport and transfer from HP domain to QDs and MAPI/QDs interface, (ii) exciton recombination, and (iii) recombination of transferred charge carriers. In addition, electron and hole recombination processes in HP is also produced. Using a kinetic model and analyzing the TA signals, we observed that 85–89% of both electrons and holes were transferred to the HP/QDs interface trap states, and to the valence band (VB) of the QDs. Up to 7% charges formed excitons in HP domain in the close vicinity of interface. A small fraction of photoexcited charges (8–15%) were not affected by the presence of QDs, and thus, their deactivation followed the standard processes of neat HP, see Figure III.3g. The changes in the values are related to the QDs concentration in the matrix. The analysis of the data shows the important role of trap states and gives clues for the further improvement of this hybrid system. The size of D1 and D2 domains depends on the QD concentration and on the carrier diffusion length in HP, consequently this method can be also used to determine the diffusion length of the HP layer as we showed.[69]

The interaction of HP and QDs has been studied not only for hybrid organic-inorganic HP but also with a fully inorganic HP. Jung et al. pointed out that PbS QDs and $CsPbBr_3$ present just ~ 0.5% lattice mismatch, much lower than the lattice mismatch between PbS and MAPI, ~ 5%.[52] They studied theoretically the bond formation and carrier confinement at the HP-QD interface. By calculating the surface energy at different facets of PbS and $CsPbBr_3$, they could construct the interface slab models along (100) orientation. Using the models and calculating the interface energy taking into account different terminations, the growth mechanism of HP-QD interface is elucidated. (100) facet of $CsPbBr_3$ with a termination of $PbBr_2$ spontaneously grows on the (100) facet of PbS by locating Pb on S and Br on Pb with the presence of a strong chemical interaction attributed to heteropolar bond formation.[52]

Finally, combined systems of HP and colloidal QDs have also demonstrated the potentiality for the development of advanced optoelectronic devices, not by the enhancement of the properties already presented in HP or colloidal QDs but by presenting new ones. Single layers and bilayers of MAPI and colloidal core/shell PbS/CdS QDs were prepared, using two different QD sizes, with diameter 2.3 and 3 nm.[25] Figure III.4a shows the normalized photoluminescence (PL) of the single HP and QD layers. In addition, bilayers formed by both combinations of QD/HP and HP/QD were also studied with a type II alignment due to the relative large bandgap of the PbS QDs in

comparison with other experiments. Interestingly bilayer samples presents a new feature in the near infrared region (NIR) that it is not observed for single layer samples, HP or QD, as can be observed in Figure III.4b. In this region perovskite single layer does not present any PL while for single layer colloidal QD sample just the queue of the band edge emission is observed. However bilayers presents an emission at 1200-1600 range blue shifted for QDs with smaller size, see Figure III.4b. The intensity of this emission increases when samples are excited with wavelengths shorter than the perovskite bandgap and it is attributed to the formation of an exciplex state between HP and QD.[25] The exciplex emission has been also observed in perovskite films with embedded QDs.[26]

The use of different emitters produced LEDs with color tuned by the applied bias, see Figure III.4c. The color can be easily controlled as the ratio between QD and HP EL intensity emission follows a linear relationship, see Figure III.4d. Interestingly, the emission from HP-QD exciplex state is observed not only by optical pumping, Figure III.4b, but also by electrical injection, Figure 4e, with a voltage threshold as low as 0.77 V, see Figure III.4f.[25] The possibility of band gap tuning of the HP by the use of different cations and anions and of the colloidal QDs can potentially develop dual LEDs working with very different wavelength depending of the applied bias.

Moreover the combination of HP and colloidal QDs can have also an interesting potentiality for the development of advanced photovoltaic devices. Due to the reciprocity principle, if an electron and hole from an exciplex state can recombine producing a photon, the reciprocal process in which a photon can produce an electron-hole pair at the exciplex state is also possible. This possibility opens the door to the preparation of Intermediate Band Gap Solar Cells (IBSCs) taking benefit from the HP and QD synergies.

The concept of IBSC was developed by Luque and Martí.[70] In an IBSC there are one or several intermediate bands at the band gap of a wide gap semiconductor, been E_G the band gap energy, see Figure III.4g, for the case of just one intermediate band. Photons with energy higher than E_G can be absorbed by the matrix semiconductor, process 1 in Figure III.4g. Moreover, intermediate bands would act as stepping stones allowing low energy photons transfer electrons from the VB of the wide band gap semiconductor to its CB by the absorption of a couple of photons with energies E_H and E_L, processes 2 and 3 in Figure III.4g. In order to take advantage of the intermediate band this level has to be isolated from the extracting contact and three quasi Fermi levels can be defined for VB, CB and intermediate band.[70-71] This fact allow that the IBSC retains the V_{oc} of the wide band gap semiconductor defined by the splitting of electrons in CB and holes in VB Fermi levels, E_{Fn} and E_{Fh}

respectively, but with higher photocurrent due to the sub-band gap photon absorption, see Figure III.4g. In an optimum situation of an IBSC, a half filled intermediate bandgap can either receive electrons from the VB of the matrix compound (process 2 in Figure III.4g) and promote electrons from the intermediate band state into the CB of the matrix (process 3 in Figure III.4g). Theoretical calculations predicts a maximum photoconversion efficiency of 63% under high solar concentration for an cell with an optimum IB state in contrast with a maximum of 41% predicted for single absorber by the Shockley-Queisser limit at the same conditions,[70] with a performance higher than an optimized tandem cell formed by a couple of absorbers. IBSC will have higher theoretical quantum efficiency than tandem cells at any illumination condition. A tandem cell has a maximum quantum efficiency of 0.5 in all the spectra, needing two photons to extract one electron. In the case of IBSCs the same situations accounts for photons with energy lower than E_G, whereas for photons with higher energy quantum efficiency of 1 is possible.
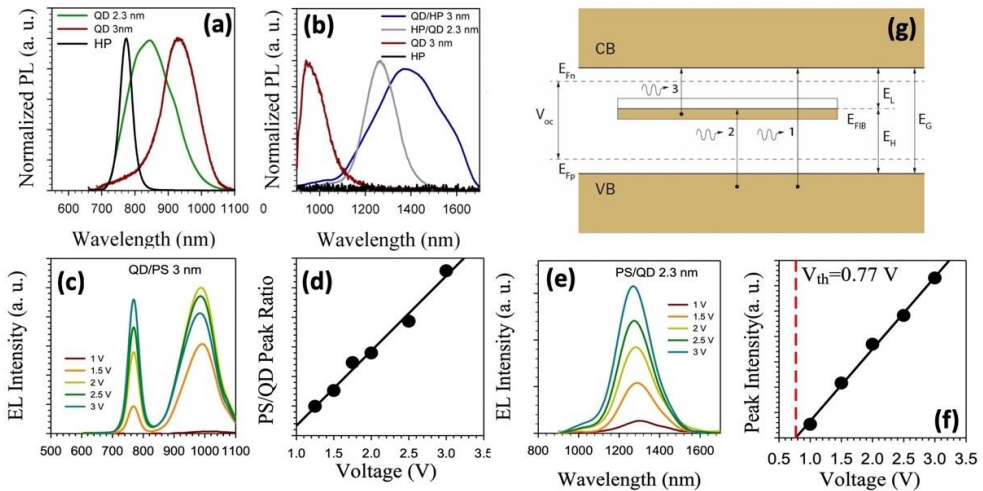
Figure III.4: (a) PL of single layers of MAPI, and core/shell PbS/CdS QDs 2.3 and 3 nm diameter size corresponding to the band gap transition. **(b)** PL in the NIR (900-1700 nm) showing a new exciplex transitions in HP-QD bilayers while no new peak is observed in for single HP or QD (for QD layer just the queue of the band gap transition). **(c)** EL at different applied bias of a bilayer sample of HP and PbS/CdS QDs of 3 nm. **(d)** Ratio between the EL intensity peak of PbS/CdS QDs and HP at different applied bias. **(e)** EL at different applied bias in the NIR region of a bilayer sample of HP and PbS/CdS QDs of 3 nm. **(f)** EL intensity peak in the NIR of PbS/CdS QDs 3nm and HP at different applied bias. **(g)** Scheme of energy configuration of an Intermediate Band Gap Solar Cell. **(a-g)** Reproduced with permission of AAAS.[25]

However, the development of an IBSC with significant efficiency has been elusive. For example the use a monocrystalline GaAs host matrix and InAs QDs grown in the Stranski–Krastanov mode, presented severe limitations in order to produce a practical solar cell. The photocurrent increase

is limited by the low QD density.[72] The density of QDs cannot be very high as QDs produce strain in the layer, and very high strain causes the formation of defects that degrades severely the cell performance.[71] However, the use of HP could help to solve these problems as strain is avoided as it is relaxed at the benign perovskite grain boundaries. Moreover, both HPs and QDs present a high versatility allowing tailoring the intermediate band and the band alignment between HP and colloidal QDs to produce an optimum IBSC.

In summary, the interaction between HP and colloidal QDs can produce interesting constructing synergies promoting the properties of each material and generating new ones. Each material obtains benefits from the interaction with the other, HP can increase the passivation of the QD surface, protecting them from the photocorrosion. Moreover, HP can benefit from the appropriate use of QDs in the selective contacts. HP matrix can also work as an excellent carrier transporter into QDs in a view of type I junction for the development of LEDs and photodetectors while QDs acted as effective seed-like effect to promote the proper crystallization of HP lattice structures, resulting in substantial morphological improvements. Furthermore the band alignment between HP and QDs can be tailored to favor the injection of photogenerated electrons and holes from one into the other. Hence this combination could lead to an improvement in performance of optoelectronic devices such as solar cells and LEDs. On the other hand, the interaction between HP and colloidal QDs also rises new properties, which do not exist in singles materials, as the formation of the exciplex state at lower energies than both HP and QD band gap.[25-26] This system presents a high potentiality in order to develop advanced optoelectronic devices as tunable color LED or intermediate band gap solar cells. However, non-radiative recombination has to be avoided as a major challenge of these advanced configurations in order to get a full benefit of this potentiality. Further study on the interaction between these families of materials undoubtedly will contribute to a further optimization of current devices and to explore new and exciting constructive synergies.

AUTHOR INFORMATION
Corresponding Author
*Address correspondence to this author: sero@uji.es Twitter: @IvanMoraSero
Notes
The authors declare no competing financial interest.

Biographies

Thi Tuyen Ngo graduated in Physics from Vietnam National University (Vietnam) in 2008 and received her Master from University of the Basque Country (Spain) in 2011. She is currently a Ph.D. student at the Institute of Advanced Materials (INAM), Jaume I University (Spain). Her study is focusing on the interaction of perovskite and other materials such as quantum dots and organic compounds. Before incorporating in a Ph.D, she worked as an assistant at Institute of Physics, Vietnam Academy Science and Technology (2008-2009) and worked in the photovoltaic cells at Cidetec (2011-2013) where she learnt about the preparation and characterization of solar cells.

Iván Mora-Seró is associated professor at the Institute of Advanced Materials (INAM) at Universitat Jaume I de Castelló. His research has been focused on crystal growth, nanostructured devices, transport and recombination properties, photocatalysis, electrical characterization of photovoltaic, electrochromic, and water splitting systems, making both experimental and

theoretical work. Recent research activity is focused on new concepts for photovoltaic conversion and light emission (LEDs and light amplifiers) based on nanoscaled devices and semiconductor materials following two mean lines: semiconductor quantum dots and lead halide perovskites. He has appear in the list of Highly Cited Researcher of Clarivate Analytics the three last years.
.

References

1. NREL photovoltaic efficiency chart: https://www.nrel.gov/pv/assets/pdfs/pv-efficiency-chart.20181221.pdf
2. Dou, L.; Yang, Y.; You, J.; Hong, Z.; Chang, W.-H.; Li, G. Solution-processed hybrid perovskite photodetectors with high detectivity. *Nat. Commun.* **2014,** *5*, 5404.
3. Jaramillo-Quintero, O. A.; Sanchez, R. S.; Rincon, M.; Mora-Sero, I. Bright Visible-Infrared Light Emitting Diodes Based on Hybrid Halide Perovskite with Spiro-OMeTAD as a Hole-Injecting Layer. *J. Phys. Chem. Lett.* **2015,** *6*, 1883-1890.
4. Tan, Z.-K. et. al. Bright light-emitting diodes based on organometal halide perovskite. *Nat. Nanotechnol.* **2014,** *9*, 687-692.
5. Alivisatos, A. P. Semiconductor Clusters, Nanocrystals, and Quantum Dots. *Science* **1996,** *271*, 933-937.
6. Lin, K. et. al. Perovskite light-emitting diodes with external quantum efficiency exceeding 20 per cent. *Nature* **2018,** *562* (7726), 245-248.
7. Suárez, I.; Juárez-Pérez, E. J.; Bisquert, J.; Mora-Seró, I.; Martínez-Pastor, J. P. Polymer/Perovskite Amplifying Waveguides for Active Hybrid Silicon Photonics. *Adv. Mater.* **2015,** *27*, 6157-6162.
8. Suárez, I.; Hassanabadi, E.; Maulu, A.; Carlino, N.; Maestri, C. A.; Latifi, M.; Bettotti, P.; Mora-Seró, I.; Martínez-Pastor, J. P. Integrated Optical Amplifier–Photodetector on a Wearable Nanocellulose Substrate. *Adv. Opt. Mater.* **2018,** *6*, 1800201.
9. Deschler, F. et. al. High Photoluminescence Efficiency and Optically Pumped Lasing in Solution-Processed Mixed Halide Perovskite Semiconductors. *J. Phys. Chem. Lett.* **2014,** *5*, 1421-1426.
10. Zhu, H.; Fu, Y.; Meng, F.; Wu, X.; Gong, Z.; Ding, Q.; Gustafsson, M. V.; Trinh, M. T.; Jin, S.; Zhu, X. Y. Lead halide perovskite nanowire lasers with low lasing thresholds and high quality factors. *Nat. Mater.* **2015,** *14*, 636-642.
11. Xing, G.; Mathews, N.; Lim, S. S.; Yantara, N.; Liu, X.; Sabba, D.; Grätzel, M.; Mhaisalkar, S.; Sum, T. C. Low-temperature solution-processed wavelength-tunable perovskites for lasing. *Nat. Mater.* **2014,** *13*, 476-480.

12. Stranks, S. D.; Hoye, R. L. Z.; Di, D.; Friend, R. H.; Deschler, F. The Physics of Light Emission in Halide Perovskite Devices. *Adv. Mater.* **2018,** *30*, 1803336.

13. Mitzi, D. B. Synthesis, Structure, and Properties of Organic-Inorganic Perovskites and Related Materials. 1999, Progress in Inorganic Chemistry, Print ISBN: 9780471326236, DOI:10.1002/9780470166499.

14. Lee, M. M.; Teuscher, J.; Miyasaka, T.; Murakami, T. N.; Snaith, H. J. Efficient Hybrid Solar Cells Based on Meso-Superstructured Organometal Halide Perovskites. *Science* **2012,** *338*, 643-647.

15. Kim, H.-S. et. al. Lead Iodide Perovskite Sensitized All-Solid-State Submicron Thin Film Mesoscopic Solar Cell with Efficiency Exceeding 9%. *Sci. Rep.* **2012,** *2*, 591.

16. Jeon, N. J.; Noh, J. H.; Yang, W. S.; Kim, Y. C.; Ryu, S.; Seo, J.; Seok, S. I. Compositional engineering of perovskite materials for high-performance solar cells. *Nature* **2015,** *517*, 476-480.

17. Bi, D. et. al. Efficient luminescent solar cells based on tailored mixed-cation perovskites. *Sci. Adv.* **2016,** *2*, e1501170.

18. Yang, W. S. et. al. Iodide management in formamidinium-lead-halide–based perovskite layers for efficient solar cells. *Science* **2017,** *356,* 1376-1379.

19. De Wolf, S.; Holovsky, J.; Moon, S.-J.; Löper, P.; Niesen, B.; Ledinsky, M.; Haug, F.-J.; Yum, J.-H.; Ballif, C. Organometallic Halide Perovskites: Sharp Optical Absorption Edge and Its Relation to Photovoltaic Performance. *J. Phys. Chem. Lett.* **2014,** *5,* 1035-1039.

20. Etgar, L.; Gao, P.; Xue, Z.; Peng, Q.; Chandiran, A. K.; Liu, B.; Nazeeruddin, M. K.; Grätzel, M. Mesoscopic $CH_3NH_3PbI_3/TiO_2$ Heterojunction Solar Cells. *J. Am. Chem. Soc.*, **2012**, *134*, 17396–17399.

21. Liu, M.; Johnston, M. B.; Snaith, H. J. Efficient planar heterojunction perovskite solar cells by vapour deposition. *Nature* **2013,** *501*, 395-398.

22. Kim, H.-S.; Mora-Sero, I.; Gonzalez-Pedro, V.; Fabregat-Santiago, F.; Juarez-Perez, E. J.; Park, N.-G.; Bisquert, J. Mechanism of carrier accumulation in perovskite thin-absorber solar cells. *Nat. Commun.* **2013,** *4*, 2242

23. Ngo, T. T.; Suarez, I.; Antonicelli, G.; Cortizo-Lacalle, D.; Martinez-Pastor, J. P.; Mateo-Alonso, A.; Mora-Sero, I. Enhancement of the Performance of Perovskite Solar Cells, LEDs, and Optical Amplifiers by Anti-Solvent Additive Deposition. *Adv. Mater.* **2017,** *29*, 1604056.

24. Ning, Z.; Gong, X.; Comin, R.; Walters, G.; Fan, F.; Voznyy, O.; Yassitepe, E.; Buin, A.; Hoogland, S.; Sargent, E. H. Quantum-dot-in-perovskite solids. *Nature* **2015,** *523*, 324-328.

25. Sanchez, R. S.; de la Fuente, M. S.; Suarez, I.; Muñoz-Matutano, G.; Martinez-Pastor, J. P.; Mora-Sero, I. Tunable light emission by exciplex state formation between hybrid halide perovskite and core/shell quantum

dots: Implications in advanced LEDs and photovoltaics. *Sci. Adv.* **2016,** *2*, e1501104.

26. Ngo, T. T.; Suarez, I.; Sanchez, R. S.; Martinez-Pastor, J. P.; Mora-Sero, I. Single step deposition of an interacting layer of a perovskite matrix with embedded quantum dots. *Nanoscale* **2016,** *8*, 14379-14383.

27. Shirasaki, Y.; Supran, G. J.; Bawendi, M. G.; Bulovic, V. Emergence of colloidal quantum-dot light-emitting technologies. *Nat. Photon* **2013,** *7*, 13-23.

28. Owen, J.; Brus, L. Chemical Synthesis and Luminescence Applications of Colloidal Semiconductor Quantum Dots. *J. Am. Chem. Soc.* **2017,** *139*,10939-10943.

29. Pal, B. N.; Ghosh, Y.; Brovelli, S.; Laocharoensuk, R.; Klimov, V. I.; Hollingsworth, J. A.; Htoon, H. 'Giant' CdSe/CdS core/shell nanocrystal quantum dots as efficient electroluminescent materials: strong influence of shell thickness on light-emitting diode performance. *Nano Lett.* **2012,** *12*, 331-6.

30. Sun, L.; Choi, J. J.; Stachnik, D.; Bartnik, A. C.; Hyun, B. R.; Malliaras, G. G.; Hanrath, T.; Wise, F. W. Bright infrared quantum-dot light-emitting diodes through inter-dot spacing control. *Nat. Nanotechnol.* **2012,** *7*, 369-73.

31. Wood, V.; Panzer, M. J.; Bozyigit, D.; Shirasaki, Y.; Rousseau, I.; Geyer, S.; Bawendi, M. G.; Bulovic, V. Electroluminescence from nanoscale materials via field-driven ionization. *Nano Lett.* **2011,** *11*, 2927-32.

32. Lan, X. et. al. 10.6% Certified Colloidal Quantum Dot Solar Cells via Solvent-Polarity-Engineered Halide Passivation. *Nano Lett.* **2016,** *16*, 4630-4.

33. Im, J.-H.; Lee, C.-R.; Lee, J.-W.; Park, S.-W.; Park, N.-G. 6.5% efficient perovskite quantum-dot-sensitized solar cell. *Nanoscale* **2011,** *3*, 4088-4093.

34. Nozik, A. J. Quantum Dot Solar Cells. *Physica E* **2002,** *14*, 115-200.

35. Kongkanand, A.; Tvrdy, K.; Takechi, K.; Kuno, M.; Kamat, P. V. Quantum Dot Solar Cells. Tuning Photoresponse through Size and Shape Control of CdSe-TiO2 Architecture. *J. Am. Chem. Soc.* **2008,** *130*, 4007-4015.

36. Wang, J.; Li, Y.; Shen, Q.; Izuishi, T.; Pan, Z.; Zhao, K.; Zhong, X. Mn doped quantum dot sensitized solar cells with power conversion efficiency exceeding 9%. *J. Mater. Chem. A* **2016,** *4*, 877-886.

37. Carey, G. H.; Abdelhady, A. L.; Ning, Z.; Thon, S. M.; Bakr, O. M.; Sargent, E. H. Colloidal Quantum Dot Solar Cells. *Chem. Rev.* **2015**, *115*, 12732–12763

38. Ren, Z.; Wang, J.; Pan, Z.; Zhao, K.; Zhang, H.; Li, Y.; Zhao, Y.; Mora-Sero, I.; Bisquert, J.; Zhong, X. Amorphous TiO2 Buffer Layer Boosts

Efficiency of Quantum Dot Sensitized Solar Cells to over 9%. *Chem. Mater.* **2015,** *27*, 8398-8405.

39. Sanehira, E. M.; Marshall, A. R.; Christians, J. A.; Harvey, S. P.; Ciesielski, P. N.; Wheeler, L. M.; Schulz, P.; Lin, L. Y.; Beard, M. C.; Luther, J. M. Enhanced mobility $CsPbI_3$ quantum dot arrays for record-efficiency, high-voltage photovoltaic cells. *Sci. Adv.* **2017,** *3*, eaao4204.

40. Pan, Z.; Rao, H.; Mora-Seró, I.; Bisquert, J.; Zhong, X. Quantum dot-sensitized solar cells. *Chem. Soc. Rev.* **2018,** *47*, 7659-7702.

41. Mora-Seró, I. et. al. Nanoscale Interaction between CdSe or CdTe Nanocrystals and Molecular Dyes Fostering or Hindering Directional Charge Separation. *Small* **2010,** *6*, 221–225.

42. Blas-Ferrando, V. M.; Ortiz, J.; González-Pedro, V.; Sánchez, R. S.; Mora-Seró, I.; Fernández-Lázaro, F.; Sastre-Santos, Á. Synergistic Interaction of Dyes and Semiconductor Quantum Dots for Advanced Cascade Cosensitized Solar Cells. *Adv. Funct. Mater.* **2015,** *25*, 3220-3226.

43. Hu, L.; Wang, W.; Liu, H.; Peng, J.; Cao, H.; Shao, G.; Xia, Z.; Ma, W.; Tang, J. PbS colloidal quantum dots as an effective hole transporter for planar heterojunction perovskite solar cells. *J. Mater. Chem. A* **2015,** *3*, 515-518.

44. Etgar, L.; Gao, P.; Qin, P.; Graetzel, M.; Nazeeruddin, M. K. A hybrid lead iodide perovskite and lead sulfide QD heterojunction solar cell to obtain a panchromatic response. *J. Mater. Chem. A* **2014,** *2*, 11586-11590.

45. Seo, G.; Seo, J.; Ryu, S.; Yin, W.; Ahn, T. K.; Seok, S. I. Enhancing the Performance of Sensitized Solar Cells with PbS/CH3NH3PbI3 Core/Shell Quantum Dots. *J. Phys. Chem. Lett.* **2014,** *5*, 2015-2020.

46. Yang, Z.; Janmohamed, A.; Lan, X.; García de Arquer, F. P.; Voznyy, O.; Yassitepe, E.; Kim, G.-H.; Ning, Z.; Gong, X.; Comin, R.; Sargent, E. H. Colloidal Quantum Dot Photovoltaics Enhanced by Perovskite Shelling. *Nano Lett.* **2015,** *15*, 7539-7543.

47. Yang, Z.; Voznyy, O.; Walters, G.; Fan, J. Z.; Liu, M.; Kinge, S.; Hoogland, S.; Sargent, E. H. Quantum Dots in Two-Dimensional Perovskite Matrices for Efficient Near-Infrared Light Emission. *ACS Photonics* **2017,** *4*, 830-836.

48. Gong, X.; Yang, Z.; Walters, G.; Comin, R.; Ning, Z.; Beauregard, E.; Adinolfi, V.; Voznyy, O.; Sargent, E. H. Highly efficient quantum dot near-infrared light-emitting diodes. *Nat. Photonic* **2016,** *10*, 253-257.

49. Liu, C.; Peng, H.; Wang, K.; Wei, C.; Wang, Z.; Gong, X. PbS quantum dots-induced trap-assisted charge injection in perovskite photodetectors. *Nano Energy* **2016,** *30*, 27-35.

50. Garcia de Arquer, F. P. et.al. Field-emission from quantum-dot-in-perovskite solids. *Nat. Commun.* **2017,** *8*, 14757.

51. Moradi, Z.; Fallah, H.; Hajimahmoodzadeh, M. Nanocomposite perovskite based optical sensor with broadband absorption spectrum. *Sens. Actuators, A* **2018,** *280*, 47-51.

52. Jung, Y.-K.; Butler, K. T.; Walsh, A. Halide Perovskite Heteroepitaxy: Bond Formation and Carrier Confinement at the PbS–CsPbBr3 Interface. *J. Phys. Chem. C* **2017,** *121*, 27351-27356.

53. Yang, Y.; Wang, W. Effects of incorporating PbS quantum dots in perovskite solar cells based on CH3NH3PbI3. *J. Power Sources* **2015,** *293*, 577-584.

54. Dang, V. Q.; Byun, M.; Kang, J.; Kim, C.; Jung, P.-H.; Kim, Y.-D.; Lee, N.-E.; Lee, H. Low temperature fabrication of hybrid solar cells using co-sensitizer of perovskite and lead sulfide nanoparticles. *Org. Electron.* **2017,** *50*, 247-254.

55. Sidhik, S.; Esparza, D.; Martínez-Benítez, A.; Lopez-Luke, T.; Carriles, R.; Mora-Sero, I.; de la Rosa, E. Enhanced Photovoltaic Performance of Mesoscopic Perovskite Solar Cells by Controlling the Interaction between CH *J. Phys. Chem. C* **2017,** *121*, 4239-4245.

56. Yang, H.; Zhang, Y.; Hills-Kimball, K.; Zhou, Y.; Chen, O. Building bridges between halide perovskite nanocrystals and thin-film solar cells. *Sustainable Energy & Fuels* **2018,** *2*, 2381-2397.

57. Cha, M.; Da, P.; Wang, J.; Wang, W.; Chen, Z.; Xiu, F.; Zheng, G.; Wang, Z.-S. Enhancing Perovskite Solar Cell Performance by Interface Engineering Using $CH_3NH_3PbBr_{0.9}I_{2.1}$ Quantum Dots. *J. Am. Chem. Soc.* **2016,** *138*, 8581-8587.

58. Ip, A. H. et. al. Hybrid passivated colloidal quantum dot solids. *Nat. Nanotechnol.* **2012,** *7*, 577-582.

59. Dirin, D. N.; Dreyfuss, S.; Bodnarchuk, M. I.; Nedelcu, G.; Papagiorgis, P.; Itskos, G.; Kovalenko, M. V. Lead Halide Perovskites and Other Metal Halide Complexes As Inorganic Capping Ligands for Colloidal Nanocrystals. *J. Am. Chem. Soc.* **2014,** *136*, 6550-6553.

60. Ning, Z.; Dong, H.; Zhang, Q.; Voznyy, O.; Sargent, E. H. Solar Cells Based on Inks of n-Type Colloidal Quantum Dots. *ACS Nano* **2014,** *8*, 10321-10327.

61. Lan, X. et. al. 10.6% Certified Colloidal Quantum Dot Solar Cells via Solvent-Polarity-Engineered Halide Passivation. *Nano Lett.* **2016,** *16*, 4630-4634.

62. Liu, M. et. al. Hybrid organic–inorganic inks flatten the energy landscape in colloidal quantum dot solids. *Nat. Mater.* **2016,** *16*, 258.

63. Kulbak, M.; Gupta, S.; Kedem, N.; Levine, I.; Bendikov, T.; Hodes, G.; Cahen, D. Cesium Enhances Long-Term Stability of Lead Bromide Perovskite-Based Solar Cells. *J. Phys. Chem. Lett.* **2016,** *7*, 167-172.

64. Swarnkar, A.; Marshall, A. R.; Sanehira, E. M.; Chernomordik, B. D.; Moore, D. T.; Christians, J. A.; Chakrabarti, T.; Luther, J. M. Quantum

Dot–Induced Phase Stabilization of α-CsPbI$_3$ Perovskite for High-Efficiency Photovoltaics. *Science* **2016,** *354*, 92-95.

65. Zhang, X.et. al. Inorganic CsPbI3 Perovskite Coating on PbS Quantum Dot for Highly Efficient and Stable Infrared Light Converting Solar Cells. *Adv. Energy Mater.* **2018,** *8*, 1702049.

66. Heo, J. H.; Jang, M. H.; Lee, M. H.; Shin, D. H.; Kim, D. H.; Moon, S. H.; Kim, S. W.; Park, B. J.; Im, S. H. High-Performance Solid-State PbS Quantum Dot-Sensitized Solar Cells Prepared by Introduction of Hybrid Perovskite Interlayer. *ACS Appl. Mater. Interfaces* **2017,** *9*, 41104-41110.

67. Li, S.-S. et. al. Intermixing-seeded growth for high-performance planar heterojunction perovskite solar cells assisted by precursor-capped nanoparticles. *Energy Environ. Sci.* **2016,** *9*, 1282-1289.

68. Han, J.; Luo, S.; Yin, X.; Zhou, Y.; Nan, H.; Li, J.; Li, X.; Oron, D.; Shen, H.; Lin, H. Hybrid PbS Quantum-Dot-in-Perovskite for High-Efficiency Perovskite Solar Cell. *Small* **2018,** *14*, 1801016.

69. Galar, P.; Piatkowski, P.; Ngo, T. T.; Gutiérrez, M.; Mora-Seró, I.; Douhal, A. Perovskite-quantum dots interface: Deciphering its ultrafast charge carrier dynamics. *Nano Energy* **2018,** *49*, 471-480.

70. Luque, A.; Martí, A. Increasing the Efficiency of Ideal Solar Cells by Photon Induced Transitions at Intermediate Levels. *Phys. Rev. Lett.* **1997,** *78* (26), 5014-5017.

71. Luque, A.; Marti, A.; Stanley, C. Understanding intermediate-band solar cells. *Nat. Photonics* **2012,** *6*, 146-152.

72. Blokhin, S. A. et. al. AlGaAs/GaAs photovoltaic cells with an array of InGaAs QDs. *Semiconductors* **2009,** *43*, 514-518.

Chapter IV

Single step deposition of an interacting layer of a perovskite matrix with embedded quantum dots

IV.1. Candidate's contribution

The nature and extent of my contribution to the work in the chapter IV is described following:

Nature of contribution	Extent of contribution
- Synthesis and characterization of PbS core and PbS/CdS core/shell quantum dots (QDs). - Solve the solubility limit of QDs in DMF, common solvent for perovskite preparation. - Prepare perovskite films and devices with embedded QDs. - Characterization of films and devices: absorbance, PLQY, SEM and PL and EL in visible range. - Preparation of the first draft of the manuscript. - Edit the manuscript according to the comments of co-authors and referees. - Write the draft for replying the referees.	80 %

IV.2. Published manuscript

Single Step Deposition of an Interacting Layer of Perovskite Matrix with Embedded Quantum Dots.

Thi Tuyen Ngo,[1] Isaac Suarez,[2] Rafael S. Sanchez,[1] Juan P. Martinez-Pastor,[2] and Ivan Mora Sero[1,*]

[1] Institute of Advanced Materials (INAM), UniversitatJaume I, 12006 Castelló, Spain.
[2] UMDO, Instituto de Ciencia de los Materiales, Universidad de Valencia, 46071 Valencia, Spain.

[*] Corresponding authors: sero@uji.es

ABSTRACT.
Hybrid lead halide perovskite derivatives (HP) have emerged as very promising materials for the development of optoelectronic devices in the last few years. At the same time, inorganic nanocrystals with quantum confinement (QDs) possess unique properties that make them suitable materials for the development of photovoltaics, imaging and lighting applications, among others. In this work, we report on a new methodology for the deposition of high quality, large grain size and pinhole free HP films ($CH_3NH_3PbI_3$, termed MAPI) with embedded PbS and PbS/CdS core/shell Quantum Dots (QDs). The strong interaction between both semiconductors is revealed by the formation of an exciplex state, which is monitored by photoluminescence and electroluminescence experiments. The radiative exciplex relaxation is centered in the near infrared region (NIR), ≈ 1200 nm, which correspond to lower energies than the corresponding band gap of both perovskite (HP) and QDs themselves. Our approach allows fabricating multi-wavelength light emitting diodes (LEDs) based on a HP matrix with embedded QDs, which show considerably low turn-on potentials. The presence of the exciplex state of HP and QDs opens up a broad range of possibilities with important implications in both LEDs and solar cells.

TOC Figure:
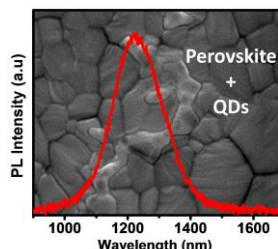
High quality pinhole free perovskite halide thin layer exhibiting IR exciplex state emission have been prepared introducing Pb/CdS QDs in single step deposition process.

Nowadays, the research focused on the development and applicability of hybrid lead halide perovskite materials (HP) probably constitutes the hottest topic in the photovoltaics field due to several reasons. Firstly, certified photoconversion efficiencies (PCEs) as high as 22.1% have been reported so far.[1] Moreover, the impressive rise in the conversion efficiencies has been reached only few years after the first reports on HP based liquid electrolyte solar cells in 2009.[2] Very importantly, it has been demonstrated that HP shows reduced non-radiative recombination pathways; this fact has significantly contributed to reach high PCEs.[3, 4] Additionally, the application of HP derivatives for the development of light emitting devices,[5] as LEDs,[6-8] light amplifiers[9] or lasers,[10-12] has been already demonstrated, which is a consequence of the outstanding properties of these materials. It is worth pointing out that HP can be prepared from solution methods at low processing temperatures and, consequently, using low cost fabrication techniques. Furthermore, HP can be easily combined with other materials as colloidal Quantum Dots (QDs),[13, 14]which can induce interesting synergies, thus giving rise to new properties or phenomena that do not exist for the single materials.

Colloidal QDs constitute a very interesting family of nanomaterials that have been extensively studied for optoelectronic applications during the last two decades due to their size-tunable bandgap, relatively facile synthesis, high monodispersity, and the possibility of being processed in solution.[15-18] Despites the high potentiality of developing advanced optoelectronic systems by exploiting the combination of HP and QDs, there are only few examples in the literature reporting on these issues; PbS QDs combined with HP has been the most general system studied so far.

Particularly, precedents in the literature report on the utilization of HP as a capping agent of QDs, thus providing QD/HP core/shell structures,[19-21]which have shown outstanding efficiencies, close to 9%, in colloidal QD solar cell configuration.[19] PbS QDs have been deposited on perovskite layers for photovoltaic applications, which enhances the light harvesting at IR wavelengths and therefore, the photogenerated short-circuit current (J_{sc}).[22, 23] However a more intimate interaction between HP and QDs has been obtained by the preparation of layers that consists of a HP matrix with embedded QDs using two-step spin coating method.[13] This approach has an enormous potentiality for the development of different optoelectronic devices. Highly efficient QD based near-infrared light-emitting diodes have been obtained by combining a HP matrix with PbS QDs with good lattice matching that forms a type I junction.[24] In addition, PbS QDs have been also used as efficient seeds for the preparation high-performance planar heterojunction perovskite solar cells.[25] We have recently analyzed the interaction between HP and PbS/CdS core-shell QDs bilayers that form a type II junction.[14] More specifically, we reported on the identification of an exciplex emission that results from the strong interaction between both semiconductors films, by means of optical pumping and electrical injection at energies lower than the bandgap of the single materials. As a continuation of our previous work, we envisaged that this effect could be much more pronounced if the QDs were inserted into the HP films instead of stacking layers of the corresponding single materials. Therefore, in the present paper we propose a novel one step spin coating method to produce a nanocomposite that consists of either core PbS or core/shell PbS/CdS QDs embedded into a HP matrix. This method permits to obtain very uniform HP-QDs layers, with significantly larger HP grain size, compared to bare HP (reference sample), which clearly exhibit exciplex emission.

PbS/CdS core/shell QDs were generally synthesized using oleic acid (OA) that controls the dimension of QDs and prevents their aggregation. However OA-capped QDs are not soluble in dimethylformamide (DMF), which is the commonly employed solvent to dissolve the HP precursor, and therefore a ligand exchange treatment becomes necessary to overcome this solubility limitation. Fig. IV.1a shows the ligand exchange processes. Core/shell PbS/CdS QDs capped with OA ligands were originally dispersed in octane, and mixed with a DMF solution containing HP precursors (PbI$_2$ and CH$_3$NH$_3$I). In this step, two separated phases were detected: QDs dispersed in octane on the top and HP dissolved in DMF at the bottom (Bottle 1). After stirring the mixed solution, OA is replaced by a CH$_3$NH$_3$PbI$_3$ (MAPI) HP capping and QDs were transferred into DMF phase

with perovskite precursors (dark phase, Bottle 2). HP capped QDs were precipitated with toluene, dried and finally dispersed in a solution containing the HP precursors (HP-QDs solution, Bottle 3) that will be used for the spin coating deposition of the HP with embedded QDs films (see the details in the experimental part see Supporting Information). The absorbance and photoluminescence (PL) in solution of HP capped QDs is red shifted (see Fig. IV.S1a and IV.S1b) and the PL quantum yield is significantly reduced after ligand exchange, from 18% to 0.9% see Fig. IV.S1b.
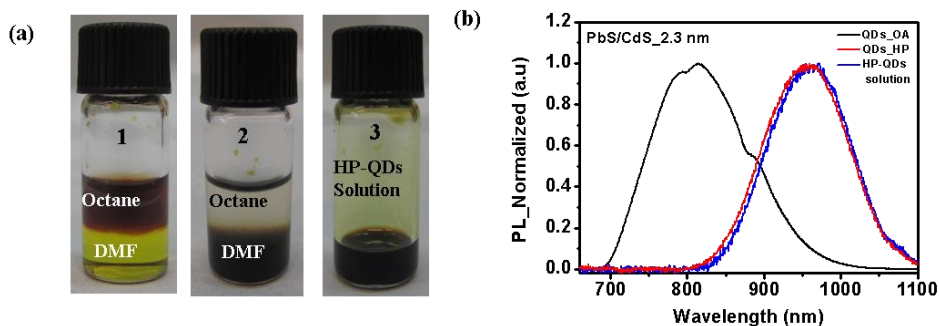
Fig IV.1. (a) Pictures of the different phases of QD ligand exchange process. Bottle 1: two phase solution formed by DMF with perovskite precursors at the bottom and PbS/CdS core/shell QDs capped with OA dissolved in octane on the top. Bottle 2: after 30 minutes stirring, the QDs were transferred into DMF since OA was exchanged by a HP shell. Bottle 3: HP capped QDs were precipitated with toluene, dried and finally dispersed in a DMF solution containing HP precursors (PbI2 and CH3NH3I, 1:1molar ratio); this solution is used for the deposition of perovskite layer with embedded QDs. (b) Photoluminescence spectra of PbS/CdS QDs in solution before (OA capped), after ligand exchange (HP capped) and the final HP-QDs solutions ($\lambda_{excitation}$ = 650 nm).

Fig. IV.1b shows the PL spectra of the QDs solutions before (OA capped) and after ligand exchange (HP capped). The PL peak after ligand exchange was red shifted depending on the QD size, being150 nm for QDs of 2.3 nm in diameter (from 812 nm to 962 nm, Fig IV.1b and Fig IV.S1c) and 83 nm for QDs of 3 nm in diameter (from 893 nm to 976 nm, Fig. IV.S1d), thus indicating that this effect is more significant for the smaller sized QDs, which is in good correlation with previous reports.[20] HP capping allows the wave function to spread out of QDs, thus reducing the quantum confinement that provokes the strong red-shift. The PL emission of the QD/HP nanocrystals dispersed in the HP solution (HP-QDs solution) did not vary compared to that resulting from dispersing QD/HP in DMF, see Fig. IV.1b, IV.S1c and IV.S1d. This fact indicates that HP shell does not dissociated into the corresponding precursors or does not suffer from chemical variations after being dispersed in DMF, which demonstrates the

robustness of the HP shell. The PLQY of HP-QDs solution was calculated as a function of QD concentration, which decreases linearly from 1.6% to 1% when QD concentration was increased from 200 to 400 mg/ml (Fig. IV.S2).

HP and HP-QDs films were spin coated onto compact TiO_2 at 9000 rpm from the HP and HP-QDs solutions, respectively inside a glove box. The films were annealed at 65ºC for 1 minute and subsequently at 100ºC during 2 minutes. Very homogenous, pinhole free morphology was obtained for both HP and HP-QDs films (Fig. IV.2a and IV.2b respectively). The introduction of QDs in the solution containing the perovskite precursors has a dramatic effect of on the grain size, which is increased in 4-5 fold. These results point to the significant role of the QDs on the nucleation of the HP crystals, as it has been recently reported.[25] The increase of grain size produced a slight red shift, around 4 nm in the HP emission (Fig. IV.S3). This shift could be attributed to the increase of perovskite grain size.[26] Very interestingly, crystal grains with a size similar to the layer thickness are obtained (see Figs. IV.2c and IV.2d), which is a crucial aspect for obtaining high performance optoelectronic devices. The presence of QDs also produces an increase of the film thickness (see Fig. IV.S4), from 210 nm (HP film without QDs) to 365 and 420 nm, when QDs are dispersed in HP solutions with concentrations of 300 and 400 mg/ml, respectively. Independently of the thickness, very homogeneous films are obtained for the different conditions used with our novel preparation methodology.

Fig. IV.3 shows that HP layers with embedded QDs exhibit the PL emission band ascribed to the exciton recombination in the HP, but no additional QD contribution is observed within the comprised spectral range (Fig IV.3a). However, these composite films exhibit a strong exciplex emission (≈ 1.02 eV) that is at a lower energies than the bandgaps of the corresponding single semiconductors, as shown in Fig IV.3b. As we reported previously, the observed exciplex relaxation corresponds to the radiative recombination of electrons from the conduction band (CB) of HP with those holes present in the valence band (VB) of QDs.[14]
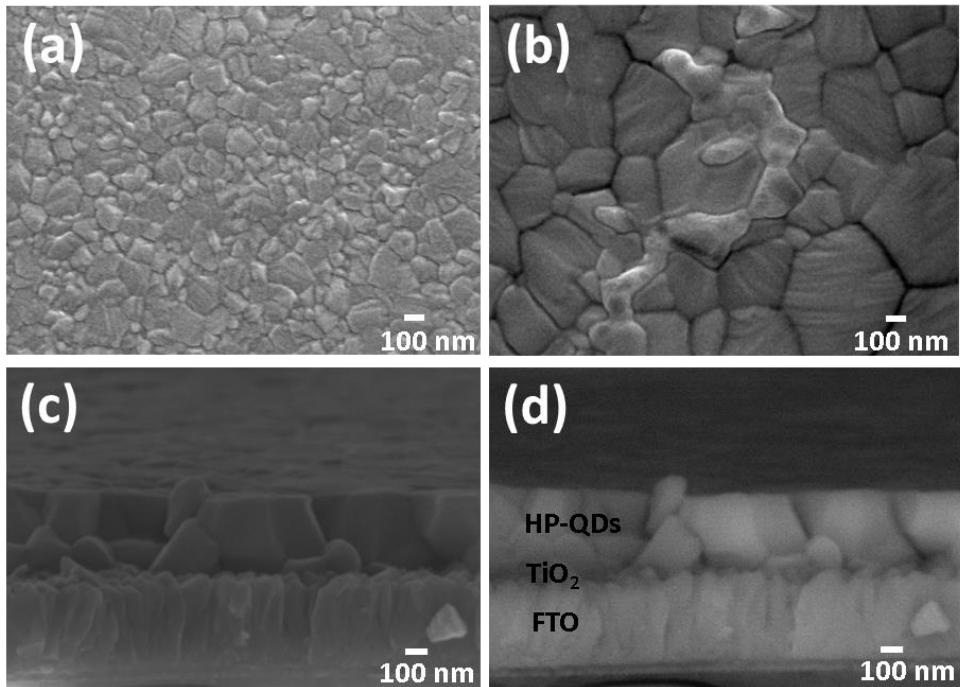
Fig IV.2. SEM secondary electron images of the top view of HP films **(a)**without and **(b)** with PbS/CdS core/shell QDs 2.3 nm with the concentration of 300 mg/ml. Cross section image of (b) sample using **(c)** secondary electrons and **(d)** backscattered electrons that allows a clearer distinction among the different layers.
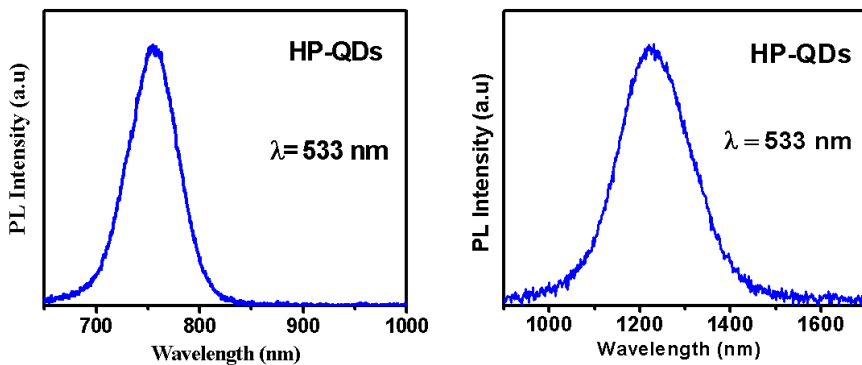
Fig IV.3. Room temperature PL spectra at **(a)** 600-1000 nm (Si photodetector) and **(b)** 900-1700 nm (InGaAs photodetector) wavelength ranges of HP-QDs (PbS/CdS 2.3 nm in diameter) film in which HP capped QDs were added in the solution of HP with a concentration of 300 mg/ml. The HP-QDs films were spin coated at 9000 rpm and annealed at 65°C for 1 minute and then at 100°C during 2 minutes.

In addition to optical pumping, electronic injection (electroluminescence, EL) was also investigated by the preparation of complete LED devices based on the configuration depicted in Fig. IV.4a; using a compact TiO_2 layer and spiro-OMeTAD as electron and hole injecting layers, respectively.[6] For those devices containing QDs, three EL emission signals that correspond to direct exciton recombination in HP and QDs (Fig. IV.4b) and the indirect HP-QD exciplex (Fig IV.4c) are observed, respectively. Note that there is a slight shift in the exciplex peak position comparing Fig. IV.4c with Fig. IV.3b, which arises from small variations of the QD size distributions from batch to batch syntheses. It is worth highlighting that the EL signal of the HP moiety of the HP-QDs composite sample is quenched by approximately one order of magnitude (see Figs. IV.S5, IV.S6, IV.S7a) compare to the reference sample without embedded QDs. Moreover, QD EL intensity increases as the applied voltages increases, and this signal enhancement is even more evident at lower QD concentration (Fig. IV.S7b). In addition, the position of QD emission was dependent on the QD concentration in the HP-QDs solution; more specifically the quenching of HP emission is expected from the type II junction, as already reported in our previous study based on HP-QDs bilayers (Fig. IV.S8),[14] which in turn promotes the origin of the exciplex state (Fig. IV.4c).
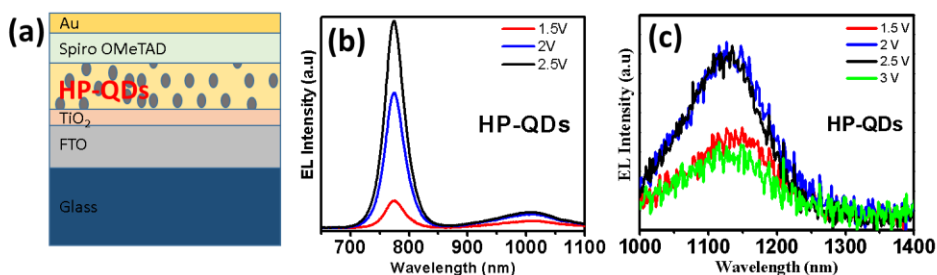
Fig IV.4. (a) Schematic of the LED configuration. Electroluminescence at **(b)** 600-1100 nm (Si photodetector) and **(c)** 1000-1400 nm (InGaAs photodetector) wavelength range of HP-QDs devices at different applied voltages with PbS/CdS core/shell 2.3 nm QDs (300 mg/ml) embedded in HP matrix. HP-QDs film was spin coated at 9000 rpm then annealed at 65°C for 1 minute and at 100°C during 2 minutes.

Finally, the samples prepared with embedded single core PbS QDs are compared to those devices prepared with PbS/CdS core/shell QDs (see Fig. IV.S9). Briefly, the OA ligands of the PbS core were exchanged with a HP shell, following the same procedures as for the PbS/CdS core/shell QDs (including the concentration of these QDs in the solution of HP). In

agreement with our previous work,[27] the CdS shell induces a notable enhancement of the EL signal, not only from the QDs but also from the HP, as one would expect from the efficient passivation of the surface states (Fig. IV.S9).

In summary, we have developed a new method for producing HP layers with embedded core and core/shell QDs that yields highly homogeneous, low roughness and pinhole free HP-QDs composite films. The introduction of embedded QDs has a dramatic effect on the perovskite crystal grains, whose size is enlarged by a 4-5 fold factor, compared to the reference samples without QDs; it is worth mentioning that the crystal size measured for HP-QDs films is in the same order of magnitude as the overall layer thickness. Very importantly, the strong interaction between HP and the embedded QDs is promoting the emission from HP-QDs exciplex; therefore, our approach constitutes a valuable proof of concept on the coupling of these two important families of materials. In particular, exploiting our methodology and device configuration constitutes a suitable tool for producing intimately packed films, where the interaction between HP and QDs can be induced and monitored by applying both optical pumping and electrical injection. The development of high quality layers and devices that not only show optical but also electrically induced exciplex states, opens up a highly interesting scenario for the development of new and advanced optoelectronic devices; from wavelength tunable LEDs to intermediate bandgap solar cells.

REFERENCES

1.   http://www.nrel.gov/ncpv/images/efficiency_chart.jpg
2.   A. Kojima, K. Teshima, Y. Shirai and T. Miyasaka, *J. Am. Chem. Soc.*, 2009, **131**, 6050-6051.
3.   W. Tress, N. Marinova, O. Inganäs, M. K. Nazeeruddin, S. M. Zakeeruddin and M. Graetzel, *Adv. Energy Mater.*, 2015, **5**, n/a-n/a.

4. D. Bi, W. Tress, M. I. Dar, P. Gao, J. Luo, C. Renevier, K. Schenk, A. Abate, F. Giordano, J.-P. Correa Baena, J.-D. Decoppet, S. M. Zakeeruddin, M. K. Nazeeruddin, M. Grätzel and A. Hagfeldt, *Science Advances*, 2016, **2**, e1501170.

5. B. R. Sutherland and E. H. Sargent, *Nat Photon*, 2016, **10**, 295-302.

6. O. A. Jaramillo-Quintero, R. S. Sanchez, M. Rincon and I. Mora-Sero, *J. Chem. Phys. Lett.*, 2015, **6**, 1883-1890.

7. Z.-K. Tan, R. S. Moghaddam, M. L. Lai, P. Docampo, R. Higler, F. Deschler, M. Price, A. Sadhanala, L. M. Pazos, D. Credgington, F. Hanusch, T. Bein, H. J. Snaith and R. H. Friend, *Nat Nano*, 2014, **9**, 687-692.

8. H. Cho, S.-H. Jeong, M.-H. Park, Y.-H. Kim, C. Wolf, C.-L. Lee, J. H. Heo, A. Sadhanala, N. Myoung, S. Yoo, S. H. Im, R. H. Friend and T.-W. Lee, *Science*, 2015, **350**, 1222-1225.

9. I. Suárez, E. J. Juárez-Pérez, J. Bisquert, I. Mora-Seró and J. P. Martínez-Pastor, *Adv. Mater.*, 2015, **27**, 6157-6162.

10. G. Xing, N. Mathews, S. S. Lim, N. Yantara, X. Liu, D. Sabba, M. Grätzel, S. Mhaisalkar and T. C. Sum, *Nat Mater*, 2014, **13**, 476-480.

11. F. Deschler, M. Price, S. Pathak, L. E. Klintberg, D.-D. Jarausch, R. Higler, S. Hüttner, T. Leijtens, S. D. Stranks, H. J. Snaith, M. Atatüre, R. T. Phillips and R. H. Friend, *J. Chem. Phys. Lett.*, 2014, **5**, 1421-1426.

12. H. Zhu, Y. Fu, F. Meng, X. Wu, Z. Gong, Q. Ding, M. V. Gustafsson, M. T. Trinh, S. Jin and X. Y. Zhu, *Nat Mater*, 2015, **14**, 636-642.

13. Z. Ning, X. Gong, R. Comin, G. Walters, F. Fan, O. Voznyy, E. Yassitepe, A. Buin, S. Hoogland and E. H. Sargent, *Nature*, 2015, **523**, 324-328.

14. R. S. Sanchez, M. S. de la Fuente, I. Suarez, G. Muñoz-Matutano, J. P. Martinez-Pastor and I. Mora-Sero, *Science Advances*, 2016, **2**, e1501104.

15. P. V. Kamat, *J. Phys. Chem. C*, 2008, **112**, 18737–18753.

16. S. A. McDonald, G. Konstantatos, S. Zhang, P. W. Cyr, E. J. D. Klem, L. Levina and E. H. Sargent, *Nat Mater*, 2005, **4**, 138-142.

17. A. J. Nozik, M. C. Beard, J. M. Luther, M. Law, R. J. Ellingson and J. C. Johnson, *Chem. Rev.*, 2010, **110**, 6873-6890.

18. G. H. Carey, A. L. Abdelhady, Z. Ning, S. M. Thon, O. M. Bakr and E. H. Sargent, *Chem. Rev.*, 2015.

19. Z. Yang, A. Janmohamed, X. Lan, F. P. García de Arquer, O. Voznyy, E. Yassitepe, G.-H. Kim, Z. Ning, X. Gong, R. Comin and E. H. Sargent, *Nano Lett.*, 2015, **15**, 7539-7543.

20. D. N. Dirin, S. Dreyfuss, M. I. Bodnarchuk, G. Nedelcu, P. Papagiorgis, G. Itskos and M. V. Kovalenko, *J. Am. Chem. Soc.*, 2014, **136**, 6550-6553.

21. G. Seo, J. Seo, S. Ryu, W. Yin, T. K. Ahn and S. I. Seok, *J. Chem. Phys. Lett.*, 2014, **5**, 2015-2020.

22.   L. Etgar, P. Gao, P. Qin, M. Graetzel and M. K. Nazeeruddin, *Journal of Materials Chemistry A*, 2014, **2**, 11586-11590.

23.   L. Hu, W. Wang, H. Liu, J. Peng, H. Cao, G. Shao, Z. Xia, W. Ma and J. Tang, *Journal of Materials Chemistry A*, 2015, **3**, 515-518.

24.   X. Gong, Z. Yang, G. Walters, R. Comin, Z. Ning, E. Beauregard, V. Adinolfi, O. Voznyy and E. H. Sargent, *Nat Photon*, 2016, **10**, 253-257.

25.   S.-S. Li, C.-H. Chang, Y.-C. Wang, C.-W. Lin, D.-Y. Wang, J.-C. Lin, C.-C. Chen, H.-S. Sheu, H.-C. Chia, W.-R. Wu, U. S. Jeng, C.-T. Liang, R. Sankar, F.-C. Chou and C.-W. Chen, *Energy & Environmental Science*, 2016, **9**, 1282-1289.

26.   V. D'Innocenzo, A. R. Srimath Kandada, M. De Bastiani, M. Gandini and A. Petrozza, *Journal of the American Chemical Society*, 2014, **136**, 17730-17733.

27.   R. S. Sanchez, E. Binetti, J. A. Torre, G. Garcia-Belmonte, M. Striccoli and I. Mora-Sero, *Nanoscale*, 2014, **6**, 8551-8555.

Single Step Deposition of an Interacting Layer of Perovskite Matrix with Embedded Quantum Dots.

Thi Tuyen Ngo,[1] Isaac Suarez,[2] Rafael S. Sanchez,[1] Juan P. Martinez-Pastor,[2] and Ivan Mora Sero[1],*

[1] Institute of Advanced Materials (INAM), Universitat Jaume I, 12006 Castelló, Spain.
[2] UMDO, Instituto de Ciencia de los Materiales, Universidad de Valencia, 46071 Valencia, Spain.

* Corresponding authors: sero@uji.es

Experimental Section:

TiO$_2$ compact layer: SnO$_2$:F (FTO) substrates were cleaned with soap, sonicated in distilled water, ethanol and a mixture of acetone/isopropanol (30:70 v/v ratio) for 15minutes and then treated with aUV−O$_3$ lamp for 15minutes. The TiO$_2$ compact layer was deposited by spray pyrolysis at 450°C, consuming 28ml of a solution of titanium di-isopropoxide bis(acetylacetonate), 75% vol. 2-propanol, in absolute ethanol (1:39, v/v ratio); the films were annealed at 450°C for 30 minutes.

PbS/CdS QD synthesis and Ligand exchange: Core/shell QDs were synthesized according to procedure previously reported.[26] Briefly, for the synthesis of 2.3-nm PbS nanocrystals, a three-necked round-bottom flask containing 0.9 g (4 mmol) of PbO, 2.0 g (7 mmol) of Oleic acid and 36 ml of 1-octadecene (ODE) was heated up to 150°C under N$_2$ to form Pb-oleate moieties. The solution was degassed for 30 minutes under vacuum, and 3 ml (6.7 mmol) of trioctylphosphine (90%) was injected. Then the temperature was reduced to 110°C and a mixture of 0.42 ml (2 mmol) of hexamethyldisilathiane (HMDS) and 4 ml ODE was quickly injected to the flask. The temperature of solution was left to decrease to room temperature.

The reaction product was cleaned three times with ethanol/acetone (1:1, v/v), centrifuged (3000 rpm for 10 minutes) and dispersed in toluene (100 mg/ml).

For the growth of CdS shell, 0.44 g (3.4 mmol) of CdO and 2.4 g (8.5 mmol) of OA and 40 ml of ODE was heated at 220°C under air to dissolve CdO, cooled down to 150°C and then degassed for 1 hour under vacuum and the temperature was then reduced to 70°C. Next, 5 ml of as-prepared PbS QDs (100 mg/ml) was rapidly injected and after 5 minutes of reaction at 70°C, the temperature was decreased by adding the nonsolvent mixture (ethanol/acetone, 1:1, v/v). The product was washed following the same washing steps as for PbS nanocrystals.

For the synthesis of 3-nm PbS/CdS core/shell QDs, an identical procedure was applied for the synthesis of 2.3 nm QDs, however 2.7 g (9.6 mmol)of OA was used for PbS formation and 0.34 g(2.6 mmol) of CdO and 1.85 g (6.5 mmol)of OA were used for the growth of CdS shell.

For ligand exchange, 1 ml of QDs (PbS or PbS/CdS core/shell) dispersed in octane (10 mg/ml) was added into 1 ml of dimethylformamide (DMF) solution containing 117 mg of PbI_2 and 50 mg of MAI (CH_3NH_3I).[13] After stirring for 30 minutes, QDs had transferred from the top octane phase to the bottom DMF, see Fig. IV.1a. After removing the octane, the QD solution was washed three more times using octane to remove the organic residue. Subsequently, the QDs were precipitated by the addition of toluene. After removing all the liquid, QDs were dried under vacuum for several hours then dispersed in the solution of HP.

Perovskite solution: 622 mg (1.35 mmol) of PbI_2 were added in the solution containing 1ml of DMF and 95 µl of dimethyl sulfoxide (DMSO). This solution was heated at 65°C to dissolve PbI_2, then cooled down to room temperature. Subsequently, the PbI_2 solution was poured into a vial containing 215 mg (1.35 mmol) of MAI to obtain the final solution for the perovskite deposition.[27]

Perovskite-QDs solution: QDs ligand exchanged were dispersed in the solution of HP with the concentration varying from 200 to 400 mg/ml.

Film deposition: HP and HP-QDs layers were spin coated on TiO_2substrates from the corresponding HP and HP-QDs solutions, at different spin rates to obtain different layer thicknesses. Diethylether was

added to the film when the spin coater was running. HP and HP-QDs films were annealed during 1 minute at 65°Cand then, 2 minutes at 100°C.

Spiro OMeTAD and Gold: Spiro OMeTAD solution was prepared by dissolving 72.3 mg of spiro-OMeTAD (2,2′,7,7′-tetrakis(N,N-di-p-methoxyphenylamine)-9,9-spirobifluorene in 1 ml of chlorobenzene, then mixed with 28.8 µl of 4-tert-butylpyridine and 17.5 µl of a stock Li⁺ solution (which contained 520 mg/ml bis-trifluoromethylsulfonylamine lithium salt in acetonitrile). Spiro OMeTAD layer was spin coated on HP or HP-QDs films at 4000 rpm for 30s. Finally, 60 nm of gold were thermally evaporated in an ultrahigh vacuum chamber on top of Spiro OMeTAD layer to make complete devices.[6]

Characterization of samples in solution, on film, and devices: The morphology of the films was analyzed by scanning electron microscopy (SEM) using a JSM7001F (Field emission scanning electron microscope). The absorbance and photoluminescence (PL) spectra of the QDs in solution, before and after ligand exchange, were obtained by using a spectrophotometer based on a CCD detector (Andor-iDUSDV420A-OE) coupled with a spectrograph as a diffraction grating (Newport 77400). A commercial continuous laser diode (650 nm, 5 mW) was used as an excitation source. Photoluminescence (PL) experiments for films were carried out by pumping the surface of the samples with a 533 nm DSPP (diode pumped solid state) laser and a 780 nm semiconductor diode. Back scattered PL was then collected with the aid of a microscope objective and dispersed in an Ocean Optics HR4800 and NIRQUEST512 spectrographs at visible (400-1000 nm) and infrared wavelengths (900-1700 nm), respectively. EL experiments were performed by applying an electric field in the HP-QD layer integrated in a diode configuration and collecting the emission of the film with a similar set-up (objective lens and spectrograph). Measurements have been carried out using a non-sealed sample holder. Sample holder has a gas connection to flow N_2 continuously during the EL measurements.

Quantum yield calculation. PLQY in solution was calculated from the equation below:

$$PLQY_s = PLQY_{Ref} \frac{Abs_{ref}}{Abs_s} \frac{I_s}{I_{ref}} \left(\frac{n_s}{n_{ref}} \right)^2$$

In which, *s* and *ref* mean sample and reference respectively. *Abs* is the value of absorbance at 650 nm, and *I* is the integrated PL of solution which is excited by 650 nm – laser diode. *n* is the refractive index of solvent.

Commercial Indocyanine green (reference) and original QDs (capped with OA ligand) were dispersed in methanol and toluene, respectively. After ligand exchange, HP capped QDs were dispersed in DFM without HP precursors (QDs_HP solution) and with HP precursors with the concentration varying from 200 to 400 mg/ml (HP-QDs solutions). Very low volume of each solution was taken and diluted in its corresponding solvent to obtain the value of absorbance close to 0.1 at 650 nm. PL spectra was measured using a commercial continuous laser diode (650 nm, 5 mW).
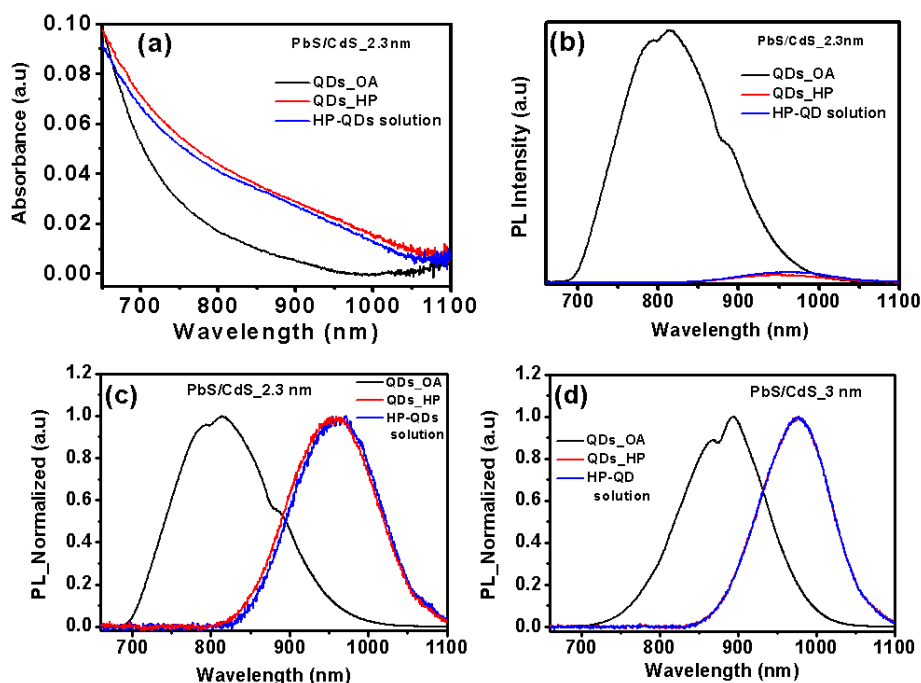
Fig IV.S1. Solution absorbance **(a)** and Photoluminescence (PL) spectra **(b)** for PbS/CdS core/shell QDs 2.3 nm diameter size. Normalized PL for PbS/CdS core/shell QDs of 2.3 nm **(c)** and 3 nm size. **(d)** Spectra before (OA capped) and after ligand exchange with perovskite precursors (HP capped) and of the final HP-QDs solutions are plotted ($\lambda_{excited}$ = 650 nm).
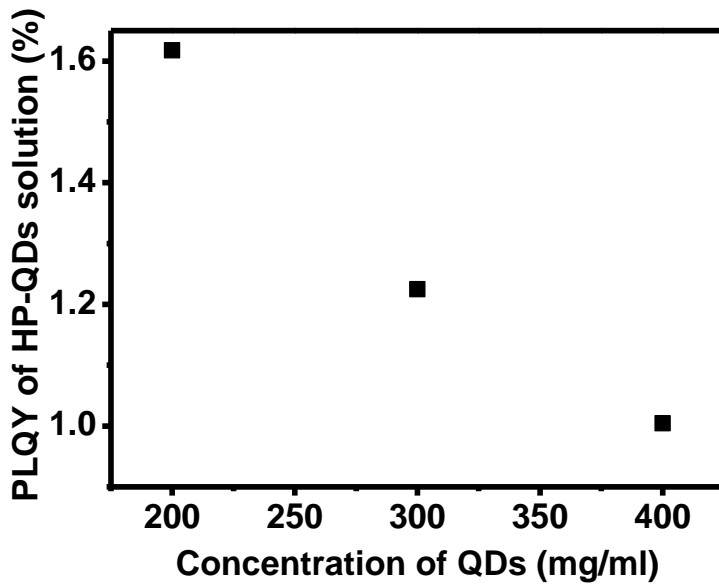
Fig IV.S2. Quantum Yield of perovskite solution containing different QD concentration.
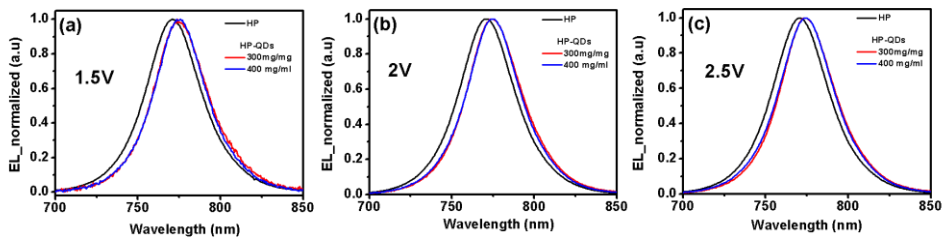
Fig IV.S3. Normalized EL at HP emission of LED devices without QDs (HP) and with PbS/CdS core/shell 2.3 nm QDs (HP-QDs) with the concentration of 300 mg/ml and 400 mg/ml at different applied bias. HP and HP-QDs films were spin coated at 9000 rpm and annealed at 65ºC for 1 minute then at 100ºC during 2 minutes.
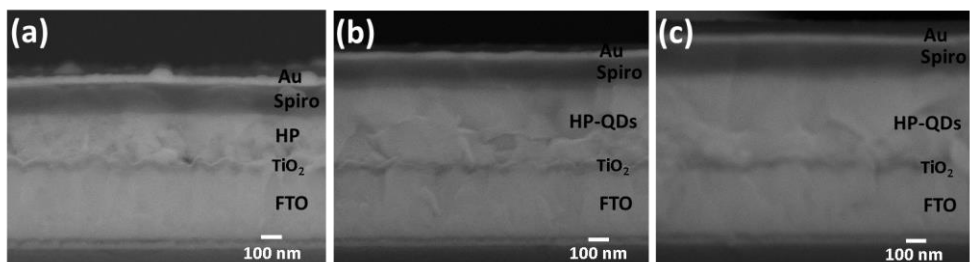
Fig IV.S4. Cross section SEM images from backscattered electrons of LED devices **(a)** without QDs and with different concentrations of PbS/CdS core/shell QDs 2.3 nm: **(b)** 300 mg/ml and **(c)** 400 mg/ml. Concentration of perovskite precursors was kept constant, all HP and HP-QDs films were spin coated at 9000 rpm and annealed at 65°C in 1 minute then at 100°C in 2 minutes
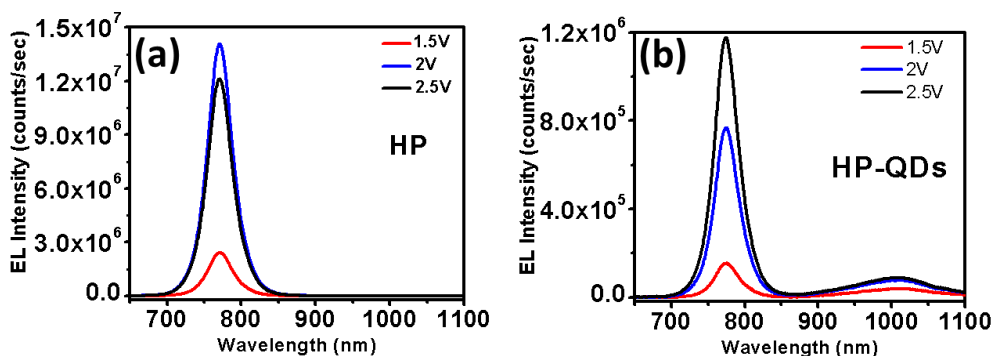
Fig IV.S5. Electroluminescence of LED devices **(a)** without QDs **(b)** and with PbS/CdS core/shell 2.3 nm QDs with the concentration of 300 mg/ml at different applied bias. HP and HP-QDs films were spin coated at 9000 rpm and annealed at 65°C for 1 minute then at 100°C during 2 minutes.
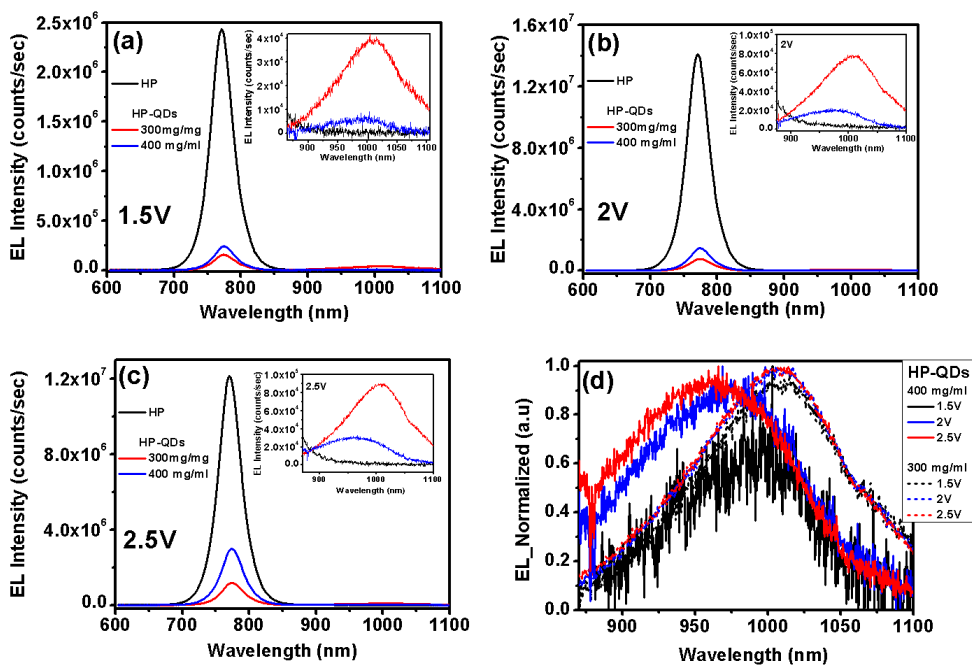
Fig IV.S6. Electroluminescence of LED devices based on $CH_3NH_3PbI_3$ (MAPI) perovskite (HP) and HP-QDs absorbers at different applied voltages **(a, b, c)** and normalized EL intensity of QD emission signal **(d)**. In which HP capped QDs were dispersed in HP solution with concentration of 300 and 400 mg/ml. HP and HP-QDs films were spin coated at 9000 rpm and annealed at 65°C for 1 minute then at 100°C during 2 minutes.
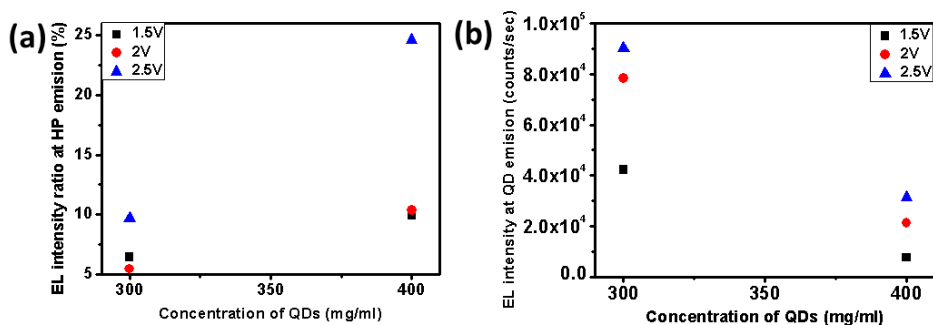
Fig IV.S7. (a) The EL intensity ratio at the HP emission maximum of HP-QDs samples versus reference samples (without embedded QDs), whose EL intensity was normalized to 100%. **(b)** EL intensity of HP-QD devices at the emission maximum of QDs as a function of QD concentration.
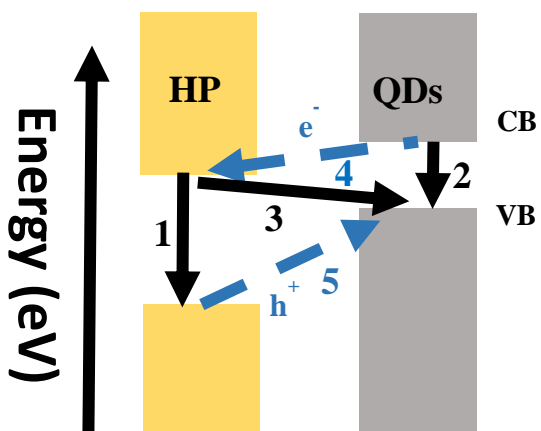
Fig IV.S8. Proposed relative energy diagram. Solid arrows indicate the emission and dotted arrows indicate the charge carrier transfers.
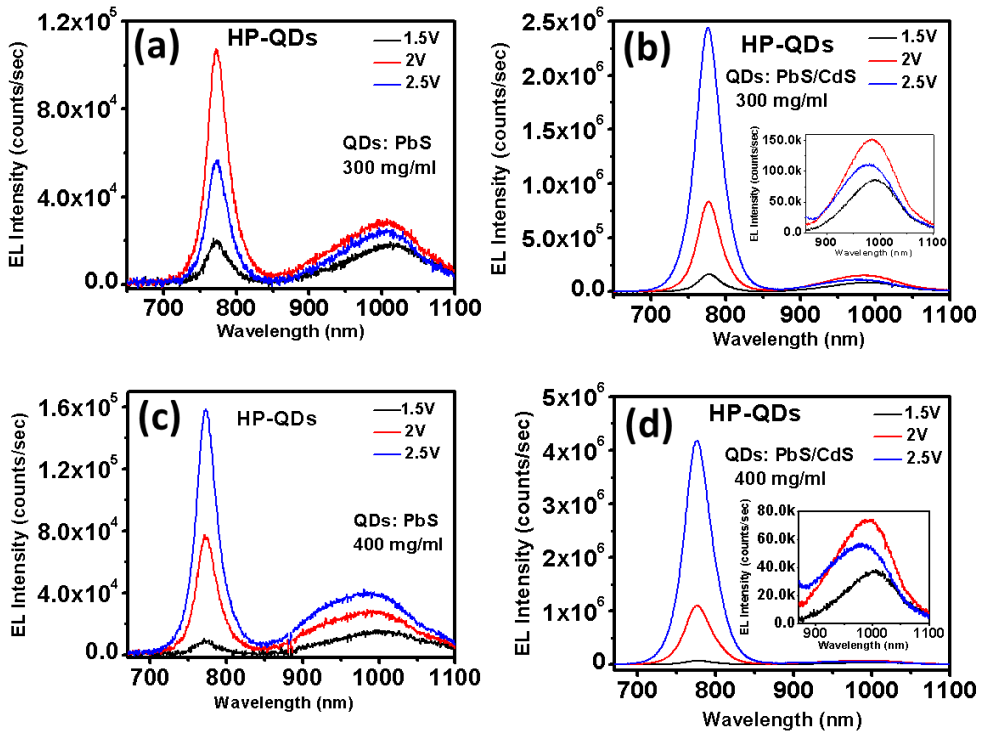
Fig IV.S9. Electroluminescence HP-QDs devices at different applied voltages in **(a, c)** with PbS core 2.3nm QDs and **(b, d)** PbS/CdS core/shell 2.3 nm QDs embedded **(a, b)** QD concentration of 300 mg/ml and **(c, d)** 400 mg/ml. All the HP-QDs films were spin coated at 5000 rpm and annealed at 65°C for 1 minute then at 100°C during 2 minutes.

Chapter V

PbS Quantum Dots as Additives in Methylammonium Halide Perovskite Solar Cells: the Effect of Quantum Dot Capping

V.1. Candidate's contribution

The nature and extent of my contribution to the work in the chapter V is described following:

Nature of contribution	Extent of contribution
- Synthesis and characterization of PbS quantum dots (QDs). - Ligand-exchange of QDs from oleic acid capping ligands to other different ligands. - Preparation of perovskite films and devices with embedded QDs. - Characterization of films and devices. - Preparation of the first draft of the manuscript. - Edit the manuscript according to the comments of co-authors and referees - Write the draft for replying the referees	80 %

V.2. Submitted manuscript

PbS Quantum Dots as Additives in Methylammonium Halide Perovskite Solar Cells: the Effect of Quantum Dot Capping

Thi Tuyen Ngo,[1] Sofia Masi,[1] Perla F. Mendez,[1,2] Miri Kazes,[3] Dan Oron,[3] and Iván Mora Seró[1*]

[1] Institute of Advanced Materials (INAM), Jaume I University, 12006 Castellón, Spain
[2] Facultad de Ciencias Químico Biológicas, Universidad Autónoma de Sinaloa, Cd. Universitaria, Av. de las Américas y Josefa Ortiz S/N, 80000, Culiacán, Sinaloa, México
[3] Department of Physics of Complex Systems, Weizmann Institute of Science, Rehovot 76100, Israel

*Corresponding Authors: sero@uji.es

Abstract

Colloidal PbS quantum dots (QDs) have been successfully employed as additives in Halide Perovskite Solar Cells (PSCs) acting as nucleation centers in the perovskite crystallization process. For this strategy, the surface functionalization of the QD, controlled via the use of different capping ligands, is likely of key importance. In this work, we examine the influence of the PbS QD capping on the photovoltaic performance of methylammonium lead iodide PSCs. We test PSCs fabricated with PbS QDs additives with different capping ligands including methylammonium lead iodine (MAPI), cesium lead iodine (CsPI) and 4-aminobenzoic acid (ABA). Both the presence of PbS QDs and the specific capping used have a significant effect on the properties of the deposited perovskite layer, which affects, in turn, the photovoltaic performance. For all capping ligands used, the inclusion of PbS QDs leads to the formation of perovskite films with larger grain size, improving in addition the crystalline preferential orientation and the crystallinity. Yet differences between capping agents were observed. The use of QDs with ABA capping had higher impact on the morphological properties while the employment of CsPI ligand was more effective on the optical properties of the perovskite films. Taking advantage of the improved properties, PSCs based on the perovskite films with embedded PbS QDs exhibit an enhanced photovoltaic performance, observing the highest increase with ABA capping. Moreover, the bulk recombination via trap states is reduced when the ABA ligand is used as capping of the PbS QD additives incorporated in the perovskite film. We demonstrate how surface chemistry engineering of solution-processed perovskite films with PbS QD additives can open a new approach towards the design of high quality materials, which paves the way to improved perovskite optoelectronic properties and more efficient photovoltaic devices.

TOC Figure:
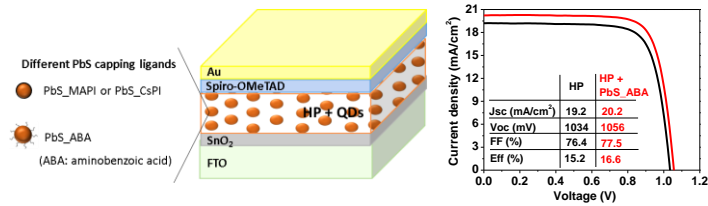
V.1. Introduction

Lead halide perovskites (HP) have attracted worldwide attention predominantly due to the rapid progress in HP-based photovoltaics. The certified photoconversion efficiency (PCE) of Halide Perovskite Solar Cells (PSCs) has reached over 25%[1] in 2019, a staggering improvement on the already remarkable breakthrough in 2012 with PCEs around 10%, first reported for all-solid PSCs.[2-3] The unprecedented quick progress in PCE of PSCs has been mainly attributed to the superb optoelectronic properties of HP materials such as high absorption coefficient and long carrier diffusion lengths.[4-5] Beside, HP have also been demonstrated as promising materials for light emitting diodes (LEDs),[6-8] photodetectors,[9] light amplifiers[10-11] and lasers.[12-14]

In the optimization process of PSCs a large variety of approaches has been evaluated, including the use of different device configurations[2, 15] and different HP materials.[16] The quality of the HP layer has been also improved in various ways including solvent,[17] compositional[18-19] and interface engineering.[20-21] Solution deposition techniques have been extensively used in the fabrication of PSCs. These solution methods also allow the easy combination of HP with other materials, such as organic molecules,[22-24] polymers,[25-29] or colloidal quantum dots (QDs).[30-31] The interaction between HP and QDs can produce interesting constructive synergies.[32-33] In particular, the combination of PbS QDs and methylammonium lead iodine (MAPI) perovskite has been studied as both materials possess a six-coordinated Pb atoms with similar Pb-Pb distances (6.26A° for MAPI and 5.97A° for PbS), with less than 4.6% of lattice mismatch.[31] One recent report showed that with a proper amount of PbS QDs with organic capping (mixture of oleic acid,

106

oleylamine and trioctylphosphine), the properties of HP film including morphological, optical and structural properties can be improved, increasing the performance of PSCs from 16.3% for pure MAPI to 18.6% for hybrid HP-QD absorbers.[34] We showed that the interaction between HP and PbS/CdS QDs capped with MAPI ligand gives rise to a new light emission peak (photoluminescence or electroluminescence) from an exciplex state at lower bandgap than both HP and PbS/CdS QDs, detected either by optical pumping or electrical injection.[30] Moreover a positive effect of embedded QDs on HP morphology, with an increase of grain size, was also observed.[30, 34-35] These works demonstrated that a small amount of dispersed PbS QDs in the HP precursor solution can serve as effective seed-like nucleation centers to promote the formation of HP lattice structures, resulting in a better HP layer quality and improved optoelectronic properties[34-35] A similar effect on perovskite properties was also obtained for the case of intermixing SnS QDs, capped with triethanolamine, into a MAPI perovskite although the lattice mismatch between those materials is higher.[36]

In QD solar cells, the QD capping has a clear impact on the device performance.[37-39] Recently HP precursors such as MAI[40] and lead mixed halide (PbI$_2$ + PbBr$_2$)[41] and HP, such as MAPI [42] and CsPI, [43] have been used as the ligands of PbS QDs. The PCE of PbS QD solar cells has been improved, reaching over 11% for the lead mixed halide capping.[41] In addition, in the combination of QDs and HP where the improvement of HP properties was observed, different QD capping ligands, being organic molecules[34, 36], HP precursor (MAI)[35] and MAPI,[30] were separately used. The question remains whether the choice of ligand can also be exploited for controlling the structural and optoelectronic properties of HP and in turn the efficiency of the QD-containing PSCs.

In this work, ligands of as-synthesized PbS QDs with an oleate (OA) capping were exchanged with three different ligands including MAPI, cesium lead iodide (CsPI) and 4-aminobenzoic acid (ABA) and then separately dispersed in a solution containing HP precursors (PbI$_2$ and MAI) at different concentrations. Hybrid HP-PbS QD films were prepared via a one-step spin-coating method.[30] With a small amount of embedded PbS QDs, we observed an increase in HP grain sizes, reduction in non-radiative recombination, better preferential orientation and increased crystallinity of HP for all three different ligands, with a more prominent effect for the ABA capping. Hybrid methylammonium lead iodide-PbS (HP-PbS) QD films have been used in the fabrication of planar PSCs with SnO$_2$ as electron selective layer. This is a very promising configuration for commercialization of PSCs as SnO$_2$ [21] does not require high temperature treatments and since the planar architecture presents

advantages in term of cost and environmental impact in comparison with cells containing a mesoporous layer.[44] We observed that the use of small concentrations of PbS QDs in planar perovskite solar cells SnO$_2$/HP-PbS/spiro-OMeTAD showed an increase in the PCE comparing with reference cells without PbS QDs. More importantly, the effect of PbS capping ligands was detected and the highest increase in PCEs was obtained for ABA capping ligand, with the champion cell exhibiting a PCE of 16.6%.

V.2. Experimental section

V.2.1. Synthesis of PbS QDs.

PbS QDs were synthesized according to previously reported procedure with some modifications.[30] Briefly, a three-necked round-bottom flask containing PbO (0.9g), Oleic acid (OA, 2.7 g) and 1-octadecene (ODE, 36 ml) was heated up to 120 °C under vacuum for 90 minutes. The temperature was raised to 150 °C for 15 minutes to form Pb-oleate. Next, N$_2$ was introduced to the system and 3 ml of trioctylphosphine (90%) was injected, consequently the temperature was reduced to 110 °C. At which, a mixture of 0.42 ml hexamethyldisilathiane (HMDS) and 4 ml ODE was quickly injected to the flask. The temperature was then gradually decreased to room temperature. The reaction product was cleaned 3 times with ethanol/acetone (1:1, v/v), centrifuged (3000 rpm for 10 minutes) and dispersed in octane (10 mg/ml). The photoluminescence (PL) and absorbance of as-synthesized PbS QDs are presented in Fig. V.S1. The size of PbS QDs was estimated to be ~ 3.5 nm, according to literature[45]

$$E_o = 0.41 + \frac{1}{0.0252d^2 + 0.283d}$$

where d is the diameter of PbS QDs and E$_o$ is the energy of emitted photons at the peak of the PL spectrum.

V.2.2. PbS ligand exchange.

Exchange to methylammonium lead iodide (MAPI) ligand. The PbS ligand exchange from oleate (OA) to MAPI ligand was performed following a previously reported procedure[30] with a small modification. 115 mg of PbI$_2$ and 40 mg of CH$_3$NH$_3$I (MAI) were dispersed in 1 ml of dimethylformamide (DMF), forming 0.25 M of MAPI solution. Then, 0.5 ml of QDs dispersed in octane (10 mg/ml) was added into 0.5 ml of 0.25 M MAPI solution. After stirring for 30 minutes, QDs had transferred from the top octane phase to the bottom DMF. After removing the octane, the QD solution was washed three more times using octane to remove the organic residue. Subsequently, the QDs

were precipitated by the addition of toluene, then, centrifuged at 3500 rpm for 5 minutes. After removing all the liquid, QDs were dried under vacuum for several hours.

Exchange to cesium lead iodine (CsPI) ligand. The process for the exchange from oleate (OA) to CsPI ligand was identical to that for the exchange to MAPI, however 65 mg of CsI was used instead.

Exchange to 4-aminobenzoic acid (ABA) ligand. 1 ml of 0.05 M ABA in DMF was diluted with 1 ml of absolute ethanol. Then 2 ml of PbS_OA QDs (2.5 mg/ml in octane) were added into the ABA solution. Similar to the case of exchange to MAPI or CsPI, after mixing ABA and PbS solutions and shaking the mixture for a few minutes, where phase transfer took place, the QDs had transferred to DMF, leading the color change of the bottom phase from transparent to dark, and the opposite for the top phase (dark to transparent). PbS QDs were cleaned, precipitated, centrifuged and dried as described above. During the ligand exchange, PbS QDs were protected from light as much as possible.

To simplify, PbS QDs exchanged to MAPI, CsPI and ABA are termed hereafter PbS_MAPI, PbS_CsPI and PbS_ABA respectively.

V.2.3. SnO$_2$ compact layer. FTO substrates were cleaned with soap, sonicated in distilled water, ethanol and isopropanol for 15 minutes and then treated with an UV (ultraviolet)−O$_3$ lamp for 15 minutes. The SnO$_2$ compact layer was prepared according to a previous report[46] with a small variation. 296 µl of commercial SnO$_2$ solution (Tin(IV) oxide, 15 % in H$_2$O colloidal dispersion liquid from Alfa Aesar) was diluted with 1.71 ml of ultrapure water. Then, 100 µl of such diluted SnO$_2$ solution was poured on FTO substrate and spin-coated at 3000 rpm (acceleration of 3000 rpm) for 40 seconds. SnO$_2$ films were annealed at 150 °C for 30 minutes.

V.2.4. Perovskite (HP) and HP-PbS solution and film preparation. 1.33 M MAPI solution was prepared by dissolving 612 mg of PbI$_2$ and 211 mg of MAI in dimethyl sulfoxide (DMSO) at 70 °C. Dried PbS QDs with different ligands were separately dispersed in 0.4 ml of 1.33 M MAPI solution. The amount of PbS QDs introduced in the ligand exchange was 5 mg for each exchange and we assumed that there was no loss of PbS QDs during the ligand exchange. Therefore, their concentration in 0.4 ml of MAPI solution was considered to be 12.5 mg/ml, which was used as the mother solutions. The HP-PbS mother solutions were further diluted with 1.33 M MAPI solution to a weight concentration of PbS QDs of 50 and 100 µg/ml. The MAPI and

MAPI-PbS films were prepared by spin-coating 1.33 M MAPI solution without and with PbS QDs at 2000 rpm for 10 seconds (acceleration of 200 rpm) then at 6000 rpm for 30 seconds (acceleration of 2000 rpm). At the 25th second of the spinning, ethyl acetate was poured on the films. MAPI and MAPI-PbS films were annealed at 130 ºC for 10 minutes. All solution and film deposition were prepared inside a glove box filled with N_2.

V.2.5. Spiro OMeTAD and Gold. Spiro OMeTAD solution was prepared by dissolving 72.3 mg of spiro-OMeTAD(2,2′,7,7′-tetrakis(N,N-di-p-methoxyphenylamine)-9,9-spirobifluorene) in 1 ml of chlorobenzene, then mixed with 28.8 μl of 4-tert-butylpyridine and 17.5 μl of a stock Li^+ solution (which contained 520 mg/ml bis-trifluoromethylsulfonylamine lithium salt in acetonitrile). Spiro OMeTAD layer was spin-coated on HP or HP-QDs films at 4000 rpm for 30 seconds (acceleration of 800 rpm). Finally, 80 nm of gold were thermally evaporated in an ultrahigh vacuum chamber on top of Spiro OMeTAD layer to make complete devices.

V.2.6. Sample preparation for Fourier-transform infrared (FT-IR) measurement. ABA was dispersed in DMSO, 38 mg/ml. PbS_OA QDs were exchanged to ABA capping ligand following the procedure listed above. After ligand exchange, PbS_ABA QDs were dried and dissolved in 0.6 ml of 1.33 M of perovskite precursors (PbI_2 and MAI).

V.2.7. Characterization of samples in solution and film. The morphology of the films was analyzed by scanning electron microscopy (SEM) using a JSM7001F (Field emission scanning electron microscope). The absorbance spectrum of as-synthesized PbS QDs (with oleate ligand, PbS_OA) was measured using a Cary 500 Scan Varian UV-VIS-NIR spectrophotometer. The photoluminescence (PL) of PbS_OA, PbS_MAPI, and PbS_CsPI QDs in solution was carried out using a CCD detector (InGaAs Andor-iDUS DU490A-2.2) coupled with an adaptive focus imaging spectrograph (Kymera KY-193i-B2). A commercial continuous laser (532 nm, GL532RM-150) was used as an excitation source. While PL of PbS_ABA QDs in solutions were measured using a Fluorolog system (Horiba JOBNYVON) with a 532 nm excitation wavelength. PL spectra of MAPI and MAPI-PbS films were also measured using the same Fluorolog system and excitation. For the PL measurement, a long-pass filter 20CGA-590 was used in order to block the excitation source. A Bruker AXS-D4 Endeavor Advance X-ray with Cu Kα radiation was used to measure the x-ray diffraction (XRD) spectra of MAPI and hybrid MAPI-PbS films. Fourier-transform infrared (FT-IR) was measured using a FT-IR 6200 spectrometer (Jasco) with the ATR Pro One (Jasco) equipped with diamond crystal.

V.2.8. Device characterization. *Photocurrent density-voltage (JV) characteristic*. JV curves of solar cells were measured under a xenon arc lamp simulator equipped with an AM 1.5 spectral filter (Solar simulator 69920, Newport). The intensity was adjusted to provide 1 sun (100 mW cm^{-2}) by using a calibrated silicon solar cell. The *J-V* characteristics were recorded by scanning the potential from higher than the open circuit voltage (Voc) to -0.05 V (backward mode) at approximately 45 mV/s. *Incident photon to current efficiency (IPCE) measurement*. The IPCE measurements were performed employing a 150 W Xenon lamp coupled with a computer-controlled monochromator. The photocurrent was measured using an optical power meter 70310 from Oriel Instruments. A Si photodiode was used to calibrate the system.

V.3. Results and Discussion

The absorbance and PL spectra of as-synthesized PbS QDs used in this present work, with oleate ligands (OA), are shown in Fig. V.S1. As can be seen, the PL spectrum presents a fairly narrow peak, pointing to a homogeneous distribution of PbS sizes which was estimated to be ~ 3.5 nm (see the experimental section). The as-synthesized PbS QDs were capped with oleate (OA), which serves to control the dimension of QDs, as well as to prevent their aggregation in the organic solution and electronically passivate the QD surface. An important step to realize perovskite photovoltaic devices is exchanging these long chain ligands by short and polar ones, to favor the interaction HP-PbS QD and simultaneously make them soluble in DMF and DMSO, the solvents commonly employed to dissolve the HP precursors. This process allows to overcome the solubility limitation, and to develop a one-step deposition process, that provides the opportunity for the intermixing of the PbS QDs during the growth of HP film in the easiest way possible.

We have selected MAPI and CsPI to serve as capping ligands for our PbS QDs and for their implementation in PSCs since it was previously demonstrated that those capping ligands result in a high PCE in QD solar cells,[42-43]. Further, 4-aminobenzoic acid (ABA) was chosen as PbS QD capping agent as the benzoic acid group was shown to passivate TiO$_2$ electron transporting layer in PSCs, resulting in a more efficient electron extraction.[47] The PbS QD ligand exchange was done in solution, as described in the experimental section. Briefly, as-synthesized PbS QDs with OA ligand were dispersed in octane and the exchange ligands were separately dissolved in DMF. A phase separation was obtained after mixing the QD and ligand

solutions, with the dark phase (PbS_OA in octane) on top and the ligand in DMF at the bottom. After stirring/shaking the mixed solution, phase transfer took place, and PbS QDs were transferred to the bottom phase (see Fig. V.S2 and experimental section for further details). After the ligand exchange to all these three ligands, PbS QDs presented a redshift in PL. For the case of MAPI and CsPI ligands, the redshift is probably due to the formation of core/shell structure, QDs may be bigger, reducing the confinement degree (see Fig. V.S3 and section VS.3 of supporting information). For the case of ABA ligand, the redshift could be resulted from the aggregation of QDs (see Fig. V.S4 and section VS.3 of supporting information). Interestingly in the presence of MAPI precursors, there was a change in the PL spectra, suggesting the interaction of CsPI and ABA ligands with MAPI precursors (see Fig. V.S3, V.S4 and section VS.3 of supporting information). The Fourier-transform infrared measurement of ABA based samples also pointed the same direction (see Fig. V.S5 and section VS.3 of supporting information).

The introduction of small quantities of PbS QDs with different capping ligands clearly affects the properties of the HP films. The grain sizes of HP were slightly increased when PbS was introduced. Fig. V.1 presents the histogram of HP grain size of HP film without and with PbS QDs with different capping ligands, determined from different SEM images at different places on the films. Fig. V.S6 presents the top view SEM images of HP films without and with embedded PbS QDs (50 µg/ml). The dispersion of the grain size of pure MAPI film (HP, mean of 251 nm) was similar when PbS_CsPI was embedded. The average grain size was slightly increased to 269 nm when PbS_MAPI was introduced until reaching 283 nm (~ 14% increase) after the incorporation of PbS_ABA, see Fig V.S7 for the grain size estimation.

The x-ray diffraction (XRD) spectra of HP and hybrid HP-PbS are shown in the Fig. V.2a and V.S8. The tetragonal structural phase, with (110) preferential orientation corresponding to the diffraction peak at 14.2° was obtained for all samples. The net area of diffraction peaks increased, demonstrating the increase in crystallinity when PbS QDs were introduced (see Table V.1). It is worth to note that the increase in crystallinity was obtained not only for (110) crystalline plane with the diffraction peak at 14.2° but also for (220) crystalline plane with the diffraction peak at 28.5°. However the improvement in crystallinity is dependent on the capping ligand of PbS QDs although the concentration of embedded PbS QDs was the same (50 µg/ml) for all HP+PbS samples (see Table V.1). In addition, when PbS QDs were introduced in the film, the HP precursors converted more efficiently to HP, confirmed by the smaller XRD intensity of PbI$_2$ diffraction peak at 12.7° (see Fig. V.2b). Eventually, the analysis of the XRD spectra also indicates an

increase of the (110) preferential orientation after PbS QD addition, as indicated by the increase of the ratio on the intensity of this diffraction peaks with respect to the others (see Fig. V.2a).[48]
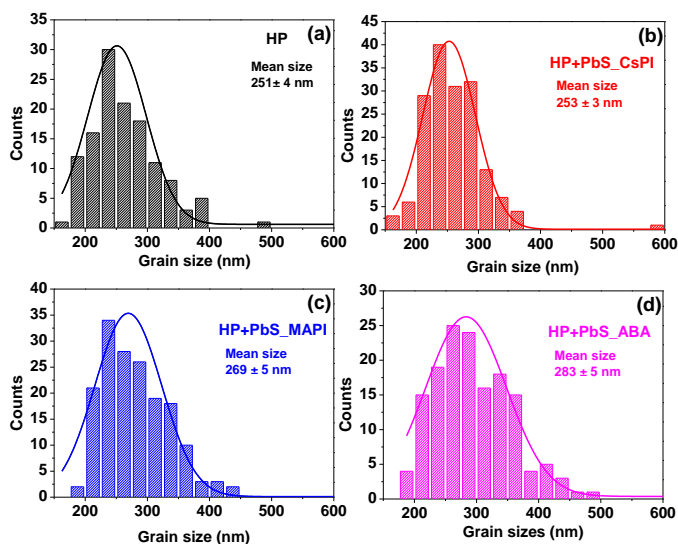

Fig V.1. Grain sizes of perovskite estimated from SEM images of (a) perovskite films without (HP) and with PbS QDs (50 µg/ml) deposited on glass of PbS QDs with the different capping ligands including (b) MAPI, (c) CsPbI and (d) 4-aminobenzoic acid (ABA).
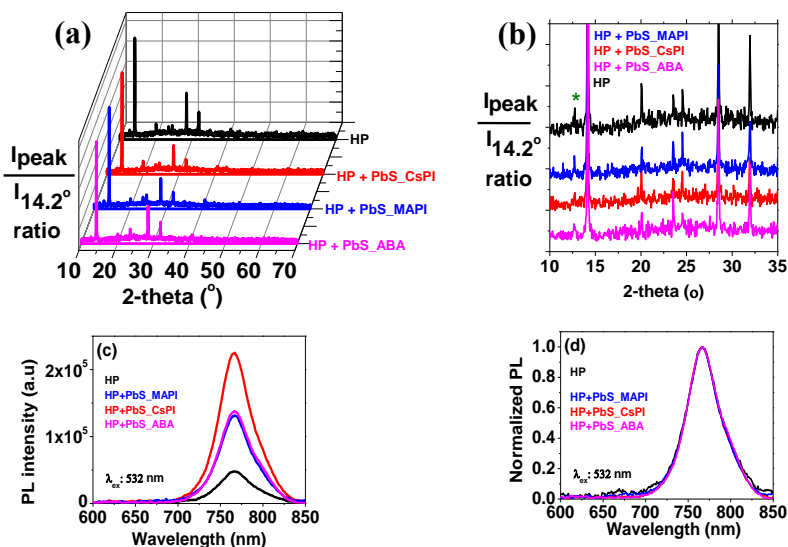

Fig V.2. Crystallographic and optical characterization of perovskite films without (HP) and with PbS QDs (50 µg/ml) deposited on glass of PbS QDs with the different capping ligands including MAPI, CsPI and 4-aminobenzoic acid (ABA). XRD spectra (a) and a zoom from 10 to 35 ° (b), * symbol indicates PbI_2 difraction peak; (c) photoluminescence (PL) and (d) and normalized PL.

Table V.1. Net area of XRD diffraction peaks and the net area difference respect to the HP reference sample.

2-theta	Net peak area (counts x 2-theta)			
		HP+PbS		
	HP	PbS_MAPI	PbS_CsPI	PbS_ABA
14.2	9.49	11.29	11.51	11.18
28.5	3.95	4.46	4.1	5.37
32	2.89	1.98	2.58	2.25
2-theta	Net area change respect to HP			
		HP+PbS		
		PbS_MAPI	PbS_CsPI	PbS_ABA
14.2		1.8	2.02	1.69
28.5		0.51	0.15	1.42

Complementarily to the improvement in the structural properties, the optical properties of the HP films were enhanced as well by the incorporation of PbS QDs. As shown in the Fig. V.2c, the photoluminescence (PL) intensity of HP films with PbS_ABA or PbS_MAPI was doubled with respect to the reference film, without PbS QDs, and it was tripled with PbS_CsPI QDs. This increase suggests that the intermixing of PbS QDs during the HP growth can reduce the non-radiative recombination. In addition, the incorporation of a small quantity of PbS QDs did not provoke any change in the optical gap of HP as no shift of PL peak position for all hybrid films was observed (see Fig. V.2d). It is important to note that the increase in the PL was not due to the increase in the film thickness as all samples presents similar thickness, ~ 330 nm, see Fig. V.S9.

The improved morphological, structural and optical properties of hybrid HP-PbS films can be attributed to the QDs serving as a nucleation site, which helps the crystalline growth of perovskites along preferred orientation with bigger grain sizes as has been pointed out in previous studies.[34-36] Additionally we also detected the dependence of HP formation on the capping ligands of embedded PbS QDs at the same concentration. Distinctly bigger perovskite grain size was obtained for ABA capping (see Fig. V.1), while the highest improvement in the photoluminescence and in the structural properties, in terms of preferential orientation and crystallinity, was achieved for the use of CsPI ligand. Additionally, the incorporation of PbS resulted in a better HP conversion from precursors with respect to the reference film, without QDs. However, the extent of HP conversion efficiency was also dependent on the capping ligands of PbS, with higher conversion for CsPI and ABA ligands (see Fig. V.2b). The origin for the dependence of hybrid HP-PbS film quality

on the PbS ligands is still unclear, and additional experiments would be needed to reveal the exact role of QD ligand in the formation of the hybrid films.

Finally, we also tested the potential application of the hybrid HP-PbS QD films in full solar cell devices. We selected a planar configuration, even though the improvement in PCE of HP solar cells by the incorporation of PbS QDs has been obtained in past experiments with a TiO_2 electron transport layer (ETL). The planar configuration was chosen since the alternative low temperature process SnO_2 layer[21, 49] could reduce the fabrication cost and environmental impacts for a future application of QDs in low-cost or large area photovoltaics.[34-36, 44] Therefore, planar solar cells were fabricated following the structure FTO/SnO_2/HP or HP-PbS/spiro-OMeTAD/Au. Fig. V.3 and Table V.2 present the statistical analysis of photovoltaic parameters of the fabricated devices.
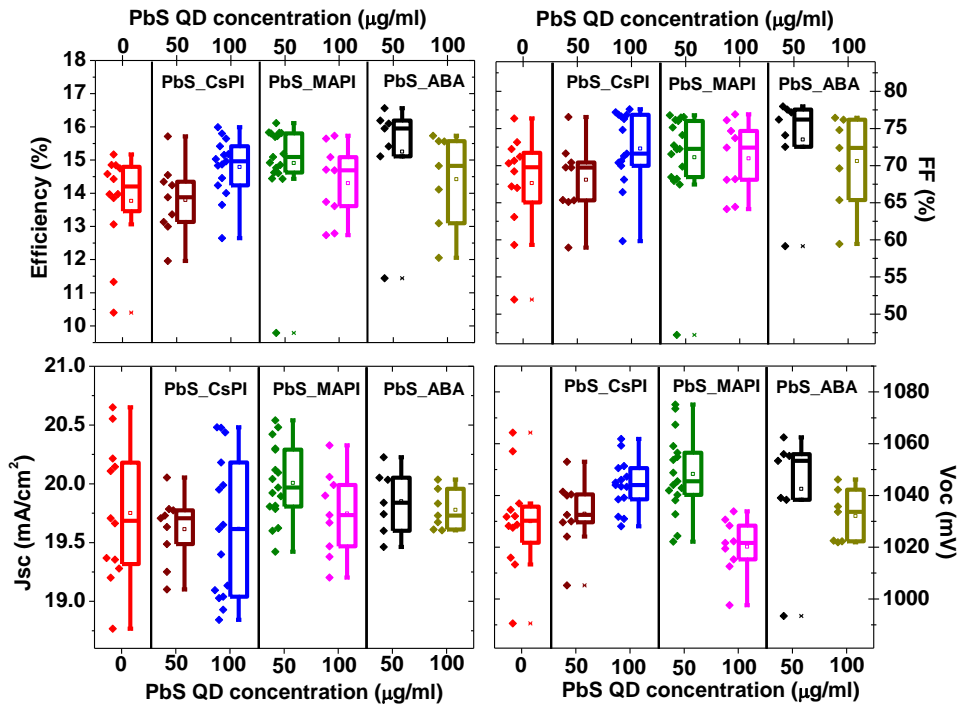
Fig V.3. Photovoltaic parameters of FTO/SnO_2/absorber/spiro-OMeTAD/Au solar cells. The different absorber layers were perovskite films without and with different PbS QD concentrations and different PbS capping ligands, including CsPI, MAPI and 4-aminobenzoic acid (ABA) separately.

Table V.2. Photovoltaic parameters of FTO/SnO$_2$/absorber/spiro-OMeTAD/Au solar cells presented in the Fig V.3

C$_{PbS}$ µg/ml	PbS ligand	Jsc [mA/cm^2]	Voc [mV]	FF [%]	Efficiency [%]
0	-	19.8 ± 0.2	1030.1 ± 5.5	67.6 ± 1.9	13.8 ± 0.4
Champion	-	19.2	1034.5	76.4	15.2
50	CsPI	19.6 ± 0.1	1032.9 ± 4.5	68.1 ± 1.7	13.8 ± 0.4
Champion		19.5	1053.0	76.6	15.7
100		19.6 ± 0.2	1044 ± 2.5	72.3 ± 1.3	14.8 ± 0.2
Champion		19.6	1050.6	77.6	16.0
50	MAPI	20.0 ± 0.1	1048.3 ± 3.7	71.1 ± 1.7	14.9 ± 0.3
Champion		20.5	1044.1	75.1	16.1
100		19.7 ± 0.1	1020.2 ± 3.7	71 ± 1.6	14.3 ± 0.4
Champion		20.0	1033.9	76.1	15.7
50	ABA	19.9 ± 0.1	1042.6 ± 8.9	73.5 ± 2.5	15.3 ± 0.7
Champion		20.2	1055.9	77.5	16.6
100		19.8 ± 0.1	1032.1 ± 3.8	70.6 ± 2.4	14.4 ± 0.5
Champion		19.7	1046.2	76.4	15.7

The average performance of the PSCs and of the champion cells were increased for all three capping ligands and for the two studied concentrations, except for the case of 50 µg/ml with CsPI capping ligand where no significant enhancement was observed. Fig. V.4 presents the photocurrent – voltage curves of best reference and the best hybrid solar cells. The performance improvement was achieved in all three photovoltaic parameters: open circuit voltage (Voc), short circuit current density (Jsc) and fill factor (FF). However, the main improvement was related to the increase in FF. The improvement in performance also depends on the type of the ligands for the same QD concentration. For the case of CsPI ligand, the addition of PbS QDs slightly reduced the Jsc from 19.8 to 19.6 mA/cm^2, however the Voc and FF were enhanced resulting the conservation and improvement in PCE for the PbS concentrations of 50 and 100 µg/ml, respectively. While for the case of the two other ligands, MAPI and ABA, better device performance was obtained for both PbS QD concentrations. Among the different capping ligands used, ABA shows the highest improvement with the average PCE of 15.3 % for a concentration of 50 µg/ml, over 10 % improvement with respect to the reference cells (average PCE of 13.8 %). A similar improvement was observed for the champion cell, with a PCE of 16.6 %, see Fig. V.4. The amelioration in solar cell performance obtained for the devices based on the hybrid HP-PbS absorbers resulted from the improvement in the film quality including morphological, optical and structural properties.

A detailed analysis of the concentration effects suggests a decrease of performance for the higher concentration in case of PbS_MAPI and PbS_ABA. The decrease of Voc also observed for the higher concentrations for MAPI and ABA capping ligands, points to an increase of recombination with the increase of QD concentration, as was previously observed.[50] Optimization of the QD concentration is crucial since the addition of PbS QDs also introduces recombination centers and consequently the beneficial effect induced during the perovskite crystalline growth has to be properly balanced by the detrimental effect of an enhanced recombination.

The dependence of Voc on the incident light intensity of planar solar cells without and with PbS_ABA QDs is shown in the Fig. V.5. As expected, for both cells the Voc increased linearly with the increase of the incident light intensity. An ideality factor, *m*, can be determined from the slope of this linear relation as:[51]

$$ m = \frac{q}{kT} * \frac{dV_{OC}}{dln\emptyset} $$

where q, k, T and ϕ are the elementary charge, Boltzmann's constant, absolute temperature and light intensity, respectively. The value of the ideality factor provides important clues about the recombination process in perovskite solar cells.[52] The calculated ideality of the reference cell was closed to 2 (2.18), similar to reported ideality value for other MAPI perovskite based sample.[53] This value of ideality factor points to a recombination mechanism through a Shockley-Read-Hall (SRH) recombination.[52, 54] When PbS_ABA was added in the HP film, the ideality factor was reduced to 1.56, revealing lower SRH bulk recombination, for which an ideality factor of 2 is expected, and a higher relative weight of surface recombination, for which an ideality factor of 1 is expected, pointing to a decrease of trap states in the bulk HP-PbS_ABA film. This result is in agreement with an increase in the PL intensity (Fig. V.2c) and an increase in Voc (Fig. V.3 and Table V.2) when PbS QDs are incorporated.
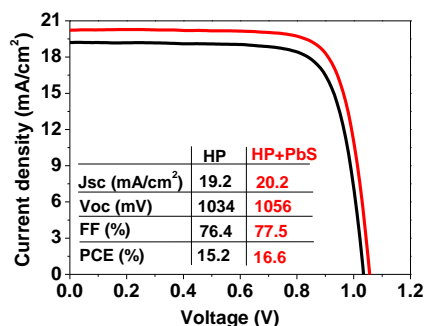
Fig V.4. Photovoltaic characteristic of best FTO/SnO₂/absorber/spiro-OMeTAD/Au solar cells. In which absorber layers were perovskite films without (HP) and with PbS QDs (50 µg/ml) and PbS QDs had 4-aminobenzoic acid (ABA) ligand.
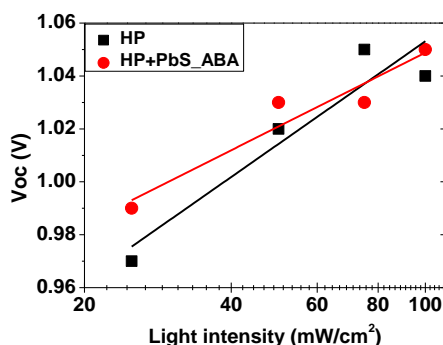
Fig V.5. Dependence of open circuit voltage on light intensity of FTO/SnO₂/absorber/spiro-OMeTAD/Au solar cells. In which absorber layers were perovskite films without (HP) and with PbS QDs (50 µg/ml) and PbS QDs had 4-aminobenzoic acid (ABA) ligand. The measurement was done at room temperature.

The incident photon to current efficiency (IPCE) of HP without and with PbS_ABA based solar cells is presented in the Fig. V.S10. Similar shape of IPCE curves was found for both cells. The incident photons were converted efficiently to current over the spectral region of 350 nm to 800 nm. The onset of photocurrent at ~ 800 nm was consistent with the bandgap of MAPI HP and no significant contribution to photocurrent from PbS was observed.

V.4. Conclusions

We show herein a detailed study of the effect of QD capping ligands on the quality of halide perovskite films obtained through intermixing of a small quantity of PbS QDs during the film crystallization. PbS QDs with three different capping ligands including MAPI, CsPI and ABA were analyzed. These QDs were added in the precursor solution of HP and hybrid HP-PbS films were prepared via a one-step spin-coater method. Systematic characterization shows that the presence of PbS QDs increases the grain sizes and decreases non-radiative recombination of MAPI perovskite. Their presence also increases the preferential orientation along (110) plane direction and crystallinity of (110) and (220) HP crystalline planes. Consequently improvements in morphological, crystalline and optical properties of HP were obtained. We attribute these improvements to PbS QDs acting as nucleation sites helping in the crystallization process. As a result of the improved

perovskite film quality, the performance of planar solar cells fabricated with low temperature processes, with SnO_2 as ETL, was enhanced with respect to the reference cells, without PbS QDs. In addition, we also observed the dependence of HP film properties on different PbS capping ligands. The ABA ligand has higher impact on the morphological properties and the CsPI ligand on the optical and structural properties. This observation could point to an improved interaction of perovskite with the organic ligand, ABA, affecting the morphology, while the CsPI likely produces a better electronic passivation at the perovskite-QD interface. The improvement in PCEs of our HP-PbS based solar cells highlights the interest of PbS QD additives for the development of perovskite optoelectronic devices, an established way to improve the performance by control of the surface properties of QDs using different capping agents.

References

1. NREL photovoltaic efficiency chart: https://www.nrel.gov/pv/cell-efficiency.html
2. Lee, M. M.; Teuscher, J.; Miyasaka, T.; Murakami, T. N.; Snaith, H. J. Efficient Hybrid Solar Cells Based on Meso-Superstructured Organometal Halide Perovskites. *Science* **2012,** *338* (6107), 643-647.
3. Kim, H.-S.; Lee, C.-R.; Im, J.-H.; Lee, K.-B.; Moehl, T.; Marchioro, A.; Moon, S.-J.; Humphry-Baker, R.; Yum, J.-H.; Moser, J. E.; Gratzel, M.; Park, N.-G. Lead Iodide Perovskite Sensitized All-Solid-State Submicron Thin Film Mesoscopic Solar Cell with Efficiency Exceeding 9%. *Scientific reports* **2012,** *2*, 591.
4. Stranks, S. D.; Eperon, G. E.; Grancini, G.; Menelaou, C.; Alcocer, M. J. P.; Leijtens, T.; Herz, L. M.; Petrozza, A.; Snaith, H. J. Electron-Hole Diffusion Lengths Exceeding 1 Micrometer in an Organometal Trihalide Perovskite Absorber. *Science* **2013,** *342* (6156), 341-344.
5. Xing, G.; Mathews, N.; Sun, S.; Lim, S. S.; Lam, Y. M.; Grätzel, M.; Mhaisalkar, S.; Sum, T. C. Long-Range Balanced Electron- and Hole-Transport Lengths in Organic-Inorganic CH3NH3PbI3. *Science* **2013,** *342* (6156), 344-347.
6. Jaramillo-Quintero, O. A.; Sanchez, R. S.; Rincon, M.; Mora-Sero, I. Bright Visible-Infrared Light Emitting Diodes Based on Hybrid Halide Perovskite with

Spiro-OMeTAD as a Hole-Injecting Layer. *The Journal of Physical Chemistry Letters* **2015,** *6* (10), 1883-1890.

7. Tan, Z.-K.; Moghaddam, R. S.; Lai, M. L.; Docampo, P.; Higler, R.; Deschler, F.; Price, M.; Sadhanala, A.; Pazos, L. M.; Credgington, D.; Hanusch, F.; Bein, T.; Snaith, H. J.; Friend, R. H. Bright light-emitting diodes based on organometal halide perovskite. *Nat Nano* **2014,** *9* (9), 687-692.

8. Lin, K.; Xing, J.; Quan, L. N.; de Arquer, F. P. G.; Gong, X.; Lu, J.; Xie, L.; Zhao, W.; Zhang, D.; Yan, C.; Li, W.; Liu, X.; Lu, Y.; Kirman, J.; Sargent, E. H.; Xiong, Q.; Wei, Z. Perovskite light-emitting diodes with external quantum efficiency exceeding 20 per cent. *Nature* **2018,** *562* (7726), 245-248.

9. Dou, L.; Yang, Y.; You, J.; Hong, Z.; Chang, W.-H.; Li, G. Solution-processed hybrid perovskite photodetectors with high detectivity. *Nat Commun* **2014,** *5*, 5404.

10. Suárez, I.; Juárez-Pérez, E. J.; Bisquert, J.; Mora-Seró, I.; Martínez-Pastor, J. P. Polymer/Perovskite Amplifying Waveguides for Active Hybrid Silicon Photonics. *Advanced Materials* **2015,** *27* (40), 6157-6162.

11. Suárez, I.; Hassanabadi, E.; Maulu, A.; Carlino, N.; Maestri, C. A.; Latifi, M.; Bettotti, P.; Mora-Seró, I.; Martínez-Pastor, J. P. Integrated Optical Amplifier–Photodetector on a Wearable Nanocellulose Substrate. *Advanced Optical Materials* **2018,** *6* (12), 1800201.

12. Deschler, F.; Price, M.; Pathak, S.; Klintberg, L. E.; Jarausch, D.-D.; Higler, R.; Hüttner, S.; Leijtens, T.; Stranks, S. D.; Snaith, H. J.; Atatüre, M.; Phillips, R. T.; Friend, R. H. High Photoluminescence Efficiency and Optically Pumped Lasing in Solution-Processed Mixed Halide Perovskite Semiconductors. *The Journal of Physical Chemistry Letters* **2014,** *5* (8), 1421-1426.

13. Zhu, H.; Fu, Y.; Meng, F.; Wu, X.; Gong, Z.; Ding, Q.; Gustafsson, M. V.; Trinh, M. T.; Jin, S.; Zhu, X. Y. Lead halide perovskite nanowire lasers with low lasing thresholds and high quality factors. *Nat Mater* **2015,** *14* (6), 636-642.

14. Xing, G.; Mathews, N.; Lim, S. S.; Yantara, N.; Liu, X.; Sabba, D.; Grätzel, M.; Mhaisalkar, S.; Sum, T. C. Low-temperature solution-processed wavelength-tunable perovskites for lasing. *Nat Mater* **2014,** *13* (5), 476-480.

15. Saliba, M.; Correa-Baena, J.-P.; Wolff, C. M.; Stolterfoht, M.; Phung, N.; Albrecht, S.; Neher, D.; Abate, A. How to Make over 20% Efficient Perovskite Solar Cells in Regular (n–i–p) and Inverted (p–i–n) Architectures. *Chemistry of Materials* **2018,** *30* (13), 4193-4201.

16. Chen, L.-J.; Lee, C.-R.; Chuang, Y.-J.; Wu, Z.-H.; Chen, C. Synthesis and Optical Properties of Lead-Free Cesium Tin Halide Perovskite Quantum Rods with High-Performance Solar Cell Application. *J Phys Chem Lett* **2016,** *7* (24), 5028-5035.

17. Jeon, N. J.; Noh, J. H.; Kim, Y. C.; Yang, W. S.; Ryu, S.; Seok, S. I. Solvent engineering for high-performance inorganic-organic hybrid perovskite solar cells. *Nat Mater* **2014,** *13* (9), 897-903.

18. Saliba, M.; Matsui, T.; Domanski, K.; Seo, J.-Y.; Ummadisingu, A.; Zakeeruddin, S. M.; Correa-Baena, J.-P.; Tress, W. R.; Abate, A.; Hagfeldt, A.; Grätzel, M. Incorporation of rubidium cations into perovskite solar cells improves photovoltaic performance. *Science* **2016,** *354* (6309), 206-209.

19. Zhang, W.; Anaya, M.; Lozano, G.; Calvo, M. E.; Johnston, M. B.; Míguez, H.; Snaith, H. J. Highly Efficient Perovskite Solar Cells with Tunable Structural Color. *Nano Letters* **2015,** *15* (3), 1698-1702.

20. Zhou, H.; Chen, Q.; Li, G.; Luo, S.; Song, T.-b.; Duan, H.-S.; Hong, Z.; You, J.; Liu, Y.; Yang, Y. Interface engineering of highly efficient perovskite solar cells. *Science* **2014,** *345* (6196), 542-546.

21. Correa Baena, J. P.; Steier, L.; Tress, W.; Saliba, M.; Neutzner, S.; Matsui, T.; Giordano, F.; Jacobsson, T. J.; Srimath Kandada, A. R.; Zakeeruddin, S. M.; Petrozza, A.; Abate, A.; Nazeeruddin, M. K.; Gratzel, M.; Hagfeldt, A. Highly efficient planar perovskite solar cells through band alignment engineering. *Energy & Environmental Science* **2015,** *8* (10), 2928-2934.

22. Masi, S.; Aiello, F.; Listorti, A.; Balzano, F.; Altamura, D.; Giannini, C.; Caliandro, R.; Uccello-Barretta, G.; Rizzo, A.; Colella, S. Connecting the solution chemistry of PbI2 and MAI: a cyclodextrin-based supramolecular approach to the formation of hybrid halide perovskites. *Chemical science* **2018,** *9* (12), 3200-3208.

23. Xu, J.; Buin, A.; Ip, A. H.; Li, W.; Voznyy, O.; Comin, R.; Yuan, M.; Jeon, S.; Ning, Z.; McDowell, J. J.; Kanjanaboos, P.; Sun, J.-P.; Lan, X.; Quan, L. N.; Kim, D. H.; Hill, I. G.; Maksymovych, P.; Sargent, E. H. Perovskite–fullerene hybrid materials suppress hysteresis in planar diodes. *Nat Commun* **2015,** *6*, 7081.

24. Ngo, T. T.; Suarez, I.; Antonicelli, G.; Cortizo-Lacalle, D.; Martinez-Pastor, J. P.; Mateo-Alonso, A.; Mora-Sero, I. Enhancement of the Performance of Perovskite Solar Cells, LEDs, and Optical Amplifiers by Anti-Solvent Additive Deposition. *Advanced Materials* **2017,** *29*, 1604056.

25. Fakharuddin, A.; Seybold, M.; Agresti, A.; Pescetelli, S.; Matteocci, F.; Haider, M. I.; Birkhold, S. T.; Hu, H.; Giridharagopal, R.; Sultan, M.; Mora-Seró, I.; Di Carlo, A.; Schmidt-Mende, L. Perovskite-Polymer Blends Influencing Microstructures, Nonradiative Recombination Pathways, and Photovoltaic Performance of Perovskite Solar Cells. *ACS applied materials & interfaces* **2018,** *10* (49), 42542-42551.

26. Giuri, A.; Masi, S.; Listorti, A.; Gigli, G.; Colella, S.; Corcione, C. E.; Rizzo, A. Polymeric rheology modifier allows single-step coating of perovskite ink for highly efficient and stable solar cells. *Nano Energy* **2018,** *54*, 400-408.

27. Chaudhary, B.; Kulkarni, A.; Jena, A. K.; Ikegami, M.; Udagawa, Y.; Kunugita, H.; Ema, K.; Miyasaka, T. Poly(4-Vinylpyridine)-Based Interfacial Passivation to Enhance Voltage and Moisture Stability of Lead Halide Perovskite Solar Cells. *ChemSusChem* **2017,** *10* (11), 2473-2479.

28. Li, X.; Ibrahim Dar, M.; Yi, C.; Luo, J.; Tschumi, M.; Zakeeruddin, S. M.; Nazeeruddin, M. K.; Han, H.; Grätzel, M. Improved performance and stability of perovskite solar cells by crystal crosslinking with alkylphosphonic acid ω-ammonium chlorides. *Nat Chem* **2015,** *7*, 703.

29. Zuo, L.; Guo, H.; deQuilettes, D. W.; Jariwala, S.; De Marco, N.; Dong, S.; DeBlock, R.; Ginger, D. S.; Dunn, B.; Wang, M.; Yang, Y. Polymer-modified halide perovskite films for efficient and stable planar heterojunction solar cells. *Sci Adv* **2017,** *3* (8), e1700106.

30. Ngo, T. T.; Suarez, I.; Sanchez, R. S.; Martinez-Pastor, J. P.; Mora-Sero, I. Single step deposition of an interacting layer of a perovskite matrix with embedded quantum dots. *Nanoscale* **2016,** *8*, 14379-14383.

31. Ning, Z.; Gong, X.; Comin, R.; Walters, G.; Fan, F.; Voznyy, O.; Yassitepe, E.; Buin, A.; Hoogland, S.; Sargent, E. H. Quantum-dot-in-perovskite solids. *Nature* **2015,** *523* (7560), 324-328.

32. Ngo, T. T.; Mora-Seró, I. Interaction between Colloidal Quantum Dots and Halide Perovskites: Looking for Constructive Synergies. *The journal of physical chemistry letters* **2019,** *10* (5), 1099-1108.

33. Liu, M.; Chen, Y.; Tan, C.-S.; Quintero-Bermudez, R.; Proppe, A. H.; Munir, R.; Tan, H.; Voznyy, O.; Scheffel, B.; Walters, G.; Kam, A. P. T.; Sun, B.; Choi, M.-J.; Hoogland, S.; Amassian, A.; Kelley, S. O.; García de Arquer, F. P.; Sargent, E. H. Lattice anchoring stabilizes solution-processed semiconductors. *Nature* **2019,** *570* (7759), 96-101.

34. Han, J.; Luo, S.; Yin, X.; Zhou, Y.; Nan, H.; Li, J.; Li, X.; Oron, D.; Shen, H.; Lin, H. Hybrid PbS Quantum-Dot-in-Perovskite for High-Efficiency Perovskite Solar Cell. *Small* **2018,** *14* (31), 1801016.

35. Li, S.-S.; Chang, C.-H.; Wang, Y.-C.; Lin, C.-W.; Wang, D.-Y.; Lin, J.-C.; Chen, C.-C.; Sheu, H.-S.; Chia, H.-C.; Wu, W.-R.; Jeng, U. S.; Liang, C.-T.; Sankar, R.; Chou, F.-C.; Chen, C.-W. Intermixing-seeded growth for high-performance planar heterojunction perovskite solar cells assisted by precursor-capped nanoparticles. *Energy & Environmental Science* **2016,** *9* (4), 1282-1289.

36. Han, J.; Yin, X.; Nan, H.; Zhou, Y.; Yao, Z.; Li, J.; Oron, D.; Lin, H. Enhancing the Performance of Perovskite Solar Cells by Hybridizing SnS Quantum Dots with CH3NH3PbI3. *Small* **2017,** *13* (32), 1700953.

37. de la Fuente, M. S.; Sánchez, R. S.; González-Pedro, V.; Boix, P. P.; Mhaisalkar, S. G.; Rincón, M. E.; Bisquert, J.; Mora-Seró, I. Effect of Organic and Inorganic Passivation in Quantum-Dot-Sensitized Solar Cells. *The journal of physical chemistry letters* **2013,** *4* (9), 1519-1525.

38. Ip, A. H.; Thon, S. M.; Hoogland, S.; Voznyy, O.; Zhitomirsky, D.; Debnath, R.; Levina, L.; Rollny, L. R.; Carey, G. H.; Fischer, A.; Kemp, K. W.; Kramer, I. J.; Ning, Z.; Labelle, A. J.; Chou, K. W.; Amassian, A.; Sargent, E. H. Hybrid passivated colloidal quantum dot solids. *Nat Nano* **2012,** *7* (9), 577-582.

39. Yang, Y.; Zhao, B.; Gao, Y.; Liu, H.; Tian, Y.; Qin, D.; Wu, H.; Huang, W.; Hou, L. Novel Hybrid Ligands for Passivating PbS Colloidal Quantum Dots to Enhance the Performance of Solar Cells. *Nano-Micro Letters* **2015,** *7* (4), 325-331.

40. Ning, Z.; Dong, H.; Zhang, Q.; Voznyy, O.; Sargent, E. H. Solar Cells Based on Inks of n-Type Colloidal Quantum Dots. *ACS nano* **2014,** *8* (10), 10321-10327.

41. Liu, M.; Voznyy, O.; Sabatini, R.; Garcia de Arquer, F. P.; Munir, R.; Balawi, A. H.; Lan, X.; Fan, F.; Walters, G.; Kirmani, A. R.; Hoogland, S.; Laquai, F.; Amassian, A.; Sargent, E. H. Hybrid organic-inorganic inks flatten the energy landscape in colloidal quantum dot solids. *Nature materials* **2017,** *16* (2), 258-263.

42. Yang, Z.; Janmohamed, A.; Lan, X.; García de Arquer, F. P.; Voznyy, O.; Yassitepe, E.; Kim, G.-H.; Ning, Z.; Gong, X.; Comin, R.; Sargent, E. H. Colloidal

Quantum Dot Photovoltaics Enhanced by Perovskite Shelling. *Nano letters* **2015,** *15* (11), 7539-7543.

43. Zhang, X.; Zhang, J.; Phuyal, D.; Du, J.; Tian, L.; Öberg, V. A.; Johansson, M. B.; Cappel, U. B.; Karis, O.; Liu, J.; Rensmo, H.; Boschloo, G.; Johansson, E. M. J. Inorganic CsPbI3 Perovskite Coating on PbS Quantum Dot for Highly Efficient and Stable Infrared Light Converting Solar Cells. *Advanced Energy Materials* **2018,** *8* (6), 1702049.

44. Alberola-Borràs, J.-A.; Vidal, R.; Juárez-Pérez, E. J.; Mas-Marzá, E.; Guerrero, A.; Mora-Seró, I. Relative impacts of methylammonium lead triiodide perovskite solar cells based on life cycle assessment. *Solar Energy Materials and Solar Cells* **2018,** *179*, 169-177.

45. Moreels, I.; Lambert, K.; Smeets, D.; De Muynck, D.; Nollet, T.; Martins, J. C.; Vanhaecke, F.; Vantomme, A.; Delerue, C.; Allan, G.; Hens, Z. Size-Dependent Optical Properties of Colloidal PbS Quantum Dots. *ACS Nano* **2009,** *3* (10), 3023-3030.

46. Yang, D.; Yang, R.; Wang, K.; Wu, C.; Zhu, X.; Feng, J.; Ren, X.; Fang, G.; Priya, S.; Liu, S. High efficiency planar-type perovskite solar cells with negligible hysteresis using EDTA-complexed SnO2. *Nature communications* **2018,** *9* (1), 3239.

47. Wojciechowski, K.; Stranks, S. D.; Abate, A.; Sadoughi, G.; Sadhanala, A.; Kopidakis, N.; Rumbles, G.; Li, C.-Z.; Friend, R. H.; Jen, A. K. Y.; Snaith, H. J. Heterojunction Modification for Highly Efficient Organic–Inorganic Perovskite Solar Cells. *ACS nano* **2014,** *8* (12), 12701-12709.

48. Yen-Chen, S.; Yu-Bing, L.; Chia-Shuo, L.; Hsiao-Chi, H.; Leeyih, W.; Chih-I, W.; King-Fu, L. Amino-Acid-Induced Preferential Orientation of Perovskite Crystals for Enhancing Interfacial Charge Transfer and Photovoltaic Performance. *Small* **2017,** *13* (22), 1604305.

49. Jiang, Q.; Zhang, L.; Wang, H.; Yang, X.; Meng, J.; Liu, H.; Yin, Z.; Wu, J.; Zhang, X.; You, J. Enhanced electron extraction using SnO2 for high-efficiency planar-structure HC(NH2)2PbI3-based perovskite solar cells. *Nature Energy* **2016,** *2*, 16177.

50. Galar, P.; Piatkowski, P.; Ngo, T. T.; Gutiérrez, M.; Mora-Seró, I.; Douhal, A. Perovskite-quantum dots interface: Deciphering its ultrafast charge carrier dynamics. *Nano Energy* **2018,** *49*, 471-480.

51. Kirchartz, T.; Deledalle, F.; Tuladhar, P. S.; Durrant, J. R.; Nelson, J. On the Differences between Dark and Light Ideality Factor in Polymer:Fullerene Solar Cells. *The journal of physical chemistry letters* **2013,** *4* (14), 2371-2376.

52. Tress, W.; Yavari, M.; Domanski, K.; Yadav, P.; Niesen, B.; Baena, J. P. C.; Hagfeldt, A.; Graetzel, M. Interpretation and evolution of open-circuit voltage, recombination, ideality factor and subgap defect states during reversible light-soaking and irreversible degradation of perovskite solar cells. *Energy & Environmental Science* **2018,** *11* (1), 151-165.

53. Almora, O.; Cho, K. T.; Aghazada, S.; Zimmermann, I.; Matt, G. J.; Brabec, C. J.; Nazeeruddin, M. K.; Garcia-Belmonte, G. Discerning recombination mechanisms and ideality factors through impedance analysis of high-efficiency perovskite solar cells. *Nano Energy* **2018,** *48*, 63-72.

54. Shockley, W.; Read, W. T. Statistics of the Recombinations of Holes and Electrons. *Physical Review* **1952,** *87* (5), 835-842.

SUPPORTING INFORMATION

PbS Quantum Dots as Additives in Methylammonium Halide Perovskite Solar Cells: the Effect of Quantum Dot Capping

Thi Tuyen Ngo,[1] Sofia Masi,[1] Perla F. Mendez,[1,2] Miri Kazes,[3] Dan Oron,[3] and Iván Mora Seró[1*]

[1] Institute of Advanced Materials (INAM), Jaume I University, 12006 Castellón, Spain

[2] Facultad de Ciencias Químico Biológicas, Universidad Autónoma de Sinaloa, Cd. Universitaria, Av. de las Américas y Josefa Ortiz S/N, 80000, Culiacán, Sinaloa, México

[3] Department of Physics of Complex Systems, Weizmann Institute of Science, Rehovot 76100, Israel

*Corresponding Authors: sero@uji.es

VS.1. Characterization of PbS_OA after the synthesis
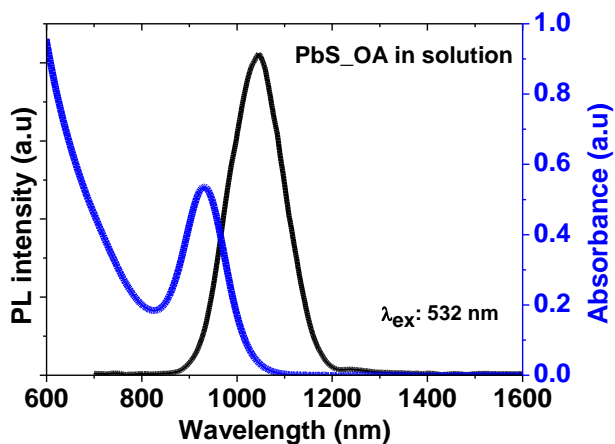
Fig V.S1. Photoluminescence (PL) and absorbance in solution of as-synthesized PbS QDs, with oleate ligand (OA), used in this work. For the PL measurement, the concentration of PbS_OA of 0.196 mg/ml in octane was prepared. And a laser of 532 nm was used as the excitation and a longpass filter 20CGA-590 was used in order to avoid the signal from the excitation source come to the CCD detector.

VS.2. Ligand exchange process
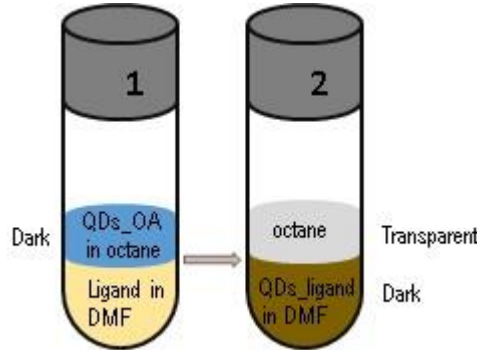
Fig V.S2. Phase transfer in the ligand exchange process of PbS QDs with 3 different ligands including 4-aminobenzoic acid (ABA), CsPI and MAPI. (1) Just mixing PbS_OA in octane with ligand in DMF. The top phase was dark which was PbS_OA dispersed in octane. The bottom phase was the ligand in DMF, which was yellow for MAPI and CsPI; colorless for ABA ligand. (2) After stirring/shaking the mixed solution, PbS QDs were transferred to the bottom phase, resulting the color change from dark to transparent of the top phase. Meanwhile the bottom phase became dark.

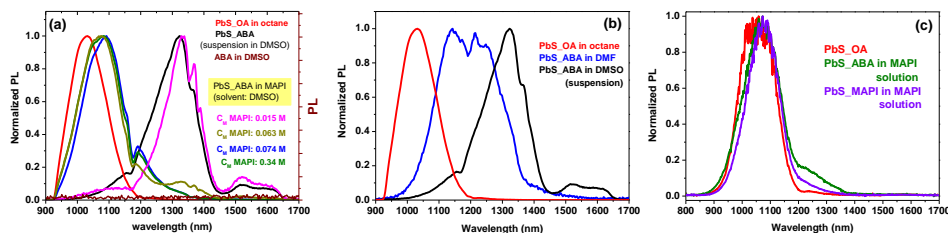## VS.3. Characterization of PbS QDs after the ligand exchange
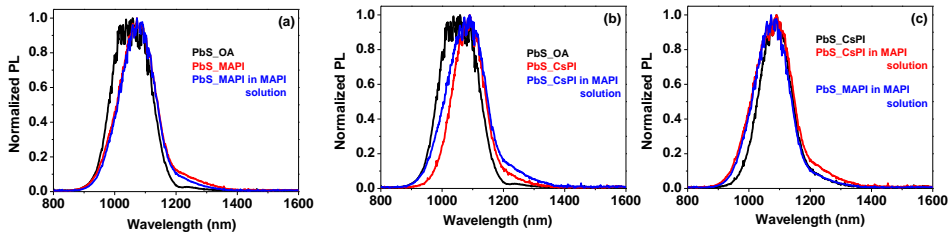
Fig V.S3. Photoluminescence (PL) in solution of PbS QDs before (as-synthesized, with OA capping ligand) and after the ligand exchange to MAPI (PbS_MAPI) and CsPI (PbS_CsPI); and after dispersing in HP perovskite precursor solution (PbI$_2$ and MAI). (a) PL spectra of the solutions correspond to MAPI and (b) CsPI capping ligands. (c) Comparison of PL of PbS_MAPI and PbS_CsPI in MAPI solution. PbS_OA QDs were dispersed in octane while PbS_MAPI and PbS_CsPI were dissolved in DMF. The solvent of PbS_MAPI or PbS_CsPI in MAPI solution was a mixture of DMF and DMSO with 10:0.95 volume ratio. The concentration of MAPI solution is 0.05 M. And the concentration of PbS QDs (with different capping ligands) was 1 mg/ml for all solutions. For the PL measurement, a laser of 532 nm was used as the excitation and a longpass filter 20CGA-590 was used in order to avoid the signal from the excitation source come to the CCD detector.

Fig. V.S3 presents the PL spectra of PbS before and after ligand exchange to MAPI and CsPI capping, and after dissolving in the solution containing MAPI precursors. In agreement with literature, after ligand exchange to both capping, MAPI and CsPI, we observed the redshift in PL spectra.[1-3] As previously reported, after the ligand exchange to MAPI or CsPI, the core/shell structure is formed.[2-3] Because of forming the shell probably QDs become bigger, hence reducing the confinement, leading the redshift in the PL spectra. Interestingly the PL spectrum of PbS_MAPI becomes narrower in a comparison with as-synthesized PbS_OA QDs (see Fig. V.S3a). And the PL spectrum is narrowest for the case of exchange to CsPI (see Fig V.S3b). This may result in improved QD passivation.[3] Moreover the PL spectra of PbS_MAPI and PbS_MAPI in a solution containing MAPI precursor are nearly identical, demonstrating the MAPI shell is not dissociated in the presence of MAPI precursors (see Fig V.S3a).[1] And for the case of PbS_CsPI, after dissolving in the MAPI solution, the position of PL peak was maintained, however the PL peak became larger, but still narrower than that of PbS_OA (see Fig V.S3b). For a better comparison, the PL of PbS_MAPI in MAPI solution was plotted together with PbS_CsPI and PbS_CsPI in MAPI solution (see Fig V.S3c). The PL of PbS_CsPI in MAPI solution was similar but not identical, suggesting CsPI shell interacts with MAPI precursors.

Fig V.S4. (a) Photoluminescence (PL) in solution of PbS QDs before (as-synthesized, with OA capping ligand) and after the ligand exchange to ABA capping (PbS_ABA) and after dispersing in a solution containing different concentration of HP precursors (PbI$_2$ and MAI). DMSO was the solvent for all solution in S4a except PbS_OA solution. The concentration of PbS in all solutions was ~ 0.46 mg/ml. (b) PL spectra of PbS_ABA in DMF and DMSO. (c) PL spectra of PbS_OA, PbS_ABA and PbS_MAPI in MAPI solution which was dissolved in a mixture of DMF and DMSO 10:0.95 v/v ratio. The concentration of PbS was 1 mg/ml for all solution in V.S4c. PbS_OA was dissolved in octane for all cases. PL spectra were measured using Fluorolog (a,b) and CCD systems (c). A 532 nm excitation wavelength and a longpass filter 20CGA-590 were used for both cases. The PL peak-shoulders wavelengths longer than 1100 nm probably due to the absorption of DMSO and DMF in the infrared.

Fig. V.S4a shows the PL spectra of PbS_OA, PbS_ABA in DMSO and PbS_ABA in DMSO with the presence of MAPI precursors with different concentrations. After ligand exchange to ABA, the solubility of PbS_ABA in DMSO is very limited and PbS_ABA QDs are unstable. They are precipitated

in DMSO after a short time, probably in one hour. The PL of PbS_ABA in DMSO (Fig V.S4a-b) was measured when PbS_ABA became precipitated (it is indicated as 'suspension'). Because of the aggregation of PbS_ABA in DMSO, strong red-shifts in PL were observed, in a comparison with as-synthesized PbS_OA QDs (Fig V.S4a). It is important to note that ABA does not emit, at least under our measurement conditions (excitation and detected wavelength window). Interestingly, by adding the precursors of MAPI, the solubility of PbS_ABA in DMSO was improved. At a very low concentration of MAPI, 0.015 M, PbS_ABA QDs are partially dissolved illustrated by reducing in PL peak's width at ~ 1300 nm and appearing the PL at ~ 1070 nm. And at 0.063 M of MAPI concentration, the solubility of PbS_ABA in DMSO was significantly enhanced. All the PL peaks after 1500 nm were disappeared and a strong reduction in PL intensity (~ 90%) of PL peak at ~ 1300 nm was observed. At the same time, the intensity of PL peak at ~ 1070 nm strongly increased. When the concentration of MAPI was increased to 0.074 M, no more aggregation of PbS_ABA was observed, the PL peak at ~ 1300 nm was completely disappeared. Further increasing in MAPI concentration did not lead to the change in PL peak's position. The improvement in PbS_ABA solubility in DMSO by the presence of MAPI precursors demonstrates a strong interaction of ABA and MAPI precursors.

As in the ligand exchange to ABA, DMF was used instead of DMSO, we compared PbS_ABA dissolved in DMSO and DMF. We experimentally found that the solubility of and stability of PbS_ABA in DMF are better than that in DMSO. However PbS_ABA in DMF still produced a strong redshift in PL (see Fig V.S4b). It is important to note that from naked eyes the solution was completely lucent. Similar to the case of DMSO solvent, in DMF solvent and in the presence of MAPI precursors, PL of PbS_ABA became blueshifted, to very close to PbS_OA before the exchange (see Fig V.S4c). Interestingly in the presence of MAPI precursors, PbS_ABA produced a larger redshift in DMSO than in DMF solvent (see Fig V.S4a and c), in a comparison with PbS_OA QDs, indicating that solvent's nature has a role on the interaction ABA with MAPI precursors. It is worth to note, the PL position was compared at the same PbS QD concentrations. And the PL spectra of PbS_ABA and PbS_MAPI in the presence of MAPI precursors are different, see Fig V.S4c, suggesting ABA still linked to PbS QDs.
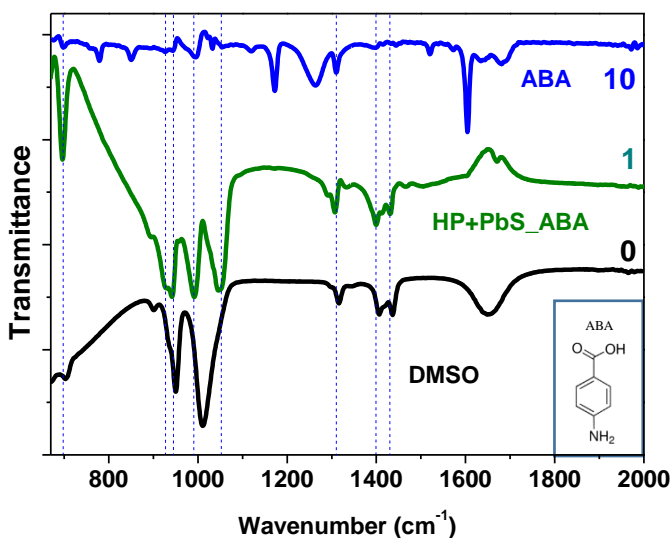
Fig V.S5. Fourier-transform infrared (FT-IR) measurement of DMSO, ABA solution in DMSO and HP+PbS_ABA in DMSO. Numbers correspond to amount of ABA in solutions. Number 1 is equivalent to 11.4 mg/ml. The concentration of PbS in HP+PbS_ABA solution is 8.3 mg/ml. Intensity of blue lines was triple. The samples were measured with DMSO as baseline. The insert presents the chemical structure of ABA.

Estimation of ABA amount. The ligand exchange from PbS_OA to PbS_ABA was described in the experimental section (section V.2.2 in the main text). 2 ml of 0.025 M ABA in a mixture of DMF+absolute ethanol and 2 ml of 2.5 mg/ml PbS_OA in octane were introduced in the ligand exchange. After the ligand exchange, QDs were dried and dispersed in 0.6 ml of 1.33 M HP precursor solution (MAI and PbI$_2$), the olive line in Fig. V.S5b. Assuming there was no loss during the ligand exchange, the concentration of PbS QDs and ABA were:

$$C_{PbS} = \frac{2 \; ml \; x \; 2.5 \; mg/ml}{0.6 \; ml} = 8.3 \; (\frac{mg}{ml})$$

$$C_{ABA} = \frac{0.025 \frac{mol}{l} x \; 137.14 \frac{g}{mol} \; x \; 2 \; ml}{0.6 \; ml} = 11.4 \; mg/ml$$

ABA in DMSO was prepared with concentration of 38 mg/ml and its FT-IR was triple, thus the concentration of ABA was considered as 38 x 3 = 114 mg/ml (corresponding to number 10, blue line).

The FT-IR measurement of ABA in DMSO shows a broad absorption with the appearance of many bands from 670 to 2000 cm^{-1}. The HP+PbS_ABA in DMSO exhibits the signals related to ABA. The band at 695 cm^{-1}, 990 cm^{-1}, 1050 cm^{-1} and 1307 cm^{-1} were observed probably due to the absorption of amine (N-H deformation vibration), aromatic carboxylic acid (O-H deformation vibration) and of carboxylic acid (C-O stretching and O-H deformation vibration) respectively.[4] The intensity of those bands is more intense in a comparison with ABA in DMSO. It is important to note that the amount ABA in DMSO is much higher than that in HP+PbS_ABA solution. On the hand, two intense bands at 1174 cm^{-1} and 1263 cm^{-1} were observed for ABA solution but not for HP+PbS_ABA samples while bands at lower intensity listed above were obtained even with higher intensity. This suggests the interaction of ABA with MAPI precursors. At wave number of 930 cm^{-1} and 1400 cm^{-1} HP+PbS_ABA in DMSO may have a signal related to ABA however the absorption of DMSO makes the analysis more complicated. The band at 1604 cm^{-1} probably due to the C=O stretching vibration of carboxylic acid from ABA was shifted to 1670 cm^{-1}.

VS.4. Characterization of HP+PbS QD films
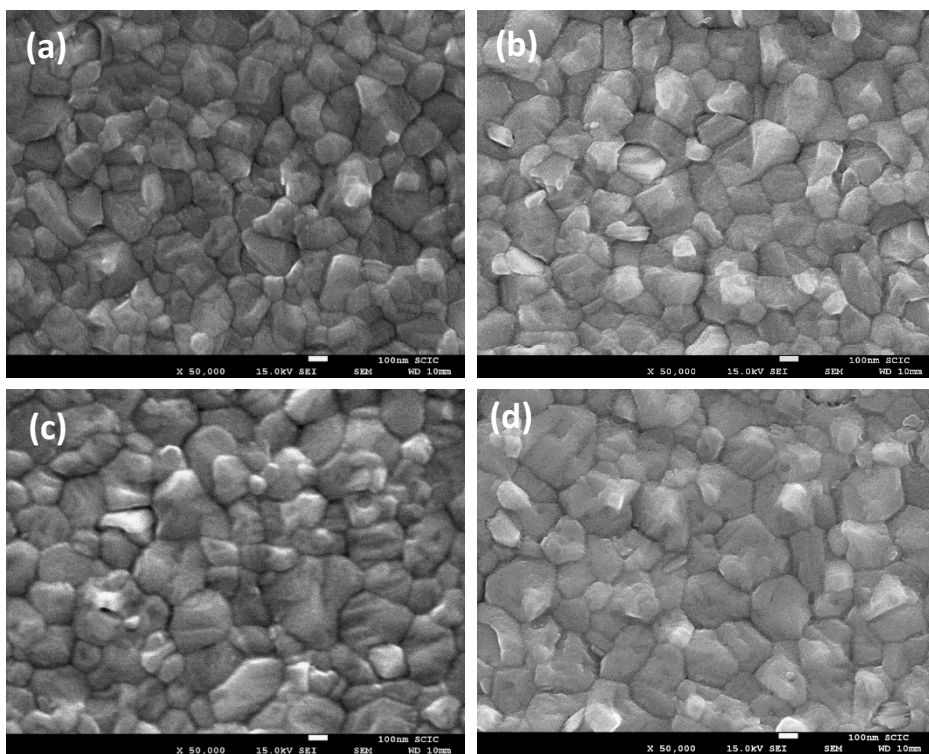
Fig V.S6. SEM of perovskite without (a) and with PbS QDs (50 µg/ml) in which PbS QDs had CsPI (b), MAPI (c) and 4-aminobenzoic acid (d) respectively. Bar scale in the figure was 100 nm.
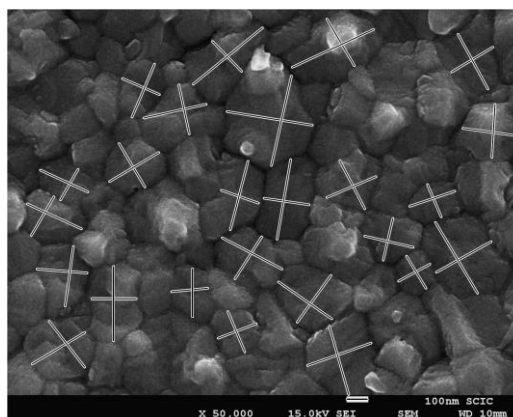
Fig V.S7. Estimation perovskite grain size from the top view SEM. The size of each grain is supposedly estimated by the average of two perpendicular lines crossing the grain with longest and shortest distance.
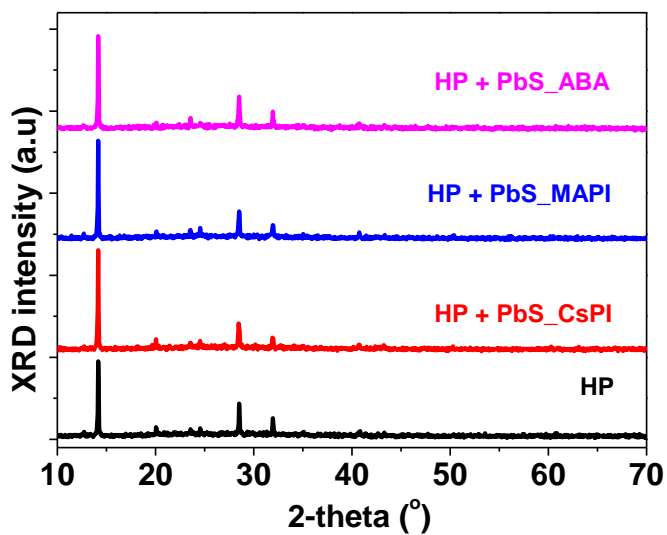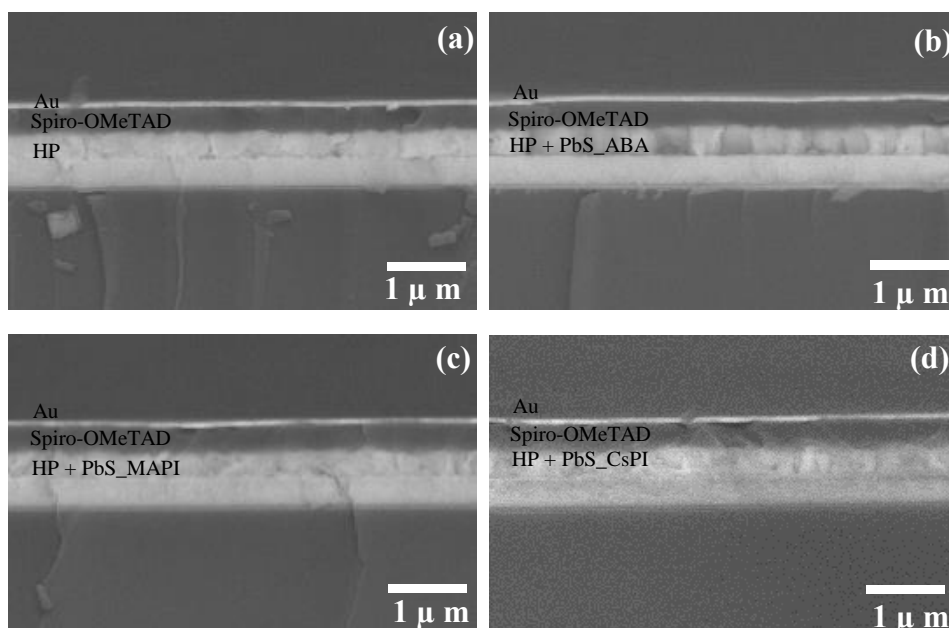
Fig V.S8. XRD of perovskite without (HP) and with PbS QDs (50 µg/ml) in which PbS QDs had CsPI, MAPI and 4-aminobenzoic acid respectively.

Fig V.S9. Cross section of FTO/SnO$_2$/absorber/spiro-OMeTAD/Au solar cells. In which absorber layer were perovskite (HP) without (a) and with PbS QDs 50 µg/ml (b-c) and 100 µg/ml (d). The ligand of PbS QDs were 4-aminobenzoic acid (ABA, b), MAPI (c) and CsPI (d).

VS.5. Characterization of HP+PbS QD based devices
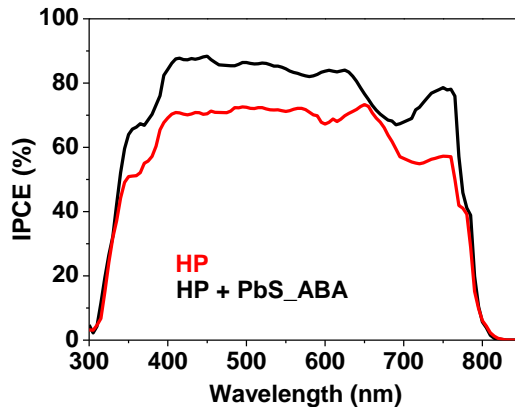
Fig V.S10. Incident photon to current efficiency (IPCE) of FTO/SnO$_2$/absorber/spiro-OMeTAD/Au solar cells, in which absorber layers were perovskite films without (HP) and with PbS QDs (50 µg/ml). The PbS QDs had 4-aminobenzoic acid (ABA) ligand.

References

1. Ngo, T. T.; Suarez, I.; Sanchez, R. S.; Martinez-Pastor, J. P.; Mora-Sero, I. Single step deposition of an interacting layer of a perovskite matrix with embedded quantum dots. *Nanoscale* **2016,** *8*, 14379-14383.
2. Yang, Z.; Janmohamed, A.; Lan, X.; García de Arquer, F. P.; Voznyy, O.; Yassitepe, E.; Kim, G.-H.; Ning, Z.; Gong, X.; Comin, R.; Sargent, E. H. Colloidal Quantum Dot Photovoltaics Enhanced by Perovskite Shelling. *Nano letters* **2015,** *15* (11), 7539-7543.
3. Zhang, X.; Zhang, J.; Phuyal, D.; Du, J.; Tian, L.; Öberg, V. A.; Johansson, M. B.; Cappel, U. B.; Karis, O.; Liu, J.; Rensmo, H.; Boschloo, G.; Johansson, E. M. J. Inorganic CsPbI3 Perovskite Coating on PbS Quantum Dot for Highly Efficient and Stable Infrared Light Converting Solar Cells. *Advanced Energy Materials* **2018,** *8* (6), 1702049.
4. Socrates, G. *Infrared and Raman characteristic group frequencies: tables and charts*. John Wiley & Sons: 2004.

Chapter VI

Enhancement of the Performance of Perovskite Solar cells, LEDs and Optical Amplifiers by Anti-Solvent Additive Deposition

VI.1. Candidate's contribution

The nature and extent of my contribution to the work in the chapter VI is described following:

Nature of contribution	Extent of contribution
- Provide a new method to introduce organic molecule additives into perovskite through the anti-solvent deposition step. - Preparation films and devices. - Characterization of films and devices: PL, SEM, EL, JV curves, IPCE, Voc decay and impedance spectroscopy measurements. - Preparation of the first draft of the manuscript.	**65 %**

VI.2. Published manuscript

Enhancement of the Performance of Perovskite Solar Cells, LEDs and Light Amplifiers by Anti-Solvent Additive Deposition

Thi Tuyen Ngo, Isaac Suarez, Gabriella Antonicelli, Diego Cortizo-Lacalle, Juan P. Martinez-Pastor,* Aurelio Mateo-Alonso* and Ivan Mora-Sero*

Thi Tuyen Ngo, Ass. Prof. Ivan Mora-Sero
Institute of Advanced Materials (INAM), Universitat Jaume I, 12006
Castelló, Spain.
E-mail: sero@uji.es
Dr. Isaac Suárez, Prof. Juan P. Martínez-Pastor
UMDO, Instituto de Ciencia de los Materiales, Universidad de Valencia,
46071 Valencia, Spain.
E-mail: Juan.Mtnez.Pastor@uv.es
Gabriella Antonicelli, Dr. Diego Cortizo-Lacalle, Prof. Aurelio Mateo-Alonso
POLYMAT, University of the Basque Country UPV/EHU, Avenida de
Tolosa 72, E-20018 Donostia-San Sebastian, Spain. Email:
amateo@polymat.eu
Prof. Aurelio Mateo-Alonso
Ikerbasque, Basque Foundation for Science, E-48011 Bilbao, Spain

Halide Perovskites (HP) have emerged as an outstanding material family for optoelectronic applications[1] because of their superior physical properties, such as high optical absorption coefficients,[2] benign defect physics,[3] long and balanced electron–hole diffusion lengths,[4] good charge transport properties even in polycrystalline films,[1a] and low non-radiative recombination.[5] Photoconversion efficiency (PCE) has reached 22.1%[6] a few years after the first reports on HP based liquid electrolyte solar cells in

135

2009.[7] Besides the application in photovoltaics, HP have been successfully employed in light emitting diodes (LED),[8] light amplifiers,[9] and lasers.[10] In addition, the success of these materials mainly lies in that high efficiency devices are prepared with HP polycrystalline films that can be grown using solution methods[5c, 11] at low processing temperatures and, consequently, using low cost fabrication techniques. Furthermore, these growth techniques allow the easy combination of HP with other materials, as for example PbS quantum dots,[12] that induce interesting synergies. This fact opens a broad range of possibilities for the interaction of HP with organic compounds beyond their use as selective contacts.[13] Organic compounds are appealing materials for electronic applications since an unlimited number of structures can be potentially synthesized and they are relatively easy to design and/or modify to meet the requirements of specific applications.

The passivation of HP plays a crucial role in the efficiency of HP-based devices as it has been shown that the presence of electron traps favors faster non-radiative decays, while long carrier lifetimes and high photoluminescence efficiencies are in general indicators of better performing HP layers. Exposure of HP films to electron deficient aromatic compounds such as pyridine[14] and PCBM[15] have resulted in enhanced efficiencies associated to the passivation of such electron traps. Among the myriad of different electron deficient aromatic compounds, nitrogen-containing polycyclic aromatic hydrocarbons (N-PAHs)[16] have recently reemerged as a platform for developing small molecule n-type semiconductors that have been able to compete with fullerenes in several applications.[17] In particular, N-PAHs containing pyrazine rings have attracted much attention as they combine a series of optimal optoelectronic and electric properties that can further tuned thanks to the recent development of straightforward and solid synthetic routes.[16]

We have developed a new method to introduce additives *in situ* in a halide perovskite thin film, during the anti-solvent deposition step.[11b, 11c, 18] Solar cell, LED and waveguide light amplifier devices have been prepared using the perovskite layer, concretely $CH_3NH_3PbI_3$ (MAPI), mixed separately with two different electron deficient heteroatom-doped PAHs, namely a twisted hexaazatrinaphthylene (HATNA)[16i, 19] and a bisthiadiazole-fusedtetraazapentacenequinone (DCL97)[20] (Figure VI.1). We have selected these two compounds among others as: i) they are novel compounds that have not been previously checked for passivation in perovskite optoelectronic devices; ii) they contain PAHs, that it has been reported to be excellent passivation agents,[14-15] displaying electrochemical LUMOs (or electron affinities) in the range of those observed for fullerene derivatives with excellent results for passivation;[15] iii) they possess different but

136

complementary electronic absorption spectra that allow the selective excitation for characterization purposes and also investigating if their absorption features might also play a role under illumination; iv) each one is soluble and chemically stable in a solvents that can be used in the anti-solving method.

With both molecules, we have observed a significant improvement of the performance of HP-based solar cell, LED and waveguide light amplifier devices. Photoconversion efficiency (PCE) of solar cells has been increased with respect to a reference cell, with no additives, while current/potential hysteresis decreased and solar cell stability increased. We have also observed an increase of the external quantum efficiency (eQE) for HP LEDs by a factor of 2-4 and the reduction of the light amplification threshold energy by a factor of 2-4 when organic additives are used. A systematic characterization of $CH_3NH_3PbI_3$ (MAPI) with additives points to a reduction in the non-radiative carrier recombination paths by the passivation of HP interface and grain boundaries in the polycrystalline film. They main scope of this work is to present a general method in order to increase the efficiency of perovskite optolectronic devices (solar cells, LEDs and light amplifiers), without introducing any additional step, and even using different solvents by the anti-solving method. The method proposed in the present paper offers the possibility to deposit perovskite mixed with many different organic and inorganic compounds, and opens a broad range of applications on perovskite optoelectronic devices as solar cells, LEDs and lasers.

There are several examples of the use of additives for the improvement of perovskite solar cells (PSCs). In most of the cases, these additives are introduced by dissolving them in the solution containing the perovskite precursors,[21] and in other cases a gaseous post treatment after the perovskite film formation is used.[14] When additives are incorporated to the solution of perovskite precursors, they play an important role in the growth of perovskite film and have an important impact in the film morphology. However, this method is restricted only to additives soluble in the non-polar solution with perovskite precursors.[21] Pyridine vapor exposure of a perovskite film decreases significantly the non-radiative recombination, however this method introduces an additional preparation step.[14] For other perovskite optoelectronic devices, there are significantly lower number of reports on the use of additives. Cho *et al.* reported record LED efficiencies by the use of 2,2′,2″-(1,3,5-benzinetriyl)-tris(1-phenyl-1-H-benzimidazole) (TPBI) additive dissolved in chloroform and using a multistep nanocrystal pinning process.[8b] This deposition process produces nanocrystalline grains,

increasing the LED current efficiency. However, this small grain size morphology does not seem to be optimum for solar cells.

We have developed a new approach that takes advantage of the anti-solvent deposition method,[11b, 11c, 18] that is, the method with which the highest PSC record efficiencies have been reported.[11a, 22] In this method, during the spin coating of *N,N*-dimethylformamide (DMF) solution, containing $CH_3NH_3PbI_3$ (hereafter MAPI) precursors (methylammonium iodide (MAI) and PbI_2), the sample is exposed to a second solvent with a non-polar character in which perovskite precursors are not soluble. This exposure produces the saturation of the solution and the fast precipitation of the precursors creating numerous perovskite nucleation centers and the corresponding formation of a flat, uniform and pinhole-free perovskite layer. Our approach consists of dissolving the additives in the anti-solvent and introduce them in the layer during the anti-solvent step, see the experimental section for more details.

HATNA and DCL97 are not soluble in DMF, which is the common solvent used for HP film fabrication. In this way, to combine HP and the organic compound in a single film, we dispersed the organic additive in an anti-solvent, which was used in the film preparation. Thin films of HP, organic additives and HP with the organic additive using the anti-solvent method have been deposited on glass substrates. The PL spectra of these layers are plotted in Figure VI.1b and VI.1c, for samples containing HATNA and DCL97, respectively. The PL spectra of HP and organic single layers are in good agreement with previous reports.[12a, 19a, 20] The PL of perovskite layer containing additives, hereafter HP-HATNA and HP-DCL97, contains PL traces of both compounds, as observed in Figure VI.1b and VI.1c, respectively, indicating their presence in the final film after the anti-solvent process. Note that in the case of HP-DCL97, Figure VI.1c, a new feature at ~650 nm not present in any of the PL spectra of the single layers is observed for the mixed sample. This peak is probably originated in the interaction between both materials, being its interpretation beyond the scope of this manuscript and it is under current research.
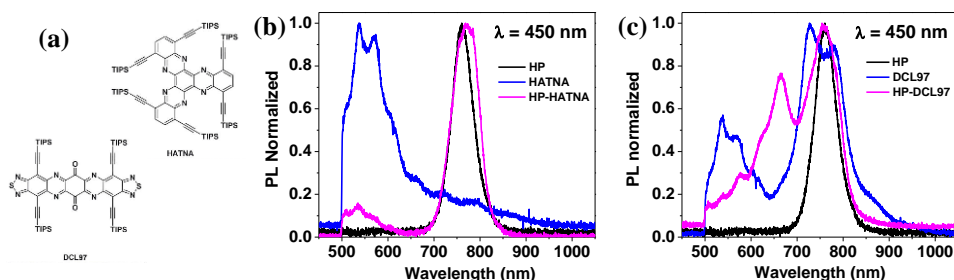
Figure VI.1: a) Scheme of the additives studied in this work. Normalized photoluminescence of perovskite (HP) reference layer **b)** HATNA film and HP with HATNA film and **c)** DCL97 and HP with DCL97.

We have not limited our study to a single type of devices and have extended the study to three different optoelectronic devices: solar cells, LEDs and waveguide light amplifiers to demonstrate the versatility of this general approach for the optoelectronic field. Solar cells were prepared using compact TiO_2 and (2,2′,7,7′-tetrakis(*N*,*N*-di-*p*-methoxyphenylamine)-9,9-spirobifluorene) (spiro-OMeTAD) as electron and hole selective contacts, respectively. Two configurations, planar and with TiO_2 mesoporous scaffold, have been analyzed. The current-voltage (J-V) curve for the prepared solar cells showed that the presence of the organic compounds improved the device performance depending on the organic concentration, see Figure VI.S1 and Table VI.S1. The concentration dependence study has been carried out preparing planar PSC samples with the following configuration: glass/FTO/compact TiO_2 /HP or HP-HATNA or HP- DCL97/spiro-OMeTAD/Au and using chlorobenzene as the anti-solvent. An increase of device efficiency, mainly due to an increase of the photocurrent, has been detected depending on the concentration, observing the highest increase for 50 mg/ml and 37.5 mg/ml for HATNA and DCL97 (see table VI.S1), respectively. In addition, solar cells containing mesoporous TiO_2 layer have been prepared with the following configuration: glass/FTO/compact TiO_2/mesoporousTiO$_2$/HP or HP-HATNA or HP-DCL97/spiro-OMeTAD/Au. For mesoporous configuration HATNA, 50 mg/ml, was introduced using diethyl ether as the anti-solvent. HATNA presents a good solubility in both diethyl ether and chlorobenzene, but high efficiency reference cells are obtained with diethyl ether instead of chlorobenzene. DCL97 is not soluble in diethyl ether, an consequently chlorobenzene has been chosen as anti-solvent in that case, allowing us to show the versatility of the method as it can be employed with different solvents. For TiO_2 mesoporous PSCs, all the photovoltaic parameters (short circuit current, J_{sc}, open circuit voltage, V_{oc}, fill factor, FF, and PCE) increase for the HP-HATNA sample in comparison with the reference HP sample, see Figure

139

VI.2a and Table VI.S2. Concretely, efficiency moves from close to 12% for the reference sample to close to 15% for HP-HATNA, see Table VI.S2, increasing a significant ~25%. It is also important to highlight that the HP-HATNA device is practically hysteresis free, see Figure VI.2a. In addition, HP-HATNA also presents a better long term stability behavior, see Figure VI.S2 and Table VI.S2. The analysis of incident photon to current efficiency (IPCE) shows a good agreement between the integrated photocurrent, see Figure VI.2b, and the J_{sc} measured in the J-V curve, see Figure VI.2a. In addition, IPCE unveils that the enhancement in the photocurrent for HP-HATNA samples is not due to the light harvesting (and subsequent charge collection) from HATNA molecules. IPCE for HP-HATNA has the same spectra that for the HP reference sample with an increased efficiency in all the wavelength range, and especially at longer wavelengths where HATNA does not absorb,[19a] see Figure VI.2b. These results point out to a clear enhancement of the perovskite layer performance by the use of HATNA additive rather than an improvement of the co-absorption by the presence of HATNA. In the case of DCL97, samples with configuration glass/FTO/compact TiO$_2$/mesoporousTiO$_2$/HP or HP-DCL97/spiro-OMeTAD/Au were also prepared, using chlorobenzene as the anti-solvent. In that case the efficiency of HP-DCL97 has increased ~75% respect a reference cell prepared with chlorobenzene anti-solvent. However in this case the reference samples without DCL97 are far away from optimization presenting a low efficiency, 5%, see Table VI.S3 for more details. Independently of the configuration, molecule employed and anti-solvent, we have observed systematically an increases of efficiency of the prepared solar cells respect the reference samples when additives were used, highlighting the huge potentiality of the method to increase the devices performance. Higher efficiencies can be expected after an accurate optimization process at each concrete configuration.

MAPI perovskite thin film with organic additives prepared by our method can be applied not only for increasing the performance of light harvesting devices, but also for light emitting systems. LEDs were prepared using HP, HP-HATNA and HP-DCL97 as active layers, and compact TiO$_2$ and spiro-OMeTAD as electron and hole transport materials respectively, following a previously reported configuration.[8a] The electroluminescence (EL) spectra of all the samples (HP, HP-HATNA and HP-DCL97) show only a peak corresponding to the perovskite emission with no parasitic contributions from the organic additives, see Figure VI.2c. The fabricated LEDs present a remarkably low threshold energy, as low as the MAPI bandgap, see Figure VI.2d. The use of additives increases the EQE by a factor of 2 and 4 for DCL97 and HATNA, respectively, as observed in Figure VI.2d.

The EQE presents its maximum value with an applied bias of 2V for the HP and HP-DCL97 samples, while for the HP-HATNA devices the maximum is observed at 2.5 V.
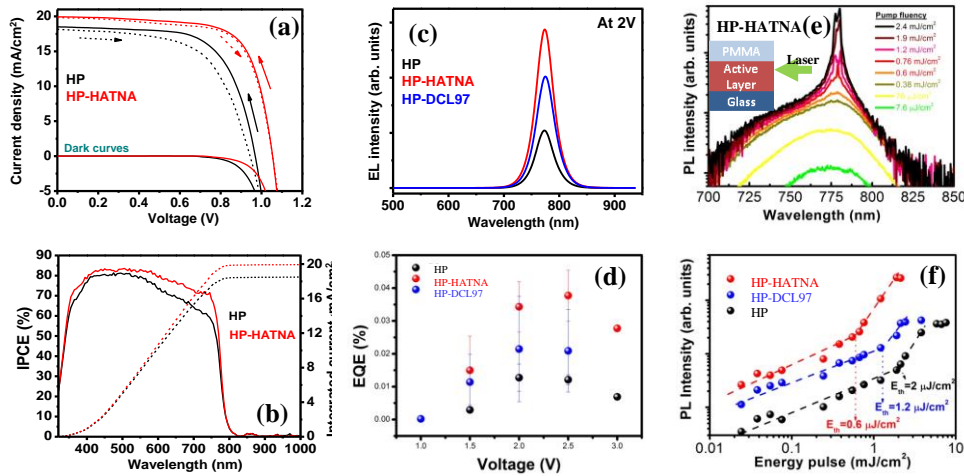

Figure VI.2: a) Current potential curve of a perovskite reference solar cell and of a perovskite with HATNA additive introduced during the anti-solving step, under dark and under 1 sun illumination, forward and reverse scans are plotted in order to show the hysteresis behavior. **b)** Incident photon to current efficiency (right axis, solid lines) and the integrated photocurrent (left axis, dashed lines) of the devices depicted in a). **c)** Electroluminescence of LEDs prepared with perovskite and perovskite with HATNA and DCL97 additives as active layer at an applied forward bias of 2 V. **d)** External quantum efficiency on the prepared LEDs. **e)** Photoluminescence obtained with side excitation,[9] see inset, of perovskite with HATNA additive deposited on glass and with a PMMA capping, see inset. Sample PL has been recorded with different excitation powers. **f)** PL intensity as function of excitation power of perovskite reference and perovskite with HATNA and DCL97 additives films sandwiched between glass and PMMA layers.

We have also investigated the anti-solvent deposition of additives in perovskite films for light amplification. Waveguide light amplifier devices were prepared using HP reference layer or HP with organic additives (HATNA or DCL97) as active layer sandwiched between glass and PMMA layer, see inset Figure VI.2e, following a configuration previously developed by us.[9] These active layers were excited by one of their side faces, see inset Figure VI.2e, by means of a pulsed laser at 533 nm. Figure VI.2e shows the emitted light spectra measured at the opposite face end for the HP-HATNA sample at different pump powers. The spectra for HP and HP-DCL97 planar waveguides are plotted in Figure VI.S3. Waveguided PL spectra correspond to that of the perovskite layer centered around 780 nm, but collapse into a narrow line for high enough pump fluencies (see Figure VI.2e), which

integrated intensity grows super-linearly, as observed in Figure VI.2f. Both are clear signatures of stimulated emission that exhibits a reduction of the energy threshold by factor of 2 or 4, when the additives DCL97 or HATNA are incorporated respectively into the HP film (Figure VI.2f and VI.S3). Another characteristic signature of the stimulated emission regime is the decrease of the PL recombination time. Time resolved PL (TRPL) analysis has been carried out to determine the characteristic decay time of the waveguided PL (Figure VI.S4) that reached our experimental system temporal response (and consequently cannot be further determined) for pump fluencies higher than 0.72, 0.5 and 0.1 nJ for HP, HP-DCL97 and HP-HATNA samples, respectively, in good agreement with the lower stimulated emission energy threshold observed in Figure VI.2f for films made by incorporating additives.

To gain further insight into the origin of the general enhancement in device performance observed for perovskite optoelectronic devices (*i.e.* solar cells, LEDs and light amplifiers), a systematic characterization by X-Ray Diffraction, scanning electron microscopy (SEM) and impedance spectroscopy (IS) has been carried out. XRD spectra of the films of perovskite with additive do not present any significant variation respect reference perovskite layer produced without additives, see Figure VI.S6, indicating no change in the crystallite size or in the preferential orientation. Moreover, a systematic characterization of the perovskite films prepared with and without additives has been carried out, see Figure VI.S7. The use of additives have a clear interfacial effect. While the use of HATNA produces an organic capping layer, that is removed when spiro-OMeTAD is deposited, the addition of DCL97 changes the roughness and surface morphology, but with no change of perovskite grain size in both cases, see Supporting Information section VI.S7 and Figure VI.S7 for more details. Consequently a first effect of the additives is the modification of the interface that could induce a beneficial effect in the final cell performance.

HP and HP-HATNA with mesoporous TiO_2 configuration have been analyzed under 0.09 sun intensity at different applied voltages. The obtained Nyquist plots at 0 V are plotted in Figure VI.3a. Two basic features at high and lower frequencies are observed. The impedance spectra have been fitted using the equivalent circuit recently reported, see Figure VI.S5. Figure VI.3b plots the resistance of the low frequency arc, R_1, obtained from the fitting of impedance spectra. R_1 is related to the charge carrier recombination (*i.e.* inversely related with the recombination rate).[23] Figure VI.3b shows the increase in recombination resistance when HATNA additive was introduced into HP film, indicating that the efficiency enhancement observed for devices with additives are due to a decrease of recombination. Dark J-V curves, see

Figure VI.2a, and open circuit voltage decay, see Figure VI.S8, are also in an agreement with this conclusion. Impedance spectroscopy cannot determine the origin of the recombination. However, for radiative recombination in perovskite solar cells has been characterized by time-resolved PL observing PL decay times in the order of tens-hundreds of ns,[4, 12b] consequently the recombination detected by impedance at µs and slower scales has a different origin been a non-radiative recombination.
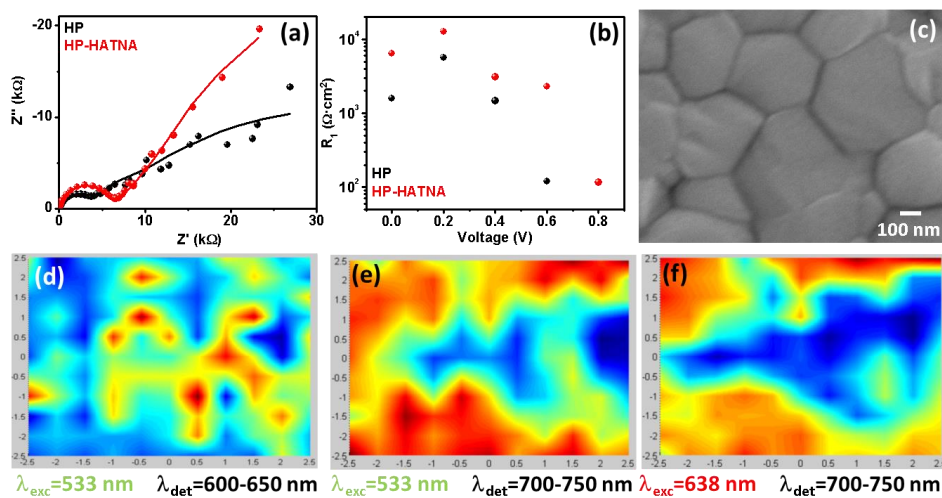

Figure VI.3: a) Nyquist plot of perovskite and perovskite with HATNA additive solar cells, plotted in Figure VI.2a, with mesoporous TiO_2 configuration and using diethyl ether as anti-solving solvent, under 0.09 sun illumination at 0 V applied bias. Symbols correspond to the experimental points while solid line is the fitting of the impedance spectra using equivalent circuit in Figure VI.S5.[24] **b)** R_1 resistance related with the recombination resistance of perovskite and perovskite with HATNA additive solar cells.[23] **c)** SEM picture of a cross section of perovskite planar layer film. Photoluminescence intensity map of a sample of perovskite with DCL97 additive, excitation wavelength, λ_{exc}, and the range of detected wavelengths, λ_{det}, are indicated in each map. **d)** PL from DCL97, where PL from perovskite has been subtracted, see Figure VI.S9, for further details. **e)** and **f)** PL from perovskite, see Figure VI.S9 for further details, for two different λ_{exc}. Vertical and horizontal scales for the maps are in µm.

Finally, to understand in which way the additives introduced by the anti-solvent deposition method reduces recombination in the perovskite layers, a PL mapping of the film surface has been carried out using a commercial Scientific Xplora micro-Raman system with 533 nm and 638 nm laser excitation. The integration of PL at different detection wavelengths, λ_{det}, for HP-DCL97 sample and the subtraction of the HP PL allows to obtain a mapping of the DCL97 PL, Figure VI.3d, and HP PL, Figure VI.3e, see Figure

VI.S9 for further details of the decoupling of both PL contributions. These results have been doubly checked by using a second excitation wavelength, λ_{exc} =638 nm, see Figure VI.3f. Comparing, the PL maps in Figures VI.3d and VI.3e are clearly complementary: the maximum intensities of PL from DCL97 are observed in areas where the PL from HP is minimum and vice versa. Moreover, the observed PL valleys and peaks form a network with features of hundreds nm, similar to the grain size observed in HP films by SEM (Figure VI.3c). A similar analysis performed on different parts of the HP-DCL97 sample surface yielded analogous results, as shown in Figure VI.S10 for the PL map in a different place of the sample surface. This complementary PL emission coinciding with the perovskite grain size points out the hypothesis that DCL97 molecules tend to locate at the grain boundaries of the perovskite film. Hence, the main role of the introduced additives to decrease the recombination of HP film is the passivation of the grain boundaries. Passivation of grain boundaries has previously shown beneficial effects for the increase of the solar cell photoconversion efficiency,[15] PL emission,[14] and the stability of HP devices.[25]

Through this versatile and general approach (three different optoelectronic devices, two different additive molecules, two different configurations with mesoporous scaffold and planar devices, two different solvent for the anti-solving step) we observe a systematic increase of performance in all the cases when additives are used. In this work, we show by XRD that additives do not produce a change in the crystallite size or preferential orientation while grain size is not modified as it has been determined by the SEM analysis. The main role of additive is the passivation of the grain boundaries and/or perovskite interface because electron-deficient N-PAHs produces a reduction of non-radiative recombination that leads to a notable increase of the main figures of merit of perovskite optoelectronic devices, including solar cells, LEDs and light amplifiers. The process consists in the introduction of additives in an anti-solvent during the perovskite spin coating deposition. We have used this method to increase systematically the performance of perovskite solar cells with planar and mesoscopic configurations, the eQE of perovskite LEDs by a factor of 2-4 and to reduce the stimulate emission threshold by a factor of 2-4 by the introduction of DCL97 and HATNA additives in comparison with devices prepared in the same way with the same anti-solvent but without additives. The use of DCL97 and HATNA additives has allowed us to verify the presence of the additives in the prepared film by PL measurements and to track the final situation of these molecules in the film, detecting their presence at the grain boundaries. We have also observed a decrease of the HP recombination due to the use of additives by impedance spectroscopy. These observations point to a

passivating effect of the grain boundaries by the introduction of additives. It is important to highlight that it is a general method that can be used for the introduction of a broad range of different additives. The design of specific additives with particular properties or functionalization can enhance further the performance of the optoelectronic devices. For example, the lower threshold energy obtained for the HP-HATNA films in comparison to the HP-DCL97 is probably due to the fact that HATNA does not absorb light at the excitation wavelength, but still passivating the perovskite layer. This work opens an interesting research field on the interaction of perovskite with other compounds with important implications in the enhancement of the perovskite optoelectronic devices.

Experimental Section

*Synthesis of HATNA and DCL97:*The synthesis of HATNA[16i, 19] and DCL97[20] was carried out following previously reported methods and scaled-up accordingly to obtain ~100 mg batches.

TiO$_2$ compact layer: SnO$_2$:F (FTO) substrates were cleaned with soap, sonicated in distilled water, ethanol and a mixture of acetone/isopropanol (30:70 v/v ratio) for 15minutes and then treated with an UV (ultraviolet)−O$_3$ lamp for 15minutes. The TiO$_2$ compact layers were manually deposited by spray pyrolysis at 450°C, consuming 5ml of a solution of titanium di-isopropoxide bis(acetylacetonate, 75% vol. 2-propanol) in absolute ethanol (1:9, v/v ratio); the films were annealed at 450°C for 30 minutes.

TiO$_2$ mesoporous (scaffold): TiO$_2$ paste (Dyesol 30NRd, 30 nm average particle size) dissolved in absolute ethanol (150 mg/ml) was spin coated on TiO$_2$ compact layers at 1500 rpm from. The films were pre-heated at 100°C for 10 minutes and then at 500°C for 30 minutes.

Perovskite solution: 622 mg (1.35 mmol) of PbI$_2$ was added in the solution containing 1ml of DMF and 95 µl of dimethyl sulfoxide (DMSO). This solution was heated at 65°C to dissolve PbI$_2$, then cooled to room temperature. Subsequently PbI$_2$ solution was poured into a container containing 215 mg (1.35 mmol) of MAI to make final solution for HP deposition.

Perovskite film deposition: HP films were prepared by spin coating at 4000 rpm for substrates with mesoporousTiO$_2$ scaffolds and at 5000 rpm for substrates only with TiO$_2$ compact layer. Anti-solvent (chlorobenzene or diethyl ether) ~ 200 µl, was poured in the films when the spin coater was

running after 7s of spinning start. Perovskite films were annealed at 65ºC for 1 minute and consequently 100ºC for 2 minutes.

Organic additive solutions: HATNA and DCL97 solutions were prepared by dissolving HATNA or DCL97 in anti-solvent (chlorobenzene or diethyl ether) separately with the concentration varying from 12.5 to 50 mg/ml. Reference perovskite films have been prepared using both solvents, diethyl ether and chlorobenzene, during the anti-solving step but without additives. For a fair comparison each sample prepared with additives is compared with a reference perovskite sample which was prepared using the same solvent during the anti-solving step.

Spiro-OMeTAD and Gold: Spiro-OMeTAD solution was prepared by dissolving 72.3 mg spiro-OMeTAD(2,2′,7,7′-tetrakis(*N,N*-di-*p*-methoxyphenylamine)-9,9-spirobifluorene) in 1 ml of chlorobenzene, then mixed with 28.8 µl of 4-*tert*-butylpyridine and 17.5 µl of a stock Li$^+$ solution (which contained 520 mg/ml *bis*-trifluoromethylsulfonylamine lithium salt in acetonitrile). Spiro OMeTAD layer was spin coated on HP or HP with additives films at 4000 rpm for 30s. Finally, 60 nm of gold were thermally evaporated in an ultrahigh vacuum chamber on top of a Spiro-OMeTAD layer as charge extracting contact.

Characterization: The morphology of the films was analyzed by scanning electron microscopy (SEM) using a JSM7001F (field emission scanning electron microscope). J-V curves of solar cells were measured under a xenon arc lamp simulator equipped with an AM 1.5 spectral filter (Sun 2000, ABET Technologies). The intensity was adjusted to provide 1 sun (100 mW cm^{-2}) by using a calibrated silicon solar cell. The *J-V* characteristics were recorded by scanning the potential from high voltage to zero (reverse mode) and from zero to high voltage (forward mod) at approximately 45 mV/s. The IPCE measurements were performed employing a 150 W Xenon lamp coupled with a computer-controlled monochromator; the photocurrent was measured using an optical power meter 70310 from Oriel Instruments, using a Si photodiode to calibrate the system. The impedance spectroscopy measurements were performed under 0.09 sun illumination, calibrated with an NREL-calibrated Si solar cell, and under N$_2$ flow. The measurements were carried out by means of a FRA equipped PGSTAT-30 from Autolab at different forward voltage bias and applying a 20 mV voltage AC perturbation over the constant applied bias with the frequency ranging between 1 MHz and 0.05 Hz. The use of 0.09 sun illumination prevent cell degradation during the impedance measurement, see Fig. VI.S11, and also keep the illumination conditions as it has been shown that working conditions of perovskite layer varies significantly when the layer

is illuminated.[23b] The EL spectra of LED devices based on HP absorber without and with organic compounds (HATNA or DCL97) in situ were obtained by using a spectrophotometer based on a CCD detector (Andor-iDUSDV420A-OE) synchronized with the potentiostat (Gamry Reference 3000). The combination of both apparatus allowed registering optical variations (absorbance, transmittance, light emission, etc.) while applying an external electrical stimulus (voltage or current) with a maximum time resolution in the milliseconds scale. EL measurements have been carried out under dark conditions and under N_2 flow at room temperature. The eQE measurements were performed by calibrating the optical equipment with a commercial GaAs infrared LED (model EL-23G, peak emission centered at λ_{max}= 940 nm, 28.3 $W \cdot sr^{-1} \cdot m^{-2}$). Photoluminescence (PL) experiments were carried out by pumping the surface of the samples with a 533 nm DSPP (diode pumped solid state) laser and a 780 nm semiconductor diode. Back scattered PL was then collected with the aid of a microscope objective and dispersed in an Ocean Optics HR4800 spectrograph.

Stimulated emission experiments were performed by exciting the surface of the samples with aNd:Yag 533nm pulsed laser (1 ns, 20 KHz) and collecting the emitted PL with a 20x microscope objective. PL spectra were obtained by dispersing the light in an Ocean Optics HR4800 spectrograph, and time resolved photoluminescence (TRPL) were carried out by focusing the PL into a Hamamatsu C5658-3769 avalanche photodetector connected to a BOXCARDPCS-150 electronics from Becker & Hickl GmbH. The PL map were obtained by using a commercial Scientific Xplora micro-Raman system with 533 nm and 638 nm laser excitation. XRD has been characterized employing a Bruker AXS-D4 Endeaver Advance X-ray diffractometer using Cu Kα radiation.

Supporting Information
Supporting Information is available online from the Wiley Online Library or from the author.

147

[1]   a) T. M. Brenner, D. A. Egger, L. Kronik, G. Hodes, D. Cahen, *Nature Reviews Materials* **2016**, *1*, 15007;b) M. A. Green, A. Ho-Baillie, H. J. Snaith, *Nat Photon* **2014**, *8*, 506-514;c) S. D. Stranks, H. J. Snaith, *Nat Nano* **2015**, *10*, 391-402;d) B. R. Sutherland, E. H. Sargent, *Nat Photon* **2016**, *10*, 295-302.

[2]   S. De Wolf, J. Holovsky, S.-J. Moon, P. Löper, B. Niesen, M. Ledinsky, F.-J. Haug, J.-H. Yum, C. Ballif, *The Journal of Physical Chemistry Letters* **2014**, *5*, 1035-1039.

[3]   a) W.-J. Yin, T. Shi, Y. Yan, *Advanced Materials* **2014**, *26*, 4653-4658;b) W.-J. Yin, T. Shi, Y. Yan, *Applied Physics Letters* **2014**, *104*, 063903.

[4]   a) S. D. Stranks, G. E. Eperon, G. Grancini, C. Menelaou, M. J. P. Alcocer, T. Leijtens, L. M. Herz, A. Petrozza, H. J. Snaith, *Science* **2013**, *342*, 341-344;b) G. Xing, N. Mathews, S. Sun, S. S. Lim, Y. M. Lam, M. Grätzel, S. Mhaisalkar, T. C. Sum, *Science* **2013**, *342*, 344-347.

[5]   a) W. Tress, N. Marinova, O. Inganäs, M. K. Nazeeruddin, S. M. Zakeeruddin, M. Graetzel, *Advanced Energy Materials* **2015**, *5*, n/a-n/a;b) J. S. Manser, P. V. Kamat, *Nat Photon* **2014**, *8*, 737-743;c) D. Bi, W. Tress, M. I. Dar, P. Gao, J. Luo, C. Renevier, K. Schenk, A. Abate, F. Giordano, J.-P. Correa Baena, J.-D. Decoppet, S. M. Zakeeruddin, M. K. Nazeeruddin, M. Grätzel, A. Hagfeldt, *Science Advances* **2016**, *2*, e1501170.

[6]   M. A. Green, K. Emery, Y. Hishikawa, W. Warta, E. D. Dunlop, *Progress in Photovoltaics: Research and Applications* **2016**, *24*, 905-913.

[7]   A. Kojima, K. Teshima, Y. Shirai, T. Miyasaka, *Journal of the American Chemical Society* **2009**, *131*, 6050-6051.

[8]   a) O. A. Jaramillo-Quintero, R. S. Sanchez, M. Rincon, I. Mora-Sero, *The Journal of Physical Chemistry Letters* **2015**, *6*, 1883-1890;b) H. Cho, S.-H. Jeong, M.-H. Park, Y.-H. Kim, C. Wolf, C.-L. Lee, J. H. Heo, A. Sadhanala, N. Myoung, S. Yoo, S. H. Im, R. H. Friend, T.-W. Lee, *Science* **2015**, *350*, 1222-1225;c) Z.-K. Tan, R. S. Moghaddam, M. L. Lai, P. Docampo, R. Higler, F. Deschler, M. Price, A. Sadhanala, L. M. Pazos, D. Credgington, F. Hanusch, T. Bein, H. J. Snaith, R. H. Friend, *Nat Nano* **2014**, *9*, 687-692;d) L. Gil-Escrig, G. Longo, A. Pertegas, C. Roldan-Carmona, A. Soriano, M.

Sessolo, H. J. Bolink, *Chemical Communications* **2015**, *51*, 569-571;e) Y.-H. Kim, H. Cho, J. H. Heo, T.-S. Kim, N. Myoung, C.-L. Lee, S. H. Im, T.-W. Lee, *Advanced Materials* **2015**, *27*, 1248-1254.

[9]   I. Suárez, E. J. Juárez-Pérez, J. Bisquert, I. Mora-Seró, J. P. Martínez-Pastor, *Advanced Materials* **2015**, *27*, 6157-6162.

[10] a) G. Xing, N. Mathews, S. S. Lim, N. Yantara, X. Liu, D. Sabba, M. Grätzel, S. Mhaisalkar, T. C. Sum, *Nat Mater* **2014**, *13*, 476-480;b) F. Deschler, M. Price, S. Pathak, L. E. Klintberg, D.-D. Jarausch, R. Higler, S. Hüttner, T. Leijtens, S. D. Stranks, H. J. Snaith, M. Atatüre, R. T. Phillips, R. H. Friend, *The Journal of Physical Chemistry Letters* **2014**, *5*, 1421-1426;c) H. Zhu, Y. Fu, F. Meng, X. Wu, Z. Gong, Q. Ding, M. V. Gustafsson, M. T. Trinh, S. Jin, X. Y. Zhu, *Nat Mater* **2015**, *14*, 636-642.

[11] a) W. S. Yang, J. H. Noh, N. J. Jeon, Y. C. Kim, S. Ryu, J. Seo, S. I. Seok, *Science* **2015**, *348*, 1234-1237;b) N. J. Jeon, J. H. Noh, Y. C. Kim, W. S. Yang, S. Ryu, S. I. Seok, *Nat Mater* **2014**, *13*, 897-903;c) N. Ahn, D.-Y. Son, I.-H. Jang, S. M. Kang, M. Choi, N.-G. Park, *Journal of the American Chemical Society* **2015**, *137*, 8696-8699.

[12] a) T. T. Ngo, I. Suarez, R. S. Sanchez, J. P. Martinez-Pastor, I. Mora-Sero, *Nanoscale* **2016**;b) R. S. Sanchez, M. S. de la Fuente, I. Suarez, G. Muñoz-Matutano, J. P. Martinez-Pastor, I. Mora-Sero, *Science Advances* **2016**, *2*, e1501104;c) X. Gong, Z. Yang, G. Walters, R. Comin, Z. Ning, E. Beauregard, V. Adinolfi, O. Voznyy, E. H. Sargent, *Nat Photon* **2016**, *10*, 253-257;d) Z. Ning, X. Gong, R. Comin, G. Walters, F. Fan, O. Voznyy, E. Yassitepe, A. Buin, S. Hoogland, E. H. Sargent, *Nature* **2015**, *523*, 324-328;e) S.-S. Li, C.-H. Chang, Y.-C. Wang, C.-W. Lin, D.-Y. Wang, J.-C. Lin, C.-C. Chen, H.-S. Sheu, H.-C. Chia, W.-R. Wu, U. S. Jeng, C.-T. Liang, R. Sankar, F.-C. Chou, C.-W. Chen, *Energy & Environmental Science* **2016**, *9*, 1282-1289.

[13] S. F. Völker, S. Collavini, J. L. Delgado, *ChemSusChem* **2015**, *8*, 3012-3028.

[14] D. W. de Quilettes, S. M. Vorpahl, S. D. Stranks, H. Nagaoka, G. E. Eperon, M. E. Ziffer, H. J. Snaith, D. S. Ginger, *Science* **2015**, *348*, 683-686.

[15] Y. Shao, Z. Xiao, C. Bi, Y. Yuan, J. Huang, *Nat Commun* **2014**, *5*, 5784.

[16] a) A. Mateo-Alonso, *Chem. Soc. Rev.* **2014**, *43*, 6311--6324;b) U. H. F. Bunz, J. U. Engelhart, B. D. Lindner, M. Schaffroth, *Angew. Chem. Int. Ed.* **2013**, *52*, 3810-3821;c) U. H. F. Bunz, *Chem. Eur. J.* **2009**, *15*, 6780-6789;d) M. Stępień, E. Gońka, M. Żyła, N. Sprutta, *Chem. Rev.* **2016**;e) A. B. Marco, C. Gozalvez, M. Olano, X. Sun, A. Atxabal, M. Melle-Franco, L. E. Hueso, A. Mateo-Alonso, *Physical Chemistry Chemical Physics* **2016**, *18*, 11616-11619;f) L. Jiang, A. C. Papageorgiou, S. C. Oh, Ö. Sağlam, J. Reichert, D. A. Duncan, Y.-Q. Zhang, F. Klappenberger, Y. Guo, F. Allegretti, S. More, R. Bhosale, A. Mateo-Alonso, J. V. Barth, *ACS Nano* **2016**, *10*, 1033-1041;g) A. B. Marco, D. Cortizo-Lacalle, C. Gozalvez, M. Olano, A. Atxabal, X. Sun,

M. Melle-Franco, L. E. Hueso, A. Mateo-Alonso, *Chem. Commun.* **2015**, *51*, 10754-10757;h) R. Garcia, M. Melle-Franco, A. Mateo-Alonso, *Chem. Commun.* **2015**, *51*, 8037-8040;i) D. Cortizo-Lacalle, A. Pertegas, L. Martinez-Sarti, M. Melle-Franco, H. J. Bolink, A. Mateo-Alonso, *J. Mater. Chem. C* **2015**, *3*, 9170-9174;j) S. More, S. Choudhary, A. Higelin, I. Krossing, M. Melle-Franco, A. Mateo-Alonso, *Chem. Commun.* **2014**, *50*, 1976-1979;k) S. More, R. Bhosale, A. Mateo-Alonso, *Chem. Eur. J.* **2014**, *20*, 10626–10631;l) M. Grzelczak, N. Kulisic, M. Prato, A. Mateo-Alonso, *Part. Part. Syst. Charact.* **2014**, *31*, 121-125;m) R. García, S. More, M. Melle-Franco, A. Mateo-Alonso, *Org. Lett.* **2014**, *16*, 6096-6099;n) S. More, R. Bhosale, S. Choudhary, A. Mateo-Alonso, *Org. Lett.* **2012**, *14*, 4170-4173;o) N. Kulisic, S. More, A. Mateo-Alonso, *Chem. Commun.* **2011**, *47*, 514-516;p) A. Mateo-Alonso, N. Kulisic, G. Valenti, M. Marcaccio, F. Paolucci, M. Prato, *Chem. Asian. J.* **2010**, *5*, 482-485;q) M. Grzelczak, N. Kulisic, M. Prato, A. Mateo-Alonso, *Chem. Commun.* **2010**, *46*, 9122-9124;r) A. Mateo-Alonso, C. Ehli, K. H. Chen, D. M. Guldi, M. Prato, *J. Phys. Chem. A* **2007**, *111*, 12669-12673;s) A. M. Alonso, R. Horcajada, M. Motevalli, J. H. P. Utley, P. B. Wyatt, *Org. Biomol. Chem.* **2005**, *3*, 2842-2847;t) A. M. Alonso, R. Horcajada, H. J. Groombridge, R. Chudasama, M. Motevalli, J. H. P. Utley, P. B. Wyatt, *Org. Biomol. Chem.* **2005**, *3*, 2832-2841;u) A. M. Alonso, R. Horcajada, H. J. Groombridge, R. Mandalia, M. Motevalli, J. H. P. Utley, P. B. Wyatt, *Chem. Commun.* **2004**, 412-413;v) G. J. Richards, J. P. Hill, T. Mori, K. Ariga, *Org. Biomol. Chem.* **2011**, *9*, 5005-5017;w) U. H. F. Bunz, *Pure and Applied Chemistry* **2010**, *82*, 953-968;x) G. J. Richards, J. P. Hill, N. K. Subbaiyan, F. D'Souza, P. A. Karr, M. R. J. Elsegood, S. J. Teat, T. Mori, K. Ariga, *J. Org. Chem.* **2009**, *74*, 8914-8923.

[17]   a) J. E. Anthony, A. Facchetti, M. Heeney, S. R. Marder, X. Zhan, *Adv. Mater.* **2010**, *22*, 3876-3892;b) Z. Liang, Q. Tang, J. Liu, J. Li, F. Yan, Q. Miao, *Chemistry of Materials* **2010**, *22*, 6438-6443.

[18]   M. Xiao, F. Huang, W. Huang, Y. Dkhissi, Y. Zhu, J. Etheridge, A. Gray-Weale, U. Bach, Y.-B. Cheng, L. Spiccia, *Angewandte Chemie* **2014**, *126*, 10056-10061.

[19]   a) G. Tregnago, C. Fléchon, S. Choudhary, C. Gozalvez, A. Mateo-Alonso, F. Cacialli, *App. Phys. Lett.* **2014**, *105*, 143304;b) F. Selzer, C. Falkenberg, M. Hamburger, M. Baumgarten, K. Müllen, K. Leo, M. Riede, *Journal of Applied Physics* **2014**, *115*, 054515;c) J. Clark, R. Archer, T. Redding, C. Foden, J. Tant, Y. Geerts, R. H. Friend, C. Silva, *J. App. Phys.* **2008**, *103*, 124510.

[20]   D. Cortizo-Lacalle, C. Gozalvez, M. Olano, X. Sun, M. Melle-Franco, L. E. Hueso, A. Mateo-Alonso, *Organic Letters* **2015**, *17*, 5902-5905.

[21]   a) X. Li, M. Ibrahim Dar, C. Yi, J. Luo, M. Tschumi, S. M. Zakeeruddin, M. K. Nazeeruddin, H. Han, M. Grätzel, *Nat Chem* **2015**, *7*, 703-711;b) P.-W.

Liang, C.-Y. Liao, C.-C. Chueh, F. Zuo, S. T. Williams, X.-K. Xin, J. Lin, A. K. Y. Jen, *Advanced Materials* **2014**, *26*, 3748-3754;c) C.-Y. Chang, C.-Y. Chu, Y.-C. Huang, C.-W. Huang, S.-Y. Chang, C.-A. Chen, C.-Y. Chao, W.-F. Su, *ACS Applied Materials & Interfaces* **2015**, *7*, 4955-4961;d) Q. Dong, Z. Wang, K. Zhang, H. Yu, P. Huang, X. Liu, Y. Zhou, N. Chen, B. Song, *Nanoscale* **2016**, *8*, 5552-5558;e) C.-C. Chueh, C.-Y. Liao, F. Zuo, S. T. Williams, P.-W. Liang, A. K. Y. Jen, *Journal of Materials Chemistry A* **2015**, *3*, 9058-9062.

[22] M. Saliba, T. Matsui, J.-Y. Seo, K. Domanski, J.-P. Correa-Baena, M. K. Nazeeruddin, S. M. Zakeeruddin, W. Tress, A. Abate, A. Hagfeldt, M. Gratzel, *Energy & Environmental Science* **2016**, *9*, 1989-1997.

[23] a) A. Dualeh, T. Moehl, N. Tétreault, J. Teuscher, P. Gao, M. K. Nazeeruddin, M. Grätzel, *ACS Nano* **2014**, *8*, 362-373;b) E. J. Juarez-Perez, R. S. Sanchez, L. Badia, G. Garcia-Belmonte, Y. S. Kang, I. Mora-Sero, J. Bisquert, *The Journal of Physical Chemistry Letters* **2014**, *5*, 2390-2394;c) V. Gonzalez-Pedro, E. J. Juarez-Perez, W.-S. Arsyad, E. M. Barea, F. Fabregat-Santiago, I. Mora-Sero, J. Bisquert, *Nano Letters* **2014**, *14*, 888-893;d) B. Suarez, V. Gonzalez-Pedro, T. S. Ripolles, R. S. Sanchez, L. Otero, I. Mora-Sero, *The Journal of Physical Chemistry Letters* **2014**, *5*, 1628-1635.

[24] A. Guerrero, G. Garcia-Belmonte, I. Mora-Sero, J. Bisquert, Y. S. Kang, T. J. Jacobsson, J.-P. Correa-Baena, A. Hagfeldt, *The Journal of Physical Chemistry C* **2016**, *120*, 8023-8032.

[25] T. A. Berhe, W.-N. Su, C.-H. Chen, C.-J. Pan, J.-H. Cheng, H.-M. Chen, M.-C. Tsai, L.-Y. Chen, A. A. Dubale, B.-J. Hwang, *Energy & Environmental Science* **2016**, *9*, 323-356.

[26] I. Zarazua, J. Bisquert, G. Garcia-Belmonte, *The Journal of Physical Chemistry Letters* **2016**, *7*, 525-528.

The table of contents

We report a novel method in order to increase the efficiency of perovskite optoelectronic devices demonstration its goodness for perovskite solar cells, LEDs and light amplifiers. The method is based on the introduction of organic additives during the anti-solvent step in the perovskite thin film deposition process. Additives passivate grain boundaries reducing the non-radiative recombination. The method can be easily extended to other additives.

Keyword perovskite, solar cell, LED, light amplifier, recombination

Thi Tuyen Ngo, Isaac Suarez, Gabriella Antonicelli, Diego Cortizo-Lacalle, Juan P. Martinez-Pastor,* Aurelio Mateo-Alonso* and Ivan Mora-Sero*

Title Enhancement of the Performance of Perovskite Solar Cells, LEDs and Light Amplifiers by Anti-Solvent Additive Deposition

ToC figure
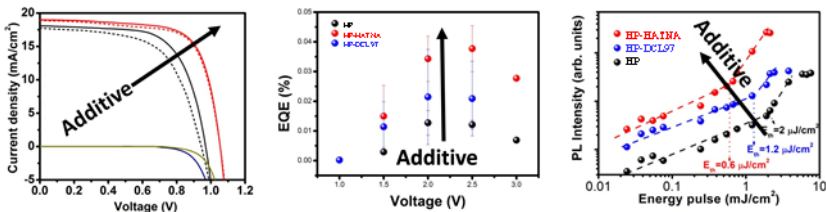
Enhancement of the Performance of Perovskite Solar Cells, LEDs and Light Amplifiers by Anti-Solvent Additive Deposition

Thi Tuyen Ngo, Isaac Suarez, Gabriella Antonicelli, Diego Cortizo-Lacalle, Juan P. Martinez-Pastor,* Aurelio Mateo-Alonso* and Ivan Mora-Sero*

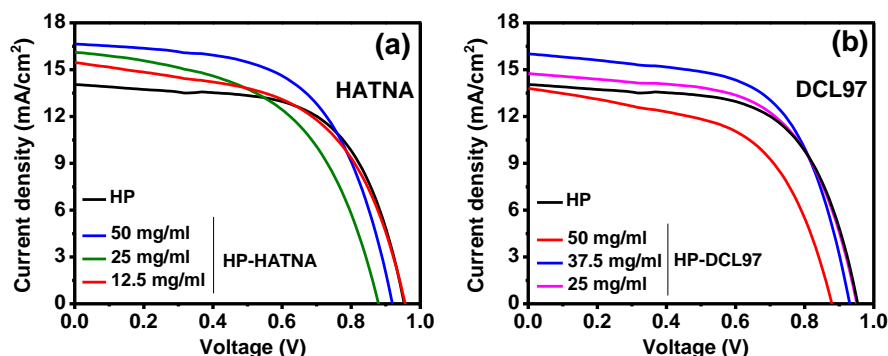**VI.S1. Study of the solar cell performance as function the additive concentration**.

Figure VI.S1. J-V curves solar cells with planar configuration (no-mesoporous TiO_2 layer) using (a) HP-HATNA and (b) HP-DCL97 films as light harvesting layers in a comparison with reference HP samples, without organic additive. Active HP, HP-HATNA and HP-DCL97 layers were spin coated on TiO_2 compact at 5000 rpm, annealed at 65°C for 1 minute and 100°C for 2 minutes consequently. HP-organic film was prepared using a solution of organic compounds dispersed in chlorobenzene with different concentration from 12.5 to 50 mg/ml as an anti-solvent.

Table VI.S1: Average photovoltaic parameters (short circuit current, J_{sc}, open circuit voltage, V_{oc}, fill factor, FF, and photoconversion efficiency, PCE) under AM1.5 simulated sunlight for planar perovskite solar cell configuration (glass/FTO/compact TiO_2 /HP or HP-HATNA or HP- DCL97/spiro-OMeTAD/Au). At least five cells have been prepared at each condition.

Samples	$C_{organic}$ Mg/ml	Jsc (mA/cm^2)	Voc (V)	FF (%)	PCE %
HP	0	13.4 ± 0.3	0.89 ± 0.01	57.0 ± 1.0	6.9 ± 0.3
HP-HATNA	50	16.8 ± 0.4	0.94 ± 0.01	53.0 ± 2.0	8.42 ± 0.24
	25	14.2 ± 1.1	0.89 ± 0.14	49.0 ± 4.0	6.3 ± 0.9
	12.5	15.7 ± 0.5	0.88 ± 0.02	52.3 ± 2.0	7.07 ± 0.52
HP-DCL97	50	11.9 ± 0.5	0.88 ± 0.01	56.1 ± 0.7	5.8 ± 0.3
	37.5	14.9 ± 0.4	0.920 ± 0.003	59.1 ± 0.8	8.1 ± 0.30
	25	14.3 ± 0.6	0.90 ± 0.02	57.5 ± 0.8	7.39 ± 0.4

VI.S2. Study of the stability of solar cell performance.
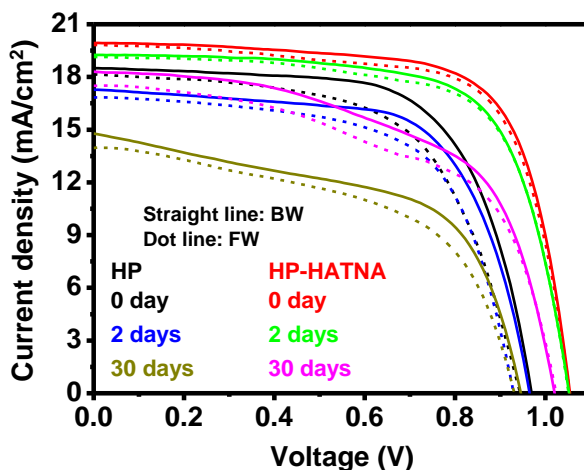
Figure VI.S2. J-V curves solar cells with mesoporous configuration using HP without (reference) and with HATNA additive, at different times after solar cell preparation. In which absorber layers were spin coated on mesoporous TiO_2 at 4000 rpm, annealed at 65ºC for 1 minute and 100ºC for 2 minutes consequently. HP-HATNA film was prepared using a solution of HATNA compounds dispersed in diethyl ether with the concentration of 50 mg/ml. Solar cell were stored on ambient conditions under dark.

Table VI.S2: Photovoltaic parameters (short circuit current, J_{sc}, open circuit voltage, V_{oc}, fill factor, FF, and PCE), at different times after solar cell preparation, under AM1.5 simulated sunlight for mesoporous perovskite solar cell configuration (glass/FTO/compact TiO_2/mesoporous TiO_2/HP or HP-HATNA/spiro-OMeTAD/Au). Solar cell were stored on ambient conditions under dark. BW: J-V scan from voltage higher than Voc to 0 V; FW: J-V scan from 0 V to voltage higher than Voc.

Samples	Time (days)	Scan	Jsc (mA/cm^2)	Voc (V)	FF (%)	PCE (%)
HP	0	BW	18.5	0.969	65.6	11.76
		FW	18.15	0.943	60.5	10.35
	2	BW	17.27	0.964	65.6	10.92
		FW	16.87	0.929	63.1	9.89
	30	BW	14.78	0.945	56.2	7.85
		FW	13.66	0.931	55.1	7.01
HP-HATNA	0	BW	19.93	1.054	70.8	14.87
		FW	19.82	1.054	70	14.62
	2	BW	19.26	1.052	69.2	14.02
		FW	19.16	1.051	68.8	13.85
	30	BW	18.31	1.02	57.9	10.81
		FW	17.54	1.023	55.8	10.01

Table VI.S3: Average photovoltaic parameters (short circuit current, J_{sc}, open circuit voltage, V_{oc}, fill factor, FF, and PCE) under AM1.5 simulated sunlight for mesoporous perovskite solar cell configuration (glass/FTO/$TiO_{2\_compact}$/TiO_{2_meso}/HP or HP-DCL97/spiro-OMeTAD/Au) in which DCL97 was dispersed in chlorobenzene with the concentration of 37.5 mg/ml.

Samples	Jsc (mA/cm^2)	Voc (V)	FF (%)	PCE (%)
HP	9.2 ± 0.4	0.870 ± 0.007	63.0 ± 2.0	5.0 ± 0.3
HP-DCL97	13.7 ± 0.6	0.891 ± 0.014	72.2 ± 1.2	8.9 ± 0.5

VI.S3. Photoluminescence at different excitation power for waveguide light amplifying devices.
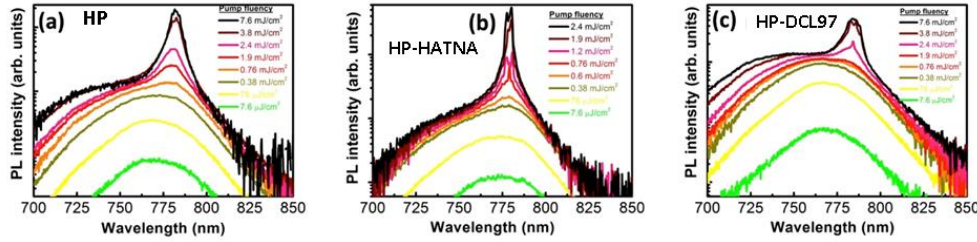

Figure VI.S3. Photoluminescence obtained with side excitation,[9] see inset Figure VI.2e, of (a) reference HP; (b) HP-HATNA and (c) HP-DCL97 additive deposited on glass and with a PMMA capping, see inset Figure VI.2e. Sample PL has been recorded with different excitation powers.

VI.S4. Time Resolved Photoluminescence for waveguide light amplifying devices.

Time Resolved Photoluminescence (TRPL) measurements were fitted with the following equation in order to extract the recombination times involved in the system:

$$I = A \cdot \left(e^{-\frac{t}{\tau_1}} - e^{-\frac{t}{\tau_{rise}}} \right) + B \cdot e^{-\frac{t}{\tau_2}} + C \cdot e^{-\frac{t}{\tau_3}} \qquad (1)$$

Here τ_{rise} was fixed to 10 ps and τ_1, τ_2, τ_3, A, B, C are fitting parameters.

TRPL for HP reference sample, see Figure VI.S4a, can be fitted with two exponential decays. The long one is about 5 ns, and the shorts start from 0.4-0.5 ns to 0.02-0.1 ns (response of the system). For high powers, it becomes necessary to include a third exponential decay with a small width to improve the fitting a bit. Curve presented the same spectra (response of the system reached) for pump fluencies higher than 0.72 nJ. When additives are added to the HP film, Figure VI.S4b and VI.S4c, it becomes necessary to include a third exponential decay, even for low excitation fluencies. Indeed, recombination times do not change (τ_1=20-100ps, τ_2=400-500 ps,τ_3=5ns) with the excitation, but only the weights (A,B,C). The higher the excitation fluency, the weight A (shorter time) becomes more and more important. Curves presented the same spectra (response of the system reached) for pump fluencies higher than 0.1 nJ and 0.5 nJ for HP-HATNA and HP-DCL97, respectively.
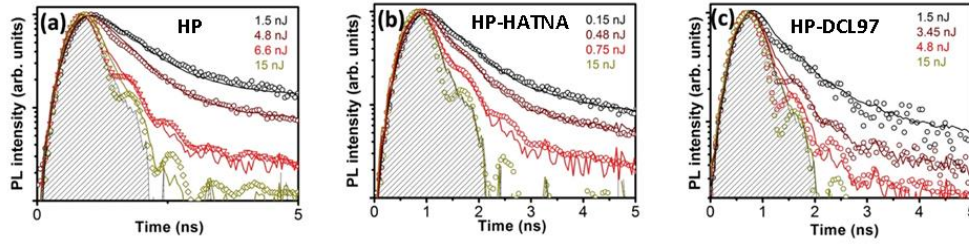
156

Figure VI.S4. Time Resolved Photoluminescence (TRPL) for waveguide light amplifying devices with an active layer of (a) reference HP; (b) HP-HATNA and (c) HP-DCL97 additive, deposited on glass and with a PMMA capping, see inset Figure VI.2e. TRPL has been recorded with different excitation powers. Shadow area represents the response of the system.

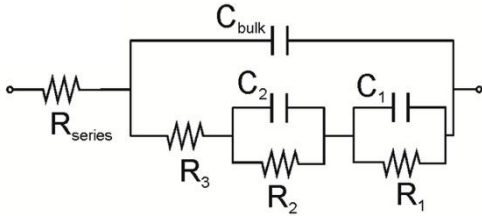## VI.S5. Equivalent circuit using for fitting the impedance results.

Figure VI.S5. Equivalent circuit for PSCs.[24] R_{series} is the series resistance of substrate and wiring, C_{bulk} is the geometrical capacitance of the sample. R_2 and C_2 are resistance and capacitance related with the contact/perovskite interface, C_1 has been related with an accumulation capacitance[26] while R_1 is related with the recombination resistance (inversely related with the recombination rate).[23]
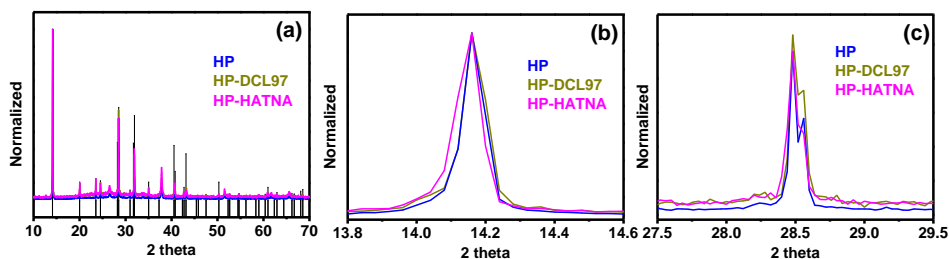
VI.S6. X-Ray Diffraction (XRD).

Figure VI.S6. (a) Normalized intensity of XRD spectra, black lines correspond to powder pattern of MAPI. (b) Zoom of the peak for diffractions corresponding to (110) and (002) planes. (c) Zoom of the peak for diffractions corresponding to (220) and (004) planes.

VI.S7. Scanning Electron Microscopy (SEM).

SEM analysis permits to highlight differences between the two additives. While HATNA dissolved in diethyl ether produces a layer on top of the perovskite film see Figure VI.S7l and m, this is not the case of DCL97 dissolved in chlorobenzene, no capping layer on top of perovskite was observed, see Figure VI.S7c and VI.S7d. The HATNA layer is removed during the deposition of spiro-OMeTAD dissolved in chlorobenzene as HATNA is soluble in this solvent, see Figure VI.S7p and VI.S7q. Moreover, addition of DCL97 produces a change of the surface roughness, as it can be clearly appreciated from the comparison between Figure VI.S7e and Figure VI.S7f which are the top views of HP layer without and with DCL97 additive, respectively, using chlorobenzene as anti-solvent. This observation points to a change in the interfacial properties of layer with additives that could have a beneficial effect in the performance of the optoelectronic devices. While in perovskite layer without DCL97 additive the grains of perovskite are clearly recognized, see Figure VI.S7e, when DCL97 is added during the anti-solving step the surface morphology changes making difficult to observe the grains, see Figure VI.S7f. However from cross section, see Figure VI.S7a and VI.S7c, it can be observed that no significant change in the grain size is produced when DCL97 is added.

In the case of HATNA added, using diethyl ether as anti-solvent, a clear different behavior is observed with the formation of a HATNA capping layer on top of the perovskite layer, see Figure VI.S7l and VI.S7m, and top

view Figure VI.S7h. Nevertheless in the case of DCL97 no significant change in grain size has been detected, compare Figure VI.S7i and VI.S7l. It is important to highlight that this HATNA capping is removed when spiro-OMeTAD is deposited as HATNA is soluble in chlorobenzene where spiro-OMeTAD is dissolved, resulting a similar thickness for organic layers are observed in full devices without and with HATNA additive, see Figure VI.S7o and VI.S7q.

Finally, note that reference samples presents larger grain size when diethyl ether is used as anti-solvent instead of chlorobenzene, compare Figure VI.S7g and VI.S7e, producing a lower performance for samples fabricated with chlorobenzene, compare Figure VI.2a and Table VI.S3.
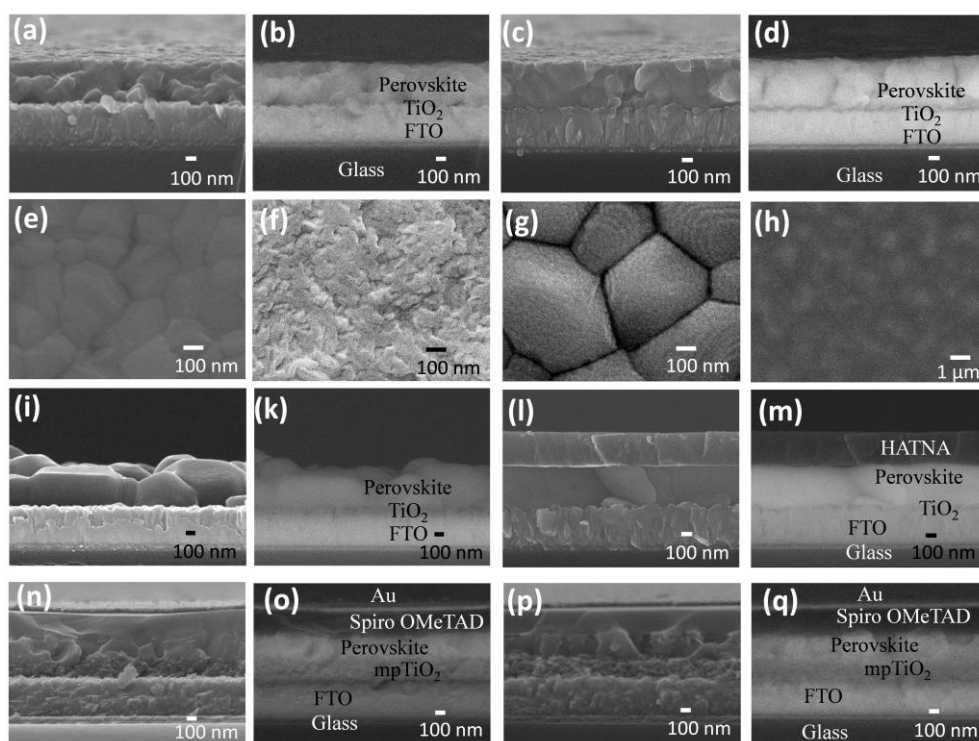
Figure VI.S7. SEM micrographs obtained with secondary electrons (SE) and with backscattered electrons (BE). BE are highly sensitive to the composition, showing with a clear color the areas containing heavy atoms as Pb, while organic compounds present a darker contrast. HP film prepared with chlorobenzene anti-solvent (a) cross section (SE), (b) cross section (BE) and (e) top view. HP+DCL97 film prepared with chlorobenzene anti-solvent (c) cross section (SE), (d) cross section (BE) and (f) top view. HP film prepared with diethyl ether anti-solvent (i) cross section (SE), (k) cross section (BE) and (g) top view. HP+HATNA film prepared with diethyl ether anti-solvent (l) cross section (SE), (m) cross section (BE) and (h) top view. Complete device with glass/FTO/compact TiO_2/mesoporous (ms) TiO_2/HP/spiro-OMeTAD/Au configuration prepared with diethyl ether anti-solvent (n) cross section (SE), (o) cross section (BE). Complete device with glass/FTO/compact

TiO$_2$/mesoporous (ms) TiO$_2$ /HP-HATNA/spiro-OMeTAD/Au configuration prepared with diethyl ether anti-solvent (p) cross section (SE), (q) cross section (BE).
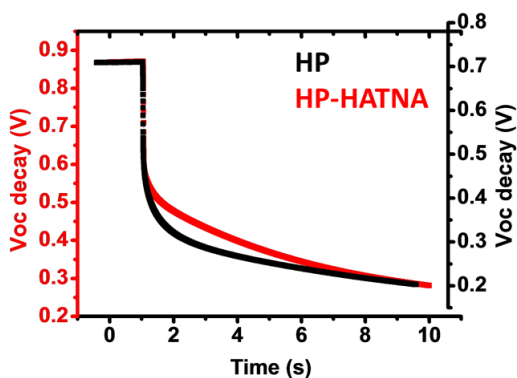
VI.S8. Open Circuit Voltage Decay.

Figure VI.S8. Voc decay measured at 0.09 sun.

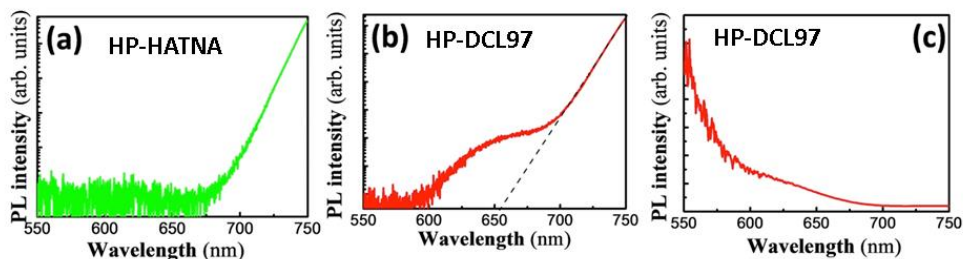## VI.S9. Photoluminescence mapping of perovskite film with additives.

Figure VI.S9. PL spectra for λ_{exc}=533 nm excitation wavelength of (a) HP-HATNA and (b) HP-DCL97. This λ_{exc} can just excite HP in the case of HP-HATNA and just the HP PL queue is observed at 700-750 detection wavelengths, λ_{dec}. The detected wavelengths have not been extended to longer wavelengths in order to avoid the saturation of the detector. In the case of HP-DCL97 both HP and DCL97 are excited with λ_{exc}=533 nm, and in addition to the HP PL queue a shoulder in the perovskite spectra at λ_{dec} =600-700 nm can be observed in (b). Consequently in order to discriminate the PL produced by HP or by DCL97 PL maps are recorded for different λ_{dec}. Figure VI.3e shows the integrated PL for λ_{dec} =700-750 nm that

160

takes only into account the PL from the HP, see (b). In order to obtain the PL coming from DCL97, the HP contribution, obtained from the linear fitting of the HP PL queue (dashed line in b), is subtracted to the PL spectra in (b) obtaining the bare contribution of DCL97 plotted in (c). Figure VI.3d shows the integrated PL for λ_{dec} =600-650 nm, after removing the HP contribution, that takes only into account the PL from the DCL97.

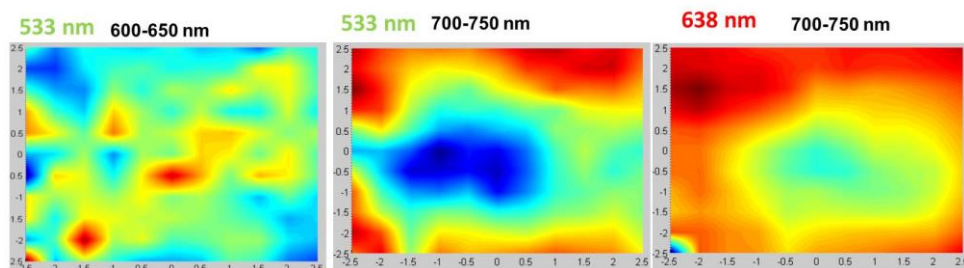## VI.S10. Photoluminescence mapping of HP-DCL97 sample at an alternative position than the reported in Figure VI.3.

Figure VI.S10. Photoluminescence intensity map of a sample of perovskite with DCL97 additive, excitation wavelength, λ_{exc}, and the range of detected wavelengths, λ_{det}, are indicated in each map with green-red color and with black color respectively. **a)** PL from DCL97, where PL from perovskite has been subtracted, see Figure VI.S9, for further details. **b)** and **c)** PL from perovskite, see Figure VI.S9, for further details, for two different λ_{exc}. Vertical and horizontal scales for the maps are in μm.

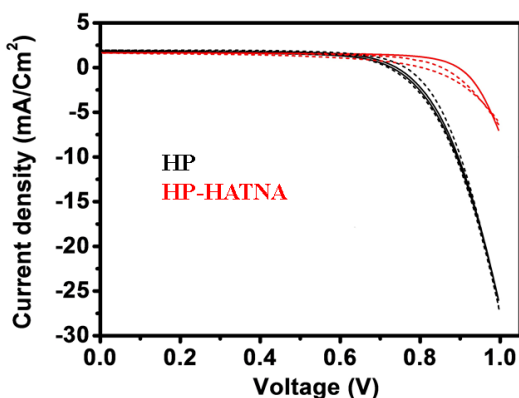## VI.S11. Solar cell stability during impedance measurement.

Figure VI.S11. J-V curve at 0.09 sun of devices based on HP and HP-HATNA absorbers before (solid line) and after Impedance measurement (dash line).

Chapter VII

Spray-Pyrolyzed ZnO as Electron Selective Contact for Long-Term Stable Planar CH₃NH₃PbI₃ Perovskite Solar Cells

VII.1. Candidate's contribution

The nature and extent of my contribution to the work in the chapter VII is described following:

Nature of contribution	Extent of contribution
- Preparation of films and devices. - Characterization of films and devices: absorbance, PL, SEM, JV curves, impedance spectroscopy, IPCE and EL. - Preparation the first draft of the manuscript. - Edit the manuscript according to the comments of co-authors and referees. - Write the draft for replying the referees.	**75 %**

VII.2. Published manuscript

Spray-Pyrolyzed ZnO as Electron Selective Contact for Long Term Stable Planar CH₃NH₃PbI₃ Perovskite Solar Cells.

Thi Tuyen Ngo[1], Eva María Barea[1], Ramon Tena-Zaera[2] and Iván Mora-Seró[1,*]

[1] Institute of Advanced Materials (INAM), University Jaume I, Avenida de Vicent Sos Baynat, s/n, 12006 Castelló de la Plana, Castellón (Spain)
[2] CIDETEC, Parque Tecnológico de San Sebastián, Paseo Miramón, 196, Donostia–San Sebastián 20014 (Spain)
Corresponding author: sero@uji.es

Abstract

Electron selective contacts (ESCs) play an important role in the performance of perovskite solar cells (PSCs). ZnO has attracted an important attention as a good material for ESCs because of its matched energy levels with those of perovskite, its high transmittance in the visible region and its high electron mobility. Here we reported the use ZnO thin layers prepared by spray pyrolysis as ESC for PSCs. Our ZnO based planar CH₃NH₃PbI₃ (MAPI) devices were not only stable in a humidity of 35% but also improved the performance even after more than 1 month of preparation, due to an increase of charge transfer at the ZnO interface as it has been characterized by Impedance Spectroscopy. The formation of ZnO depending on the preparation conditions such as gas flow, zinc acetate solution concentrations and substrate temperatures effect on the performance of stability of MAPI solar cells, and also the low-hysteresis reported for these samples were discussed in this study. We have also observed that long term structural evolution of perovskite film also depends on the ZnO substrate and its deposition method.

VII.1. INTRODUCTION.

Perovskite solar cells (PSCs) have developed rapidly over the past few years due to the promising properties of perovskite materials such as high absorption over the visible range and long diffusion length. The power conversion efficiency of PSCs has been recorded over 22%.[1] Such high performance of PSCs needs not just an outstanding perovskite absorber layer

163

but also excellent selective contacts for an optimum charge separation. As a result, the design and materials properties of the selective contacts are crucial for solar cell performance.[2-6] Concretely, the electron selective contact (ESC) is a blocking layer that prevents holes from reaching the transparent conductive electrode, fluorine-doped tin oxide (FTO), avoiding interfacial recombination. For high performance solar cells, ESCs should meet the following criteria: (a) good optical transmittance in the visible range, which reduces the optical energy loss; (b) the energy levels of ESCs should match that of perovskite materials, which improve the electron extraction efficiency and block holes; (c) good electron mobility; (d) high film quality by easy fabrication methods.[6]

Among the ESC materials, ZnO has attracted much attention to be used as an ESC in DSSCs and polymer solar cells,[7] but also in PSCs since the early stages.[8] Because, first of all, ZnO has a very high transmittance in the visible spectra and more importantly ZnO has a proper bandgap, energy band alignment suitable with those of perovskite. Second, ZnO possesses a very high electron mobility (bulk ZnO 205-300 $cm^2V^{-1}s^{-1}$ and nanowire ZnO 1000 $cm^2V^{-1}s^{-1}$) which can potentially improve the electron transport efficiency and reduce the recombination loss.[3, 9-10] Third, the extraction properties of ZnO may be maintained if no chemical reaction between ZnO and CH_3NH_3I is produced,[11] although for certain ZnO surfaces (i.e. including some absorbates) deprotonation of $CH_3NH_3^+$ (MA^+) cation may occur during thermal treatments.[3] Fourth, various ZnO nanostructures such like nanowires,[12] nanotubes,[13] nanobelts,[14] nanorings,[15] nanoflowers,[16] nanorods,[17] and so on, can be easily fabricated by controlling the growth rates along different directions.

Recently ZnO as ESC for PSCs has been studied systematically.[3, 8, 18-22] In 2015 Jiaxing Song's group published a PSCs glass/ITO/ZnO/MAPI/spiroOMeTAD/Ag structure given a conversion efficiency of 13.9%. Interestingly their devices exhibited a good stability, with a conversion efficiency that was maintained around 90% after 22 days exposed to ambient condition.[23] In the same year, Qin Hu et al. modified ZnO layer by linking it with polymer and increased the conversion efficiency to 15.96%.[24] By using triple cation perovskite absorber 2 years later Jiaxing Song et al. reported 18.9% of conversion efficiency ZnO based PSCs,[25] confirming the possibility to use ZnO as efficient ESCs in PSCs.

In this study, we used a spray pyrolysis method, which is low cost and quite suitable for large area thin films with good reproducibility, to prepare ZnO thin layers. Using spray-pyrolyzed ZnO thin films, we prepared planar

PSCs following a structure FTO/ZnO/MAPI/Spiro OMeTAD/Au and focused on their stability. In which ZnO thin films were spray-pyrolyzed with different conditions such as different gas flow (N_2 or O_2), substrate temperatures and zinc acetate solution concentrations. Our devices not only presented a very good stability but also the performance improvement even after 34 days storing at around 35% of humidity.

VII.2. EXPERIMENTAL SECTION

VII.2.1. Device preparation

ZnO thin layer. Substrates (SnO_2:F, FTO or SnO_2:In, ITO) substrates were sonicated in distilled water with soap, distilled water, ethanol and propanol-2 for15 minutes and then treated with an UV−O_3 lamp for 15 minutes. The ZnO layer was deposited by spray pyrolysis with 2 different recipes. For the first recipe, ZnO was performed according to procedure previously reported with some modification.[26] Briefly, ZnO was spray pyrolyzed from 5 ml solution containing 0.3M zinc acetate dihydate in a mixed of distilled water and propanol-2 (1:1 volume ratio). The pH of zinc acetate solution was adjusted to 4 by adding acetic acid. When FTO substrate temperature reached to 450°C, zinc acetate solution was sprayed on their surface using N_2 or O_2 flow. After spraying, ZnO layer was annealed at the same temperature (450°C) for 30 minutes then cooled to room temperature.

For the second recipe, the concentration of zinc acetate solution was reduced to 0.1M. And distilled water was mixed with ethanol instead of propanol-2 with a volume ratio 1:3. Acetic acid was also added to the solution to produce a pH of 5. ZnO layers were deposited on FTO and ITO at different substrate temperatures from 300°C to 450°C (300°C for ITO) and from different zinc acetate volumes. After spraying, ZnO was also annealed for 30 minutes. O_2 flow is used in these cases.

To simplify, ZnO films obtained from N_2 and O_2 flow were named ZnO_N_2 and ZnO_O_2 respectively.

Perovskite. Perovskite solution was prepared by dissolving 622 mg (1.35 mmol) of PbI_2 and 215 mg (1.35 mmol) of MAI in a co-solvent containing 1ml of N,N-dimethylformamide (DMF) and 95 μl of dimethyl sulfoxide (DMSO). A thin film deposition was done inside a glove box by spin

165

coating 50 μl of perovskite solution at 5000 rpm. Diethyl ether was added to the film when the spin coater was running, 5-6s after the spinning starts. Finally perovskite film was annealed at 100°C for 3 minutes.

Spiro OMeTAD and Gold. Spiro OMeTAD solution was prepared by dissolving 72.3 mg of spiro-OMeTAD (2,2′,7,7′-tetrakis(N,N-di-p-methoxyphenylamine)-9,9-spirobifluorene) was dissolved in 1 ml of chlorobenzene, then mixed with 28.8 μl of 4-tertbutylpyridine and 17.5 μl of a stock Li$^+$ solution (which contained 520 mg/ml bistrifluoromethylsulfonylamine lithium salt in acetonitrile). Spiro OMeTAD layer was spin coated on perovskite films at 4000 rpm for 30s. Finally, 60 nm of gold were thermally evaporated in an ultrahigh vacuum chamber on top of Spiro OMeTAD layer to make complete devices.

VII.2.2. Film and device characterization

Thin film characterization. The morphology and structural properties of the ZnO and MAPI perovskite films was analysed by scanning electron microscopy (SEM) using a JSM7001F (Field emission scanning electron microscope), a Bruker AXS-D4 Endeavor Advance X-ray(XRD) using Cu Kα radiation. Absorbance of those films were measured by using a Cary 300 Bio UV-VIS spectrophotometer respectively. And Photoluminescence (PL) spectra of MAPI films were obtained by using a spectrophotometer based on a CCD detector (Andor-iDUSDV420A-OE) coupled with a spectrograph as a diffraction grating (Newport 77400). A commercial continuous laser diode (650 nm, 5 mW) was used as an excitation source. Morphology and conductivity of ZnO films were investigated using Atomic Force Microscopy. The morphology of the ZnO films was investigated using AFM (Concept Scientific Instrument) in resiscope mode. While the current maps of the ZnO films were recorded using a diamond coated tip at an applied bias of 1V in N$_2$ flow.

Device characterization. J–V curves of solar cells were measured under a xenon arc lamp simulator equipped with an AM 1.5 spectral filter (Sun 2000, ABET Technologies). The intensity was adjusted to provide 1 sun (100 mW cm^{-2}) by using a calibrated silicon solar cell. The J–V characteristics were recorded by scanning the potential from high voltage to zero (backward scan mode, BW) and from zero to high voltage (forward scan mode, FW) at ≈45 mV/s. The IPCE measurements were performed employing a 150 W xenon lamp coupled with a computer-controlled monochromator; the photocurrent was measured using an optical power meter 70310 from Oriel Instruments, using a Si photodiode to calibrate the system. Electroluminescence (EL)

experiments were performed by applying an electric field in the perovskite layer integrated in a diode configuration and collecting the emission of the film with a similar set-up of PL measurement. Measurements have been carried out using a non-sealed sample holder. Sample holder has a gas connection to flow N_2 continuously during the EL measurements. The eQE estimations were performed by calibrating the optical equipment with a commercial GaAs infrared LED (model EL-23G, peak emission centered at $\lambda_{max} = 940$ nm, 28.3 W sr^{-1} m^{-2}).

VII.3. RESULTS AND DISCUSSION

Our ZnO thin films were deposited by spray pyrolysis method. It is worth to mention that spray pyrolysis itself is a method which involves spraying a solution onto a heated substrate. The droplets of a spray solution, after hitting on the substrate surface, spread into a disk shaped structure and undergo thermal decomposition. The shape and size of the disk depends on the momentum and volume of the droplet. Consequently, the film will be initially composed of overlapping disks which will finally become grains with specific orientation on the heated substrate.[26] It has been previously discussed, many factors can affect on the film formation such as spray rate, precursor solution[26] (nature of solvents, type of salts and concentration) and substrate temperatures[27] and so on. All these factors affect on the morphology, structural, electrical and optical properties of spray-pyrolyzed films.[26-27] In agreement with previous discussions, we also found the morphology dependence of ZnO films formed at different substrate temperatures (see Figure VII.S1).

In this study, ZnO films were deposited with different gas components, N_2 and O_2 flows. Figure VII.1a shows the absorbance, transmittance spectra and top view SEM of ZnO films deposited on FTO, obtained by spraying zinc acetate using two these different gas, during the spray pyrolysis process. In agreement with literature, our ZnO films are very transparent in the visible range.[28] This fact contributes to reduce the optical losses. The ZnO films obtained from N_2 and O_2 flow have a similar morphology, see Figure VII.1b and VII.1c. However, ZnO_N_2 exhibits slightly bigger grains. And this difference in grain size is also confirmed by AFM measurement (see Figure VII.S2). ZnO deposition process is carried out in ambient condition. Consequently, even we used N_2 flow, O_2 from air is presented during ZnO film formation. In this sense, the main difference between the ZnO depositions is the different ratio of O_2 in the gas, being obviously much higher when O_2 flow is used. Tseng et al. reported the ZnO deposition by sputtering from a

mixed Ar and O_2 gas with different ratio of O_2.[28] In their study, they observed no influence of gas on ZnO crystallinity and morphology. However, it is important to note that all their ZnO films were obtained without substrate heating while our spray-pyrolyzed ZnO was archived with substrates heated at 450°C. The differences in substrate heating temperatures and O_2 ratio in the gas may explain the grain size difference of ZnO obtained with N_2 and O_2 flow respect previous reports in the literature.

In addition to the grain size dependence, we also observed the optical band offset dependence on the components of gas used during the ZnO spray pyrolysis process. As seen in the Figure VII.1a and VII.S3a, ZnO spray-pyrolyzed with O_2 flow shows slightly higher bandgap than ZnO prepared with N_2 flow. This obtaining is in agreement with literature which has been reported that the bandgap of spray-pyrolyzed ZnO can be modified by changing the spray conditions such as spray rates, spray solution concentrations and substrate temperatures.[26-27] In the range of employed temperatures (~350°C), the amount of oxygen in the gas used affects on the decomposition and oxidation of precursors in the solution, resulting the different properties, including the optical properties, in formation of ZnO thin films. Additionally we also found the concentration of a spray solution can change the bandgap of spray-pyrolyzed ZnO as well (see Figure VII.S3b). However the volume of a spray solution does not change the absorption offset of ZnO films. Increasing the volume only results an increase in absorption (See Figure VII.S3c).
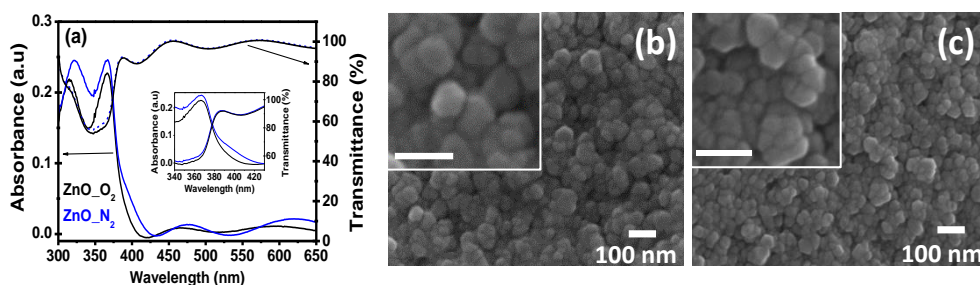

Figure VII.1. (a) Absorbance and transmittance; and SEM images from secondary electrons of ZnO layer deposited on FTO from 0.3 M zinc acetate solution at 450°C with (b) nitrogen (named ZnO_N_2) and (c) oxygen flow (named ZnO_O_2), bar scale in insect is 100 nm.
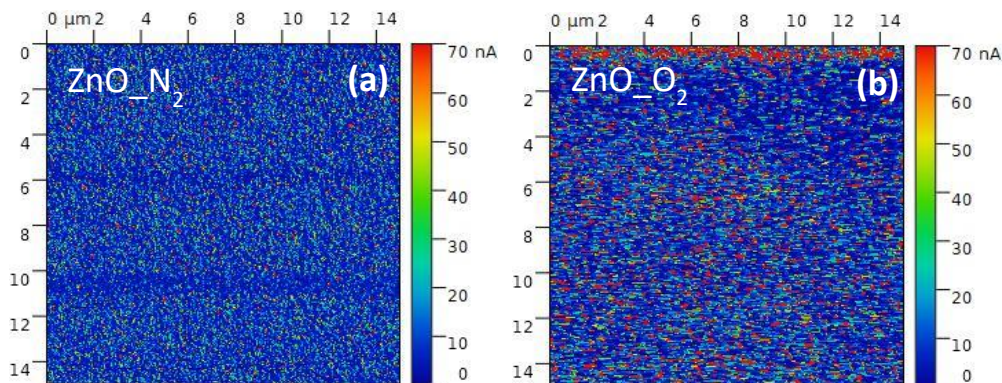
Figure VII.2. Conductive atomic force microscopy (C-AFM) of ZnO layer deposited on FTO from 0.3 M zinc acetate solution at 450°C with nitrogen (a, named ZnO_N$_2$) and oxygen flow (b, named ZnO_O$_2$).

We moreover archived the difference in the conductivity of spray-pyrolyzed ZnO films obtaining by using N$_2$ or O$_2$ flow. The conductive atomic force microscopy measurement pointed out both those ZnO films contain homogeneous current contribution on the surface. However ZnO_N$_2$ exhibits lower current, indicating lower conductivity than ZnO_O$_2$ (see Figure VII.2), as impedance spectroscopy analysis also confirms, see below. It has been previously reported that the concentration and pH of a spray solution, and spay rate can affect on the electrical resistivity of ZnO films.[26] Here we found that the components of gas used in a spray pyrolysis also play a role in a conductivity of formed films.

The absorbance spectra of fresh MAPI films deposited on ZnO prepared with N$_2$ and O$_2$ flow show a strong absorption at the wavelength between 400 nm to 800 nm (see Figure VII.S4a). No difference between the absorbance spectra of MAPI films coated on ZnO_N$_2$ or ZnO_O$_2$ thin layers were observed, indicating no thickness difference. Figure VII.S4b and VII.S4c present the cross section of fresh MAPI/ZnO_N$_2$ film. Both ZnO compact and MAPI perovskite layers are very homogeneous and fully coverage, with 50 nm and 270 nm thickness, respectively. The photoluminescence (PL) spectra of those perovskite layers deposited on ZnO_N$_2$ or ZnO_O$_2$ substrates were similar as well (see Figure VII.S4a). MAPI perovskite coated on ZnO_N$_2$ and ZnO_O$_2$ presents the tetragonal structural phase, with (110) preferential orientation, with diffraction peak at 14.2°, see Figure VII.S5a and VII.S5b. However, the degree of preferential orientation is not exactly the same for both fresh samples as fresh MAPI/ZnO_O$_2$ presents higher X-Ray Diffraction (XRD) intensity at peak 14.2° diffraction compared with fresh MAPI/ZnO_N$_2$, see Figure VII.S5c. This finding is in agreement with the observation of Tseng's group.[28] Smaller full width at half maximum (FWHM)

169

of fresh MAPI coated on ZnO_O$_2$ (see Figure VII.S6a and Table VII.S1) suggests higher perovskite crystallite size is obtained.
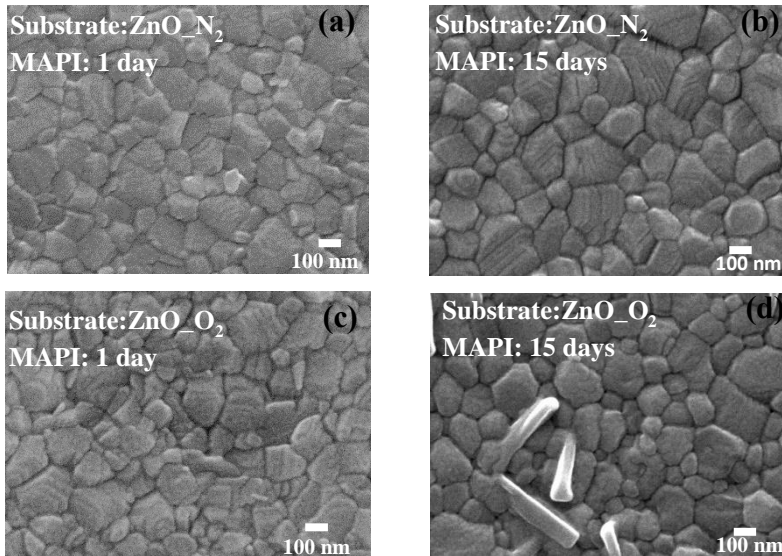

Figure VII.3. (a-d) Top view of 1 day and 15 day-old MAPI deposited on FTO/ZnO_N$_2$ (a-b) and FTO/ZnO_O$_2$ substrates (c-d). MAPI films were stored under dark and at room temperature and at around 35% of humidity.

Figure VII.3 presents Scanning Electron Microscopy (SEM) images of the top view of fresh and old MAPI films deposited on ZnO prepared with both N$_2$ and O$_2$ flow. The top view SEM of fresh MAPI/ZnO_O$_2$ also shows slightly bigger grain size than fresh MAPI/ZnO_N$_2$, see Figures VII.3a and VII.3c. This observation is in agreement with XRD measurement, higher XRD intensity and lower FWHM at peak 14.2° fresh for MAPI/ZnO_O$_2$ film (Figure VII.S5c, VII.S6a and Table VII.S1). It is worth noting that, in XRD measurements, we did not observe the XRD pattern of ZnO due to its extremely thin thickness (see Figure VII.S5a and VII.S5b). Thus, we could not analyse the dependence of ZnO structure on the components of gas used.

However, the most interesting feature regarding the samples morphology is observed after aging. The morphology of MAPI films deposited on ZnO_N$_2$ and ZnO_O$_2$ changed oppositely after 15 days stored at room temperature under dark and at around 35% of humidity conditions. For ZnO_N$_2$ substrate, MAPI film showed an increase in grain size for a 15 days-old film, see Figure VII.3a and VII.3b. Evolution of FWHM in XRD (i.e. crystallite sizes) also points in the same direction, see Figure VII.S5d, VII.S6c and Table VII.S1. Similar results obtained by the study of Roose et al. They

prepared mixed halide cation perovskite (from a solution containing FAI, PbI_2, MABr, $PbBr_2$ and CsI) on SnO_2 compact layer. They demonstrated that smaller crystallites within perovskite films spontaneously coalescence into larger ones, even when complete devices are stored in the dark at room temperature.[29] It is important to note that our MAPI perovskite films are composed by pure iodine phase, which is known less stable than perovskite containing Cs cation, and stored at around 35% of humidity condition. Moreover the preferential orientation of MAPI film belong the plane (110) which is perpendicular to the substrate[30] is slightly improved after 15 days, see Table VII.S1.

Oppositely to MAPI perovskite films deposited on ZnO_N_2 thin layer, aging perovskite coated on ZnO_O_2 substrate shows no appreciable change on grain size, see Fig VII.3c and VII.3d. A detailed analysis of XRD, see Figure VII.S5e, VII.S6b and Table VII.S1, points to a decrease in the degree of preferential orientation along the (110) plane direction comparing aged cell with the fresh one, and also a slight increase of FWHM confirming the crystallite size evolution ZnO_O_2 is not similar to the observed for ZnO_N_2. Here we found that ZnO preparation method play an important role in the long term stability of MAPI perovskite. We have previously observed that kind of substrate, comparing organic PEDOT and several inorganic oxides had an impact on the perovskite degradation process.[31-34] Here we show that not just the substrate type but the preparation and termination method has influence on long term PSC stability.

It has been reported that the combination of light and O_2, in dry air, induced the degradation of MAPI perovskite films, and consequently the performance of solar cells. O_2 diffusion on MAPI films is accompanied by the photo-induced formation of highly reactive superoxide O_2^- species. This reactive O_2^- species can deprotonate the methylammonium cation of photo-excited $MAPbI_3^*$, leading to the formation of PbI_2, water, methylamine and iodine.[35-38] We have detected the formation of platelet-like grains, suggesting PbI_2, on $MAPI/ZnO\_O_2$ film after 15 days, see Figure VII.3d and Figure VII.S7b. However, note that in our storage conditions O_2 and water are presented but no illumination. Thus the required conditions for a degradation caused by a combination of light and O_2 were not fulfilled. On the other hand, it is well known that the presence of water can accelerate the degradation of MAPI perovskite. It is important to note that we stored $MAPI/ZnO\_O_2$ and $MAPI/ZnO\_N_2$ in the same conditions. And the platelet-like grains were clearly observed for aged $MAPI/ZnO\_O_2$ samples while it was not clearly visible for aged $MAPI/ZnO\_N_2$ films. The study of Nathan et al pointed out that water adsorption of perovskite is heavily influence by the orientation of

171

the methylammonium cations close to surface. And depending on methylammonium orientation, the water molecules can infiltrate into hollow site of the surface and get trapped.[39] As it has been discussed above, our ZnO spray-pyrolyzed with N_2 or O_2 flow gave different surficial termination which affected on the growth and orientation of perovskite coated on, and further affected on the water adsorption of perovskite. Thus we supposed that the presence of platelet-like grains ascribed to a water adsorption of perovskite which originally related by the O_2 rich condition of ZnO formed in the spray pyrolysis process.
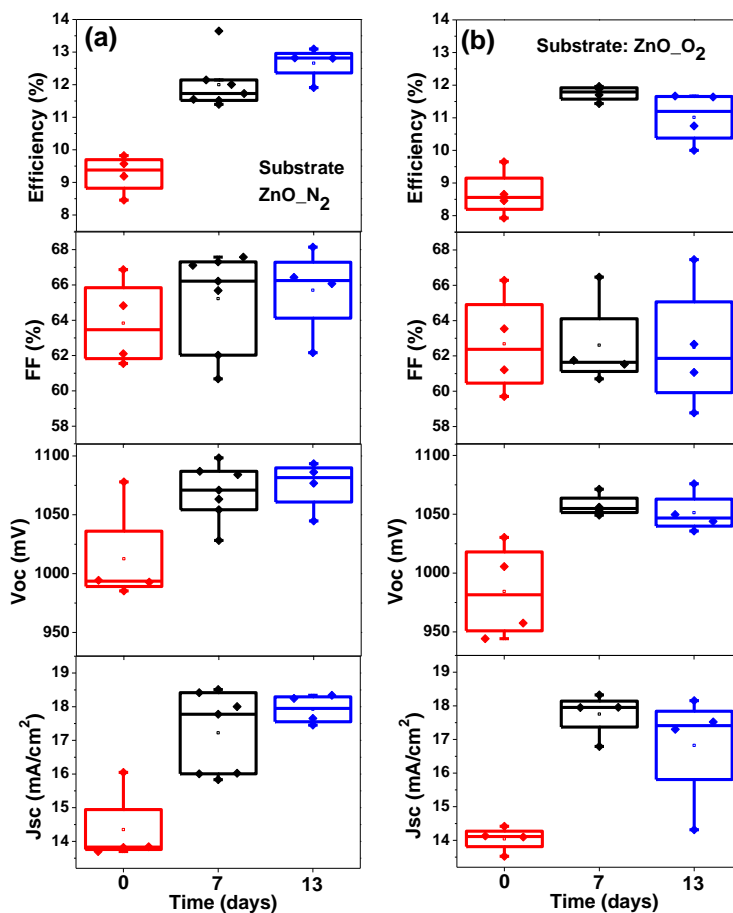
Figure VII.4. Performance at 1 sun illumination of planar based ZnO devices with a structure of FTO/ZnO/MAPbI$_3$/Spiro OMeTAD/Au respect to the time. In which ZnO was spray-pyrolyzed from 0.3 M zinc acetate solution at 450°C with nitrogen (a) and oxygen flow (b). Full devices were stored under dark and at room temperature and at around 35% of humidity.

Time (days)	Substrate: ZnO_N₂			
	Jsc [mA/cm²]	Voc [mV]	FF [%]	PCE [%]
0	14.3 ± 0.2	1010.7 ± 8.3	61.3 ± 1	8.9± 0.1
7	17.5 ± 0.4	1066.5 ± 8.1	65.1 ± 1	12.1 ± 0.3
13	17.9 ± 0.2	1075.3 ± 10.8	65.7 ± 1.2	12.7 ± 0.3
Time (days)	Substrate: ZnO_O₂			
	Jsc [mA/cm²]	Voc [mV]	FF [%]	PCE [%]
0	14 ± 0.2	984.4 ± 20.2	62.7 ± 1.4	8.7 ± 0.4
7	17.8 ± 0.3	1057.6 ± 4.8	62.6 ± 1.3	11.8 ± 0.1
13	16.8 ± 0.2	1051.4 ± 8.3	62.5 ± 1	11 ± 0.1

Table VII.1. Statistic photovoltaic parameters at 1 sun of planar based spray-pyrolyzed ZnO devices showed in the Figure VII.4.

Full PSCs have been prepared using both kinds of spray-pyrolyzed ZnO layers with N₂ and O₂ flow, with a configuration of FTO/ZnO/MAPI/spiro OMeTAD/Au. ZnO based PSCs were characterized by measuring the current density-voltage (J-V) curves under 1 sun illumination. Figure VII.4 presents the statistics of photovoltaic parameters of those devices respect to the fabrication time. Comparing the performance of PSCs fabricated using both ZnO substrates, no significant differences can be appreciated on fresh samples where ZnO_N₂ based devices showed slightly better performance on average, see Figure VII.4 and Table VII.1. However fresh perovskite coated ZnO_O₂ shows slightly bigger grain sizes (Figure VII.3a and VII.3c), higher crystallinity and better preferential orientation belong (110) plane (Figure VII.S5c, VII.S6a and table VII.S1) than film coated ZnO_N₂ substrates. And it has been previously reported that (110) plane of perovskite crystallites tends to align in the direction perpendicular with substrate and this preferential orientation affects on the charge transfer and photovoltaic performance.[30] Thus the lower performance of ZnO_O₂ based devices could be due to different ZnO bandgap obtaining by using different gas, N₂ or O₂ flow (Figure VII.1a and VII.S3a) and probably due to the different band offsets. In the study of Tseng et al, they supposed for ZnO sputtered with Ar, the energy levels (conduction and valence band) down shift, which can enhance electron injection from perovskite to ZnO and block the hole more efficiently. And they got better performance for devices containing ZnO sputtered with Ar,[28] the same trend as we observed.

Nevertheless the main difference on the performance of ZnO based PSCs depending on the deposition conditions is observed for aged samples. For ZnO_N₂ based PSCs, big improvements of 36% and 43% in photoconversion efficiency is observed after 7 and 13 days, respectively, see

Figure VII.4a and Table VII.1. This improvement in average is due to the increasing of all solar cell parameters, photocurrent, J_{sc}, open circuit voltage, V_{oc} and fill factor, FF, but especially J_{sc}, see Figure VII.4 for the averaged results and Figure VII.5a for a single cell. This improvement could be understood by the morphological and structural evolution experienced by these samples, as it has been previously discussed, with an increase in grain sizes, crystallinity and also in the degree of preferential orientation belong (110) plan of MAPI film deposited on ZnO_N_2, which is caused by the coalescence of smaller crystallites into larger ones.[29] Interestingly our ZnO_N_2 based devices presented the performance improvement not only until 13 days-age but also after more than 1 month, see Figure VII.5b. In addition, the measurement of incident photon to current efficiency (IPCE), Figure VII.S8a, pointed out to a good agreement between the integrated photocurrent calculated from IPCE data and the J_{sc} measured from J-V curves, reverse scan, see Figure VII.S8. In fact, these devices present low hysteresis as it can be appreciated for the champion cell an efficiency close to 14%, see Figure VII.S9, in good agreement with the observation for other ZnO-based PSCs.[23-24]
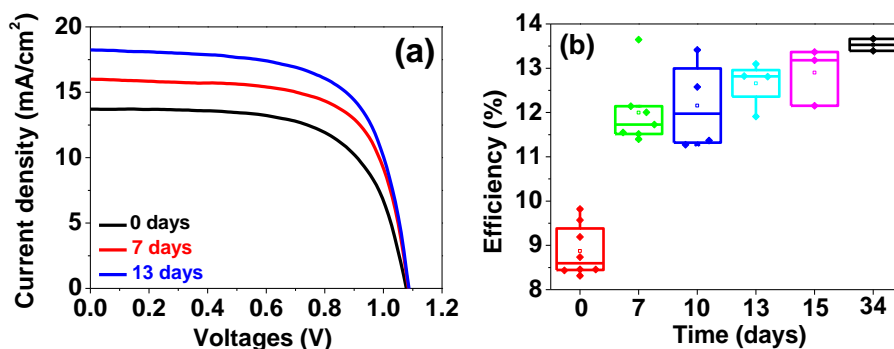

Figure VII.5. Current density-voltage (J-V) characteristic, reverse scan, (a) and efficiency (b) of FTO/ZnO_N$_2$/MAPI/Spiro OMeTAD/Au at 1 sun illumination measured in different time. All devices were stored under dark at room temperature and at around 35% of humidity. ZnO was spray-pyrolyzed from 0.3 M zinc acetate solution at 450°C with nitrogen flow.

For ZnO_O_2 based PSCs, similar to ZnO_N_2 based devices, an enhancement of 36% in efficiency was observed after 7 days, see Figure VII.4b and Table VII.1. Then the performance of devices were slightly reduced after 13 days. The increase in conversion efficiency of ZnO_O_2 PSCs after 7 days should have the same origin with in ZnO_N_2 PSCs. The coalescence of smaller crystallite into larger ones also takes place in MAPI perovskite coated on ZnO_O_2. However, as discussed above, MAPI/ZnO_O_2

174

films were degraded after 15 days of preparation, the crystallinity and preferential orientation belong (110) plane were reduced, which causes a decrease in device performance (note that MAPI films and devices were stored under the same conditions, see experimental section for more details). Thus the reduction in the performance after 13 days should be the results of the competition processes in $MAPI_3$ films, which are (1) the coalescence of smaller crystallite into larger ones and (2) the degradation caused by the interfacial defects induced by the O_2 rich fabrication conditions of the ZnO layers.

Interestingly the performance improvement after 7 days of preparation for ZnO_O_2 based PSCs was also obtained for spray-pyrolyzed ZnO at different FTO substrate temperatures, Figure VII.S10 and Table VII.S2. Additionally we see again clearly the ZnO spray pyrolysis conditions, in this case it is different heated substrate temperatures, affect on the performance of devices. The highest efficiency was obtained for fresh devices based on ZnO deposited at 350°C. After 7 days, almost devices showed an improvement in efficiency however the amount of efficiency increased was not the same for devices containing ZnO prepared at different temperatures. Moreover, as it can be seen in the Figure VII.S1, ZnO fabricated at 350°C (ZnO_350°C) exhibits bigger grains than that deposited at 300°C (ZnO_300°C). And fresh PSCs based on ZnO_350°C show higher efficiency than fresh PSCs based on ZnO_300°C (see Table VII.S2). And this observation was the same trend for devices containing ZnO_O_2 and ZnO_N_2 performed at 450°C, higher grain sizes for ZnO_N_2 (see Figure VII.1b and VII.1c) and better performance for ZnO_N_2 based fresh PSCs (see Table VII.1). Moreover, the concentration of ZnO spray solution also affects on the performance of devices. Comparing PSC devices prepared with ZnO_O_2 prepared at 450°C however with 2 different concentrations, 0.1M and 0.3M (named ZnO_0.1M and ZnO_0.3M respectively), ZnO_0.3M based PSCs gave a better performance (see Table VII.1 and VII.S2) (note that the amount of Zn^{2+} in solutions was maintained the same). This is probably due to lower absorbance of ZnO_0.3M films which produced less optical loss (see Figure VII.S3b).

Furthermore the stability of ZnO_O_2 based PSCs also depends on the formation of ZnO. As showed above, the performance was slightly reduced after 13 days for devices containing ZnO_O_2 prepared from 0.3M zinc acetate solution and at 450°C. However, ZnO_O_2 substrates prepared at lower zinc acetate solution concentration (0.1M) and lower substrate temperature (at 350°C), exhibit an improvement of the performance even 30 days after their preparation, see Figure VII.S11 and table VII.S3. This analysis highlights that the use of O_2 flow is not the only parameter affecting the ZnO surface and

consequently the PSC performance. The formation of ZnO depends on many factors, i.e. solution concentration, pH, temperature, gas and the flow rate, that needs an accurate optimization in order to get an appropriated ZnO surface termination not just for the fresh devices but for the aged ones with enhanced performance. The potential application of our ZnO deposition method has been verified for different substrates as FTO and ITO; and also different electronic devices as solar cells and LEDs as well, see Figure VII.S12 and Table VII.S4. And it is worth to note that our ZnO based PSC also presents a good performance recovered after the electrical injection (see Figure VII.S13).
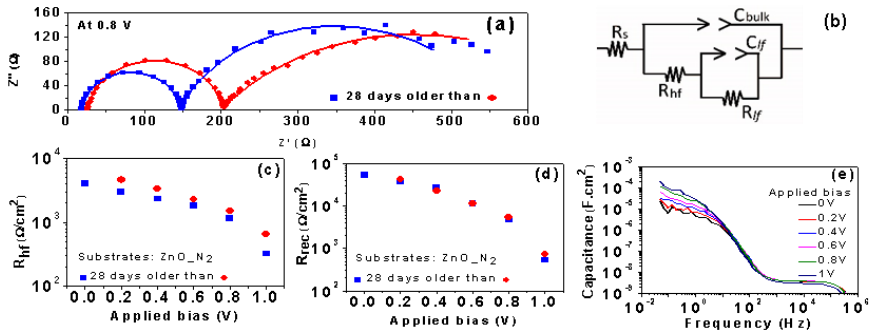
Figure VII.6. (a) Nyquist plot of perovskite devices based on ZnO_N_2 substrates, prepared on different time under 1 sun illumination at 0.8V DC applied bias. Symbols correspond to the experimental points while solid line is the fitting of the impedance spectra using equivalent circuit in (b),[40-42] constant phase elements (PE) has been used instead of perfect capacitors for a better fitting. (c) R_{hf} related to charge transport and to the recombination and (d) the sum of R_{lf} and R_{hf} (R_{rec}) resistance related to the recombination of those devices respectively. (e) Capacitance at different applied bias of an older device presented in fig a-d.

For further understanding of device behaviours, impedance spectroscopy measurements under working conditions, i.e. 1 sun illumination, at different applied DC voltages have been carried out. By comparing fitted data obtained from the impedance measurement of ZnO_O_2 and ZnO_N_2 based PSCs, we found that ZnO_O_2 based devices have lower contact series resistance, R_s (see Figure VII.S14), indicating ZnO_O_2 is higher conductive than ZnO_N_2. This finding is in agreement with the conductive AFM measurement (see Figure VII.2). However the PSCs based on ZnO_N_2 or ZnO_O_2 have similar short circuit current (J_{sc}), (see Figure VII.4 and table VII.1).

We moreover measured the impedance spectroscopy of a fresh sample prepared on ZnO_N_2 substrates and of a sample prepared on the same substrate 28 days after its fabrication (see Figure VII.6a), under working conditions, i.e. 1 sun illumination, at different applied DC voltages. Nyquist

plot presents two arc features at high frequency voltage (*hf*), left arc, and at low frequency (*lf*), right arc in Figure VII.6a. This is common feature observed in the impedance analysis of different kinds of PSCs, were two regions at *hf* (higher than ~500 Hz) and *lf* (lower than ~500 Hz) can be differentiated.[43-45] However, in some cases arcs at *lf* or *hf* regions decouple in more than one arcs.[40, 43, 46] The experimental data obtained from impedance measurements have been fitted using the equivalent circuit depicted in Figure VII.6b.[40-41] Despites there is no full interpretation of the complete physical meaning of each one of these elements, the implications of some of them is qualitatively understood. It has been shown that $R_{rec}=R_{hf}+R_{lf}$ obtained from impedance spectroscopy analysis allows to reconstruct the J-V which implies that this resistance has a recombination character inversely proportional to the recombination rate.[41-42] Figure VII.6d compares R_{rec} from fresh and aged sample and no significant difference can be appreciated. However, R_{hf} is clearly lower for aged sample (Figure VII.6c). It has been reported that this resistance receives contributions from the selective contacts and its decrease has been related with an increase of the charge transfer at the contacts with a consequent enhancement of the photocurrent.[40, 43] R_{hf} is plotted on a linear scale in Figure VII.S15. This analysis indicates that the enhancement of photovoltaic properties of aged samples is due to a reduction of the charge transfer resistance at the ZnO interface.

One of the most interesting features of the prepared cells using spray-pyrolized solar cells is the low hysteresis observed, see Figure VII.S9. This low hysteresis can be attributed to the reduced low frequency capacitance, C_{lf}, observed when spray-pyrolized ZnO substrates are used, see Figure 6e. PSC cells using TiO_2 as electron selective contact exhibit a huge C_{lf} under illumination.[47] This capacitance is associated with an accumulation capacitance,[41, 48] and it is significantly reduced in inverted cells with no TiO_2 contact that show no hysteresis.[49] In the case of ZnO substrates the observed values for low frequency accumulation capacitance, see Figure VII.6e, are significantly lower than the observed for TiO_2 substrates,[47] as the observed ones for inverted cell,[49] in good agreement with the low hysteresis obtained in this samples, see Figure VII.S9.

VII.4. CONCLUSIONS

In summary, here we report the preparation of ZnO thin film by spray pyrolysis with good qualities as homogeneous, full substrate coverage and high transmittance in visible range for ESC applications. Our ZnO based PSCs not only showed a good stability but also an improvement in performance after

fabrication. Concretely, the conversion efficiency increased quickly (36%) after 7 days of preparation, then slightly increased after more than 1 month of preparation, with samples stored under dark at room temperature and at a humidity of around 35%. The improvement in performance is related with morphological caused as the coalescence of smaller crystallites in MAPI films into bigger ones, resulting the enhancement in the grain size and an increase of (110) preferential orientation. We show ZnO preparation method influence this long term evolution of perovskite layer. Impedance characterization has indicated that these morphological changes of aged samples improve the charge carrier extraction at ZnO contact, enhancing significantly photocurrent and consequently photovoltage and fill factor. ZnO substrates also present low accumulation capacitance, observed at low frequencies, and consequently presenting low hysteresis. Since the relationship between the selective contacts and the hysteresis is well known, the influence of substrate on other important properties of perovskite materials, but less studied, as morphology evolution has not been pointed out. This work highlights the effect of substrate, and concretely of selective contact on the improvement properties of halide perovskite and could contribute to produce devices with long term stability.

References
(1) Yang, W. S.; Park, B.-W.; Jung, E. H.; Jeon, N. J.; Kim, Y. C.; Lee, D. U.; Shin, S. S.; Seo, J.; Kim, E. K.; Noh, J. H.; Seok, S. I. Iodide management in formamidinium-lead-halide–based perovskite layers for efficient solar cells. *Science* **2017**, *356* (6345), 1376-1379, DOI: 10.1126/science.aan2301.
(2) Grätzel, M. The light and shade of perovskite solar cells. *Nature materials* **2014,** *13*, 838, DOI: 10.1038/nmat4065.
(3) Zhang, P.; Wu, J.; Zhang, T.; Wang, Y.; Liu, D.; Chen, H.; Ji, L.; Liu, C.; Ahmad, W.; Chen, Z. D.; Li, S. Perovskite Solar Cells with ZnO Electron-Transporting Materials. *Advanced materials* **2017**, 1703737, DOI: 10.1002/adma.201703737.
(4) Green, M. A.; Ho-Baillie, A.; Snaith, H. J. The emergence of perovskite solar cells. *Nat Photon* **2014,** *8* (7), 506-514, DOI: 10.1038/nphoton.2014.134.
(5) Chueh, C.-C.; Li, C.-Z.; Jen, A. K. Y. Recent progress and perspective in solution-processed Interfacial materials for efficient and stable polymer and organometal perovskite solar cells. *Energy & Environmental Science* **2015,** *8* (4), 1160-1189, DOI: 10.1039/c4ee03824j.

(6) Fakharuddin, A.; Schmidt-Mende, L.; Garcia-Belmonte, G.; Jose, R.; Mora-Sero, I. Interfaces in Perovskite Solar Cells. *Advanced Energy Materials* **2017,** *7*, 1700623, DOI: 10.1002/aenm.201700623.

(7) Zhang, C.; Luo, Q.; Wu, H.; Li, H.; Lai, J.; Ji, G.; Yan, L.; Wang, X.; Zhang, D.; Lin, J.; Chen, L.; Yang, J.; Ma, C. Roll-to-roll micro-gravure printed large-area zinc oxide thin film as the electron transport layer for solution-processed polymer solar cells. *Organic Electronics* **2017,** *45*, 190-197, DOI: https://doi.org/10.1016/j.orgel.2017.03.015.

(8) Liu, D.; Kelly, T. L. Perovskite solar cells with a planar heterojunction structure prepared using room-temperature solution processing techniques. *Nat Photon* **2014,** *8* (2), 133-138, DOI: 10.1038/nphoton.2013.342

(9) Liu, H.; Huang, Z.; Wei, S.; Zheng, L.; Xiao, L.; Gong, Q. Nano-structured electron transporting materials for perovskite solar cells. *Nanoscale* **2016,** *8* (12), 6209-6221, DOI: 10.1039/c5nr05207f.

(10) Zhang, Q.; Dandeneau, C. S.; Zhou, X.; Cao, G. ZnO Nanostructures for Dye-Sensitized Solar Cells. *Advanced materials* **2009,** *21* (41), 4087-4108, DOI: 10.1002/adma.200803827.

(11) Dong, X.; Hu, H.; Lin, B.; Ding, J.; Yuan, N. The effect of ALD-Zno layers on the formation of CH3NH3PbI3 with different perovskite precursors and sintering temperatures. *Chemical communications* **2014,** *50* (92), 14405-14408, DOI: 10.1039/c4cc04685d.

(12) Vayssieres, L. Growth of Arrayed Nanorods and Nanowires of ZnO from Aqueous Solutions. *Advanced materials* **2003,** *15* (5), 464-466, DOI: 10.1002/adma.200390108.

(13) Mensah, S. L.; Kayastha, V. K.; Ivanov, I. N.; Geohegan, D. B.; Yap, Y. K. Formation of single crystalline ZnO nanotubes without catalysts and templates. *Applied physics letters* **2007,** *90* (11), 113108, DOI: 10.1063/1.2714186.

(14) Ronning, C.; Gao, P. X.; Ding, Y.; Wang, Z. L.; Schwen, D. Manganese-doped ZnO nanobelts for spintronics. *Applied physics letters* **2004,** *84* (5), 783-785, DOI: 10.1063/1.1645319.

(15) Ding, Y.; Kong, X. Y.; Wang, Z. L. Doping and planar defects in the formation of single-crystal ZnO nanorings. *Physical Review B* **2004,** *70* (23), 235408.

(16) Wang, Y.; Li, X.; Wang, N.; Quan, X.; Chen, Y. Controllable synthesis of ZnO nanoflowers and their morphology-dependent photocatalytic activities. *Separation and Purification Technology* **2008,** *62* (3), 727-732, DOI: https://doi.org/10.1016/j.seppur.2008.03.035.

(17) Gao, P. X.; Ding, Y.; Wang, Z. L. Crystallographic Orientation-Aligned ZnO Nanorods Grown by a Tin Catalyst. *Nano letters* **2003,** *3* (9), 1315-1320, DOI: 10.1021/nl034548q.

(18) Heo, J. H.; Lee, M. H.; Han, H. J.; Patil, B. R.; Yu, J. S.; Im, S. H. Highly efficient low temperature solution processable planar type CH3NH3PbI3 perovskite flexible solar cells. *Journal of Materials Chemistry A* **2016,** *4* (5), 1572-1578, DOI: 10.1039/c5ta09520d.

(19) An, Q.; Fassl, P.; Hofstetter, Y. J.; Becker-Koch, D.; Bausch, A.; Hopkinson, P. E.; Vaynzof, Y. High performance planar perovskite solar cells by ZnO electron

transport layer engineering. *Nano Energy* **2017,** *39* (Supplement C), 400-408, DOI: https://doi.org/10.1016/j.nanoen.2017.07.013.

(20) Lin, L.; Jiang, L.; Qiu, Y.; Yu, Y. Modeling and analysis of HTM-free perovskite solar cells based on ZnO electron transport layer. *Superlattices and Microstructures* **2017,** *104* (Supplement C), 167-177, DOI: https://doi.org/10.1016/j.spmi.2017.02.028.

(21) Azmi, R.; Hadmojo, W. T.; Sinaga, S.; Lee, C.-L.; Yoon, S. C.; Jung, I. H.; Jang, S.-Y. High-Efficiency Low-Temperature ZnO Based Perovskite Solar Cells Based on Highly Polar, Nonwetting Self-Assembled Molecular Layers. *Advanced Energy Materials* **2018,** *8*, 1701683, DOI: 10.1002/aenm.201701683.

(22) Zhang, J.; Juarez-Perez, E. J.; Mora-Sero, I.; Viana, B.; Pauporte, T. Fast and low temperature growth of electron transport layers for efficient perovskite solar cells. *Journal of Materials Chemistry A* **2015,** *3* (9), 4909-4915, DOI: 10.1039/C4TA06416J.

(23) Jiaxing, S.; Ji, B.; Enqiang, Z.; Xiao-Feng, W.; Wenjing, T.; Tsutomu, M. Efficient and Environmentally Stable Perovskite Solar Cells Based on ZnO Electron Collection Layer. *Chemistry Letters* **2015,** *44* (5), 610-612, DOI: 10.1246/cl.150056.

(24) Hu, Q.; Liu, Y.; Li, Y.; Ying, L.; Liu, T.; Huang, F.; Wang, S.; Huang, W.; Zhu, R.; Gong, Q. Efficient and low-temperature processed perovskite solar cells based on a cross-linkable hybrid interlayer. *Journal of Materials Chemistry A* **2015,** *3* (36), 18483-18491, DOI: 10.1039/c5ta04695e.

(25) Song, J.; Liu, L.; Wang, X.-F.; Chen, G.; Tian, W.; Miyasaka, T. Highly efficient and stable low-temperature processed ZnO solar cells with triple cation perovskite absorber. *Journal of Materials Chemistry A* **2017,** *5* (26), 13439-13447, DOI: 10.1039/c7ta03331a.

(26) Vimalkumar, T. V. Highly conductive and transparent ZnO thin film using Chemical Spray Pyrolysis technique: Effect of doping and deposition parameters. Ph. D. Cochin University of Science and Technology, 2011.

(27) Prasada Rao, T.; Santhosh Kumar, M. C.; Ganesan, V. Effect of annealing on the structural, optical and electrical properties of ZnO thin films by spray pyrolysis. *Indian Journal of Physics* **2011,** *85* (9), 1381, DOI: 10.1007/s12648-011-0160-1.

(28) Tseng, Z.-L.; Chiang, C.-H.; Wu, C.-G. Surface Engineering of ZnO Thin Film for High Efficiency Planar Perovskite Solar Cells. *Scientific reports* **2015,** *5*, 13211, DOI: 10.1038/srep13211

(29) Roose, B.; Ummadisingu, A.; Correa-Baena, J.-P.; Saliba, M.; Hagfeldt, A.; Graetzel, M.; Steiner, U.; Abate, A. Spontaneous crystal coalescence enables highly efficient perovskite solar cells. *Nano Energy* **2017,** *39* (Supplement C), 24-29, DOI: https://doi.org/10.1016/j.nanoen.2017.06.037.

(30) Yen-Chen, S.; Yu-Bing, L.; Chia-Shuo, L.; Hsiao-Chi, H.; Leeyih, W.; Chih-I, W.; King-Fu, L. Amino-Acid-Induced Preferential Orientation of Perovskite Crystals for Enhancing Interfacial Charge Transfer and Photovoltaic Performance. *Small* **2017,** *13* (22), 1604305, DOI: doi:10.1002/smll.201604305.

(31) Climent-Pascual, E.; Hames, B. C.; Moreno-Ramirez, J. S.; Alvarez, A. L.; Juarez-Perez, E. J.; Mas-Marza, E.; Mora-Sero, I.; de Andres, A.; Coya, C.

Influence of the substrate on the bulk properties of hybrid lead halide perovskite films. *Journal of Materials Chemistry A* **2016,** *4* (46), 18153-18163, DOI: 10.1039/C6TA08695K.

(32) Peng, Y.; Cheng, Y.; Wang, C.; Zhang, C.; Xia, H.; Huang, K.; Tong, S.; Hao, X.; Yang, J. Fully doctor-bladed planar heterojunction perovskite solar cells under ambient condition. *Organic Electronics* **2018,** *58*, 153-158, DOI: https://doi.org/10.1016/j.orgel.2018.04.020.

(33) Chunhua, W.; Chujun, Z.; Shitan, W.; Gang, L.; Huayan, X.; Sichao, T.; Jun, H.; Dongmei, N.; Conghua, Z.; Kongxian, D.; Yongli, G.; Junliang, Y. Low-Temperature Processed, Efficient, and Highly Reproducible Cesium-Doped Triple Cation Perovskite Planar Heterojunction Solar Cells. *Solar RRL* **2018,** *2* (2), 1700209, DOI: doi:10.1002/solr.201700209.

(34) Huang, K.; Wang, C.; Zhang, C.; Tong, S.; Li, H.; Liu, B.; Gao, Y.; Dong, Y.; Gao, Y.; Peng, Y.; Yang, J. Efficient and stable planar heterojunction perovskite solar cells fabricated under ambient conditions with high humidity. *Organic Electronics* **2018,** *55*, 140-145, DOI: https://doi.org/10.1016/j.orgel.2018.01.029.

(35) Aristidou, N.; Eames, C.; Sanchez-Molina, I.; Bu, X.; Kosco, J.; Islam, M. S.; Haque, S. A. Fast oxygen diffusion and iodide defects mediate oxygen-induced degradation of perovskite solar cells. *Nature communications* **2017,** *8*, 15218, DOI: 10.1038/ncomms15218

(36) Bryant, D.; Aristidou, N.; Pont, S.; Sanchez-Molina, I.; Chotchunangatchaval, T.; Wheeler, S.; Durrant, J. R.; Haque, S. A. Light and oxygen induced degradation limits the operational stability of methylammonium lead triiodide perovskite solar cells. *Energy & Environmental Science* **2016,** *9* (5), 1655-1660, DOI: 10.1039/c6ee00409a.

(37) Yang, J.; Siempelkamp, B. D.; Mosconi, E.; De Angelis, F.; Kelly, T. L. Origin of the Thermal Instability in CH3NH3PbI3 Thin Films Deposited on ZnO. *Chemistry of Materials* **2015,** *27* (12), 4229-4236, DOI: 10.1021/acs.chemmater.5b01598.

(38) Aristidou, N.; Sanchez-Molina, I.; Chotchuangchutchaval, T.; Brown, M.; Martinez, L.; Rath, T.; Haque, S. A. The Role of Oxygen in the Degradation of Methylammonium Lead Trihalide Perovskite Photoactive Layers. *Angewandte Chemie International Edition* **2015,** *54* (28), 8208-8212, DOI: 10.1002/anie.201503153.

(39) Koocher, N. Z.; Saldana-Greco, D.; Wang, F.; Liu, S.; Rappe, A. M. Polarization Dependence of Water Adsorption to CH3NH3PbI3 (001) Surfaces. *The journal of physical chemistry letters* **2015,** *6* (21), 4371-4378, DOI: 10.1021/acs.jpclett.5b01797.

(40) Guerrero, A.; Garcia-Belmonte, G.; Mora-Sero, I.; Bisquert, J.; Kang, Y. S.; Jacobsson, T. J.; Correa-Baena, J.-P.; Hagfeldt, A. Properties of Contact and Bulk Impedances in Hybrid Lead Halide Perovskite Solar Cells Including Inductive Loop Elements. *The Journal of Physical Chemistry C* **2016,** *120* (15), 8023-8032, DOI: 10.1021/acs.jpcc.6b01728.

(41) Zarazua, I.; Han, G.; Boix, P. P.; Mhaisalkar, S.; Fabregat-Santiago, F.; Mora-Seró, I.; Bisquert, J.; Garcia-Belmonte, G. Surface Recombination and

Collection Efficiency in Perovskite Solar Cells from Impedance Analysis. *The journal of physical chemistry letters* **2016,** *7* (24), 5105-5113, DOI: 10.1021/acs.jpclett.6b02193.

(42) Zarazúa, I.; Sidhik, S.; Lopéz-Luke, T.; Esparza, D.; De la Rosa, E.; Reyes-Gomez, J.; Mora-Seró, I.; Garcia-Belmonte, G. Operating Mechanisms of Mesoscopic Perovskite Solar Cells through Impedance Spectroscopy and J–V Modeling. *J. Chem. Phys. Lett.* **2017,** *8* (24), 6073-6079, DOI: 10.1021/acs.jpclett.7b02848.

(43) Juarez-Perez, E. J.; Wuβler, M.; Fabregat-Santiago, F.; Lakus-Wollny, K.; Mankel, E.; Mayer, T.; Jaegermann, W.; Mora-Sero, I. Role of the Selective Contacts in the Performance of Lead Halide Perovskite Solar Cells. *The journal of physical chemistry letters* **2014,** *5* (4), 680-685, DOI: 10.1021/jz500059v.

(44) Dualeh, A.; Moehl, T.; Tétreault, N.; Teuscher, J.; Gao, P.; Nazeeruddin, M. K.; Grätzel, M. Impedance Spectroscopic Analysis of Lead Iodide Perovskite-Sensitized Solid-State Solar Cells. *ACS nano* **2014,** *8* (1), 362-373, DOI: 10.1021/nn404323g.

(45) Pockett, A.; Eperon, G. E.; Peltola, T.; Snaith, H. J.; Walker, A.; Peter, L. M.; Cameron, P. J. Characterization of Planar Lead Halide Perovskite Solar Cells by Impedance Spectroscopy, Open-Circuit Photovoltage Decay, and Intensity-Modulated Photovoltage/Photocurrent Spectroscopy. *The Journal of Physical Chemistry C* **2015,** *119* (7), 3456-3465, DOI: 10.1021/jp510837q.

(46) Guillén, E.; Ramos, F. J.; Anta, J. A.; Ahmad, S. Elucidating Transport-Recombination Mechanisms in Perovskite Solar Cells by Small-Perturbation Techniques. *The Journal of Physical Chemistry C* **2014,** *118* (40), 22913-22922, DOI: 10.1021/jp5069076.

(47) Juarez-Perez, E. J.; Sanchez, R. S.; Badia, L.; Garcia-Belmonte, G.; Kang, Y. S.; Mora-Sero, I.; Bisquert, J. Photoinduced Giant Dielectric Constant in Lead Halide Perovskite Solar Cells. *The journal of physical chemistry letters* **2014,** *5* (13), 2390-2394, DOI: 10.1021/jz5011169.

(48) Zarazua, I.; Bisquert, J.; Garcia-Belmonte, G. Light-Induced Space-Charge Accumulation Zone as Photovoltaic Mechanism in Perovskite Solar Cells. *The journal of physical chemistry letters* **2016,** *7* (3), 525-528, DOI: 10.1021/acs.jpclett.5b02810.

(49) Kim, H.-S.; Jang, I.-H.; Ahn, N.; Choi, M.; Guerrero, A.; Bisquert, J.; Park, N.-G. Control of I–V Hysteresis in CH3NH3PbI3 Perovskite Solar Cell. *J. Chem. Phys. Lett.* **2015,** *6* (22), 4633-4639, DOI: 10.1021/acs.jpclett.5b02273.
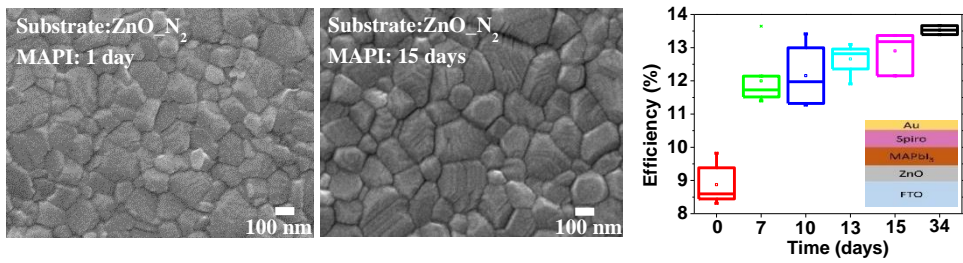
TOC Figure

Supporting information

Spray-pyrolyzed ZnO as electron selective contact for long term stable planar CH₃NH₃PbI₃ perovskite solar cells.

Thi Tuyen Ngo[1], Eva María Barea[1], Ramon Tena-Zaera[2] and Iván Mora-Seró[1,*]

[1]Institute of Advanced Materials (INAM), Jaume I University, Avenida de VicentSosBaynat, s/n, 12071 Castellón de la Plana, Castellón (Spain)
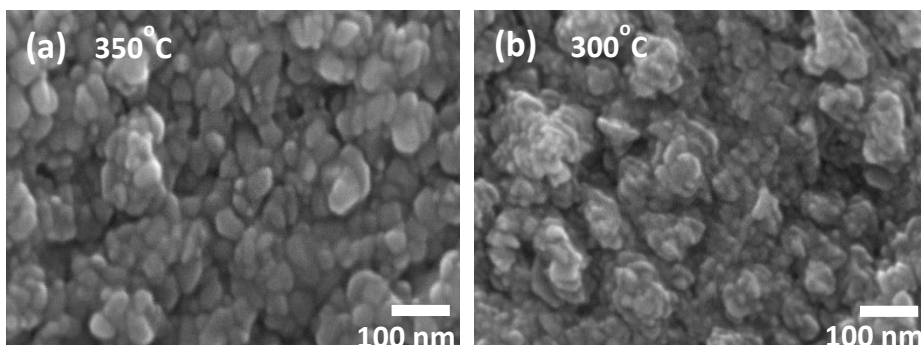[2]CIDETEC, Parque Tecnológico de San Sebastián, Paseo Miramón, 196, Donostia–San Sebastián 20014 (Spain)

Figure VII.S1. Top view SEM from secondary electrons of ZnO spray-pyrolyzed from 0.1 M zinc acetate solution at 350ºC (a) and 300ºC (b) with oxygen flow.
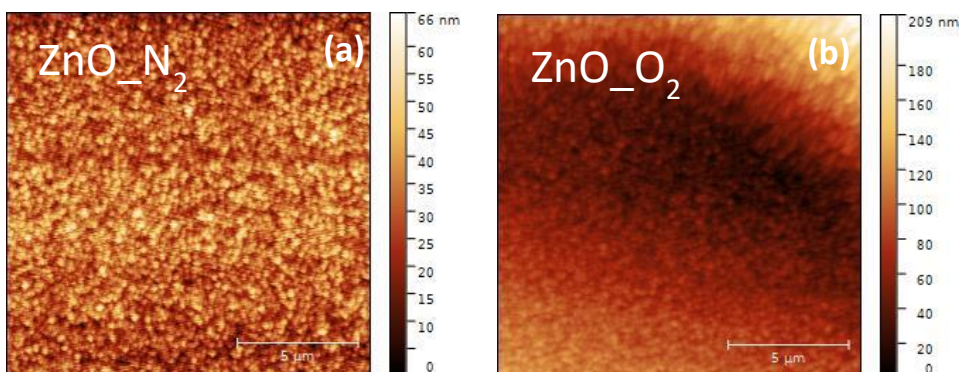

Figure VII.S2. Atomic force microscopy (AFM) of ZnO layer deposited on FTO from 0.3M of zinc acetate solution at 450ºC with nitrogen (a, named ZnO_N₂) and oxygen flow (b, named ZnO_O₂).
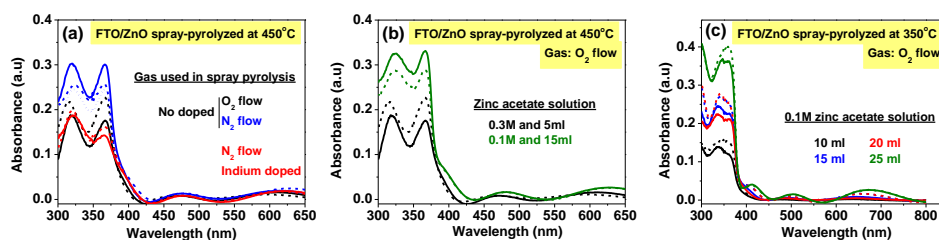
Figure VII.S3. Absorbance spectra of spray-pyrolyzed ZnO from (a) 5 ml of 0.3 M zinc acetate solution at 450°C with nitrogen and oxygen flow; (b) different volume and zinc acetate concentration solution at 450°C with oxygen flow, the amount of Zn^{2+} ions was maintained the same in the spray solutions and (c) different volume of 0.1M zinc acetate solution at 350°C with oxygen flow.
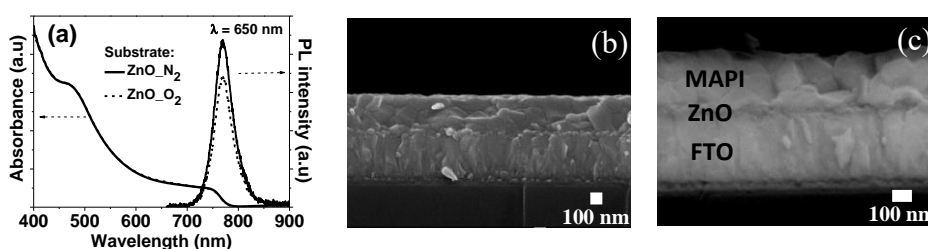

Figure VII.S4. (a) Absorbance and photoluminescence (PL) of fresh MAPI on ZnO layer spray-pyrolysized from 0.3 M zinc acetate solution at 450°C with nitrogen and oxygen flow. Cross section SEM images from secondary (b) and backscattered electrons of fresh MAPI film deposited on ZnO prepared with N_2 flow.
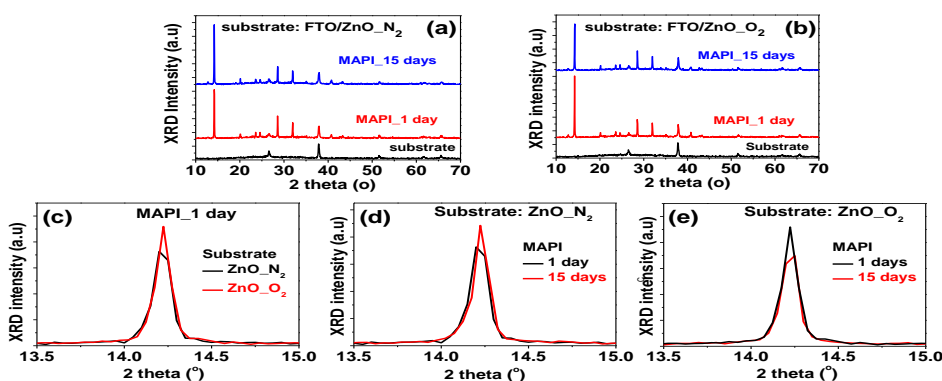

Figure VII.S5. (a-b) XRD pattern of 1 day and 15 day-old MAPI deposited on FTO/ZnO_N_2 (a) and FTO/ZnO_O_2 substrates (b). In which ZnO was spray-pyrolyzed from 0.3 M zinc acetate solution at 450°C with nitrogen and oxygen flow. The XRD pattern of substrate is belong to SnO_2 (reference pattern: 9163). There is no detection of ZnO peaks due to its extremely thin thickness. (c-e) Comparison of XRD intensity at 14.2° of those MAPI films which were stored under dark and at room temperature and at around 35% of humidity.
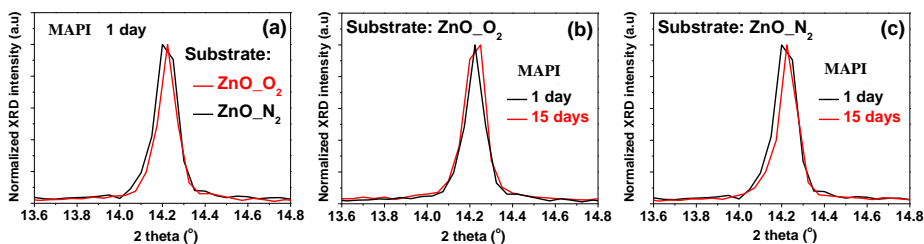
Figure VII.S6. Normalized XRD intensity at 14.2° of 1 day and 15 days-old MAPI deposited on FTO/ZnO_N$_2$ and FTO/ZnO_O$_2$ substrates. In which ZnO was spray-pyrolyzed from 0.3 M zinc acetate solution at 450°C with nitrogen and oxygen flow. Those MAPI films which were stored under dark and at room temperature and at around 35% of humidity.

2 theta (o)	FWHM			
	Substrate: ZnO_N$_2$		Substrate: ZnO_O$_2$	
	MAPI: 1 day	MAPI: 15 days	MAPI: 1 day	MAPI: 15 days
14.2	0.117	0.101	0.104	0.111
2 theta (o)	XRD intensity (%)			
	Substrate: ZnO_N$_2$		Substrate: ZnO_O$_2$	
	MAPI: 1 day	MAPI: 15 days	MAPI: 1 day	MAPI: 15 days
14.2	100	100	100	100
28.6	47.2	31.2	30.4	43.3
32	33.7	24.2	24.9	31.7

Table VII.S1. Full width at half maximum (FWHM) and normalized XRD intensity of 1 day and 15 days-old MAPI film deposited on FTO/ZnO_N$_2$ and FTO/ZnO_O$_2$ compact layer. In which ZnO was spray-pyrolyzed from 0.3 M zinc acetate solution at 450°C with nitrogen and oxygen flow. MAPI films were stored under dark and around 35% of humidity.
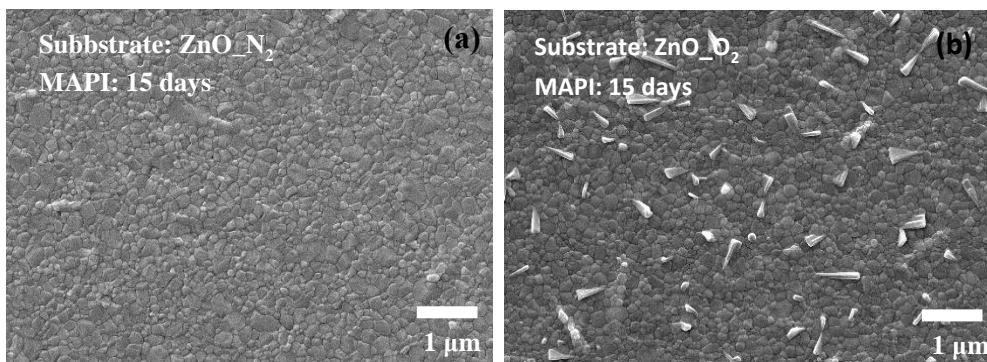
Figure VII.S7. Low magnification top view SEM of 15 days-old MAPI deposited on FTO/ZnO_N$_2$ (a) and FTO/ZnO_O$_2$ substrates (b). In which ZnO was spray-pyrolyzed from of 0.3 M zinc acetate solution at 450°C with nitrogen and oxygen flow. MAPI films were stored under dark and at room temperature and at around 35% of humidity.
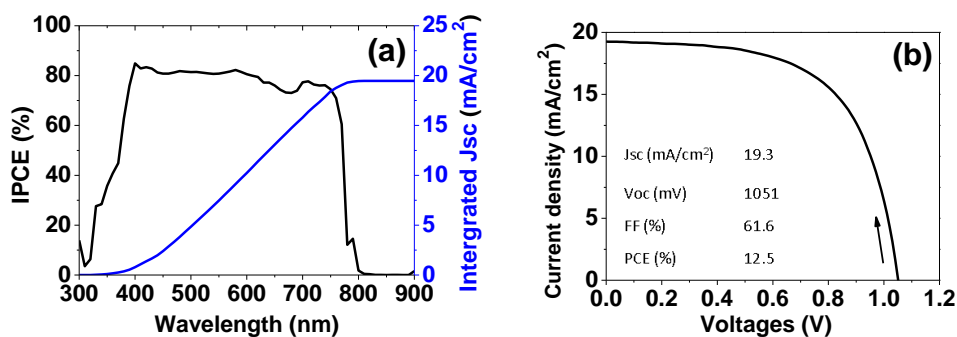

Figure VII.S8. IPCE spectra and integrated short circuit current density (Jsc) of FTO/ZnO_N$_2$/MAPI/Spiro OMeTAD/Au (a) and its J-V curve, reverse scan, measured at 1 sun illumination. In which ZnO was spray-pyrolyzed from 0.3 M zinc acetate solution at 450°C with nitrogen flow.
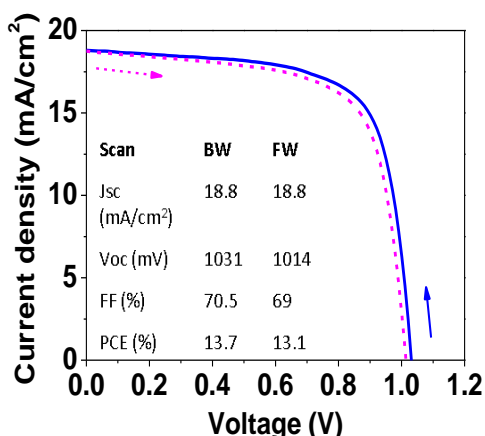

Figure VII.S9. Current density-voltage (J-V) characteristic best device after 34 days prepared with a structure of FTO/ZnO_N$_2$/MAPI/Spiro OMeTAD/Au at 1 sun illumination. In which ZnO was spray-pyrolyzed from 0.3 M zinc acetate solution at 450°C with nitrogen flow. Sample was stored under dark at room temperature and at around 35% of humidity.
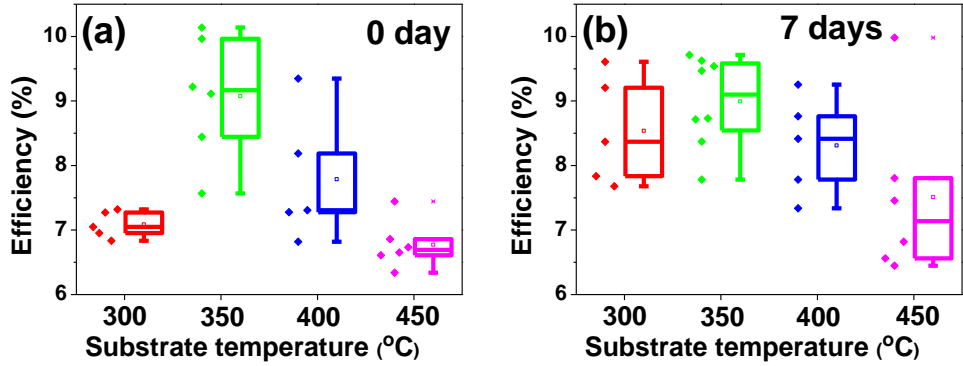
187

Figure VII.S10. Performance at 1 sun illumination of planar based ZnO_O_2 devices with a structure of FTO/ZnO/MAPI/Spiro OMeTAD/Au measured immediately (a) and 7 days after the preparation (b). In which ZnO was spray-pyrolyzed from 15 ml of 0.1 M zinc acetate solution at different substrate temperatures with oxygen flow. Full devices were stored under dark, at room temperature and at around 35% of humidity. The concentration of zinc acetate solution was reduced 1/3 times however the solution volume was increased 3 times to maintain the same amount of Zn^{2+}, in comparison with the samples used in Table VII.1. The best efficiency for fresh devices was archived for ZnO prepared at 350°C and this value is similar to that obtained for ZnO spray-pyrolyzed at 450°C with higher concentration of zinc acetate solution (table VII.1 and table VII.S2). The reason is at different solution concentrations and different substrate temperatures, ZnO was formed differently.

Time [days]	Subs_temp [°C]	Jsc [mA/cm²]	Voc [mV]	FF [%]	PCE [%]
0	300	15.5 ± 0.1	934.2 ± 16.7	46.4 ± 0.7	7.1 ± 0.1
7		16.1 ± 0.1	1006.2 ± 8.9	53.5 ± 1	8.5 ± 0.3
0	350	15.9 ± 0.1	1010.4 ± 9.4	50.2 ± 1.6	9.1 ± 0.3
7		15.6 ± 0.2	1021.5 ± 6.9	57.8 ± 0.9	9 ± 0.2
0	400	16.9 ± 0.2	831.6 ± 21.8	52 ± 0.4	7.8 ± 0.4
7		14.9 ± 0.1	981 ± 18.7	55.2 ± 0.5	8.3 ± 0.3
0	450	16.1 ± 0.2	773.4 ± 16.1	49.1 ± 1.2	6.8 ± 0.1
7		13.8 ± 0.3	933.8 ± 17	57.9 ± 0.8	7.5 ± 0.4

Table VII.S2. Statistic photovoltaic parameters at 1 sun of planar based ZnO thin film devices showed in the Figure VII.S10.
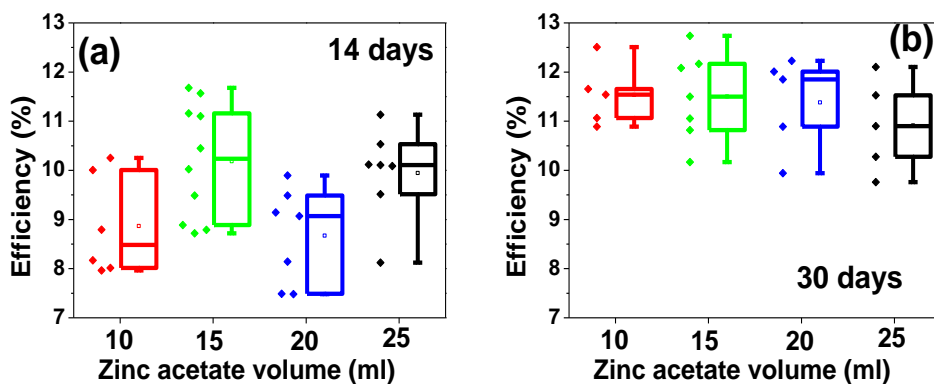
Figure VII.S11. Performance at 1 sun illumination of planar based ZnO_O_2 devices with a structure of FTO/ZnO/MAPI/Spiro OMeTAD/Au measured 14 days (a) and 30 days (b) after the preparation. In which ZnO was spray-pyrolyzed from different volume of 0.1 M zinc acetate solution at 350ºC substrate temperatures with oxygen flow. Full devices were stored under dark and at room temperature and at around 35% of humidity.

Time [days]	Zinc acetate volume [ml]	PCE [%]
14	10	8.9 ± 0.3
30		11.5 ± 0.3
14	15	10.1 ± 0.3
30		11.3 ± 0.2
14	20	8.7 ± 0.3
30		11.4 ± 0.4
14	25	9.9 ± 0.3
30		10.9 ± 0.4

Table VII.S3. Statistic photovoltaic parameters of planar based ZnO thin film devices showed in the Figure VII.S11.

Subtrates	Jsc mA/cm^2	Voc mV	FF %	PCE %
FTO/ZnO	15.78	1067.35	45.14	7.60
ITO/ZnO	12.84	1012.12	59.70	7.76

Table VII.S4. Photovoltaic parameters at 1 sun illumination of fresh (0 day-old) planar based ZnO devices with a structure of ZnO/MAPI/Spiro OMeTAD/Au. In which ZnO was spray-pyrolyzed from of 0.1 M zinc acetate solution at 300ºC substrate (FTO or ITO) temperatures with oxygen flow.
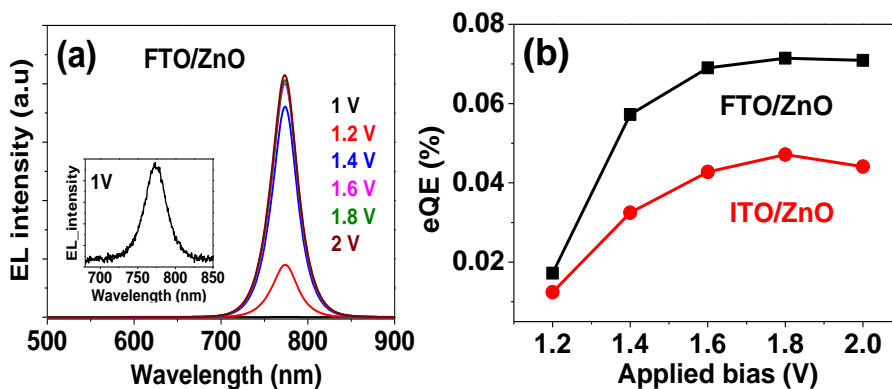
Figure VII.S12. (a) EL spectra and eQE (b) of fresh (0 day-old) LED devices with a structure of ZnO/MAPI/Spiro OMeTAD/Au at different applied bias. In which ZnO was spray-pyrolyzed from 0.1M zinc acetate solution at 300°C substrate (FTO or ITO) temperatures with oxygen flow.
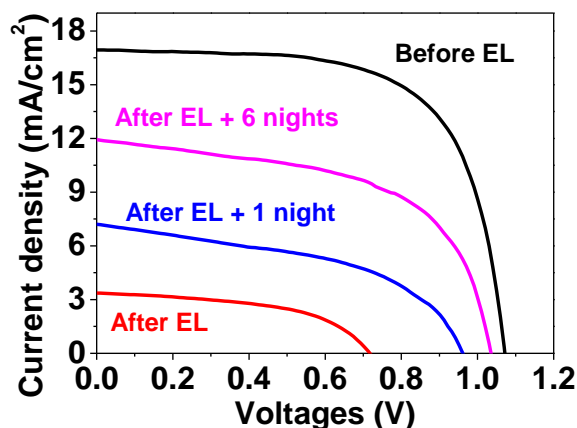

Figure VII.S13. Performance at 1 sun illumination of un-encapsulated planar based ZnO devices with a structure of FTO/ZnO/MAPI/Spiro OMeTAD/Au before and after the EL measurement at 1.8 V applied bias. In which ZnO was spray-pyrolyzed from 0.3M zinc acetate solution at 450°C with oxygen flow. Full devices were stored under dark and at room temperature and at around 35% of humidity. It is well known that after the electroluminescence (EL) measurement un-encapsulated MAPI devices degraded. Our devices showed a significant drop after the characterization as LED. However the performance was recovered partially with time storing the device under dark at room temperature and with a humidity of around 35%.
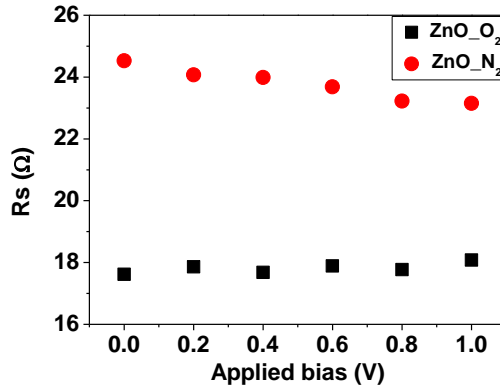
Figure VII.S14. Fitted contact resistance, Rs, of impedance spectroscopy measurement of PSCs based on ZnO_N$_2$ or ZnO_O$_2$ substrates at 1 sun illumination
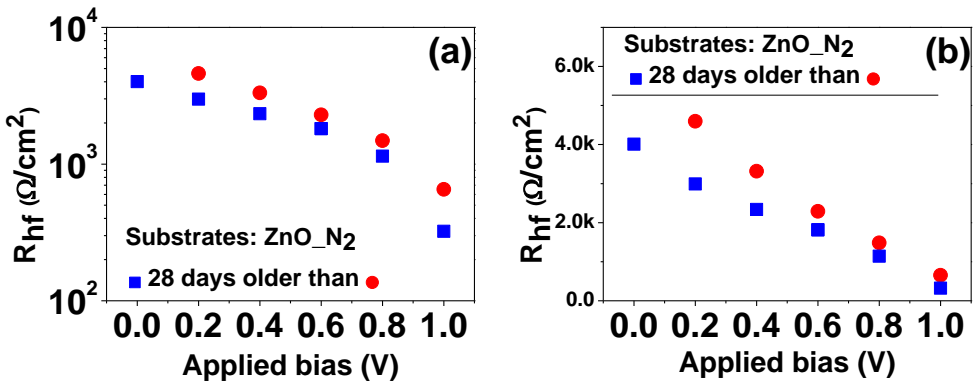

Figure VII.S15. *R$_{hf}$* related to charge transport and to the recombination obtaining in the Figure VII.6, plotted in log (a) and linear scale (b).

Chapter VIII. Discuss of the Results

Along all this thesis we have highlighted that HPs are a very promising materials, possessing amazing properties such as high absorption coefficient and long charge carrier diffusion length. Structurally all the cations and anions forming HPs can be easily exchanged to meet specific requirements. They have been potentially applied in different optoelectronic devices including solar cells, light emitting diodes (LEDs), photodetectors or light amplifiers. The simplicity in the preparation and the flexibility in the structure permit HPs effortlessly to integrate with other materials. The combination of HP with some different materials is discussed in the chapter I.2. These combinations have showed many advantages such as enhanced properties of composite or advanced device configuration. Taking into account the interest of HP and the advantage of combining materials, this thesis focuses on the study of the interaction of HP (concretely MAPI) with different materials looking for the potential applications, mainly in photovoltaics but also with interest in LEDs and light amplifiers. In order to reach this goal, several objectives have been targeted, which are listed in the chapter I.3. In the present chapter, we highlight the accomplishment of the objectives proposed and discuss about the general results obtained.

HP is the central material of this work. Its properties are crucial affecting of course the interaction with other materials. Consequently, having good quality of HP is very important and it is a prerequisite. Regarding this point, during the doctoral study we were able to prepare MAPI HP with state-of-the-art quality. This is illustrated by the obtaining high efficiencies for HP solar cells (the reference cells) in the publications presented in the chapter V, VI and VII.

One of the materials that we selected for the interaction with HP are colloidal QDs, concretely PbS core and PbS/CdS core/shell QDs. The synthesis and characterization of QDs are also indispensable. During the doctoral study, including a three-months-research stay at Weizmann Institute of Science, Israel, we could synthesize PbS, PbSe core and PbS/CdS, PbSe/CdSe core/shell QDs highly emissive and low dispersion of size. In the chapter I.2.1a we presented the photoluminescence (PL), absorbance spectra

and TEM images of as-synthesized PbS QDs with different sizes from 2.9 nm to 8.2 nm. PbS core and PbS/CdS core/shell QDs of 2.3 nm; and PbS core QDs of 3.5 nm have been used to study the interaction with MAPI HP which are showed in the publications presented in the chapter IV and V respectively. The other kind of developed colloidal QDs will be employed in future investigation which will be mentioned in the chapter IX. The capping ligand surrounding the QD surface is a key factor in the properties of colloidal QDs, because QDs have a high surface-volume ratio and at the surface the crystalline periodicity is disrupted creating dangling bonds that have to be properly passivated. Therefore the capping ligand not only serves as an agent to control the growth of QDs during the synthesis but also work as a QD passivation agent. Moreover, the capping ligand significantly affects the solubility of QDs in different solvents, in particular the common solvents (DMF and DMSO) of the HP preparation. In the thesis, we also performed different ligand exchange to overcome the solubility limit of as-synthesized QDs in order to produce HP films with embedded QDs, chapter IV and V. The effect of QD capping ligand on the interaction with HP is studied and presented in the chapter V.

From the observation of the interaction between HP and different materials, first we found that in the agreement with literature, HP is relatively facile to prepare and to combine with other materials employing different methods. In fact, HP allows QDs to intersperse into its matrix, forming embedded QD-HP hybrid material, but also HP ably links with organic molecules, being HATNA and DCL97 on the surface resulting the passivation of surface. Second, the quality of HP is strongly dependent not only on the preparation but also on which materials it is combined with.

For the combination with QDs, the morphology and properties, including optical and structural properties, of HP films can be easily changed by embedding QD inside its matrix. With a proper amount of intermixed PbS QDs, generally small, the quality of HP can be significantly improved. As discussed in the chapter V, the grains of MAPI HP were enlarged when PbS QDs was introduced with the concentration of 50 µg/ml. The photoluminescence (PL) intensity was significantly increased comparing with HP reference film, without QDs. The HP precursors were converted more efficiently to HP when PbS QDs were added, which was indicated by the reduction in intensity of PbI_2 diffraction peak. In addition, the preferential orientation of HP crystalline along (110) plane direction was also improved. These effects were originated by the seed-like site function of PbS QDs to promote the crystallization of HP. As a result the quality of HP films improved, the solar cells based on hybrid HP-PbS QDs showed a better performance comparing with reference cells, without QDs. More importantly

in our work we discovered that capping ligand of PbS QDs also played a role in the crystallization of HP. At the same concentration of intermixed PbS QDs (C_{PbS}), the extent of improvement in HP properties is capping-ligand dependent. In this work, we tested three different capping ligands of PbS QDs, accurately MAPI, cesium lead iodide (CsPI) and 4-aminobenzoic acid (ABA). And we observed that ABA ligand had a stronger influence on the HP morphology while CsPI ligand highly affected on the HP's optical property. For a planar solar cell devices based on those hybrid HP-PbS absorbers, the highest improvement in the performance was achieved for ABA ligand used.

As discussed above at low embedded QD concentration (C_{PbS}, ~ 50 µg/ml), the performance of hybrid HP-QDs based solar cells was improved. However when we increased the C_{QDs} in MAPI matrix, the performance of HP-QD solar cells was reduced, especially the photocurrent, as illustrated in the Table VIII.1. The reduction was higher for higher C_{QDs}. This observation probably is due to distortion in the MAPI lattice as PbS and MAPI possess low but still ~ 5% of lattice mismatch.[1] We carried out the PL measurement of HP-PbS QD films. And we detected a quenching in the emission of HP (Fig VIII.1). This quenching indicates the charge carriers transferred from HP to PbS QDs. Analyzing the charge dynamics of HP-QD films as a function of embedded PbS/CdS QD concentrations, we found that the transient absorption (TA) signal became shorter, referring faster charge carriers transferred, upon increasing the C_{QDs}. The significant change in the TA signal started at C_{QDs} of 0.6 mg/ml and at lower than 0.46 mg/ml the TA decays were governed by the behaviour of net HP[2] (publication not included in the thesis). Note that the C_{QDs} reported in this publication was calculated with the mass of MAPI ligand included, resulting the C_{QDs} were 4 and 3 mg/ml, or 0.24 wt% and 0.18 wt% of PbS QDs in HP matrix respectively. These C_{QDs} were 0.6 and 0.46 mg/ml when the MAPI ligand was not included, and they are the C_{QDs} calculation which is used for the all discussion throughout the body of this thesis. This result points to an enhanced recombination for too high QD concentrations.

C_QDs	Jsc (mA/cm^2)	Voc (mV)	FF (%)	PCE (%)
0 mg/ml	17.07	1069	59.61	10.87
	15.62	1095	61.58	10.53
1 mg/ml	7.29	1008	49.8	3.7
10 mg/ml	0.68	797	43.89	0.24
	0.73	831	48.98	0.30
62 mg/ml	0.54	704	43.08	0.16

Table VIII.1. Photovoltaic parameters of planar TiO$_2$/Absorber/Spiro-OMeTAD/Au solar cells. Absorbers were MAPI perovskite without and with PbS/CdS QDs of 3 nm with different concentrations and QDs had MAPI ligand.
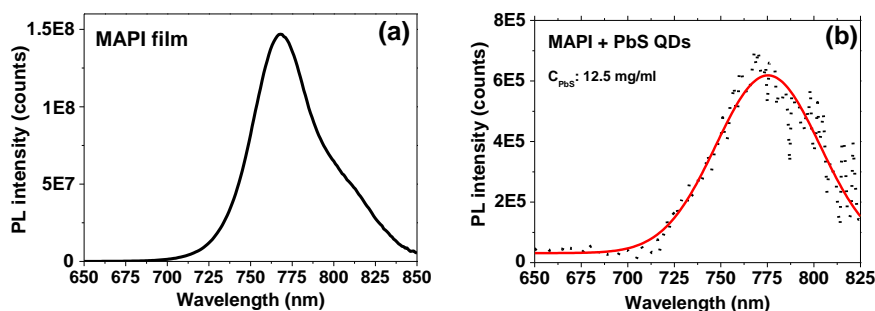

Fig VIII.1. PL of MAPI films without (a) and with embedded PbS QDs_capped MAPI ligand. Dots and solid line in the Fig b are corresponding to experimental data and the fitting respectively.

Beside the PL of HP quenching, the Jsc of solar cells based on HP-QD films was reduced when C$_{QDs}$ was increased in the range of mg/ml (Table VIII.1), we observed that the grains of the HP-QD film were much more enlarged, which was shown in the chapter IV. (Note that the C$_{QDs}$ of 300 mg/ml in MAPI matrix reported in this publication was calculated with the mass of MAPI ligand included, and according to the C$_{QDs}$ calculation presented in the entire thesis without the mass of MAPI ligand, it was ~ 30 mg/ml). We have showed that the morphology of HP was changed depending on not only the C$_{QDs}$ but also on the PbS QD ligands embedded in HP matrix. The properties including optical and structural properties which already presented in HP material were also dependent on the C$_{QDs}$ and their ligands, leading the dependence in the performance of devices.

The most important result obtained from the combination of perovskite and QDs is the appearition of a new PL emission in the combined samples of HP and QDs (PbS core and PbS/CdS core/shell QDs) which does not exist

single HP or QDs themselves, as we analysed in chapter IV. By forming a type II energy band alignment at MAPI/QD interface, the electrons in HP CB can recombine with holes in QD VB, resulting the formation of exciplex emission at energy lower than the bandgap of both HP and QDs. In addition, in our work as QDs were embedded into HP matrix, their interaction can take place deeply in the bulk film. Moreover, as discussed above about the dependence of charge dynamics of hybrid HP-QD films on the embedded QD concentration, by controlling the concentration of QDs the interaction could be tuned. Furthermore, due to the reciprocity principle, if an electron and hole from an exciplex state can recombine producing a photon, the reciprocal process in which a photon can produce an electron-hole pair at the exciplex state is also possible. This possibility opens the door for the preparation of IBSCs taking benefit from the HP and QD synergies. In an IBSC there are one or several intermediate bands, resulting from the exciplex states, lying in the bandgap of a wide gap semiconductor. Intermediate bands would act as stepping stones allowing low energy photons transfer electrons from the VB of the wide bandgap semiconductor to its CB. Theoretical calculation predicts a very high maximum photoconversion efficiency could be obtained for IBSCs (chapter III). However, there are three two main problems in the preparation of IBSC, which are (i) in order to maintain the Voc of the wide bandgap semiconductor, the intermediate band level has to be isolated from the extracting contact. (ii) To form the intermediate band, the concentration of QDs need to be high, which produce a strain due to the lattice mismatch of HP and QDs in the layer, and very high strain causes the formation of defects that degrades severely the cell performance (Table VIII.1). Nonetheless, the strain could be reduced by using mixed halide Br-I perovskite[3] or inorganic perovskite[4] in order to reduce the lattice mismatch between HP and PbS QDs. (iii) To avoid that intermediate states act as traps promoting non-radiative recombination.

We show that HP can get the benefit from the combination with colloidal QDs, as obtaining proper crystallization of HP lattice structures, chapter V. The building up of constructive synergies in the HP-QD combination shows important benefits in the development of optoelectronic devices, as detecting the exciplex emission, chapter V, and the possible implementation of IBSC concept. In addition, QDs also benefit from their combination with HP. It has been previously demonstrated that HPs and HP precursors such as MAPI[5-6], $CsPbI_3$ [7], methylammonium iodine (MAI)[8], lead halides[9] can passivate the PbS QD surface, leading the improvement QD solar cells, chapter III.

The second combination of materials that we have studied within this thesis is the interaction between MAPI perovskite and organic molecules, being HATNA and DCL97, chapter VI. These molecules were separately

introduced to HP films through the anti-solvent deposition step. Differently to the case of embedding QDs into MAPI matrix, the introduction of HATNA and DCL97 through the anti-solvent step did not cause the change in MAPI structure, confirming by obtaining very similar XRD spectra of MAPI films with and without the organic additives. Grain sizes and crystallinity of HP was clearly affected by embedded QDs and their capping ligands but not in the case of organic additives. However the introduction of organic molecules produced a visual interfacial effect which was dependent on the nature of organic molecules used. In particular, the employment of HATNA resulted in an organic capping layer, which was removed during the deposition of spiro-OMeTAD. While the addition of DCL97 additives changed the film roughness and surface morphology.

The IPCE spectrum of HP-HATNA cell in a comparison with the reference cell, without organic additives, showed an increase in the all wavelength range, especially in the range where the absorption of HATNA is negligible. Hence the increase in the photocurrent obtained in HP-HATNA devices was not due to the co-absorption by the presence of HATNA, but related to better quality of HP. The PL mapping measurement detected at different wavelength ranges (600 - 650 nm and 700 - 750 nm) of HP-DCL97 film showed a full complementary signal, maximum intensities of PL from DCL97 (detected at 600 – 650 nm) were observed in the area where the PL intensities from HP were minimum and vice versa. Moreover, the PL peaks and valley formed a network with feature of hundreds nm size, similar to the size of HP grains. This observation suggested that the organic molecules were located at the grain boundaries of MAPI HP surface. Putting together the IPCE and PL mapping measurement, we concluded that the role of the organic molecules additives is to passivate HP at their grain boundaries resulting in a the better film quality with the subsequent improvement in the performance of HP-organic-based optoelectronic devices including solar cells, LEDs and light amplifiers. The passivation effect was supported by the IS measurement which shows the increase of recombination resistance when HATNA was introduced. In addition, the use of HATNA compound significantly reduced the hysteresis in the photocurrent-voltage scan and showed a better long-term stability in the comparison with the reference cell, without organic additives. HATNA derivatives were also employed as an electron transport material (ETM) in an inverted HP solar cell by another group.[10-11] Coincidentally they also obtained high photoconversion efficiencies (PCEs), extremely low hysteresis and good stabilities including thermal and moisture stabilities. Higher moisture stability was also observed due to the encapsulation function of HATNA as it is naturally hydrophobic. It is worth to note that in our case the encapsulation effect by the presence of HATNA should be much less in

the comparison with their study as the amount of HATNA was much lower in our case.

The interaction of HP with colloidal QDs and organic molecules is produced in different regions of the photovoltaic device. In the interaction with QDs, the interaction carries out within the HP bulk film, while in the interaction with organic molecules it occurs preferentially in the top surface of the HP layer. We observed that the formation and properties of HP were influenced differently. The introduction of organic compounds only caused the interfacial change, due to our preparation method. However embedding QDs in HP matrix has a bigger impact in both morphology and structure of HP. On one hand QDs can act as seed-like sites to promote the crystallization of HP. On the other hand, the crystal lattice of HP can be distorted (expanded or shrunk) caused by the mismatched lattice of QDs and HP. Certainly this distortion depends majority on QD concentrations and on the QD's ligands. And logically the type and the size of QDs used also have an influence on HP's morphology and structure however this is beyond of the scope of the thesis.

In HP optoelectronic devices, electron transport materials (ETMs) is usually needed to extract efficiently electrons from the active layer to the external load or to inject electrons from external load into an active layer. It has been well documented that the transmittance of ETMs and the band alignment between ETM and HP is a key factor in the performance of devices. Within this thesis, we have investigated another aspect of ETMs which is the 'substrate role' for the formation of HP because in the regular (n-i-p) configuration, HP is directly deposited on an ETM, chapter VII. In fact, the surface of ETMs strongly influences on the nuclei creation and the growth of HP. As discussed in the chapter I.2.3, there is a number of factors of ETMs affecting on the formation of HP such as the nature,[12-15] the structure (planar or mesoporous)[16-17] and temperature.[18-20] In this study we showed that not only the preparation methods[14, 21] of ETMs but also the preparation conditions[13, 21] affect the formation of HP. Interestingly, we observed the effect of ETMs on not only fresh HP films and devices but also on aged ones. Briefly we prepared ZnO ETMs by spray pyrolysis methods, however using two different gas components (N_2 and O_2 flows) which provided the different ratio of O_2 in gas. At high FTO substrate's temperature (450ºC), it is exercised that the difference amount of O_2 affects the thermal decomposition and oxidation of precursors. This fact explain the difference in ZnO films obtained in morphology, conductivity and absorption offset by using these two gas components. Those different characters of ZnO ETMs slightly altered the formation of MAPI HP films, however the effect of those characters was

observed much stronger during the storage. Better film quality in term of grain sizes and degree of preferential orientation was obtained for MAPI film deposited on ZnO prepared with N_2 gas (ZnO_N_2) while MAPI coated on another ZnO (prepared with O_2 gas, ZnO_O_2) degraded after 15 days of preparation. Similar effect was obtained for planar solar cell devices, improvement in PCE even after more than one month of preparation for the use of ZnO_N_2 while other devices containing ZnO_O_2 started to decrease after 13 days. Interestingly the performance of ZnO_O_2 based devices could be improved, still showing an increase in PCE after one month of preparation, by modifying the spray pyrolysis conditions as concentration of precursors and FTO's temperatures. Here we showed that the ETMs not only have an important role in the electron extraction but also in the formation and the evolution of HP, consequently in the device performance as well as long term device stability.

References

1. Ning, Z.; Gong, X.; Comin, R.; Walters, G.; Fan, F.; Voznyy, O.; Yassitepe, E.; Buin, A.; Hoogland, S.; Sargent, E. H. Quantum-dot-in-perovskite solids. *Nature* **2015,** *523* (7560), 324-328.
2. Galar, P.; Piatkowski, P.; Ngo, T. T.; Gutiérrez, M.; Mora-Seró, I.; Douhal, A. Perovskite-quantum dots interface: Deciphering its ultrafast charge carrier dynamics. *Nano Energy* **2018,** *49*, 471-480.
3. Gong, X.; Yang, Z.; Walters, G.; Comin, R.; Ning, Z.; Beauregard, E.; Adinolfi, V.; Voznyy, O.; Sargent, E. H. Highly efficient quantum dot near-infrared light-emitting diodes. *Nat Photon* **2016,** *10* (4), 253-257.
4. Jung, Y.-K.; Butler, K. T.; Walsh, A. Halide Perovskite Heteroepitaxy: Bond Formation and Carrier Confinement at the PbS–CsPbBr3 Interface. *The Journal of Physical Chemistry C* **2017,** *121* (49), 27351-27356.
5. Yang, Z.; Janmohamed, A.; Lan, X.; García de Arquer, F. P.; Voznyy, O.; Yassitepe, E.; Kim, G.-H.; Ning, Z.; Gong, X.; Comin, R.; Sargent, E. H. Colloidal Quantum Dot Photovoltaics Enhanced by Perovskite Shelling. *Nano letters* **2015,** *15* (11), 7539-7543.
6. Dirin, D. N.; Dreyfuss, S.; Bodnarchuk, M. I.; Nedelcu, G.; Papagiorgis, P.; Itskos, G.; Kovalenko, M. V. Lead Halide Perovskites and Other Metal Halide Complexes As Inorganic Capping Ligands for Colloidal Nanocrystals. *Journal of the American Chemical Society* **2014,** *136* (18), 6550-6553.
7. Zhang, X.; Zhang, J.; Phuyal, D.; Du, J.; Tian, L.; Öberg, V. A.; Johansson, M. B.; Cappel, U. B.; Karis, O.; Liu, J.; Rensmo, H.; Boschloo, G.; Johansson, E. M. J. Inorganic CsPbI3 Perovskite Coating on PbS Quantum Dot for Highly Efficient and Stable Infrared Light Converting Solar Cells. *Advanced Energy Materials* **2018,** *8* (6), 1702049.

8. Ning, Z.; Dong, H.; Zhang, Q.; Voznyy, O.; Sargent, E. H. Solar Cells Based on Inks of n-Type Colloidal Quantum Dots. *ACS nano* **2014,** *8* (10), 10321-10327.

9. Liu, M.; Voznyy, O.; Sabatini, R.; García de Arquer, F. P.; Munir, R.; Balawi, Ahmed H.; Lan, X.; Fan, F.; Walters, G.; Kirmani, Ahmad R.; Hoogland, S.; Laquai, F.; Amassian, A.; Sargent, Edward H. Hybrid organic–inorganic inks flatten the energy landscape in colloidal quantum dot solids. *Nature materials* **2016,** *16*, 258.

10. Zhao, D.; Zhu, Z.; Kuo, M.-Y.; Chueh, C.-C.; Jen, A. K.-Y. Hexaazatrinaphthylene Derivatives: Efficient Electron-Transporting Materials with Tunable Energy Levels for Inverted Perovskite Solar Cells. *Angewandte Chemie International Edition* **2016,** *55* (31), 8999-9003.

11. Zhu, Z.; Zhao, D.; Chueh, C.-C.; Shi, X.; Li, Z.; Jen, A. K. Y. Highly Efficient and Stable Perovskite Solar Cells Enabled by All-Crosslinked Charge-Transporting Layers. *Joule* **2018,** *2* (1), 168-183.

12. Climent-Pascual, E.; Hames, B. C.; Moreno-Ramírez, J. S.; Álvarez, A. L.; Juarez-Perez, E. J.; Mas-Marza, E.; Mora-Seró, I.; de Andrés, A.; Coya, C. Influence of the substrate on the bulk properties of hybrid lead halide perovskite films. *Journal of Materials Chemistry A* **2016,** *4* (46), 18153-18163.

13. Yang, J.; Siempelkamp, B. D.; Mosconi, E.; De Angelis, F.; Kelly, T. L. Origin of the Thermal Instability in CH3NH3PbI3 Thin Films Deposited on ZnO. *Chemistry of Materials* **2015,** *27* (12), 4229-4236.

14. Dong, X.; Hu, H.; Lin, B.; Ding, J.; Yuan, N. The effect of ALD-Zno layers on the formation of CH3NH3PbI3 with different perovskite precursors and sintering temperatures. *Chemical communications* **2014,** *50* (92), 14405-14408.

15. Olthof, S.; Meerholz, K. Substrate-dependent electronic structure and film formation of MAPbI3 perovskites. *Scientific reports* **2017,** *7*, 40267.

16. Grancini, G.; Marras, S.; Prato, M.; Giannini, C.; Quarti, C.; De Angelis, F.; De Bastiani, M.; Eperon, G. E.; Snaith, H. J.; Manna, L.; Petrozza, A. The Impact of the Crystallization Processes on the Structural and Optical Properties of Hybrid Perovskite Films for Photovoltaics. *The journal of physical chemistry letters* **2014,** *5* (21), 3836-3842.

17. Pascoe, A. R.; Yang, M.; Kopidakis, N.; Zhu, K.; Reese, M. O.; Rumbles, G.; Fekete, M.; Duffy, N. W.; Cheng, Y.-B. Planar versus mesoscopic perovskite microstructures: The influence of CH3NH3PbI3 morphology on charge transport and recombination dynamics. *Nano Energy* **2016,** *22*, 439-452.

18. Zhang, H.; Zhao, C.; Li, D.; Guo, H.; Liao, F.; Cao, W.; Niu, X.; Zhao, Y. Effects of substrate temperature on the crystallization process and properties of mixed-ion perovskite layers. *Journal of Materials Chemistry A* **2019,** *7* (6), 2804-2811.

19. Wang, Y.; Liu, S.; Zeng, Q.; Wang, R.; Qin, W.; Cao, H.; Yang, L.; Li, L.; Ji, W.; Yin, S. Controllable Crystal Film Growth via Appropriate Substrate-Preheating Treatment for Perovskite Solar Cells Using Mixed Lead Sources. *IEEE Journal of Photovoltaics* **2018,** *8* (1), 162-170.

20. Tidhar, Y.; Edri, E.; Weissman, H.; Zohar, D.; Hodes, G.; Cahen, D.; Rybtchinski, B.; Kirmayer, S. Crystallization of Methyl Ammonium Lead Halide Perovskites: Implications for Photovoltaic Applications. *Journal of the American Chemical Society* **2014,** *136* (38), 13249-13256.

21. Tseng, Z.-L.; Chiang, C.-H.; Wu, C.-G. Surface Engineering of ZnO Thin Film for High Efficiency Planar Perovskite Solar Cells. *Scientific reports* **2015,** *5*, 13211.

Chapter IX. Conclusions and Future investigation

In this chapter we present the conclusions drawn from the five articles included in the thesis and published in recognized scientific international journals. Within this thesis we have studied the interaction of MAPI HP with three different materials, being QDs, organic molecules and ETMs. The interaction was carried out in three different positions of HP films including two surfaces (top and bottom surfaces) and within bulk film. All these materials have a strong influence on the formation and properties of HP, as well as HP film stability, consequently impact on the performance and stability of HP devices.

- Beside the role of electron extraction and injection, ETMs also have a strong influence on not only the formation of fresh HP but also on the evolution of HP with storage time. Consequently ETMs not only affect the performance of fresh devices but also on the device stability. Any modification in the preparation of ETMs can lead the variation HP film quality and later in HP device performance and stability.

- The organic molecules were introduced to HP during the anti-solvent deposition step. Therefore the introduction of those organic molecules mostly affect the HP top surface. Concretely grain boundaries of HP' surface were efficiently passivated by the presence of organic molecules resulting in a better film quality and device performance.

- QDs were dissolved in a solution containing HP precursors, thereby the incorporation of colloidal QDs heavily impacts on the formation of HP films.

  - The crystallization of HP is promoted faster when QDs were introduced as they act as nucleation centers. The crystallization of HP is dependent on the concentration of QDs, higher concentration produces a faster crystallization.

- The nature of QD capping ligand also has an influence on the growth of HP.

- QDs in HP matrix can act as recombination centers causing the deduction in the device performance. Therefore a proper amount of QDs, usually very small, needs to introduce in HP matrix in order to get the benefit, including the improvement of morphological, optical and structure properties, from the nucleation center role of QDs.

- The interaction between HP and QDs also produces a new phenomenon/property which is the emission of the exciplex state, caused by the type II band alignment at HP/QD interface. Electrons in HP CB can recombine with holes in the VB of QDs emitting photons with lower energy than the bandgap of both two materials.

In summary, the interaction between HP and other materials studied and presented in this doctoral thesis shows that the combination of materials with different natures has a huge potentiality for the development of HP optoelectronic devices. HP is very promising material family which has been potentially applied in different optoelectronic devices, especially HP solar cells have reached high photoconversion efficiency (over 25%) in a very short time, within the last 10 years. However, remained issues in HP devices are low stabilities, use of hazardous elements and further improvement of performance. Constructive synergy can be obtained from the combination of HP and other materials, helping to solve some of these issues. We have showed a proper preparation method and its suitable conditions of electron transport materials can significantly improve not only the performance of solar cell devices but also their long-term stability. Higher HP film quality can be achieved by combining HP with either QDs or organic molecules, resulting an enhancement in the device performance. A strong reduction in hysteresis can be obtained by combining HP with organic molecules. Moreover the combination of HP and QDs induced an exciplex emission deeply in infrared region (IR) as the energy of the exciplex photons is smaller than the bandgap of both HP and QDs. This observation importantly contributes to the development of LEDs in IR. On the hand, the detection of exciplex emission also opens a possibility to prepare immediate band solar cells in order to increase the photocurrent by absorbing more photons at energies lower than the bandgap of a semiconductor absorber.

As presented in the thesis, we have obtained some advantages from the interaction between HP and QDs, which are the improvement in HP film's

quality and device performance; and the detection of exciplex emission. In those studies, we have used PbS core and PbS/CdS core/shell QDs however at only one QD size. Very interesting studies on the combination of those materials should be investigated are the effect of QD sizes and the use of different QD type, for example PbSe QDs. The Bohr radius of PbSe (46 nm) is much higher than that of PbS (18 nm), an immediate bands in solar cells can be easier achieved by embedding PbSe QDs in HP matrix. This new approach will be investigated in a future research.